



Universiteit
Leiden
The Netherlands

Sensing transport: label-free in vitro assays as an atTRACTive alternative for solute carrier transporter drug discovery

Sijben, H.J.

Citation

Sijben, H. J. (2022, November 23). *Sensing transport: label-free in vitro assays as an atTRACTive alternative for solute carrier transporter drug discovery*. Retrieved from <https://hdl.handle.net/1887/3487027>

Version: Publisher's Version

License: [Licence agreement concerning inclusion of doctoral thesis in the Institutional Repository of the University of Leiden](#)

Downloaded from: <https://hdl.handle.net/1887/3487027>

Note: To cite this publication please use the final published version (if applicable).

The research in this thesis was performed at the Division of Drug Discovery and Safety of the Leiden Academic Centre for Drug Research (LACDR), Leiden University, The Netherlands. This project has received funding from the Innovative Medicines Initiative 2 Joint Undertaking under grant agreement No 777372. This Joint Undertaking receives support from the European Union's Horizon 2020 research and innovation programme and EFPIA.

Cover design and thesis layout by Huub Sijben

This thesis was printed by GildePrint (www.gildeprint.nl)

© Huub Sijben 2022

ISBN: 978-94-6419-539-2

All rights reserved. No part of this thesis may be reproduced in any form or by any means without permission of the author.



SENSING TRANSPORT

Label-free *in vitro* assays as an attractive alternative
for solute carrier transporter drug discovery

PROEFSCHRIFT

ter verkrijging van
de graad van doctor aan de Universiteit Leiden,
op gezag van rector magnificus prof. dr. ir. H. Bijl,
volgens besluit van het college voor promoties
te verdedigen op woensdag 23 november 2022
klokke 16:15 uur

door

Hubert Jacob Sijben
geboren te Woerden, Nederland
in 1993

Promotores

Prof. dr. A.P. IJzerman
Prof. dr. L.H. Heitman

Promotiecommissie

Prof. dr. H. Irth
Prof. dr. J.A. Bouwstra
Prof. dr. D.J. Slotboom (Rijksuniversiteit Groningen)
Prof. dr. U. Gether (University of Copenhagen)
Dr. S. Sucic (Medical University of Vienna)
Dr. J.M. Zweemer

SENSING TRANSPORT

TABLE OF CONTENTS

Chapter 1

General introduction	9
----------------------------	---

Chapter 2

Targeting solute carriers to modulate receptor–ligand interactions.....	31
---	----

Chapter 3

A study of the dopamine transporter using the TRACT assay: a novel <i>in vitro</i> tool for solute carrier drug discovery.....	39
---	----

Chapter 4

Label-free high-throughput screening assay for the identification of norepinephrine transporter inhibitors	67
---	----

Chapter 5

Proteochemometric modeling identifies chemically diverse norepinephrine transporter inhibitors	93
---	----

Chapter 6

Impedance-based phenotypic readout of transporter function: a case for glutamate transporters.....	119
---	-----

Chapter 7

Molecular insights into disease-associated glutamate transporter variants using <i>in silico</i> and <i>in vitro</i> approaches.....	155
---	-----

Chapter 8

General discussion, conclusions and future perspectives	185
---	-----

Appendix

Table A.1–A.2.....	219
--------------------	-----

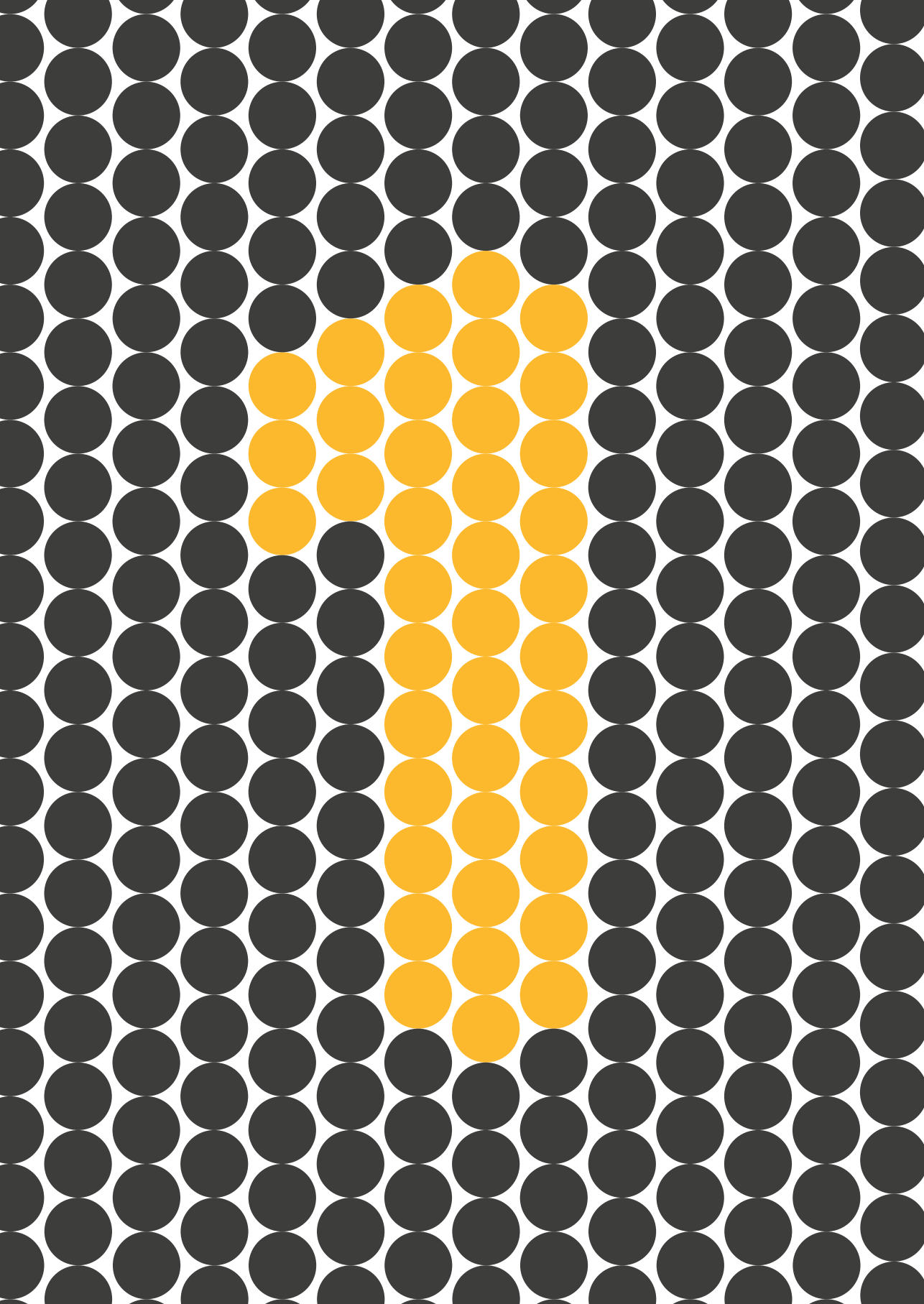
Summary.....	239
--------------	-----

Nederlandse samenvatting.....	243
-------------------------------	-----

List of publications.....	247
---------------------------	-----

Curriculum vitae.....	249
-----------------------	-----

Acknowledgements.....	251
-----------------------	-----



CHAPTER 1

General introduction

Solute carrier (SLC) transporters are a large and diverse class of relatively understudied transmembrane proteins. Due to their critical role in cellular homeostasis, physiological processes and disease development, there is a great number of SLCs that have the potential to be viable drug targets for the treatment of disease. Robust assays are required to identify and characterize potential drugs for SLCs, which are often screened *in vitro* using cell-based or cell-free systems. Conventional assays either require the use of chemical labels, which i) can be invasive and compromise a cell's physiology, ii) are based on end-point measurements, iii) use cell preparations and/or iv) do not allow screening of a large number of compounds. This thesis presents the development and application of novel label-free assays based on electrical impedance that allow the assessment of functional activity for three human SLCs: the dopamine transporter (DAT, SLC6A3), norepinephrine transporter (NET, SLC6A2) and excitatory amino acid transporters (EAAT, SLC1 family). With the ability to screen and characterize SLC inhibitors, these assays are a new addition to the ever-expanding toolbox for SLC transporters and could prove valuable in drug discovery programs for a wide range of diseases.

1.1 – The cell membrane, receptors and transporters

Life exists by the presence of barriers. Take any organism and its existence is legitimized by the encapsulation of its vital contents with a bilayer of lipids. This membrane demarcates the perimeter of what we define as a ‘cell’ and it is the true boundary that prevents the building blocks of life – the proteins, enzymes, organelles, genetic material and all else – from floating around purposelessly¹. As such, the membrane enforces the exact organization of a cell by keeping its contents all in one place, so that the proteins and nucleic acids that makes any single cell perform its genetically imprinted function have the opportunity to interact with each other and fulfill their role. In addition, it safeguards the cell from hostile intrusions by fending off viruses, bacteria and other micro-organisms. However, the membrane is not a mere wall that hermetically shuts off the outside from the inside. On the contrary, what makes cellular membranes truly unique – and in that sense, essential to grant the existence of life – is their ability to embed specific proteins that provide cells with a means to take up nutrients, excrete waste and allow selective communication of the cell with its environment and *vice versa*². By studying the molecular functions, tertiary structures, protein interactions, expression patterns and regulatory mechanisms of these proteins we obtain a better understanding of their roles in physiology (e.g., metabolism, signaling, homeostasis) and pathology (e.g., overactivity, deficiency, disease-related mutations)³. By utilizing this knowledge, we can rationally design and develop better drugs and interventions that – temporarily or permanently – restore or disrupt the functions of these proteins, thereby treating disease and increasing quality of life for patients^{4–6}.

Besides forming a barrier between the outside and the inside of a cell, the lipid bilayer membrane also functions to form subcellular compartments such as the nucleus, endoplasmic reticulum, lysosomes and mitochondria, each harboring their own cell-specific set of proteins. Taking a closer look at these cellular membranes, two main types of transmembrane proteins can be identified: receptors and transporters. In essence, a **receptor** is any protein that can bind a specific ligand (e.g., ions, small molecules, proteins), which either leads to a functional effect inside or outside the cell or is idle. Examples of receptors are G-protein coupled receptors (GPCR), receptor tyrosine kinases, immune receptors, enzymes, nuclear receptors and cell adhesion molecules^{7–11}. On the other hand, a **transporter** is a protein that facilitates the active or passive movement of substrates (e.g., water, ions, small molecules, peptides) across a membrane. Examples of transporters are (ligand-gated) ion channels, ATP-binding cassette (ABC) transporters and solute carrier (SLC) transporters^{12–15}. Together, these protein classes make it possible for a cell to receive extracellular signals – from its environment, other cells, or itself – and respond accordingly. Although cells can exploit other mechanisms, such as endocytosis and exocytosis, to exchange small and large molecules with its surroundings, the transporters of the transmembrane protein pools constitute the mainline of a cell’s communication. It is therefore no surprise that deficits in transporters contribute substantially to the etiology of a wide range of diseases, including genetic disorders^{16,17}, cancer^{18,19}, metabolic disease²⁰ and neurological disorders²¹, making them attractive targets for the development of therapeutic drugs.

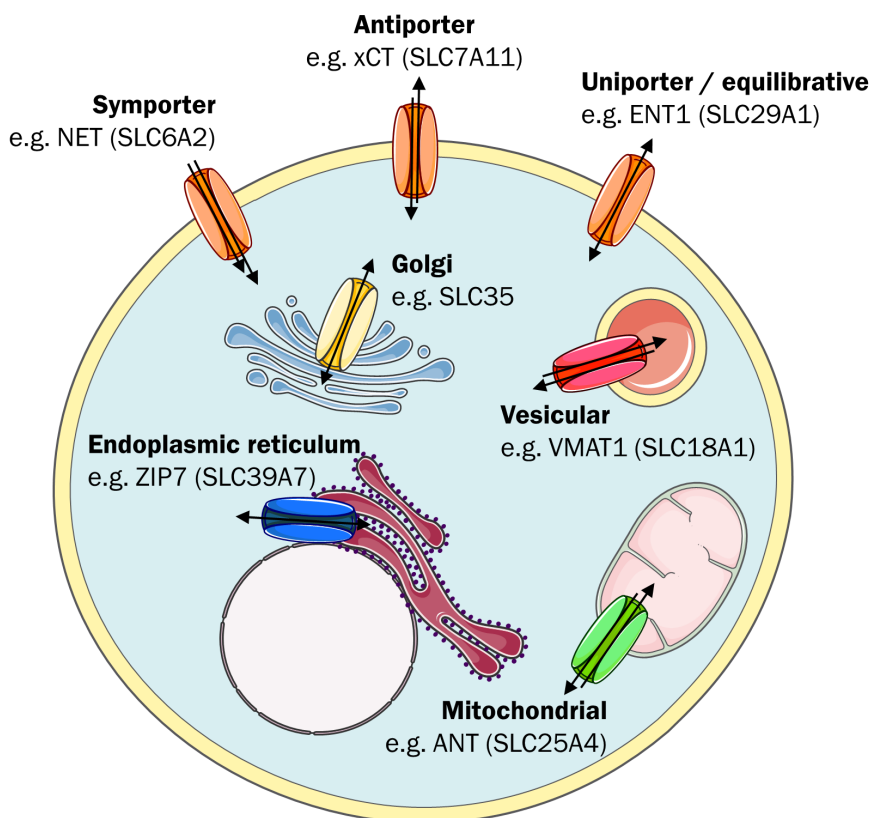


Figure 1.1 – A brief overview of the different types and subcellular localizations of solute carrier (SLC) transporters. This figure incorporates drawings from Servier Medical Art (smart.servier.com).

1.2 – Solute carrier (SLC) transporters: an understudied group of potential drug targets

By far the largest fraction of clinically approved drugs (~30%) exert their therapeutic effect primarily or indirectly by modulation of receptors of the GPCR superfamily, where GPCRs account for 12% of all approved human drug target genes²². This family has a rich history of successful drug development and continues to receive widespread attention from the scientific communities²³. However, when looking systematically at the various ‘druggable’ protein families versus the number of publications and the amount of drug-like compounds attributed to them, we learn there is one group in particular sticking out as one that has received relatively little attention: the **solute carrier (SLC)** superfamily of transporters^{24,25}.

SLCs comprise the second-largest membrane-bound protein family behind GPCRs, with roughly 450 members currently categorized into 66 major subfamilies and several ‘atypical’

transporters being unclassified^{12,14,26,27}. SLCs do not require the consumption of adenosine triphosphate (ATP) to operate and comprise both facilitative transporters – which are equilibrative and transport a substrate down its concentration gradient – and secondary active transporters – which can be antiporters or symporters that utilize an electrochemical gradient (e.g. Na⁺) to transport a substrate with or against its concentration gradient (**Figure 1.1**)¹². SLCs are mainly localized at the plasma membrane and are known to be expressed on vesicles, lysosomes, Golgi apparatus and endoplasmic reticulum, with a large subfamily (SLC25) exclusively expressed in mitochondria^{27,28}. In addition, the uptake and excretion of many pharmaceutical drugs is mediated *via* SLCs, which is crucial for drug distribution but also facilitates unwanted drug-drug interactions^{29,30}. To bring order to this multitude of attributes, the nomenclature of SLCs has been instated twenty years ago to harmonize the members of this superfamily, naming the genes as “SLC” followed by the family number, a letter (usually A) and the member number (e.g., SLC1A1)³¹. Since many SLCs were first characterized prior to this harmonization, the protein names are often related to their originally described function and can differ between species (e.g., SLC1A1 is known as EAAT3 (human) and EAAC1 (rodents))³². As such, multiple names are often linked to a single SLC, making systematic queries confusing and cumbersome.

The division of SLCs into subfamilies is mainly based on their shared tertiary protein structure (‘fold’), substrate specificity, mode of action and/or subcellular localization. As opposed to kinases or GPCRs, which share distinct structural and functional motifs and binding sites between family members, SLCs are widely different from each other even within subfamilies, which results in a notorious difficulty to develop an all-encompassing, one-size-fits-all approach to study these proteins. In part owing to the challenges that have impeded the proper characterization of transporters, the majority of SLCs have been long ‘neglected’ from a molecular biological and drug development perspective. In fact, it is estimated that roughly 30 percent of currently identified SLCs is regarded to be ‘orphan’, having no verified substrate or function ascribed to them^{32,33}. Moreover, SLCs were found to be the protein family with the greatest ‘publication asymmetry’, meaning that the vast majority of papers focused on only a few SLCs (such as the neurotransmitter (SLC6) and glucose (SLC2) transporters) and that more than 200 SLCs have less than 15 publications attributed to them²⁴. Related to this, inquiries over the past ten years have indicated that less than 5% of SLCs (<20) are targeted by approved drugs for which the mechanism of action is primarily attributed to direct modulation of the SLC, with the majority of drug classes being antidepressants (reuptake inhibitors acting *via* SLC6 family neurotransmitter transporters), antihypertensives (mainly loop diuretics acting *via* SLC12 family Na⁺/K⁺/Cl⁻ transporters) and, more recently, antidiabetics (inhibitors of Na⁺/glucose cotransporter 2 (SGLT2) of the SLC5 family)^{24,25,34,35}. While these are communally important and widely prescribed drugs, there are immense opportunities for other SLCs that are involved in the development of other diseases.

Most of the current SLC-targeting drugs were discovered before there was any knowledge on the mechanism of action or the involvement of transporters. According to Lin *et al.*, at least 84 SLCs are implicated in rare, inheritable monogenic disorders that may form the basis for the specific development of new drugs¹⁷. Indeed, new disease areas are being associated

with SLC malfunction and by a more rational drug design several compounds are currently undergoing clinical trials for at least ten SLCs that previously have not been the targets of drugs^{6,25}. As a result of the high disease relevance and druggability potential on the one hand and systematic lack of exploration on the other, there have been community-based efforts to ignite the spark and kick-start a wide-spread, full-on frontal approach to characterize SLCs in all their facets: functional deorphanization, disease association, biochemical reagent generation, structure elucidation, assay development and drug discovery^{24,36}.

1.3 – The RESOLUTE consortium: enabling SLC research

In July 2018, a group of researchers from academia, including the team which I am part of, and members of the European Federation of Pharmaceutical Industries and Associations (EFPIA) kicked off the European Innovative Medicines Initiative (IMI) consortium **RESOLUTE** – Research Empowerment on Solute Carriers (www.re-solute.eu)³⁶. The main aim of this consortium is to coordinate major efforts towards the generation of long-lasting research tools to study SLCs, ultimately leading to deorphanization on a large scale: linking each SLC to its corresponding substrate(s). To achieve this, RESOLUTE operates with an emphasis on publishing open-access data and facilitates the development and generation of: 1) plasmids and cell lines, which enable the knock-out or expression of a single SLC for functional assessment; 2) “omics” approaches to identify SLC substrates and protein interactions; 3) cell-based and cell-free assays to study SLC function and identify inhibitors and modulators; 4) purified protein and SLC-specific antibodies to facilitate structure determination and assay development. The data and conclusions presented in this thesis fully support the philosophy and overarching ambitions of RESOLUTE, to the extent that it will aid drug development in innovative ways and help propel the SLCs towards the long overdue status as one of the main drug target families.

1.4 – Assays and methodologies to study SLCs in vitro

Each SLC transporter has specific stoichiometries by which it translocates ions and/or solutes across the membrane with each transport cycle. In order to understand and measure the activity of a transporter upfront knowledge is required of the amount and identity of the ions and molecules that are involved. Since it is quite challenging to directly probe protein function in live humans or animals, the initial steps in the functional characterization of an SLC are the use of *in vitro* assays. These methodologies often use native or engineered cell systems that (over)express the SLC of interest compared to cells that lack this particular SLC. Depending on the substrate(s) and stoichiometry of a transporter and its localization in the cell, various methodologies can be employed to acquire information on the transport kinetics (activity, defined by the Michaelis-Menten constant K_m , and maximal transport velocity, defined by V_{max}) and, in case of SLC inhibitors, inhibitory potencies (IC_{50} , inhibitor concentration at which 50% of the substrate uptake/effect is inhibited)^{25,37,38}. SLC assays are broadly based on 1) direct detection of substrate binding, uptake or efflux; 2) secondary

Table 1.1 – Characteristics, advantages and limitations of previously established *in vitro* SLC assays

Assay	Label-free	Through-put level	Live cells	Real time	<div><div>+</div><div>–</div></div>	Advantages Limitations
Substrate detection – uptake and binding assays						
Radioactive substrate uptake (or binding)	No	Low – Medium	Yes	Yes	<div>+</div>	Kinetic determination (K_m , V_{max}) Versatile readout for many SLCs
					<div>–</div>	Requires radiolabeling of substrate Radioactive handling and waste disposal Less suitable for compound screening
Fluorescent substrate uptake (or binding)	No	High	Yes	Yes	<div>+</div>	Increased throughput compared to radiolabels Ease of handling and detection
					<div>–</div>	Non-physiological modification of the (endogenous) substrate – not feasible for every SLC Interference with fluorescent or quenching compounds
Biosensors	No	Medium – High	Yes	Yes	<div>+</div>	High sensitivity and specificity Direct measure of substrate concentration Suitable with intracellular SLCs
					<div>–</div>	Sensor development is time consuming Requires modification of the cell to express the sensor
MS-based transport assay	Yes	Low	Yes	No	<div>+</div>	High sensitivity and specificity Wide range of substrates, including ions Measure multiple compounds per run No labeling of the substrate
					<div>–</div>	End-point measurements, indirect kinetics Complex data output Expensive equipment and specialist skills
Cellular thermal shift assay (CETSA)	Yes	Low – Medium	Yes	No	<div>+</div>	Suitable with purified protein, cell lysates and live cells Direct interaction of compound with SLC Identification of substrates and inhibitors
					<div>–</div>	Not all compounds will stabilize the SLC Likelihood of false-negative results End-point measurements
Secondary effects – functional assays						
Fluorescent dyes	No	High	Yes	Yes	<div>+</div>	Ease of handling and detection Different types of dyes for many types of functionality – adaptable to many SLCs
					<div>–</div>	Often requires SLCs to be electrogenic Requires step to load dyes into cells
Phenotypic assays	Yes/No	Medium – High	Yes	Yes/No	<div>+</div>	Most straightforward readout based on cell viability Applicable to any SLC, irrespective of localization
					<div>–</div>	Requires knowledge on genotype-phenotype relation Substrate redundancy could limit specificity of assay
Electrophysiology						
Patch-clamp	Yes	Very low	Yes	Yes	<div>+</div>	Golden standard for channels and electrogenic SLCs Kinetic determination (K_m , V_{max}) – high time resolution Ideal for mechanistic studies
					<div>–</div>	Requires SLCs to be electrogenic Specialist skills and equipment Single cell throughput – not suited for screening
Solid-supported membranes (SSM)	Yes	Low – Medium	No	Yes	<div>+</div>	Kinetic determination (K_m , V_{max}) Variation in protein source and membrane composition Increased throughput compared to patch-clamp
					<div>–</div>	Requires electrogenic SLCs or charged substrates Membrane preparations, lacks physiologic environment of the SLC

functional effects upon substrate uptake or efflux; 3) changes in electrical currents elicited by substrate transport. A general overview of these assays is found in **Table 1.1**.

According to an analysis of the ChEMBL database, which is manually curated and reports protein-specific bioactivity data for drug-like molecules, by far the majority of substrate uptake (>43%) and binding assays (87%) use radiolabeled compounds³⁸. Historically, radioligands have been widely used to perform pharmacological experiments due to the relative ease of the detection principle and compound radiolabeling, making the technique versatile for many SLCs³⁹. The assay readout is based on the amount of radioactivity bound to the SLC (in the case of binders/inhibitors) or accumulated in the cells (in the case of substrates).

However, a major concern of the use of radioactivity is that a specialized infrastructure is required for appropriately certified lab space, personnel and waste disposal, which can be costly and is not always available. Although it remains the most universal approach to assess SLCs, high-throughput screening (HTS) is less suitable with this technique. Improvements in this regard have been made using the more high-throughput scintillation proximity assays (SPA)⁴⁰. These assays often require purified and solubilized protein which is challenging to achieve for SLCs, although whole-cell SPAs have been reported for some SLCs^{41,42}.

An alternative to radiolabels is the use of fluorescent compounds. In contrast to radioactivity, fluorescence does not require stringent safety precautions and can be measured with most conventional (and HTS) plate readers, which makes the ease of use of fluorescent techniques a major advantage⁴³. For some SLCs, fluorescent substrate analogs are available that mimic transport properties of endogenous substrates, for example the neurotransmitter analog ASP⁴⁴ and BODIPY-conjugated fatty acid analogs⁴⁵. The highly sensitive readouts and increased throughput – thanks to high-capacity, robotics-operated readers such as the fluorometric imaging plate readers (FLIPR)^{46,47} – make these assays ideal for screening, but come at the cost of a non-endogenous substrate that could display altered kinetics and the potential interference of autofluorescent and quenching compounds. In addition, fluorescent analogs are not readily available for all SLCs, making this approach not universal.

Other techniques that probe SLC function also rely on the use of fluorescence as a readout. Biosensors and dyes, which are either genetically encoded or loaded into the cell, are proteins or complex molecules that contain a moiety that fluoresces or is quenched in the presence of a (SLC) substrate or upon changes in voltage or ionic concentrations. Expression of biosensors can be genetically steered towards various subcellular membranes, offering the advantage to assess intracellular SLCs. Biosensors are often tailor-made to detect a specific substrate^{48,49}, which requires thorough optimization for each application and making them less generally applicable, but the advantage is that they can be used *in vivo*⁵⁰. Fluorescent dyes, such as membrane potential dyes or ion-specific dyes, measure indirect events following substrate transport^{44,51}. As such, these dyes are used for functional assays that can be applied to a wide range of SLCs, given that they induce these secondary effects upon substrate transport. As is the case with other label-based techniques, the loading of the fluorescent dyes could compromise the cellular physiology, making the system more artificial.

The downsides that radioactive or fluorescent labels bring along in SLC assays can be overcome by using label-free techniques, which have been gaining more traction in recent years. Liquid chromatography (LC) and mass spectrometry (MS) are increasingly employed to analyze samples of substrate-treated SLC-expressing cells – both its intracellular and extracellular contents. By quantifying the intracellular accumulation of a substrate after a given amount of time, this provides a direct measure of SLC activity, i.e. influx and efflux of substrate are indirectly detected⁵². Alternatively, LC-MS can be used for targeted and untargeted metabolomics, which allow the quantification of a selected set of metabolites (targeted)^{53,54} or the identification of unknown substrates from plasma or medium samples (untargeted)^{55,56} upon perturbation in cells expressing the transporter. These approaches, when applied successfully, give insight in the mechanism of (orphan) transporters and their role in metabolism⁵⁶. However, the highly advanced equipment and complex data output might make this approach less suited for screening, although cost-effective improvements such as matrix-assisted laser desorption/ionization (MALDI) MS-based approaches rapidly follow up each other⁵².

When the identification of SLC binders (i.e., substrates or inhibitors) is of importance, but the determination of uptake kinetics is not of interest, then other types of assays can be employed. Thermal shift assays (TSA) are based on the thermostabilization of a purified protein in the presence of a molecule that binds – and thereby stabilizes – the protein⁵⁷. The cellular thermal shift assay (CETSA) detects chemical engagement between ligands and membrane proteins on cell lysates or whole cells, which has been successfully validated for SLCs⁵⁸. In addition, the possibilities to use CETSA for screening purposes are expanding with the use of green fluorescent protein (GFP)-tagged SLCs⁵⁹. However, in all cases CETSA uses end-point measurements and is prone to false-negative hits if a compound does bind, but does not stabilize the protein. At the same time, since not every ligand stabilizes a protein upon binding, this makes the assay relatively resistant to false-positive hits⁶⁰.

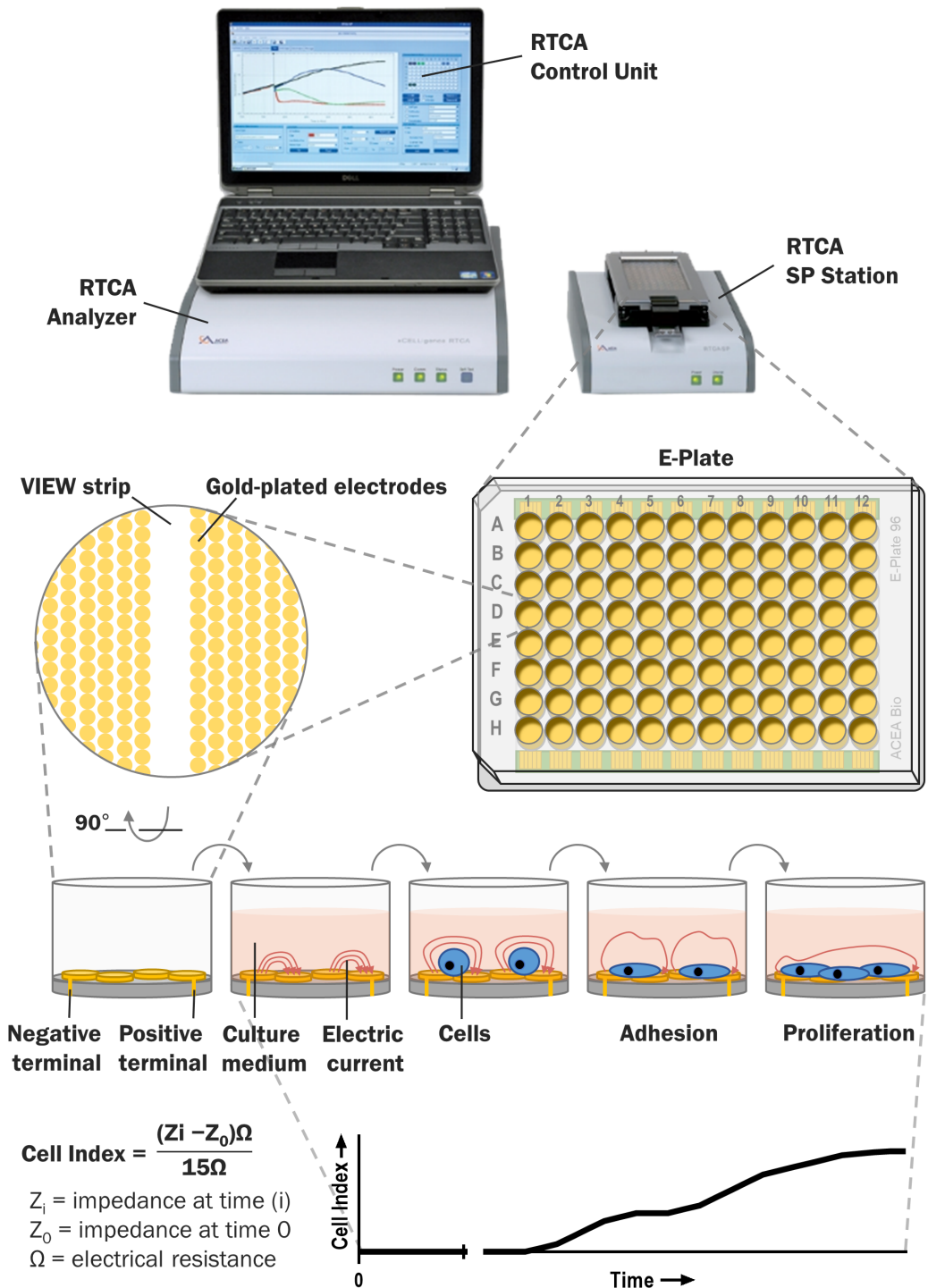
A more general approach to assess the role of a protein in a specific functional outcome is a phenotypic assay. Here, any substrate-induced downstream physiological response can be used as a readout, such as cell viability, gene expression, adhesion or differentiation. While a phenotypic assay is in general less specific and prone to false-positive results – e.g., cell death can be induced *via* multiple pathways – it can usually be performed in a high-throughput setting, making it more suitable for screening purposes⁶¹. For example, these approaches can be interesting to identify the uptake of cytotoxic drugs, by expressing and knocking-out one or multiple sets of SLCs in a model cell line⁶². In this sense, such assays are of tremendous use in determining the mechanism of action and in identifying inhibitors of an SLC. Despite its straightforward readout, the assay requires a robust establishment of the relationship between SLC function and the phenotypic response, which will be unique for each substrate and SLC. Alternatively, SLCs with undefined substrates could be screened for the transport of specific substrates that elicit a phenotypic response, aiding in the deorphanization process.

The aforementioned assays are either based on the use of labels or, if this is not the case, do not permit real-time measurements of the transport processes. A traditional technique to investigate transporters in a label-free setting is the use of patch-clamp electrophysiology, in which the rapid transporter-mediated electrical currents of a single cell are continuously detected in real-time *via* carefully applied electrodes⁶³. This method provides unmatched high-quality data on ions flowing through ion channels or SLCs, and as such is ideal for mechanistic studies⁶⁴. However, the laborious procedure, performed with skilled personnel and specialized equipment, makes this approach unsuitable for screening large numbers of compounds. Automated electrophysiology has greatly improved the handling and throughput, but the signal-to-noise ratio is too low to detect the small currents which SLC transporters usually generate.

In response to this, the arrival of the surface electrogenic event reader (SURFE²R) enabled cell-free electrophysiology of proteins in cell membrane fragments, opening up the possibility to screen large numbers of compounds⁶⁵. The technique is based on the use of solid supported membranes (SSM), to which membrane vesicles containing the transporter are adsorbed. Electrogenic substrate transport into the vesicles leads to a charge difference across the membrane, which generates a capacitive current *via* gold-plated electrodes that is monitored in real-time. Although the SSM-based method has been successfully applied to a range of SLCs⁶⁶, it requires the SLC to be electrogenic (i.e., net positive or negative charge per transport cycle) and is only operable with membrane fractions or artificial liposomes, meaning that this assay cannot be performed in live cells with the appropriate, physiologically relevant environment.

This extensive toolbox of assays that are available for SLCs demonstrates that over the past years innovative ways have been found to investigate transport activity, most of which have proven invaluable for the identification of substrates, inhibitors or modulators. However, considering the various methodologies in **Table 1.1**, it is striking that there is no single assay that ticks all of the boxes. As such, there seems to be an opportunity for a method that is both label-free, compatible with high throughput screening, uses live cells and allows real-time measurements. By making rational use of techniques that have been developed over the past twenty years, this thesis presents the development and application of a novel method that aims to improve upon the limitations of the more conventional assays.

→ **Figure 1.2** – Overview of the xCELLigence real-time cell analysis (RTCA) system. The example shows a 96-well E-plate, which is compatible with a Single Plate (SP) station, but the same principles apply to 16- and 384-well plates. The wells of the E-plate are covered with gold-plated electrodes. The VIEW strip at the bottom of each well allows the user to inspect the E-plate under a light microscope. An electric current is applied to the electrodes in the presence of a conductive medium. The presence, adhesion and proliferation of cells on the electrodes increases the impedance, which is a form of electrical resistance. Impedance is converted to the dimensionless parameter Cell Index, which is plotted in real-time.



1.5 – Label-free impedance-based biosensors: an opportunity for SLC drug discovery

To circumvent the use of chemical labels for pharmacological studies, several label-free techniques have been developed, some of which have been used to study SLCs and are mentioned in the previous section. However, if we want to interrogate a protein in its physiological environment, it is crucial to be able to perform the experiments on live cells with a relevant genetic background (e.g., disease-relevant cell lines). Thus, cell-based label-free assays offer the possibility to study target pharmacology while monitoring live cell behavior at physiological temperatures and in appropriate culture conditions.

In such settings, cells and proteins ‘behave’ more closely to how they would in the human body and provide a better representation of their native physiology. As such, cell-based label-free assays could aid in the translation of *in vitro* data towards *in vivo* outcomes, which would lead to the advancement of effective therapeutics in an earlier stage of drug development. Since these assays focus on changes in whole cell properties – adhesion, proliferation, migration, morphology – they are considered to be phenotypic assays. Techniques that are used to detect this live cell behavior mainly use optical or electrical sensors to generate a readout⁶⁷. Optical biosensors use the refractive properties of light to detect changes in cell shape or protein conformation, examples of which are surface plasmon resonance (SPR), resonant waveguide grating (RWG) and dynamic mass redistribution (DMR)⁶⁸. These techniques will not be further discussed, as these were not used in the context of this thesis.

Electrical biosensors are mostly based on **impedance** – a form of electrical resistance – and make use of highly capacitive (usually gold-plated) electrodes onto which cells can grow allowing their behavior to be monitored in real-time⁶⁹. In a pioneering study from 1984 Giaever & Keese used electrical cell-substrate impedance-sensing (ECIS) with a single electrode to infer the movement of cultured fibroblasts⁷⁰. Since then the low throughput of this system prevented it from widespread use in the screening of compounds, which ultimately led to the development of impedance-based biosensors with increased throughput such as CellKey (discontinued) and **xCELLigence (Figure 1.2)**⁷¹. Impedance-based biosensors have since been used as a versatile *in vitro* tool to study cellular properties such as adhesion⁷², viability⁷³, proliferation⁷⁴, migration⁷⁴ and contractility⁷⁵, as well as monitoring compound cytotoxicity^{75,76} and functional activity of receptor tyrosine kinases⁷⁷ and, mostly, GPCRs^{78,79}. Thanks to its broad range of possibilities, the xCELLigence was selected for the development of SLC assays and will be the prevalent technology in the chapters of this thesis.

The xCELLigence, which is often referred to as a real-time cell analyzer (RTCA), consists of a central control unit – a laptop that collects and visualizes the processed data in real-time – connected to an analyzer that receives its input from a recording station, which is a device located inside a regular cell culture incubator that holds the microtiter plates – called E-plates – onto which the cells are grown (**Figure 1.2**). Depending on the type of recording station, E-plates can contain 16, 96 or 384 wells, which makes the platform amenable to HTS applications⁸⁰. At the bottom of each well is an interleaved array of gold-plated electrodes

connected to a positive and negative terminal and in the presence of a conductive fluid (e.g., buffer or cell culture medium) a weak electrical signal can be applied. This signal is generated by voltages in the mV range with the resulting currents being in the μA range, which are non-invasive for cells allowing repeated measurements during an experiment. The voltages are applied at three predetermined, midrange frequencies – 10, 25 and 50 kHz, of which 10 kHz is the most standard⁸¹ and is used for analysis in this thesis – which produce transcellular currents that grant the detection of changes in cell density and morphology⁸². The electrical current allows the measurement of impedance – that is a combination of the electrical resistance of the solution and the impedance at the electrode surface – which can be consecutively measured by the recording station at intervals of several seconds to minutes. The analyzer receives the impedance values and converts it to a unitless parameter

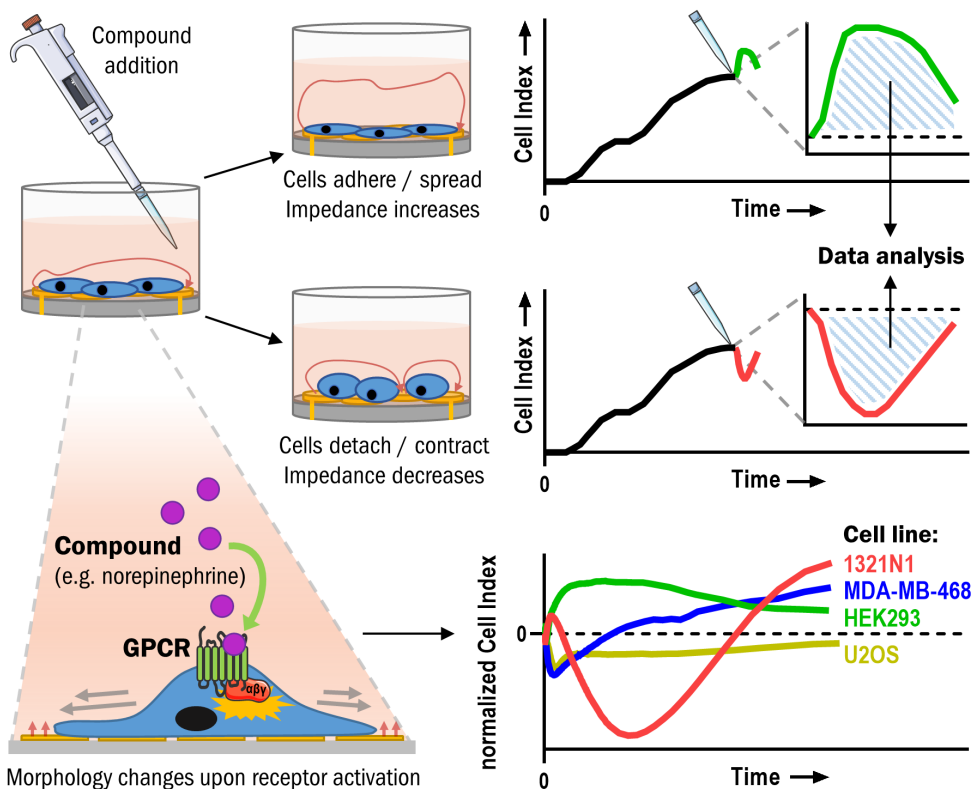


Figure 1.3 – Stimulation of cells with a compound of interest (e.g. a GPCR agonist) results in the engagement of secondary messengers (e.g., G proteins) and subsequent changes in cell morphology that are recorded as a characteristic change in impedance (i.e., Cell Index) over time. The resulting cellular response is dependent on the compound that is used, the subtype of receptor(s) expressed and the cellular background. The bottom-right illustration demonstrates that a single compound (in this case, norepinephrine) produces four different cellular responses over time in four different cell lines. This figure incorporates drawings from Servier Medical Art (smart.servier.com).

called Cell Index (CI) which is then graphed as a function of time (**Figure 1.2**). In the presence of cells, the CI at the electrode surface increases as the cells start to settle and adhere to the bottom of the well. When cells start to spread and proliferate, the CI will generally increase. When cells start to shrink and detach, the CI will generally decrease. This way, the CI is suggestive of cell number and morphology, which can be used to substantiate any hypothesis on cellular functions.

A major application of impedance-based biosensors is their use as a functional assay for GPCRs^{78,79}. A GPCR is a receptor – usually located at the plasma membrane – consisting of seven transmembrane α -helices that upon activation by a ligand (e.g., neurotransmitters, hormones, drugs) couples to intracellular G proteins and other secondary messengers that trigger cascades of downstream processes⁸³. Activation of specific heterotrimeric G proteins can generally lead to increased (G_s) or decreased (G_i) production of cyclic adenosine monophosphate (cAMP), increased Ca^{2+} levels (G_q) and activation of Rho GTPases ($G_{12/13}$), which can regulate a myriad of cellular processes including gene transcription, proliferation, cell contractility and actin cytoskeleton remodeling^{84,85}. Since each GPCR is favorably linked one or more secondary messengers, biochemical assays are used to study each pathway individually as a functional measure of GPCR activation by agonists and/or inhibition by antagonists⁸⁶. However, multiple assays would be needed to capture the entire functional profile of the GPCR, which can be costly and time-consuming. To this end, impedance-based assays have been employed to detect changes in cell morphology, resulting from upstream GPCR activation, as a change in impedance – defined as a cellular response – which can be used to assess receptor pharmacology in live cells (**Figure 1.3**)^{78,79,87}.

Impedance measurements detect the sum of all downstream cellular events that follow upon GPCR activation, which results in a characteristic change of the CI over time that is dependent on the ligand, receptor subtype, the pool of intracellular secondary messengers and the cellular background⁸⁵ (for a comprehensive overview of response profile of GPCRs in impedance assays, see Doijzen *et al.*⁸¹). By titrating the amount of ligand in different wells, potency values (EC_{50} , the concentration at which a compounds induces 50% of the maximal effect) can be determined for ligands that engage with a specific receptor, which are often comparable to those obtained in other functional assays^{88–90}. To this end, cell lines with heterologous overexpression are usually used to ensure receptor specificity, a high number of receptors on the cell surface and – ideally – a better signal-to-noise ratio. However, due to the high sensitivity of the electrical sensor, it is also possible to detect cellular responses in cells with endogenous expression of the GPCR^{91,92} and in non-adherent cells by using a plate coating⁹³, which provides a readout that is more physiologically relevant than heterologous expression systems. This vastly expands the potential applications of xCELLigence and offers advantages over other biochemical assays that are less sensitive.

So far, very little studies have made use of cell-based label-free assays to primarily investigate SLC function. There is a single paper that reports an optical DMR assay (using the EPIC technology) for the sodium-phosphate cotransporter 2b (NaPi-2b, SLC34A2) where the addition of inorganic phosphate to overexpressing MDCK cells results in an increased DMR response, although no mechanistic explanations are provided⁹⁴. In other instances

the xCELLigence was used to detect cytotoxicity induced by the uptake of bacterial cyclopeptides *via* organic anion transporting peptides (OATP1A2, 1B1 and 1B3, SLCO family) in pancreatic cancer cells⁹⁵, as well as cell adhesion which was enhanced in corneal endothelial cells overexpressing a sodium-bicarbonate transporter (NaBC1, SLC4A11)⁹⁶. However, the true potential of xCELLigence as a functional assay for SLCs had thus far not been unlocked.

Recently, a pioneering xCELLigence study by our lab (Vlachdimou *et al.*) demonstrated that cellular responses upon activation of endogenous adenosine receptors (ARs) in an osteosarcoma cell line (U2OS) were diminished in the presence of the endogenous equilibrative nucleoside transporter 1 (ENT1, SLC29A1) – a transporter of the adenosine – on the same cells⁹⁷. Pharmacological inhibition of ENT1 restored the activation of ARs, which the authors defined as a measure of transporter function that could be used as an assay to identify binding and kinetics of ENT1 inhibitors⁹⁸. Thus, these data demonstrate a novel application of impedance-based biosensors to study SLC activity in live cells without the use of chemical labels. Based on these initial findings, it is expected that this label-free assay – which is termed the ‘transport activity through receptor activation’ (**TRACT**) assay in this thesis (**Figure 1.4**) – is not exclusive to the adenosine system, but is more widely applicable to other SLCs as well.

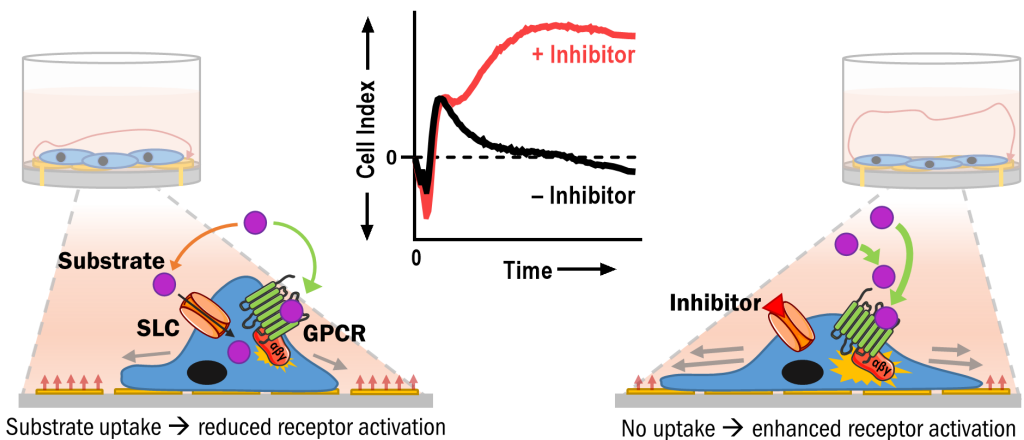


Figure 1.4 – Visualization of the ‘transport activity through receptor activation’ (TRACT) assay principle on xCELLigence. In cells that express both an SLC and GPCR that recognize the same substrate, addition of this substrate to the medium will lead to its uptake via the SLC, resulting in a reduced extracellular concentration of substrate at the cell membrane and, simultaneously, reduced activation of the GPCR which is detected as a change in impedance (i.e., Cell Index) over time. In the presence of an SLC inhibitor, the substrate will not be taken up, resulting in a relatively elevated extracellular concentration of substrate at the cell membrane. As a result, a larger fraction of the substrate is available to activate the pool of GPCRs, resulting in more drastic changes in cell morphology and Cell Index compared to the cells that did not receive the inhibitor. This figure incorporates drawings from Servier Medical Art (smart.servier.com).

1.6 – Aim and outline of this thesis

AIM

The main aim of this thesis is to explore the possibilities of the label-free impedance-based biosensor xCELLigence to study the pharmacology of selected SLCs, with the purpose to provide novel compound screening tools for drug discovery to the transporter communities and beyond. The assay principles that were described in the study by Vlachodimou *et al.*⁹⁷ were used as a starting point for the initial selection of amenable SLCs: if an SLC and GPCR, which respectively transport and are activated by the same substrate(s), are expressed on the plasma membrane of same cell, then the SLC will directly affect the extracellular concentration of the substrate(s) and thereby affect the magnitude of GPCR activation by the substrate(s). Thus, at the base of assay development is the identification of an SLC–GPCR ‘pair’. When looking at the number of known SLCs, GPCRs and endogenous substrates, besides the aforementioned couple of ENT1–ARs and adenosine, there are many more of such ‘pairs’ that play a role in physiology. An extensive overview of these can be found in the **Appendix (Table A.1)**, which will be further discussed in **Chapter 8** of this thesis.

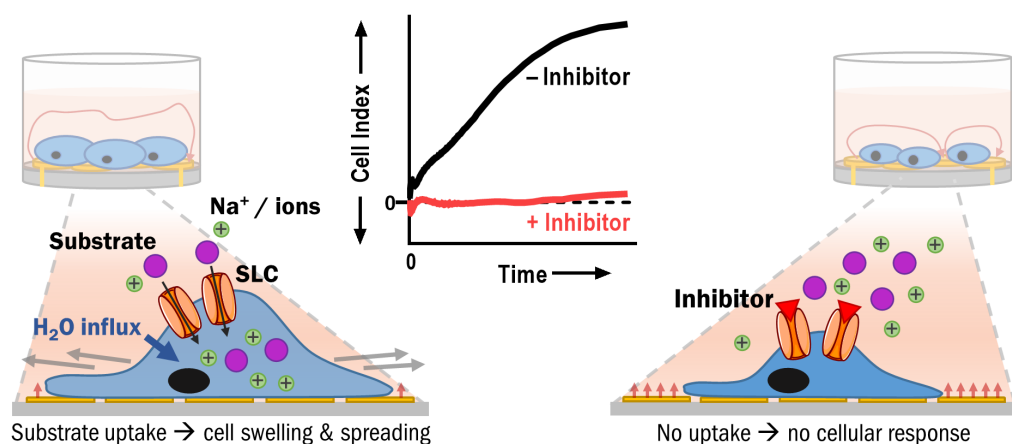


Figure 1.5 – Visualization of the impedance-based phenotypic assay based on SLC-mediated cell swelling. In cells that express an SLC that mediates uptake of a substrate and/or ions, addition of this substrate to the medium leads to influx of substrate and ions. Accumulation of these ions in the cytosol generates an osmotic gradient over the cell membrane. This causes the influx of water and regulation of the ionic content by ion channels and transporters. The resulting increase in cell volume triggers secondary events that lead to cell spreading, which increases the electrode coverage and, thus, the impedance (i.e., Cell Index). SLC inhibition prevents these cellular responses upon addition of the substrate. This figure incorporates drawings from Servier Medical Art (smart.servier.com).

OUTLINE

In **Chapter 2**, a short overview is given on the most recently described examples of SLCs that modulate the activation of GPCRs, which expand upon the traditional dogma of SLCs that remove extracellular substrate from the receptor compartment.

Chapter 3 describes the development of a TRACT assay (**Figure 1.4**) for the human dopamine transporter (DAT, SLC6A3) on the xCELLigence, which is an extension of the previously described assay for ENT1⁹⁷ and is demonstrated in two cell lines each with endogenous expression of a dopamine-responsive GPCR and heterologous expression of DAT.

Chapter 4 reports a label-free TRACT assay for the human norepinephrine transporter (NET, SLC6A2), which expands upon the previous chapter by using various substrates, testing the assay suitability with HTS and comparing inhibitors with a fluorescent substrate uptake assay.

Chapter 5 describes the application of the TRACT assay to test the inhibitory activities of compounds that were predicted by virtual screening to be inhibitors for NET, which demonstrates the applicability of the TRACT assay in a drug discovery setting.

In **Chapter 6**, the xCELLigence is used to detect the activity of excitatory amino acid transporters (EAAT, SLC1 family) using a TRACT assay and a novel impedance-based phenotypic assay based on EAAT-mediated changes in cell morphology as a result of cell swelling (**Figure 1.5**).

Chapter 7 describes the application of the phenotypic assay to characterize substrate and inhibitor responses on ten missense mutants of EAAT1 that were found in cancer patients and rare cases of episodic ataxia.

Chapter 8 concludes this thesis with an overall conclusion of the various impedance-based assays that were developed and discusses their advantages and limitations. Moreover, a mechanistic substantiation of the TRACT assays in this thesis is provided by means of previously reported models. Ultimately, a call is made to increase the awareness of the primary or confounding roles of SLCs in physiological and pharmacological studies, with an emphasis on GPCR ligands, and perspectives are provided that speculate on the future of label-free assays for SLC drug discovery.

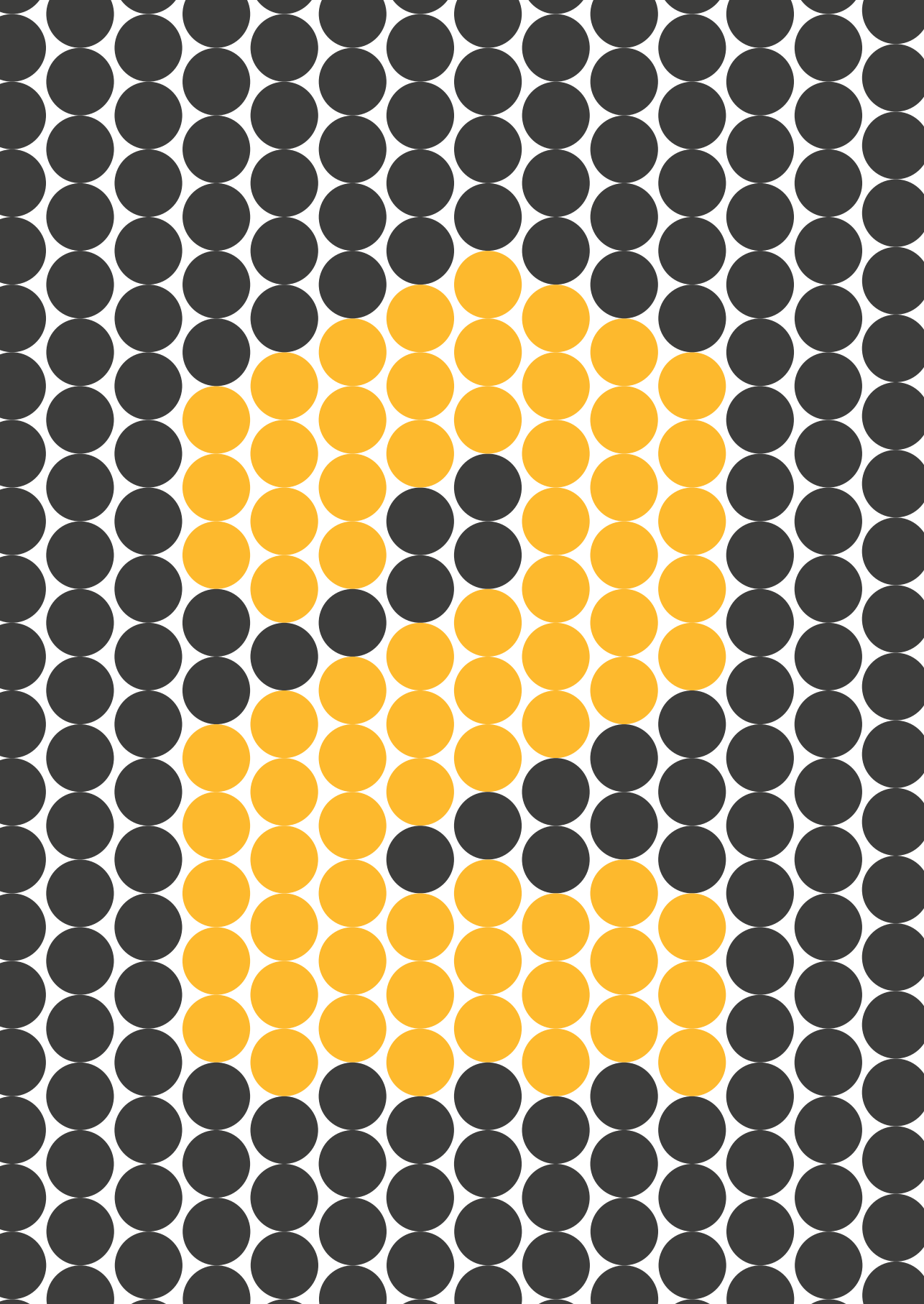
References

- Edidin, M. (2003) Lipids on the frontier: a century of cell-membrane bilayers. *Nat. Rev. Mol. Cell Biol.* **4**, 414–418.
- Robertson, J. L. (2018) The lipid bilayer membrane and its protein constituents. *J. Gen. Physiol.* **150**, 1472–1483.
- Engel, A. & Gaub, H. E. (2008) Structure and mechanics of membrane proteins. *Annu. Rev. Biochem.* **77**, 127–148.
- Congreve, M., de Graaf, C., Swain, N. A. & Tate, C. G. (2020) Impact of GPCR structures on drug discovery. *Cell* **181**, 81–91.
- Colas, C., Ung, P. M.-U. & Schlessinger, A. (2016) SLC transporters: structure, function, and drug discovery. *Medchemcomm* **7**, 1069–1081.
- Garib Singh, R. A. & Schlessinger, A. (2019) Advances and challenges in rational drug design for SLCs. *Trends Pharmacol. Sci.* **40**, 790–800.
- Alexander, S. P. H. *et al.* (2021) The concise guide to pharmacology 2021/22: G protein-coupled receptors. *Br. J. Pharmacol.* **178**, S27–S156.
- Alexander, S. P. H. *et al.* (2021) The concise guide to pharmacology 2021/22: Enzymes. *Br. J. Pharmacol.* **178**, S313–S411.
- Alexander, S. P. H. *et al.* (2021) The concise guide to pharmacology 2021/22: Nuclear hormone receptors. *Br. J. Pharmacol.* **178**, S246–S263.
- Alexander, S. P. H. *et al.* (2021) The concise guide to pharmacology 2021/22: Catalytic receptors. *Br. J. Pharmacol.* **178**, S264–S312.
- Alexander, S. P. H. *et al.* (2021) The concise guide to pharmacology 2021/22: Introduction and Other Protein Targets. *Br. J. Pharmacol.* **178**, S1–S26.
- Hediger, M. A., Cléménçon, B., Burrier, R. E. & Bruford, E. A. (2013) The ABCs of membrane transporters in health and disease (SLC series): Introduction. *Mol. Aspects Med.* **34**, 95–107.
- Thomas, C. & Tampé, R. (2020) Structural and mechanistic principles of ABC transporters. *Annu. Rev. Biochem.* **89**, 605–636.
- Alexander, S. P. H. *et al.* (2021) The concise guide to pharmacology 2021/22: Transporters. *Br. J. Pharmacol.* **178**, S412–S513.
- Alexander, S. P. H. *et al.* (2021) The concise guide to pharmacology 2021/22: Ion channels. *Br. J. Pharmacol.* **178**, S157–S245.
- Schaller, L. & Lauschke, V. M. (2019) The genetic landscape of the human solute carrier (SLC) transporter superfamily. *Hum. Genet.* **138**, 1359–1377.
- Lin, L., Yee, S. W., Kim, R. B. & Giacomini, K. M. (2015) SLC transporters as therapeutic targets: Emerging opportunities. *Nat. Rev. Drug Discov.* **14**, 543–560.
- Bhutia, Y. D., Babu, E., Ramachandran, S. & Ganapathy, V. (2015) Amino acid transporters in cancer and their relevance to ‘glutamine addiction’: Novel Targets for the design of a new class of anticancer drugs. *Cancer Res.* **75**, 1782–1788.
- El-Gebali, S., Bentz, S., Hediger, M. A. & Anderle, P. (2013) Solute carriers (SLCs) in cancer. *Mol. Aspects Med.* **34**, 719–734.
- Schumann, T. *et al.* (2020) Solute carrier transporters as potential targets for the treatment of metabolic disease. *Pharmacol. Rev.* **72**, 343–379.
- Qosa, H. *et al.* (2016) Transporters as drug targets in neurological diseases. *Clin. Pharmacol. Ther.* **100**, 441–453.
- Santos, R. *et al.* (2016) A comprehensive map of molecular drug targets. *Nat. Rev. Drug Discov.* **16**, 19–34.
- Hauser, A. S., Attwood, M. M., Rask-Andersen, M., Schiöth, H. B. & Gloriam, D. E. (2017) Trends in GPCR drug discovery: New agents, targets and indications. *Nat. Rev. Drug Discov.* **16**, 829–842.
- César-Razquin, A. *et al.* (2015) A call for systematic research on solute carriers. *Cell* **162**, 478–487.
- Wang, W. W., Gallo, L., Jadhav, A., Hawkins, R. & Parker, C. G. (2020) The druggability of solute carriers. *J. Med. Chem.* **63**, 3834–3867.
- Perland, E., Bagchi, S., Klaesson, A. & Fredriksson, R. (2017) Characteristics of 29 novel atypical solute carriers of major facilitator superfamily type: Evolutionary conservation, predicted structure and neuronal co-expression. *Open Biol.* **7**, 170142.
- Pizzagalli, M. D., Bensimon, A. & Superti-Furga, G. (2021) A guide to plasma membrane solute carrier proteins. *FEBS J.* **288**, 2784–2835.
- Ruprecht, J. J. & Kunji, E. R. S. (2020) The SLC25 mitochondrial carrier family: Structure and mechanism. *Trends Biochem. Sci.* **45**, 244–258.
- Dobson, P. D. & Kell, D. B. (2008) Carrier-mediated cellular uptake of pharmaceutical drugs: An exception or the rule? *Nat. Rev. Drug Discov.* **7**, 205–220.
- Nigam, S. K. (2014) What do drug transporters really do? *Nat. Rev. Drug Discov.* **14**, 29–44.
- Hediger, M. A. *et al.* (2004) The ABCs of solute carriers: physiological, pathological and therapeutic implications of human membrane transport proteins. *Pflügers Arch. Eur. J. Physiol.* **447**, 465–468.
- Perland, E. & Fredriksson, R. (2017) Classification Systems of Secondary Active Transporters. *Trends Pharmacol. Sci.* **38**, 305–315.

33. Meixner, E. *et al.* (2020) A substrate-based ontology for human solute carriers. *Mol. Syst. Biol.* **16**, e9652.
34. Rask-Andersen, M., Almén, M. S. & Schiöth, H. B. (2011) Trends in the exploitation of novel drug targets. *Nat. Rev. Drug Discov.* **10**, 579–590.
35. Rask-Andersen, M., Masuram, S., Fredriksson, R. & Schiöth, H. B. (2013) Solute carriers as drug targets: Current use, clinical trials and prospective. *Mol. Aspects Med.* **34**, 702–710.
36. Superti-Furga, G. *et al.* (2020) The RESOLUTE consortium: unlocking SLC transporters for drug discovery. *Nat. Rev. Drug Discov.* **19**, 429–430.
37. Weinglass, A. B., Garcia, M. L. & Kaczorowski, G. L. (2008) Technologies for transporter drug discovery. *Channels* **2**, 312–321.
38. Dvorak, V. *et al.* (2021) An overview of cell-based assay platforms for the solute carrier family of transporters. *Front. Pharmacol.* **12**, 722889.
39. Sucić, S. & Bönisch, H. (Humana Press, 2016). Classical radioligand uptake and binding methods in transporter research: an emphasis on the monoamine neurotransmitter transporters. in *Neurotransmitter Transporters: Neuromethods* (eds. Bönisch, H. & Sitte, H. H.) vol. 118 1–21.
40. Quick, M. & Javitch, J. A. (2007) Monitoring the function of membrane transport proteins in detergent-solubilized form. *Proc. Natl. Acad. Sci. U. S. A.* **104**, 3603–3608.
41. Bonge, H., Hallén, S., Fryklund, J. & Sjöström, J. E. (2000) Cytostar-T scintillating microplate assay for measurement of sodium-dependent bile acid uptake in transfected HEK-293 cells. *Anal. Biochem.* **282**, 94–101.
42. Lohmann, C. *et al.* (2007) Scintillation proximity assay for measuring uptake by the human drug transporters hOCT1, hOAT3, and hOATP1B1. *Anal. Biochem.* **366**, 117–125.
43. Fardel, O., Le Vee, M., Jouan, E., Denizot, C. & Parmentier, Y. (2015) Nature and uses of fluorescent dyes for drug transporter studies. *Expert Opin. Drug Metab. Toxicol.* **11**, 1233–1251.
44. Schwartz, J. W., Blakely, R. D. & DeFelice, L. J. (2003) Binding and transport in norepinephrine transporters: Real-time, spatially resolved analysis in single cells using a fluorescent substrate. *J. Biol. Chem.* **278**, 9768–9777.
45. Liao, J., Sportsman, R., Harris, J. & Stahl, A. (2005) Real-time quantification of fatty acid uptake using a novel fluorescence assay. *J. Lipid Res.* **46**, 597–602.
46. Schroeder, K. S. & Neagle, B. D. (1996) FLIPR: A new instrument for accurate, high throughput optical screening. *J. Biomol. Screen.* **1**, 75–80.
47. Wagstaff, R., Hedrick, M., Fan, J., Crowe, P. D. & DiSepio, D. (2007) High-throughput screening for norepinephrine transporter inhibitors using the FLIPRTetra. *J. Biomol. Screen.* **12**, 436–441.
48. Marvin, J. S. *et al.* (2013) An optimized fluorescent probe for visualizing glutamate neurotransmission. *Nat. Methods* **10**, 162–170.
49. Feng, J. *et al.* (2019) A genetically encoded fluorescent sensor for rapid and specific in vivo detection of norepinephrine. *Neuron* **102**, 745–761.
50. Sun, F. *et al.* (2018) A genetically encoded fluorescent sensor enables rapid and specific detection of dopamine in flies, fish, and mice. *Cell* **174**, 481–496.
51. Ozkan, P. & Mutharasan, R. (2002) A rapid method for measuring intracellular pH using BCECF-AM. *Biochim. Biophys. Acta* **1572**, 143–148.
52. Unger, M. S., Blank, M., Enzlein, T. & Hopf, C. (2021) Label-free cell assays to determine compound uptake or drug action using MALDI-TOF mass spectrometry. *Nat. Protoc.* **16**, 5533–5558.
53. Li, K. C. *et al.* (2021) Cell-surface SLC nucleoside transporters and purine levels modulate BRD4-dependent chromatin states. *Nat. Metab.* **3**, 651–664.
54. Granados, J. C., Nigam, A. K., Bush, K. T., Jamshidi, N. & Nigam, S. K. (2021) A key role for the transporter OAT1 in systemic lipid metabolism. *J. Biol. Chem.* **296**, 100603.
55. Wikoff, W. R., Nagle, M. A., Kouznetsova, V. L., Tsigelny, I. F. & Nigam, S. K. (2011) Untargeted metabolomics identifies enterobiome metabolites and putative uremic toxins as substrates of organic anion transporter 1 (Oat1). *J. Proteome Res.* **10**, 2842–2851.
56. Wright Muelas, M. *et al.* (2020) An untargeted metabolomics strategy to measure differences in metabolite uptake and excretion by mammalian cell lines. *Metabolomics* **16**, 107.
57. Molina, D. M. *et al.* (2013) Monitoring drug target engagement in cells and tissues using the cellular thermal shift assay. *Science* **341**, 84–87.
58. Hashimoto, M., Girardi, E., Eichner, R. & Superti-Furga, G. (2018) Detection of chemical engagement of solute carrier proteins by a cellular thermal shift assay. *ACS Chem. Biol.* **13**, 1480–1486.
59. Chatzikyriakidou, Y., Ahn, D., Nji, E. & Drew, D. (2021) The GFP thermal shift assay for screening ligand and lipid interactions to solute carrier transporters. *Nat. Protoc.* **16**, 5357–5376.
60. Jafari, R. *et al.* (2014) The cellular thermal shift assay for evaluating drug target interactions in cells. *Nat. Protoc.* **9**, 2100–2122.
61. Bailey, T. L., Nieto, A. & McDonald, P. H. (2019) A nonradioactive high-throughput screening-compatible cell-based assay to identify inhibitors of the monocarboxylate transporter protein 1. *Assay Drug Dev. Technol.* **17**, 275–284.

62. Girardi, E. *et al.* (2020) A widespread role for SLC transmembrane transporters in resistance to cytotoxic drugs. *Nat. Chem. Biol.* **16**, 469–478.
63. Neher, E. & Sakmann, B. (1976) Single-channel currents recorded from membrane of denervated frog muscle fibres. *Nature* **260**, 799–802.
64. Galli, A., Blakely, R. D. & Defelice, L. J. (1998) Patch-clamp and amperometric recordings from norepinephrine transporters: Channel activity and voltage-dependent uptake. *Proc. Natl. Acad. Sci. U. S. A.* **95**, 13260–13265.
65. Geibel, S., Flores-Herr, N., Licher, T. & Vollert, H. (2006) Establishment of cell-free electrophysiology for ion transporters: Application for pharmacological profiling. *J. Biomol. Screen.* **11**, 262–268.
66. Bazzzone, A. & Barthmes, M. (Humana Press, 2020). Functional characterization of using solid supported membranes. in *Biophysics of Membrane Proteins: Methods in Molecular Biology* (eds. Postis, V. L. G. & Goldman, A.) vol. 2168 73–103.
67. Halai, R. & Cooper, M. A. (2012) Using label-free screening technology to improve efficiency in drug discovery. *Expert Opin. Drug Discov.* **7**, 123–131.
68. Fang, Y. (2006) Label-free cell-based assays with optical biosensors in drug discovery. *Assay Drug Dev. Technol.* **4**, 583–595.
69. Solly, K., Wang, X., Xu, X., Strulovici, B. & Zheng, W. (2004) Application of real-time cell electronic sensing (RT-CES) technology to cell-based assays. *Assay Drug Dev. Technol.* **2**, 363–372.
70. Giaever, I. & Keese, C. R. (1984) Monitoring fibroblast behavior in tissue culture with an applied electric field. *Proc. Natl. Acad. Sci.* **81**, 3761–3764.
71. Lundstrom, K. (2017) Cell-impedance-based label-free technology for the identification of new drugs. *Expert Opin. Drug Discov.* **12**, 335–343.
72. Hamidi, H., Lilja, J. & Ivaska, J. (2017) Using xCELLigence RTCA instrument to measure cell adhesion. *Bio-Protocol* **7**, e2646.
73. Ke, N., Wang, X., Xu, X. & Abassi, Y. A. (Humana Press, 2011). The xCELLigence system for real-time and label-free monitoring of cell viability. in *Mammalian Cell Viability: Methods in Molecular Biology* (ed. Stoddart, M. J.) vol. 1 33–43.
74. Roshan Moniri, M. *et al.* (2015) Dynamic assessment of cell viability, proliferation and migration using real time cell analyzer system (RTCA). *Cytotechnology* **67**, 379–386.
75. Xi, B. *et al.* (2011) Functional cardiotoxicity profiling and screening using the xCELLigence RTCA cardio system. *J. Lab. Autom.* **16**, 415–421.
76. Urcan, E. *et al.* (2010) Real-time xCELLigence impedance analysis of the cytotoxicity of dental composite components on human gingival fibroblasts. *Dent. Mater.* **26**, 51–58.
77. Atienza, J. M., Yu, N., Wang, X., Xu, X. & Abassi, Y. (2006) Label-free and real-time cell-based kinase assay for screening selective and potent receptor tyrosine kinase inhibitors using microelectronic sensor array. *J. Biomol. Screen.* **11**, 634–643.
78. Yu, N. *et al.* (2006) Real-time monitoring of morphological changes in living cells by electronic cell sensor arrays: an approach to study G protein-coupled receptors. *Anal. Chem.* **78**, 35–43.
79. Scott, C. W. & Peters, M. F. (2010) Label-free whole-cell assays: Expanding the scope of GPCR screening. *Drug Discov. Today* **15**, 704–716.
80. Ke, N., Nguyen, K., Irelan, J. & Abassi, Y. A. (Humana Press, 2015). Multidimensional GPCR profiling and screening using impedance-based label-free and real-time assay. in *G Protein-Coupled Receptor Screening Assays: Methods in Molecular Biology* (eds. Prazeres, D. M. F. & Martins, S. A. M.) vol. 1272 215–226.
81. Doijen, J. *et al.* (2019) Advantages and shortcomings of cell-based electrical impedance measurements as a GPCR drug discovery tool. *Biosens. Bioelectron.* **137**, 33–44.
82. Leung, G. *et al.* (2005) Cellular dielectric spectroscopy: A label-free technology for drug discovery. *J. Assoc. Lab. Autom.* **10**, 258–269.
83. Rosenbaum, D. M., Rasmussen, S. G. F. & Kobilka, B. K. (2009) The structure and function of G-protein-coupled receptors. *Nature* **459**, 356–363.
84. Vázquez-Victorio, G., González-Espinosa, C., Espinosa-Riquer, Z. P. & Macías-Silva, M. (2016). GPCRs and actin–cytoskeleton dynamics. in *Methods in Cell Biology* vol. 132 165–188.
85. Wootten, D., Christopoulos, A., Marti-Solano, M., Babu, M. M. & Sexton, P. M. (2018) Mechanisms of signalling and biased agonism in G protein-coupled receptors. *Nat. Rev. Mol. Cell Biol.* **19**, 638–653.
86. Zhang, R. & Xie, X. (2012) Tools for GPCR drug discovery. *Acta Pharmacol. Sin.* **33**, 372–384.
87. Peters, M. F. & Scott, C. W. (2009) Evaluating cellular impedance assays for detection of GPCR pleiotropic signaling and functional selectivity. *J. Biomol. Screen.* **14**, 246–255.
88. Herenbrink, C. K. *et al.* (2016) The role of kinetic context in apparent biased agonism at GPCRs. *Nat. Commun.* **7**, 1–14.
89. Kammermann, M. *et al.* (2011) Impedance measurement: A new method to detect ligand-biased receptor signaling. *Biochem. Biophys. Res. Commun.* **412**, 419–424.
90. Stallaert, W., Dorn, J. F., van der Westhuizen, E., Audet, M. & Bouvier, M. (2012) Impedance responses reveal β 2-adrenergic receptor signaling pluridimensionality and allow classification of ligands with distinct signaling profiles. *PLoS One* **7**, e29420.

91. Nederpelt, I., Vergroesen, R. D., IJzerman, A. P. & Heitman, L. H. (2016) Persistent GnRH receptor activation in pituitary α T3-1 cells analyzed with a label-free technology. *Biosens. Bioelectron.* **79**, 721–727.
92. Hillger, J. M. *et al.* (2016) Getting personal: Endogenous adenosine receptor signaling in lymphoblastoid cell lines. *Biochem. Pharmacol.* **115**, 114–122.
93. Hillger, J. M. *et al.* (2015) Whole-cell biosensor for label-free detection of GPCR-mediated drug responses in personal cell lines. *Biosens. Bioelectron.* **74**, 233–242.
94. Wong, S.-H., Gao, A., Ward, S., Henley, C. & Lee, P. H. (2012) Development of a label-free assay for sodium-dependent phosphate transporter NaPi-IIb. *J. Biomol. Screen.* **17**, 829–834.
95. Kounnis, V. *et al.* (2015) Microcystin LR shows cytotoxic activity against pancreatic cancer cells expressing the membrane OATP1B1 and OATP1B3 transporters. *Anticancer Res.* **35**, 5857–65.
96. Malhotra, D. *et al.* (2019) Defective cell adhesion function of solute transporter, SLC4A11, in endothelial corneal dystrophies. *Hum. Mol. Genet.* **29**, 97–116.
97. Vlachodimou, A., IJzerman, A. P. & Heitman, L. H. (2019) Label-free detection of transporter activity via GPCR signalling in living cells: a case for SLC29A1, the equilibrative nucleoside transporter 1. *Sci. Rep.* **9**, 13802.
98. Vlachodimou, A., Konstantinopoulou, K., IJzerman, A. P. & Heitman, L. H. (2020) Affinity, binding kinetics and functional characterization of draflazine analogues for human equilibrative nucleoside transporter 1 (SLC29A1). *Biochem. Pharmacol.* **172**, 113747.



CHAPTER 2

Targeting solute carriers to modulate receptor–ligand interactions

Hubert J. Sijben
Giulio Superti-Furga
Adriaan P. IJzerman
Laura H. Heitman

Solute carrier transporters (SLCs) limit receptor activation *via* uptake of extracellular ligands. Novel concepts are emerging that describe the modulation of intracellular and plasma membrane receptors by ligand influx and efflux *via* SLCs, respectively. In this chapter, we evaluate recent insights and provide an outlook for developing potential therapeutic strategies.

2.1 – Solute carrier transporters

SLCs comprise a large superfamily of over 450 proteins with heterogeneous functions, structures and expression patterns. As such, the array of physiological roles that are fulfilled by SLCs make this protein class elusive, illustrated by the high publication asymmetry and relatively low number of drug discovery efforts compared with other protein superfamilies¹. Nevertheless, historically, there has been a handful of SLCs that are therapeutically relevant, including the monoamine transporters as targets for a range of antidepressants. In essence, these transport proteins facilitate the removal (i.e., uptake) of the endogenous neurotransmitter (e.g., dopamine, norepinephrine, or serotonin) from the target compartments, which contain cell surface receptors, such as G protein-coupled receptors (GPCRs) and ligand-gated ion channels. Pharmacological inhibition of monoamine transporters modulates the ligand availability for the target receptor, thereby indirectly altering secondary signaling events that contribute to a therapeutic outcome. While these have become trivial concepts in the understanding of cell signaling and drug action, the number of SLCs that modulate ligand availability is not limited to the *status quo* of the few established SLC drug targets. Over the past few years, light has been shed on novel physiological mechanisms through which SLCs mediate ligand access to receptors localized at the plasma membrane and intracellular compartments (**Figure 2.1**). In this chapter, we use five recent examples of SLC–GPCR pairings to discuss potential therapeutic implications that lie ahead.

2.2 – Modulation of ligand availability at the plasma membrane

Most GPCRs are expressed at the plasma membrane, where they are receptive to extracellular ligands that, upon binding to the receptor, result in distinct secondary messenger responses. In the traditional dogma, ligand transporters (e.g., neurotransmitter transporters) act to *limit* receptor activation *via* substrate influx (**Figure 2.1a**), whereas some transporters are now recognized to *permit* receptor activation by ligand efflux, which adds another layer of signaling regulation by SLCs.

2.2.1 – Succinate

During ischemia/reperfusion injury, the tricarboxylic acid cycle intermediate succinate is oxidized in the mitochondria to form reactive oxygen species, driving the injury. At the same time, a significant portion of succinate was found to be effluxed into the circulation *via* the proton-coupled monocarboxylate transporter 1 (MCT1, SLC16A1)². Subsequent activation of the succinate receptor (SUCNR1) on immune cells by excreted succinate induced proinflammatory responses that exacerbated the reperfusion injury (**Figure 2.1b**), although the exact contributions of SUCNR1 to this process remain a subject of investigation. Notably, MCT1 inhibition appeared to reduce infarct size in mice, likely due to limited SUCNR1 activation², which implicates MCT1 as an important mediator of reperfusion injury. Whether targeting succinate transport is an attractive therapeutic venue remains to be seen, although recently renewed interest in succinate as a signaling metabolite could provide resolution in the near future³.

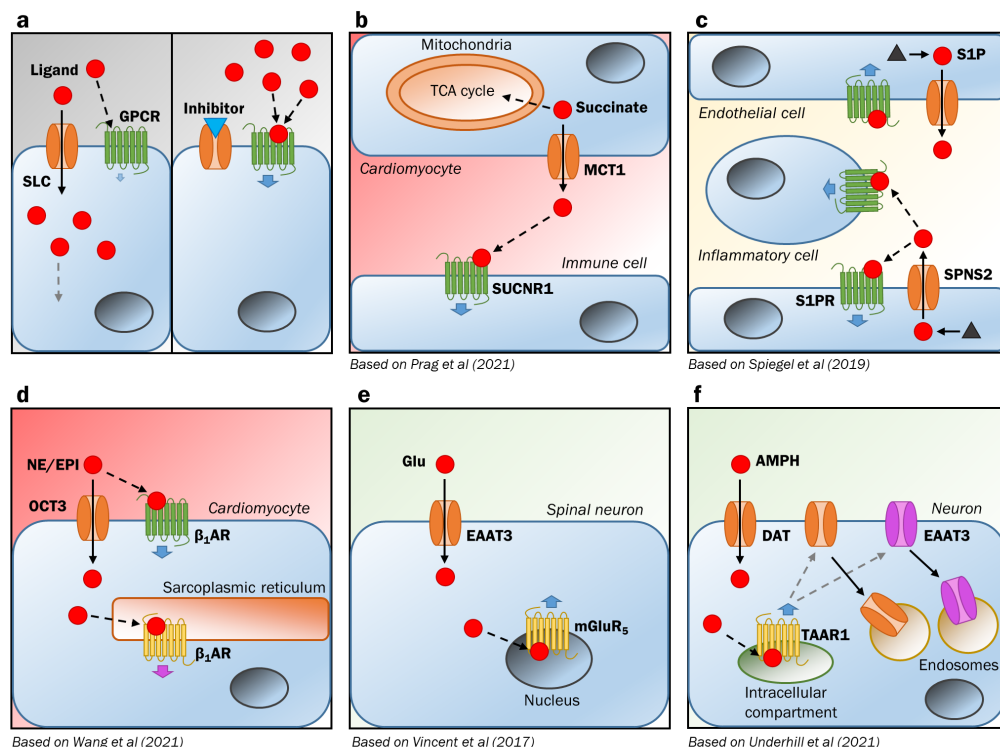


Figure 2.1 – Mechanisms of transporter-mediated modulation of receptor–ligand interactions. **(a)** Traditional dogma of a solute carrier transporter (SLC) that limits activation of a G protein-coupled receptor (GPCR) on the plasma membrane through ligand influx (left panel). SLC inhibition elevates the extracellular ligand concentration, enhancing GPCR activation (right panel). **(b)** Succinate is oxidized in the mitochondria and effluxed by monocarboxylate transporter 1 (MCT1), after which it is able to activate the succinate receptor (SUCNR1) on immune cells. TCA, tricarboxylic acid. **(c)** Sphingosine-1-phosphate (S1P) is synthesized in endothelial cells and effluxed into the (lymphatic) circulation *via* spinster homolog 2 (SPNS2). S1P activates S1P receptors (S1PRs) on circulating immune cells or endothelial cells. **(d)** Norepinephrine (NE) and epinephrine (EPI) are transported into cardiomyocytes *via* organic cation transporter 3 (OCT3), where both ligands activate beta-1 adrenergic receptors (β_1 ARs) in the sarcoplasmic reticulum. Intracellular responses are distinct from β_1 AR on the plasma membrane. **(e)** Glutamate enters neuronal cells *via* excitatory amino acid transporter 3 (EAAT3), where it activates metabotropic glutamate receptor 5 (mGluR₅) on the nuclear membrane. **(f)** Amphetamine (AMPH) is transported into the cell *via* the dopamine transporter (DAT), where it activates the trace amine-associated receptor 1 (TAAR1), which leads to internalization of DAT and EAAT3.

2.2.2 – Sphingosine-1-phosphate

Sphingosine-1-phosphate (S1P) is a potent polar signaling lipid that invokes prosurvival effects *via* activation of S1P receptors (S1PRs) in an autocrine or paracrine manner (**Figure 2.1c**). Upon intracellular biosynthesis, S1P is transported out of the cell mainly *via* spinster homolog 2 (SPNS2, SLC63A2) in lymphatic endothelial cells and through major facilitator superfamily domain-containing protein 2 (MFSD2A/B, SLC59A1/2) in vascular endothelial

cells. Increasing evidence suggests that SPNS2 has a regulatory role in metastasis, lymphocyte trafficking, and angiogenesis⁴. Mice studies indicated that the absence of SPNS2 reduces metastatic burden, likely as a result of reduced S1PR engagement, which suggests SPNS2 as a target to combat metastasis after surgical tumor resection. Our understanding of SPNS2 involvement in disease would be aided by the development of selective inhibitors of the protein, of which none are publicly available, denoting a gap in current progress.

2.3 – Modulation of ligand availability to intracellular receptors

An increasing number of GPCRs have been found to localize preferably or exclusively to membranes of intracellular compartments such as the endoplasmic reticulum, Golgi, or nucleus⁵. Moreover, it is suggested that spatially distinct localizations of the same GPCRs contribute to distinct signaling responses, which may contribute in unexpected ways to disease development⁵. As such, the question arises how these intracellular receptors gain access to their cognate ligands, with possible answers being *via* on-demand synthesis, passive diffusion, or ligand influx *via* SLCs.

2.3.1 – (Nor)epinephrine

Adrenergic signaling is mainly concerted on the plasma membrane *via* alpha- and beta-adrenergic receptors, although intracellular localization of these receptors has been reported. It was recently found that organic cation transporter 3 (OCT3, SLC22A3) is required for the influx of (nor)epinephrine to activate beta-1 adrenergic receptor (β_1 AR) at the sarcoplasmic reticulum (SR) of cardiomyocytes (**Figure 2.1d**)⁶. Knockout or inhibition of OCT3 in mice blunted β_1 AR-mediated cardiac function, indicating that OCT3 is an essential component of (nor)epinephrine-induced myocardial contractility. Thus, regulation of catecholamine uptake could be a therapeutic strategy for cardiovascular conditions.

2.3.2 – Glutamate

Glutamate transporters rapidly bind, and eventually take up, glutamate upon release in the synaptic cleft, thereby buffering the extracellular glutamate concentrations and shaping the activation kinetics of synaptic glutamate receptors⁷. Recently, the uptake of glutamate *via* excitatory amino acid transporter 3 (EAAT3/SLC1A1) in neuronal cells of the spinal cord was found to be crucial for activation of metabotropic glutamate receptor 5 (mGluR₅) on the nuclear membrane (**Figure 2.1e**). In an inflammatory pain model in rats, elevated intracellular levels of glutamate were linked to mGluR₅-mediated pain responses. Indeed, selective inhibition of neuronal EAAT3, but not glial EAAT1 or EAAT2, produced an analgesic effect in rats. This suggests a substantial contribution of intracellular mGluR₅ to pain development, which defies the notion that only glutamate receptors at the plasma membrane are involved. As such, inhibition of neuronal EAAT or intracellular mGluR₅ is among the future treatment possibilities for pain disorders⁸.

2.3.3 – Amphetamines

The interplay between SLCs and GPCRs extends beyond the modulation of ligand availability, because receptor activation can, by itself, affect transporter function and localization, indirectly influencing GPCR activation. For example, trace amine-associated receptor 1 (TAAR1) is expressed on intracellular compartments of monoaminergic neurons, and its activation by trace amines and monoamines depends on transporter-mediated influx. Amphetamines, which are used in the treatment of attention-deficit hyperactivity disorder, enter the cell *via* the dopamine transporter (DAT/SLC6A3) and activate TAAR1. This leads to endocytosis of DAT and glutamate transporter EAAT3 and subsequent potentiation of excitatory responses in dopaminergic neurons by facilitating cognate receptor–ligand interactions (**Figure 2.1f**)⁹. This identifies TAAR1 as a critical component of psychostimulant action and underlines the intricacy of transporter function and regulation in monoaminergic disorders.

2.4 – Concluding remarks and future perspectives

The relationship between SLCs and other membrane proteins, such as GPCRs, is becoming increasingly appreciated, as illustrated by the examples in this article and by the development of *in vitro* techniques that use receptors as ‘tools’ to study transporter function¹⁰. While the main focus of this chapter is on the translocation of receptor ligands, many SLCs (EAAT3, DAT, and MCT1 in this article) harness the electrochemical gradient of ions to facilitate transport and thereby alter the levels of these ions in the cytosol and the vicinity of the membrane. Several ions, most prominently Na⁺, act as allosteric modulators of many GPCRs *via* distinct and conserved binding sites¹¹, which would imply that ion-coupled SLCs beyond the examples in this article can act as indirect receptor modulators.

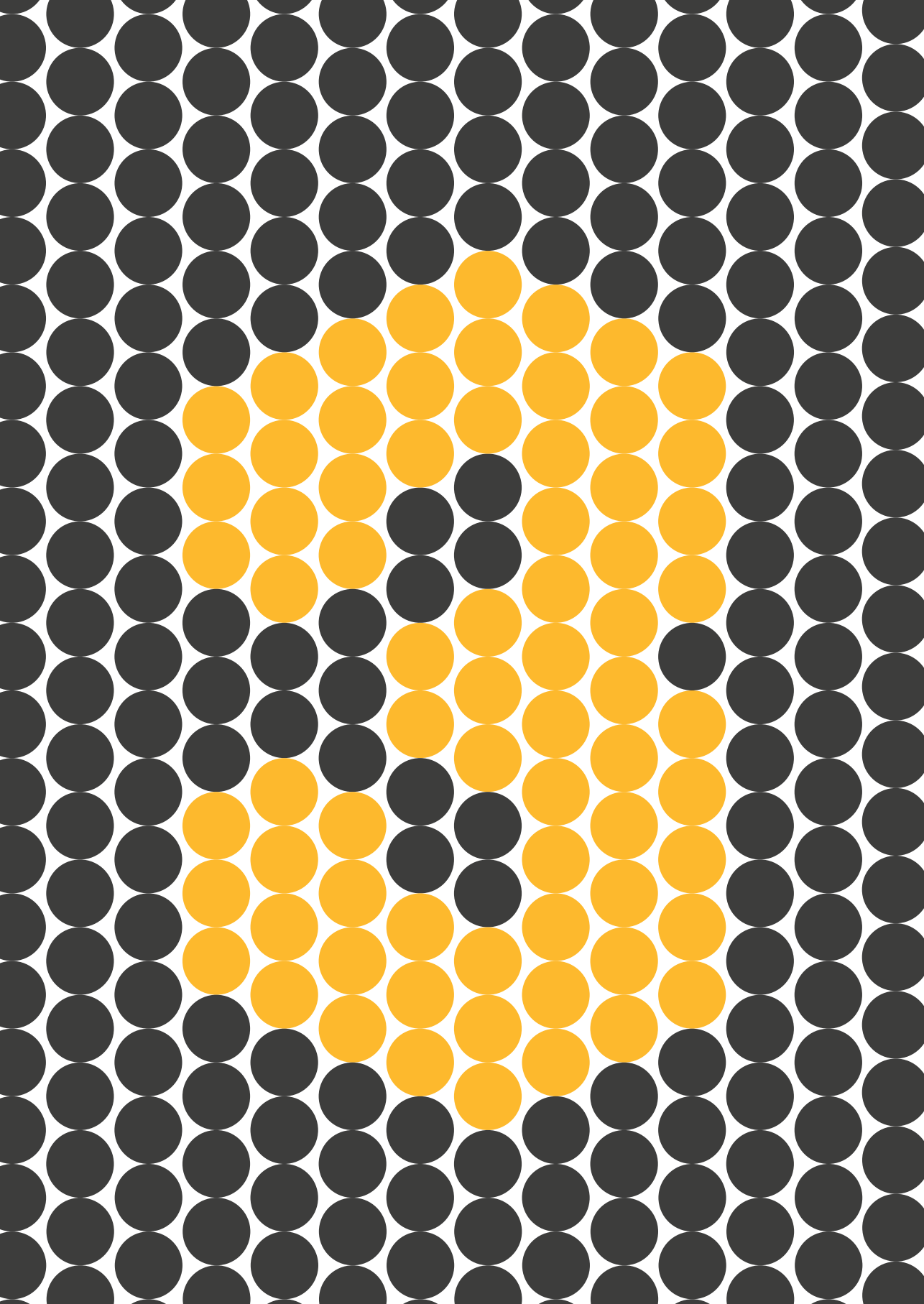
A note of caution is warranted when SLCs, such as those described in this article, are to be considered as therapeutic targets. Given that substrates may engage with other proteins or serve as metabolic intermediates, preventing their translocation could disrupt key cellular processes. If such secondary effects are detrimental and cannot be mitigated despite the specificity of the intervention, it might be more beneficial to target specific downstream proteins. In line with this, modulation of polyspecific transporters (e.g., MCT1 also transports lactate) might affect disease-unrelated pathways vital for other substrates. Moreover, ubiquitous expression of an SLC in various tissues could compromise the selectivity of the treatment. As such, the cell-specific expression and localization of both the SLC and GPCR should be evident to ensure selective targeting and prevent adverse effects.

The cases that we discuss in this chapter highlight the efforts made to connect pairs of previously characterized SLCs and GPCRs with known substrate specificities and affinities. However, based on current knowledge, we estimate that at least 100 unique SLC–GPCR pairs are conceivable (see **Appendix Table A.1**). Nevertheless, ~30% of SLCs and 15% of GPCRs have an orphan status, meaning that their function and substrate(s)/ligand(s)

are unknown^{12,13}. Ongoing efforts to deorphanize these proteins could unveil novel SLC–GPCR pairs, which could spark novel hypotheses with physiological and therapeutic implications¹³. International collaborations and consortia, such as RESOLUTE¹⁴, which aim at deorphanization, reagent generation, and function elucidation of all SLCs, substantiate the expected relevance of transporters in physiology and disease and contribute to the overall progress of putting forward SLCs as potential drug targets.

References

1. César-Razquin, A. *et al.* (2015) A call for systematic research on solute carriers. *Cell* **162**, 478–487.
2. Prag, H. A. *et al.* (2021) Mechanism of succinate efflux upon reperfusion of the ischaemic heart. *Cardiovasc. Res.* **117**, 1188–1201.
3. Fernández-Veledo, S., Ceperuelo-Mallafre, V. & Vendrell, J. (2021) Rethinking succinate: an unexpected hormone-like metabolite in energy homeostasis. *Trends Endocrinol. Metab.* **32**, 680–692.
4. Spiegel, S., Maczys, M. A., Maceyka, M. & Milstien, S. (2019) New insights into functions of the sphingosine-1-phosphate transporter SPNS2. *J. Lipid Res.* **60**, 484–489.
5. Jong, Y. J. I., Harmon, S. K. & O'Malley, K. L. (2018) GPCR signalling from within the cell. *Br. J. Pharmacol.* **175**, 4026–4035.
6. Wang, Y. *et al.* (2021) Intracellular β 1-adrenergic receptors and organic cation transporter 3 mediate phospholamban phosphorylation to enhance cardiac contractility. *Circ. Res.* **128**, 246–261.
7. Rose, C. R. *et al.* (2018) Astroglial glutamate signaling and uptake in the hippocampus. *Front. Mol. Neurosci.* **10**, 1–20.
8. Vincent, K., Wang, S. F., Laferrière, A., Kumar, N. & Coderre, T. J. (2017) Spinal intracellular metabotropic glutamate receptor 5 (mGluR5) contributes to pain and c-fos expression in a rat model of inflammatory pain. *Pain* **158**, 705–716.
9. Underhill, S. M. *et al.* (2021) Amphetamines signal through intracellular TAAR1 receptors coupled to G α 13 and G α S in discrete subcellular domains. *Mol. Psychiatry* **26**, 1208–1223.
10. Sijben, H. J., van den Berg, J. J. E., Broekhuis, J. D., IJzerman, A. P. & Heitman, L. H. (2021) A study of the dopamine transporter using the TRACT assay, a novel in vitro tool for solute carrier drug discovery. *Sci. Rep.* **11**, 1312.
11. Zarzycka, B., Zaidi, S. A., Roth, B. L. & Katritch, V. (2019) Harnessing ion-binding sites for GPCR pharmacology. *Pharmacol. Rev.* **71**, 571–595.
12. Alexander, S. P. H. *et al.* (2019) The concise guide to pharmacology 2019/20: G protein-coupled receptors. *Br. J. Pharmacol.* **176**, S21–S141.
13. Meixner, E. *et al.* (2020) A substrate-based ontology for human solute carriers. *Mol. Syst. Biol.* **16**, 1–9.
14. Superti-Furga, G. *et al.* (2020) The RESOLUTE consortium: unlocking SLC transporters for drug discovery. *Nat. Rev. Drug Discov.* **19**, 429–430.



CHAPTER 3

A study of the dopamine transporter using the TRACT assay: a novel *in vitro* tool for solute carrier drug discovery

Hubert J. Sijben
Julie J.E. van den Berg
Jeremy D. Broekhuis
Adriaan P. IJzerman
Laura H. Heitman

Members of the solute carrier (SLC) transporter protein family are increasingly recognized as therapeutic drug targets. The majority of drug screening assays for SLCs are based on the uptake of radiolabeled or fluorescent substrates. Thus, these approaches, often have limitations that compromise on throughput or the physiological environment of the SLC. In this chapter, we report a novel application of an impedance-based biosensor, xCELLigence, to investigate dopamine transporter (DAT) activity *via* substrate-induced activation of G protein-coupled receptors (GPCRs). The resulting assay, which is coined the ‘transporter activity through receptor activation’ (TRACT) assay, is based on the hypothesis that DAT-mediated removal of extracellular dopamine directly affects the ability of dopamine to activate cognate membrane-bound GPCRs. In two human cell lines with heterologous DAT expression, dopamine-induced GPCR signaling was attenuated. Pharmacological inhibition or the absence of DAT restored the apparent potency of dopamine for GPCR activation. The inhibitory potencies for DAT inhibitors GBR12909 ($pIC_{50} = 6.2, 6.6$) and cocaine ($pIC_{50} = 6.3$) were in line with values from reported orthogonal transport assays. Conclusively, this chapter demonstrates the novel use of label-free whole-cell biosensors to investigate DAT activity using GPCR activation as a readout. This holds promise for other SLCs that share their substrate with a GPCR.

3.1 – Introduction

Solute carrier (SLC) transporters are a large superfamily of membrane-spanning proteins that facilitate passive or secondary active transport of a wide variety of physiological and pharmacological solutes. As such, SLCs constitute important regulators of a cell's intra- and extracellular environment and signal transduction¹. Increasingly, the role of SLCs in onset and progression of disease is recognized². This is underlined by the 21 SLCs currently targeted by clinically approved drugs and at least 10 other SLCs that have compounds in clinical trials³. In addition, several SLCs are known to mediate drug-drug interactions and as a result are routinely assessed in drug discovery programs^{4,5}. Despite the ubiquity of these proteins in physiology and pathology only a fraction of all SLCs have been extensively investigated. This necessitates the development of methods, pharmacological tools and reagents to uncover the therapeutic potential of this relatively understudied class of proteins⁶.

One of the main challenges in propelling SLC drug discovery is the sparse implementation of high-throughput screening (HTS) strategies for *in vitro* functional assays³. As outlined in **Chapter 1 (Table 1.1)**, conventional transport inhibition assays are based on radiolabeled or fluorescent substrate uptake⁷ and pose limitations due to challenges regarding substrate synthesis, real-time measurements, and radiometric safety precautions³. However, cell-based assays using fluorescent membrane potential⁸, pH-sensitive or calcium-sensing dyes, can achieve impressive throughput using platforms such as fluorescent imaging plate readers (FLIPR)⁹, but may result in non-specific signals and require thorough signal validation. Another approach based on electrophysiological measurements (SURFE²R) can attain increased screening capacity¹⁰, although these assays require electrogenicity of the SLC, valid for a minority only, and often use liposome or membrane preparations. Taken together, this warrants development of novel assays that circumvent the drawbacks commonly associated with label-based or cell-free screening assays.

Label-free cell-based biosensors have been used to study a wide variety of therapeutic membrane-bound proteins including G protein-coupled receptors (GPCRs)^{11,12}, receptor tyrosine kinases¹³ and ion channels^{14,15}. Optical and impedance-based platforms (e.g., Epic and xCELLigence, respectively) allow real-time monitoring of changes in cell morphology, adhesion, proliferation and migration without the use of invasive and/or non-physiological labels^{16,17}. Cell-based electrical impedance assays are already used as a complementary phenotypic technology for GPCR drug discovery¹⁸, being amenable to increased throughput screening up to 384 wells per plate¹⁹. Due to high sensitivity of these label-free methods, it is possible to detect GPCR activation in endogenous as well as heterologous expression cell lines^{20,21}. Recently, a label-free whole-cell assay was reported by our research team in which the activity of the non-electrogenic equilibrative nucleoside transporter 1 (ENT1, also known as SLC29A1) was measured *via* activation of adenosine GPCRs, for which adenosine is a substrate and agonist, respectively²². In that work mammalian bone osteosarcoma (U2OS) cells with endogenous expression of both ENT1 and adenosine receptors were assessed using the xCELLigence technology.

In the current chapter we exploited the capability of the impedance-based biosensor xCELLigence to detect GPCR activation further. We developed a label-free whole-cell assay, coined the ‘transporter activity through receptor activation’ (TRACT) assay (**Figure 1.4, Chapter 1**), to detect activity of the dopamine transporter (DAT, also known as SLC6A3). Here, two human cell lines with heterologous expression of DAT were used to measure DAT function *via* activation of an endogenous GPCR by the main substrate of DAT, dopamine. DAT, a Na⁺/Cl⁻-dependent monoamine transporter²³, is a clinical target for treatment of attention-deficit/hyperactivity disorder²⁴, narcolepsy²⁵ and potentially stimulant abuse²⁶, but is also an important effector in the addictive effects of psychoactive substances such as cocaine and amphetamine²⁷. Due to a wealth of reported literature and availability of tool compounds, DAT was selected as a model transporter to develop this TRACT assay. The current observations demonstrate a proof-of-principle that real-time impedance measurements are suitable for the detection of dopamine-induced GPCR signaling in the absence or presence of DAT. Essentially, this allows simultaneous detection of the functional activity of two membrane-bound proteins *via* a single converged impedance signal. This vastly expands the possibilities for the application of label-free biosensors in SLC and GPCR drug discovery.

3.2 – Results

3.2.1 – Attenuated D₁R-mediated dopamine response in U2OS-DAT cells

To allow functional assessment of DAT U2OS cells were transiently transfected with DAT cDNA (U2OS-DAT) using empty vector (U2OS-mock) as a negative control. In whole-cell ELISA assays total expression of DAT was 2-fold higher compared to mock indicating successful transfection of U2OS cells (**Figure 3.1a**).

To assess the responsiveness of transfected U2OS cells to dopamine in the TRACT assay U2OS-DAT and U2OS-mock cells were seeded and grown in uncoated E-plates. Cells initially adhered strongly to the wells indicated by an increase in CI between 0 and 8 h, but showed a gradual decrease in CI after 8 h (**Figure 3.1b**). This decline in impedance likely reflects a small amount of cell death as a result of transient transfection, which was more outspoken in U2OS-DAT than in U2OS-mock. Subsequent stimulation of cells with increasing concentrations of dopamine resulted in an initial decrease in impedance that reached minimum nCI values after 40 to 60 min and then gradually returned to baseline (**Figure 3.1c–d**). Both cell lines responded to dopamine in a concentration-dependent manner (**Figure 3.1e**). Dopamine was less potent on U2OS-DAT cells ($pEC_{50} = 4.0 \pm 0.2$) compared to U2OS-mock cells ($pEC_{50} = 5.3 \pm 0.2$) (**Table 3.1**), showing that the presence of DAT reduces the apparent potency of dopamine.

To confirm the observed dopamine response was the result of GPCR activation U2OS-DAT cells were pretreated for 1 h with 1 μ M antagonist for dopamine, alpha- or beta-adrenergic receptors prior to stimulation with a submaximal concentration (10 μ M) of dopamine. Pretreatment with any of the antagonists had no substantial effect on the

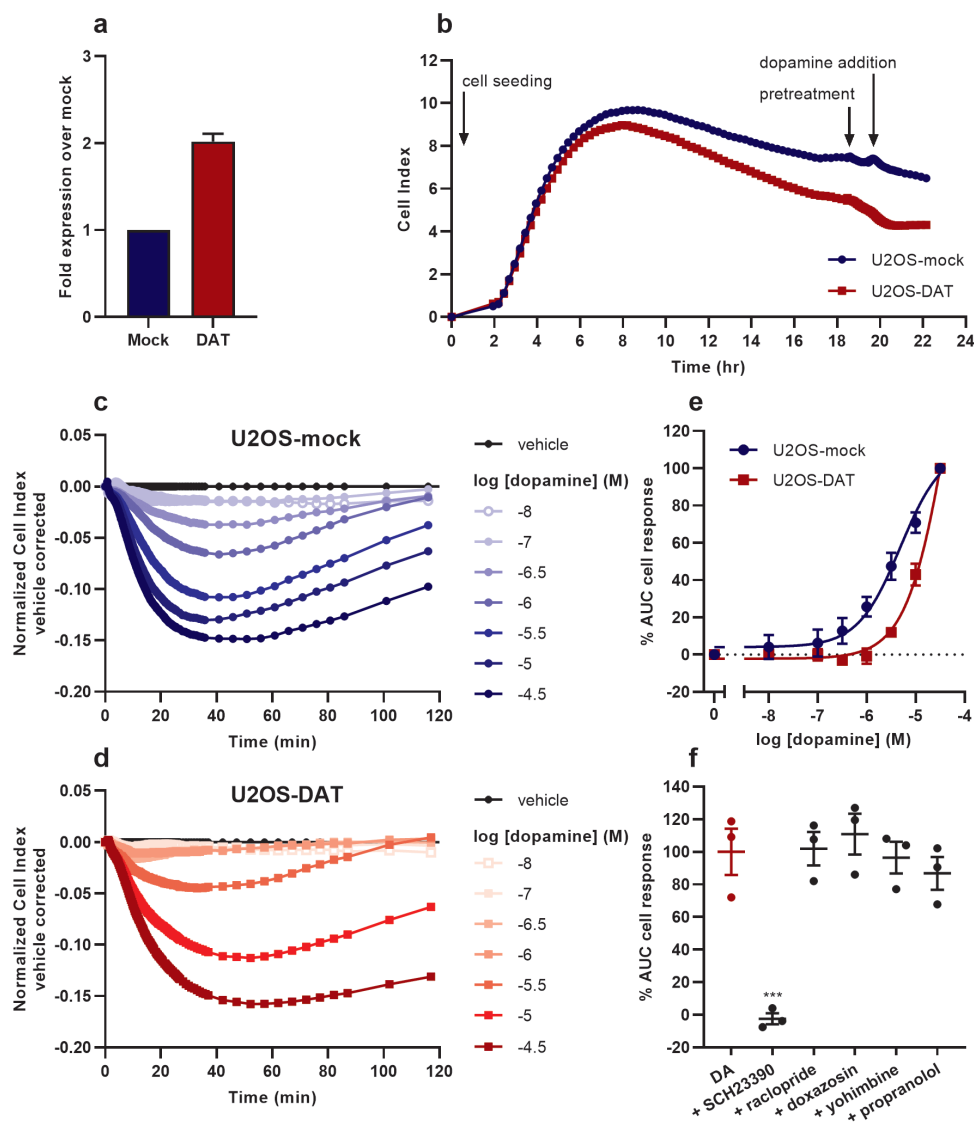


Figure 3.1 – Functional characterization of dopamine (DA) response in U2OS-mock and U2OS-DAT cells in a TRACT assay. **(a)** FLAG-tag ELISA shows detection of C-terminal FLAG-tag of DAT, represented as mean \pm S.D. of two separate experiments each performed in quintuplicate. **(b)** Representative xCELLigence growth curves after cell seeding, antagonist pretreatment and dopamine addition. **(c)** Representative vehicle-corrected xCELLigence traces of U2OS-mock and **(d)** U2OS-DAT cells after stimulation with increasing concentrations of dopamine. Data is normalized prior to agonist addition at time = 0 min. **(e)** Concentration-effect curves of dopamine on U2OS-mock and U2OS-DAT cells are shown as the net AUC of the first 120 min after stimulation normalized to the cell response of 31.6 μ M dopamine. **(f)** Cell response of 10 μ M dopamine (red bar, set at 100%) on U2OS-DAT cells pretreated for 1 h with 1 μ M of one of following GPCR antagonists: SCH23390 (dopamine D_1 -like), raclopride (dopamine D_2 -like), doxazosin (alpha-1 adrenergic), yohimbine (alpha-2 adrenergic), propranolol (beta adrenergic). Data are shown as mean \pm SEM of three to six individual experiments each performed in duplicate. Comparison of multiple mean values to vehicle control was done using a one-way ANOVA with Dunnett's post-hoc test. *** $p < 0.001$.

nCI compared to cells pretreated with vehicle (**Supplementary Figure 3.S1a**). Only SCH23390, a dopamine D1-like receptor antagonist, was able to completely abolish the dopamine-induced cell response (**Figure 3.1f**). In non-transfected U2OS cells, SCH23390, but not raclopride, eliminated the dopamine-induced response (**Supplementary Figure 3.S1b**). This demonstrates that dopamine acts as an agonist and selectively activates D₁R endogenously expressed on U2OS cells (**Figure 3.1f**).

3.2.2 – DAT inhibition by GBR12909 restores the apparent potency of dopamine in U2OS-DAT cells

To assess whether pharmacological inhibition of DAT leads to altered dopamine-induced D₁R signaling in the TRACT assay U2OS-DAT cells were pretreated for 1 h with 10 μM GBR12909, an atypical DAT inhibitor, prior to stimulation with increasing concentrations of dopamine. GBR12909 pretreatment itself did not substantially affect impedance during the 1 h incubation period (**Supplementary Figure 3.S2a**). In the presence of GBR12909 dopamine induced a decrease in nCI in U2OS-DAT cells similar to that in U2OS-mock cells (compare **Figure 3.2a to 3.1c**). Dopamine displayed a 16-fold higher apparent potency for D₁R activation in U2OS-DAT cells pretreated with 10 μM GBR12909 ($pEC_{50} = 5.2 \pm 0.2$) compared to vehicle-pretreated cells ($pEC_{50} = 4.0 \pm 0.2$) (**Figure 3.2b, Table 3.1**). Of note, the slope of the dopamine concentration-effect curve was significantly steeper ($p < 0.01$) in vehicle-treated cells (1.5 ± 0.1) than in cells treated with GBR12909 (0.9 ± 0.1) as was assessed by a variable slope regression model (**Supplementary Table 3.S1, Supplementary Figure 3.S3a**). Taken together, this suggests DAT inhibition effectively prevents uptake of extracellular dopamine leading to enhanced D₁R activation.

Table 3.1 – Apparent potency values of dopamine (pEC_{50}) and inhibitory potency values of DAT inhibitors (pIC_{50}) on U2OS-mock, U2OS-DAT or Jumpln-DAT (\pm dox) cells in TRACT experiments using a non-linear regression analysis model with a fixed pseudo-Hill slope of 1.

Cell line	Compound	$pEC_{50} \pm SEM (\mu M)$	$pIC_{50} \pm SEM (\mu M)$	<i>n</i>
U2OS-mock	Dopamine	5.3 ± 0.2 (5)	–	3
	Dopamine	$4.0 \pm 0.2^*$ (96)	–	6
U2OS-DAT	Dopamine + 10 μM GBR12909	$5.2 \pm 0.2^{##}$ (6)	–	4
	GBR12909 + 3.16 μM dopamine	–	6.2 ± 0.1 (0.6)	4
Jumpln-DAT –dox	Dopamine	5.1 ± 0.1 (8)	–	7
	Dopamine	$4.3 \pm 0.0^{+++}$ (46)	–	9
	Dopamine + 10 μM GBR12909	$4.6 \pm 0.2^{\&\&\&}$ (26)	–	4
Jumpln-DAT +dox	Dopamine + 10 μM cocaine	$4.9 \pm 0.1^{+++}$ (13)	–	4
	GBR12909 + 10 μM dopamine	–	6.6 ± 0.1 (0.2)	4
	Cocaine + 10 μM dopamine	–	6.3 ± 0.2 (0.6)	4

Values are reported as the mean \pm SEM of three to nine individual experiments performed in duplicate. Significant difference between two mean potency values was determined by unpaired two-tailed Student's t-test. * $p < 0.05$ (compared to U2OS-mock); $^{##} p < 0.01$ (compared to U2OS-DAT/dopamine); $^{+++} p < 0.001$ (compared to Jumpln-DAT –dox). Comparison of multiple mean values to vehicle control was done using a one-way ANOVA with Dunnett's post-hoc test. $^{+++} p < 0.001$ (compared to Jumpln-DAT +dox/dopamine). $^{\&\&\&} p < 0.001$ (compared to Jumpln-DAT –dox).

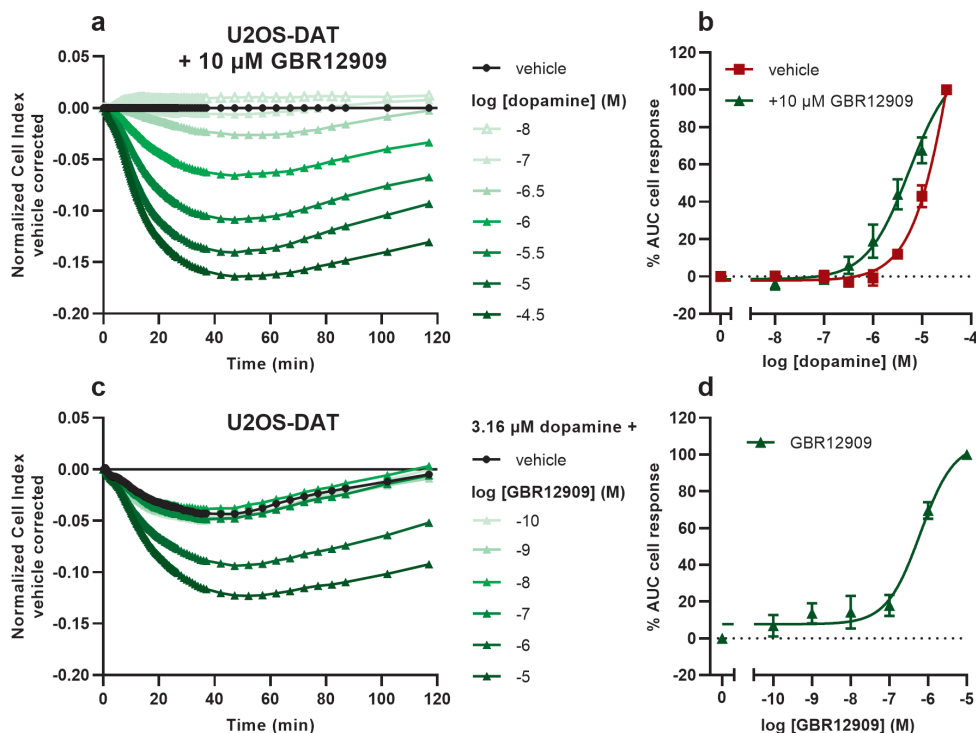


Figure 3.2 – Functional characterization of GBR12909 on DAT in U2OS-DAT cells in a TRACT assay. Cells were pretreated with vehicle, 10 μ M (a,b) or increasing concentrations (c,d) of GBR12909. Representative vehicle-corrected xCELLigence traces after stimulation with (a) increasing concentrations of dopamine or (c) 3.16 μ M dopamine. (b) Concentration-effect curves of dopamine in U2OS-DAT cells pretreated with vehicle or 10 μ M GBR12909 are shown as the net AUC of the first 120 min after stimulation normalized to the cell response of 31.6 μ M dopamine. (d) Concentration-effect curve of GBR12909 after addition of 3.16 μ M dopamine normalized to 10 μ M GBR12909. Data are shown as mean \pm SEM of three to six separate experiments each performed in duplicate.

Next, the inhibitory potency of GBR12909 was determined in the TRACT assay. U2OS-DAT cells were pretreated for 1 h with increasing concentrations of GBR12909 and subsequently stimulated with a submaximal concentration of dopamine (3.16 μ M) that resulted in the largest increase in cell response in cells pretreated with 10 μ M GBR12909 (Figure 3.2b). GBR12909 was able to concentration-dependently augment the dopamine-induced decrease in impedance compared to vehicle-pretreated cells with a pIC_{50} of 6.2 ± 0.1 (Figure 3.2c–d, Table 3.1). This demonstrates that the apparent inhibitory potency of DAT inhibitor GBR12909 can be quantified in the TRACT assay.

3.2.3 – DAT expression is higher than D_1 R in U2OS-DAT cells

To determine the relative amounts of DAT and D_1 R protein expressed on U2OS-DAT cells radioligand saturation binding experiments were performed. To this end radioligands for DAT ($[^3\text{H}]\text{WIN35,428}$) and D_1 R ($[^3\text{H}]\text{SCH23390}$) were used to determine the respective

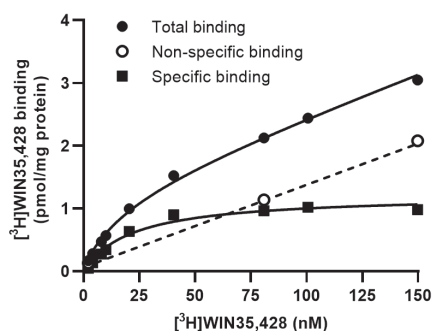


Figure 3.3 – Representative saturation binding curve of [³H]WIN35,428 to DAT on U2OS-DAT membranes. Total binding (●) and non-specific binding (○) were determined in the absence or presence of 100 μM GBR12909. Specific binding (■) was obtained by linear subtraction of non-specific binding from total binding. Data are shown as the mean of a representative graph of three separate experiments each performed in triplicate.

total amount of binding sites (B_{\max}) and equilibrium dissociation constants (K_D). No specific binding of [³H]WIN35,428 was observed on U2OS-mock membranes (**Supplementary Figure 3.S4a**). On U2OS-DAT membranes saturable binding of [³H]WIN35,428 was observed with a K_D value of 28 ± 4 nM and a B_{\max} value of 1.6 ± 0.2 pmol/mg protein (**Figure 3.3**). The presence of D₁R was assessed on membranes of non-transfected U2OS cells where [³H]SCH23390 showed saturable binding with a K_D value of 0.9 ± 0.1 nM and a B_{\max} value of 0.1 ± 0.0 pmol/mg protein (**Supplementary Figure 3.S4b**). No detectable specific binding of [³H]SCH23390 on U2OS-DAT membranes was observed (**Supplementary Figure 3.S4c**). Thus, these results suggest that (at least) 16-fold more DAT is present than D₁R on U2OS-DAT cells.

3.2.4 – Inducible DAT expression attenuates dopamine response in JumpIn-DAT cells

To validate and compare the results observed in U2OS-DAT cells a second cell line was selected. JumpIn-DAT is a HEK 293 cell line modified for dox-inducible expression of DAT. In functional label-free assays JumpIn-DAT cells were seeded and grown with or without dox in E-plates for 22–24 h. Although JumpIn-DAT cells are weakly adherent no coating was needed to detect robust CI responses. JumpIn-DAT cells attach within 4 h after seeding, which leads to a gradual increase in CI and confluence after 24 h. The presence of dox did not affect CI of JumpIn-DAT cells up to 24 h (**Figure 3.4a**).

The amount of dox was varied to modulate levels of DAT expression. Incubating JumpIn-DAT cells for 24 h with increasing concentrations of dox enhanced cell surface expression of DAT in a concentration-dependent manner compared to vehicle-treated cells (**Figure 3.4b**, teal diamonds). Consequently, this resulted in a dox concentration-dependent decrease in the dopamine-induced cell response (**Figure 3.4b**, black squares), which is in line with the idea that the presence of DAT removes extracellular dopamine leading to attenuated dopamine-induced signaling. Subsequent TRACT assays with JumpIn-DAT cells were performed in the presence of 1 μg/ml dox (+dox) or vehicle (−dox) to ensure maximal and consistent DAT expression.

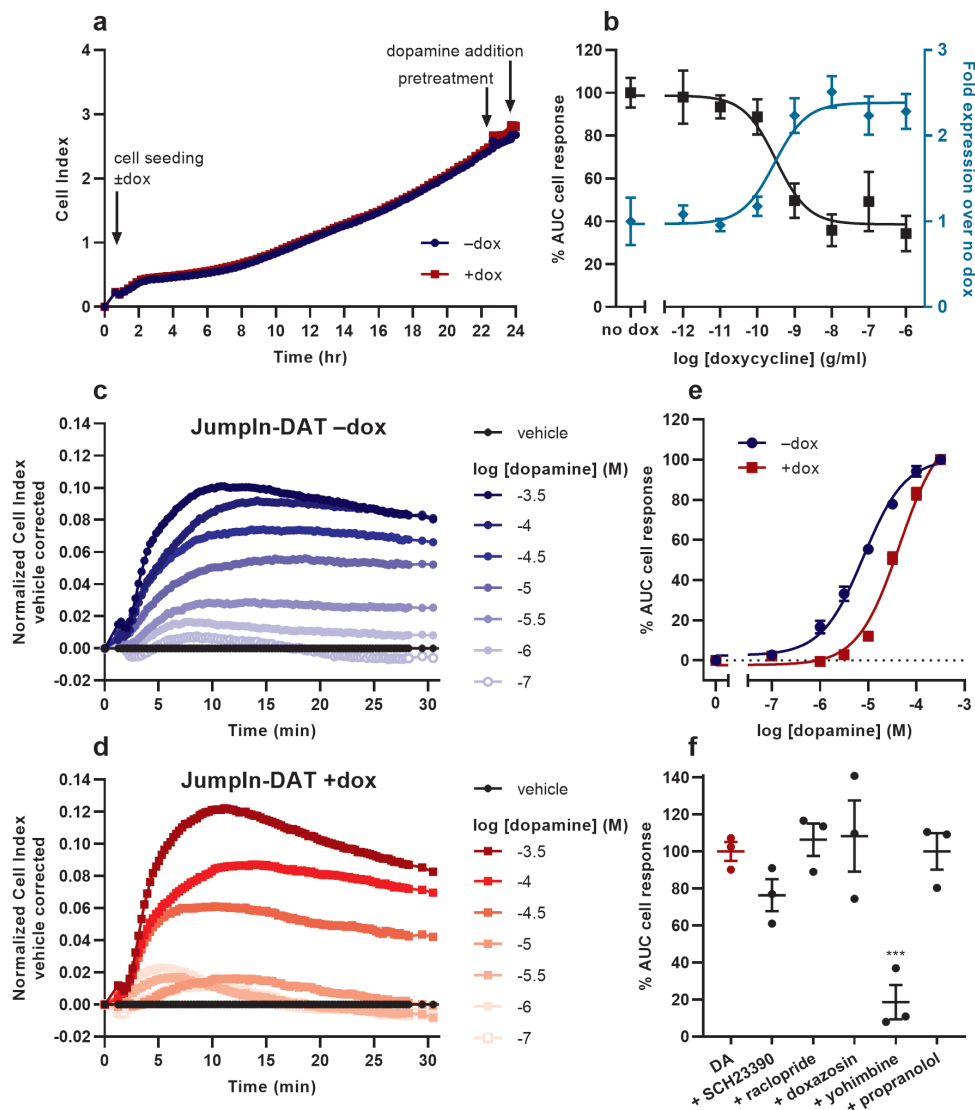


Figure 3.4 – Functional characterization of dopamine (DA) response in JumpIn-DAT cells. **(a)** Representative xCELLigence growth curves after cell seeding $\pm 1 \mu\text{g/ml}$ dox, inhibitor pretreatment and dopamine addition. **(b)** Effect of dox on JumpIn-DAT cell response (TRACT assay) upon stimulation with $10 \mu\text{M}$ dopamine (set at 100%) (\blacksquare) and effect of dox on cell surface expression of DAT detected by HA-tag ELISA (teal \blacklozenge , expressed as fold over mock). Data are shown as mean \pm SD (HA-tag ELISA) or SEM (TRACT assay) of two or three separate experiments performed in quintuplicate or duplicate, respectively. **(c)** Representative vehicle-corrected xCELLigence traces of JumpIn-DAT cells in the absence of dox (-dox) and **(d)** JumpIn-DAT cells in the presence of $1 \mu\text{g/ml}$ dox (+dox) after stimulation with increasing concentrations of dopamine. Data is normalized prior to agonist addition at time = 0 min. **(e)** Concentration-effect curves of dopamine on JumpIn-DAT cells \pm dox are shown as the net AUC of the first 30 minutes after stimulation normalized to the cell response of $316 \mu\text{M}$ dopamine. **(f)** Cell response of $31.6 \mu\text{M}$ dopamine (red bar, set at 100%) on dox-treated JumpIn-DAT cells pretreated for 1 h with $1 \mu\text{M}$ of one of following GPCR antagonists: SCH23390 (dopamine D1-like), raclopride (dopamine D2-like), doxazosin (alpha-1 adrenergic), yohimbine (alpha-2 adrenergic), propranolol (beta adrenergic). Data are shown as mean \pm SEM of three to nine individual experiments each performed in duplicate. Comparison of multiple mean values to vehicle control was done using a one-way ANOVA with Dunnett's post-hoc test. *** $p < 0.001$.

To characterize the dopamine response in JumpIn-DAT cells these were stimulated with increasing concentrations of dopamine. Impedance steadily increased reaching maximum nCI values after 10 to 15 min followed by a steady plateau (–dox) or slight decrease in nCI (+dox) after 30 min (**Figure 3.4c–d**), which is notably different from the negative nCI responses observed in U2OS cells (**Figure 3.1c–d**). Dopamine was significantly less potent ($p < 0.001$) in the TRACT assay on dox-treated cells ($pEC_{50} = 4.3 \pm 0.0$) than on vehicle-treated cells ($pEC_{50} = 5.1 \pm 0.1$) (**Figure 3.4e, Table 3.1**). This indicates that induced expression of DAT leads to extracellular removal and a decrease in the apparent potency of dopamine.

To verify dopamine-induced signaling was mediated *via* GPCR activation dox-treated cells were pretreated for 1 h in the presence of 1 μ M GPCR antagonist prior to stimulation with a submaximal concentration (31.6 μ M) dopamine. Addition of antagonists to the cells did not affect the nCI compared to cells pretreated with vehicle (**Supplementary Figure 3.S1c**). In contrast to U2OS-DAT cells the dopamine response was not affected by the dopamine D1-like receptor antagonist SCH23390, but was significantly reduced ($p < 0.001$) in the presence of alpha-2 adrenergic receptor antagonist yohimbine (**Figure 3.4f**). This suggests that DAT function can be detected in JumpIn-DAT cells albeit through distinct receptor activation compared to U2OS-DAT cells.

3.2.5 – Characterization of DAT inhibitors is possible using JumpIn-DAT cells in a TRACT assay

After characterization of the dopamine response the inhibitory potencies of two DAT inhibitors were determined in the TRACT assay. In addition to GBR12909 the dopamine-potentiating effect of cocaine was assessed. Pretreatment of dox-treated cells for 1 h with 10 μ M GBR12909 or cocaine on their own did not substantially affect impedance over time (**Supplementary Figure 3.S2b**). Subsequent stimulation with dopamine led to increased nCI values after 10 minutes at concentrations of dopamine between 1 and 31.6 μ M compared to vehicle-pretreated cells (compare **Figure 3.5a to 3.4d**). Consequently, GBR12909 enhanced the apparent potency of dopamine 2-fold ($pEC_{50} = 4.6 \pm 0.2$) compared to vehicle-pretreated cells ($pEC_{50} = 4.3 \pm 0.0$), though this was not significant ($p = 0.057$). Cocaine showed a significant ($p < 0.001$), 3-fold increase in apparent potency of dopamine ($pEC_{50} = 4.9 \pm 0.1$) (**Figure 3.5b, Table 3.1**). Of note, cocaine was thereby able to restore dopamine's apparent potency to a value close to the one observed in cells without DAT (–dox: $pEC_{50} = 5.1 \pm 0.1$; **Table 3.1**). Comparable to U2OS-DAT cells the slope of the dopamine concentration-effect curve in dox-treated cells was steeper (1.5 ± 0.1) compared to vehicle-treated cells (0.8 ± 0.1) and dox-treated cells pretreated with GBR12909 (0.8 ± 0.1) or cocaine (0.7 ± 0.1) when a variable slope regression model was used (**Supplementary Table 3.S1, Supplementary Figure 3.S3b**).

Following characterization of DAT inhibition on JumpIn-DAT cells, the inhibitory potency of GBR12909 and cocaine was assessed on dox-treated cells. Different from U2OS-DAT cells the biggest difference in dopamine response between vehicle- and dox-treated cells was observed at a submaximal concentration (10 μ M) of dopamine (**Figure 3.4e**), proposing

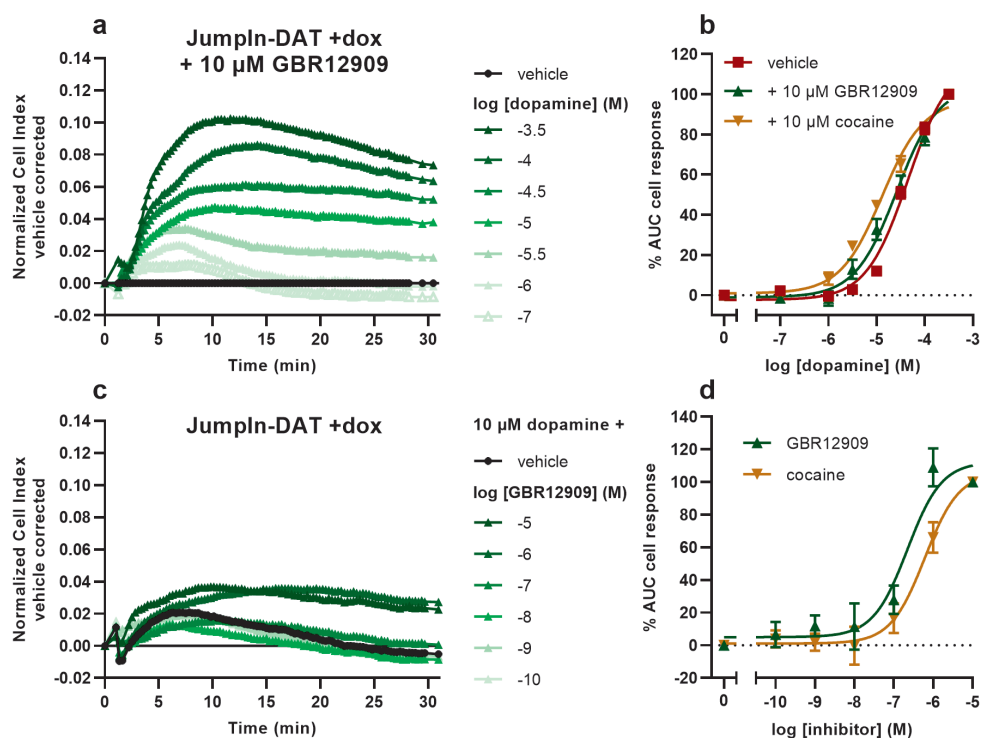


Figure 3.5 – Functional characterization of GBR12909 and cocaine on DAT in Jumpln-DAT cells in the presence of 1 μ g/ml dox (+dox) in a TRACT assay. Cells were pretreated with vehicle or 10 μ M (**a,b**) or increasing concentrations (**c,d**) of either GBR12909 or cocaine. (**a**) Representative vehicle-corrected xCELLigence traces after stimulation with increasing concentrations of dopamine or (**c**) 3.16 μ M dopamine. (**b**) Concentration-effect curves of dopamine in dox-treated Jumpln-DAT cells pretreated with vehicle or 10 μ M GBR12909 or cocaine are shown as the net AUC of the first 30 min after stimulation normalized to the cell response of 316 μ M dopamine. (**d**) Concentration-effect curve of GBR12909 and cocaine after addition of 10 μ M dopamine normalized to 10 μ M inhibitor. Data are shown as mean \pm SEM of four to nine separate experiments each performed in duplicate.

the optimal window to detect DAT inhibition. Both inhibitors showed concentration-dependent enhancement of dopamine-induced cell responses with GBR12909 being more potent ($pIC_{50} = 6.6 \pm 0.1$) than cocaine ($pIC_{50} = 6.3 \pm 0.2$) (**Figure 3.5c–d**). This provides evidence for the suitability of the TRACT assay to determine DAT inhibitor potencies.

3.3 – Discussion

Label-free, non-invasive *in vitro* functional assays for SLC transporters are scarce³. The most prevalent strategy to assess SLC function *in vitro* is still by direct measurement of labeled or modified substrate uptake in recombinant cell lines, animal tissues or SLC-containing membrane preparations. Novel label-free systems that detect SLC ligand engagement in living cells, such as the cellular thermal shift assay (CETSA)²⁸ and mass spectrometry binding

assays²⁹, require invasive processing of cells prior to or after SLC binding events. A recently described HTS-compatible label-free cell-based cytotoxicity assay for monocarboxylate transporter 1 (SLC16A1) showed promise for inhibitor screening studies³⁰, although this method demands that a selective cytotoxic substrate is available for the SLC. Moreover, in 2012 Wong *et al.* reported on the use of a label-free optical biosensor to characterize functional inhibition of the electrogenic sodium-dependent phosphate transporter 2B (SLC34A2), but this was not followed up on³¹. Previously, a non-invasive assay using xCELLigence was described by our research team to detect activity of non-electrogenic ENT1 *via* adenosine receptor (AR) signaling in U2OS cells, which endogenously express both ENT1 and ARs²². Compared to the assay by Vlachodimou *et al.*, the novelty of the assay in this chapter is the use of two cell lines with distinct endogenous GPCR expression and heterologous expression of DAT. In addition, for the first time we consider the expression levels and expression ratio between the receptor and transporter, presenting a more detailed look into the mechanism of the TRACT assay and providing a guideline for its use for other SLC-GPCR pairs.

Two mammalian cell lines were used to confirm the hypothesis that the presence of DAT reduces extracellular dopamine and thereby activation of cell surface receptors. Primary criterion for cell line selection was endogenous expression of dopamine-responsive GPCRs. U2OS cells were chosen as a suitable cell line as RNA-Seq data available from The Human Protein Atlas (www.proteinatlas.org)³² indicated expression of D₁R on these cells (The Human Protein Atlas: ENSG00000184845-DRD1). Moreover, functional activation of D₁R on U2OS cells by dopamine has been reported previously in an impedance-based assay³³. Expression of DAT is not reported in U2OS (The Human Protein Atlas: ENSG00000142319-SLC6A3), which necessitated heterologous expression of DAT. Although DAT-transfected U2OS cells were successfully used to characterize pharmacological DAT inhibition (**Figure 3.2**), the transient transfection procedure was deemed time-intensive and unfit for upscaling of experimental throughput. In addition, variation in protein expression levels and quality can vary substantially between batches of transiently transfected cells compared to stable expression systems³⁴. Therefore, an additional second cell line, HEK 293 JumpIn-DAT, was created with stable and inducible expression of DAT. Reported transcriptomics data suggest that HEK 293 JumpIn cells do not express dopamine receptors (BioSamples database (www.ebi.ac.uk/biosamples)³⁵: SAMN11893676, SAMN11893683, SAMN11893683), but rather express the alpha-2C adrenergic receptor. Dopamine has been reported to exert agonistic effects on this receptor³⁶, which was confirmed in the current chapter (**Figure 3.4f**).

Uptake by DAT is the main process responsible for removal of extracellular dopamine in dopaminergic synapses and extrasynaptic spaces³⁷. In striatal slices of mice dopamine released by electrical stimulation remained in the extracellular space more than 100-fold longer in DAT knock-out mice compared to wild-type mice with fully functional DAT, underlining the importance of DAT in dopamine clearance, signaling and tone³⁸. Analogously, in the TRACT assay expression of DAT resulted in a lower apparent potency of dopamine compared to mock-transfected or non-induced cells assuming a pseudo-Hill slope of 1 (**Figure 3.1e and 3.5e**). Interestingly, when these data were fitted to sigmoidal concentration-effect curves with a variable slope, it was evident that slopes

for dopamine concentration-effect curves on U2OS-DAT and dox-treated JumpIn-DAT cells were significantly steeper compared to cells lacking DAT (**Supplementary Figure 3.S3, Supplementary Table 3.S1**). Pretreatment with GBR12909 or cocaine restored the slopes of the dopamine concentration-effect curves in U2OS-DAT and dox-treated JumpIn-DAT cells to values close to mock or vehicle-treated cells. This observation could be explained according to concepts described by Kenakin, which postulate that a saturable removal process (e.g., dopamine uptake by DAT), of which the magnitude is dependent on the capacity of the process (V_{\max}) and the affinity of the substrate for the process (K_m), affects the free concentration of a substrate present in the medium^{39,40}. Thus, if the removal process is saturated within the concentration range of substrate used in the experiment, the presence of the removal process leads to an increased pseudo-Hill slope and a rightward shift of the substrate concentration-effect curve upon binding to surface receptors (e.g. GPCRs). This is the case for the TRACT assay in this chapter, as dopamine K_m values for DAT have been reported to be between 0.1 and 5 μM in heterologous DAT expression systems⁴¹, which are in the range of the tested dopamine concentrations. Therefore, in this context increased pseudo-Hill slopes in addition to a rightward shift of the substrate concentration-effect curve may be indicative of a functional substrate removal process and validate the functionality of the TRACT assay. A more in-depth analysis of this concept by Kenakin is presented in **Chapter 8**.

One of the main differences between the current TRACT assay and the previously reported label-free assay for ENT1²² is the use of heterologous expression of the SLC. Thus, a major benefit of this approach is being able to better control the amount of SLC and/or GPCR in the cell line, making the assay less dependent on endogenous expression levels of both proteins. In this context we determined the ratio of SLC and GPCR present on the cell surface as an indication to adequately measure SLC function, by performing saturation binding experiments on U2OS-DAT cells with radioligands for both DAT and D₁R (**Figure 3.3, Supplementary Figure 3.S2**). The amount of D₁R on non-transfected U2OS cells ($B_{\max} = 0.1 \pm 0.0$ pmol/mg protein) was approximately 16-fold lower than the amount of DAT on U2OS-DAT cells ($B_{\max} = 1.6 \pm 0.2$ pmol/mg protein). Of note, the amount of D₁R on U2OS-DAT cells was below the detection limit of the radioligand binding assay (**Supplementary Figure 3.S4c**), indicating that the transient transfection procedure negatively impacts the expression of D₁R on U2OS cells. It has been reported that off-target effects and changes in cell behavior upon transient transfection can be attributed to transfection reagents itself or the introduction of foreign DNA into cells⁴², which could explain the apparent reduction in detectable D₁R in U2OS-DAT cells. This suggests that there is at least 16-fold more DAT than D₁R in U2OS-DAT cells, which in more general terms could indicate that the SLC should be present in higher concentrations than the GPCR. This was most probably also the case in the study by Vlachodimou *et al.*, where endogenous ENT1 is abundantly expressed on U2OS cells ($B_{\max} = 31$ pmol/mg protein), although no saturation or expression data of adenosine receptors was reported on these cells⁴³. Consequently, the transport capacity (V_{\max}) of the transporter to remove enough exogenous/extracellular substrate is observed as a shift in apparent substrate potency or change in pseudo-Hill slope of the GPCR response⁴⁰. The observed differences in the

apparent dopamine potency shifts between U2OS-DAT (19-fold compared to U2OS-mock) and dox-treated JumpIn-DAT (5-fold compared to vehicle-treated) may be due to differences in the method of transfection, post-translational modifications, cell surface expression levels of both DAT and GPCR, or divergent expression patterns of regulatory proteins of DAT⁴⁴.

To validate the TRACT assay for DAT, we selected two reference DAT inhibitors (GBR12909 and cocaine) which have a 10 to 100-fold difference in affinity for DAT⁴⁵. Both cell lines were successfully used to determine the inhibitory potency of GBR12909, which is a well-known atypical DAT inhibitor with reported low nanomolar affinity for DAT^{45,46}. The presence of GBR12909 in U2OS-DAT or dox-treated JumpIn-DAT cells enhanced the response of these cells to dopamine comparable to cells lacking DAT. The inhibitory potency values for GBR12909 obtained in this chapter are in line with reported pIC₅₀ values for a fluorescence-based neurotransmitter uptake assay (6.7)⁴⁷ and 1-methyl-4-phenylpyridinium (MPP+)-induced toxicity inhibition (7.0)⁴⁸, but are slightly lower compared to pIC₅₀ values measured in [³H]dopamine uptake experiments, which show a wide range of values from 6.6 to 9.0^{45,46,49–51}. This could be due to the method used to analyze the Cell Index traces of the dopamine responses (e.g., use peak nCI instead of AUC, or use different time intervals to infer the AUC), which could in turn influence the pIC₅₀ value⁵². Moreover, the difference in potency may be explained by the presence of high (competing) concentrations of dopamine upon stimulation in the TRACT assay (3.16 – 10 μ M), whereas traditional uptake inhibition assays are usually performed in the presence of 10–100 nM [³H]dopamine⁵³. The high concentrations of dopamine could potentially mask the high affinity of compounds for DAT, as we have observed for GBR12909, which could lead to the TRACT assay detecting only compounds with a high affinity while missing out on inhibitors with low potency. However, the inhibitory potency values obtained for cocaine, a classical inhibitor that binds to the same central binding site as dopamine⁵⁴, were in line with previously reported values measured in neurotransmitter uptake assays (pIC₅₀ values range from 6.1 to 7.2)^{45,46,49,50,55}, indicating that the TRACT assay is sensitive enough to detect DAT inhibitors with varying affinities.

In summary, this chapter reports the first label-free whole-cell bioassay, termed the TRACT assay, that allows characterization of pharmacological DAT inhibition using the impedance-based xCELLigence technology. Dopamine responses were recorded in real-time in two mammalian cell lines, each *via* activation of endogenously expressed GPCRs. The presence of DAT in these cells resulted in attenuated dopamine-induced GPCR signaling, which was essentially recovered upon pretreatment with DAT inhibitors. This provided an assay window to measure inhibitory potencies of two DAT inhibitors, which were in accordance with values from previously reported orthogonal functional assays. The current chapter demonstrates the versatility of impedance-based biosensors to detect signaling events in a single cell line, which can be attributed to both GPCR activation and SLC activity. This adds SLCs to the increasing list of protein classes that can be assessed using label-free whole cell bioassays with the intended application in drug discovery programs. Consequently, this opens up unexplored venues for development of the TRACT assay as a novel drug discovery tool for SLCs that have a shared substrate with GPCRs.

3.4 – Material and methods

3.4.1 – Chemicals and reagents

Human bone osteosarcoma cells (U2OS) were kindly provided by Mr. Hans den Dulk (Leiden Institute of Chemistry, department of Molecular Physiology, Leiden University, and the Netherlands). Jump In T-REx human embryonic kidney 293 (HEK 293) cells modified for doxycycline-inducible overexpression of the wild-type human dopamine transporter (JumpIn-DAT) were provided by CeMM (Research Center for Molecular Medicine, Medical University of Vienna, Austria). Dulbecco's Modified Eagle's Medium high glucose (DMEM), doxycycline hyclate, dopamine hydrochloride, (\pm)-propranolol hydrochloride and (+)-butaclamol hydrochloride were purchased from Sigma-Aldrich (St. Louis, MO, USA). GBR12909 dihydrochloride was purchased from Toronto Research Chemicals (North York, Canada). Cocaine hydrochloride was purchased from Duchefa Farma (Haarlem, The Netherlands), where Leiden University has been certified for its use in pharmacological experiments. SCH23390 hydrochloride and raclopride were purchased from Tocris Bioscience (Bristol, United Kingdom). Yohimbine hydrochloride and doxazosin mesylate were purchased from Santa Cruz Biotechnology (Dallas, TX, USA). Radioligands [3 H]-2 β -carbomethoxy-3 β -(4-fluorophenyl)-tropane ([3 H]WIN35,428, specific activity of 82.4 Ci/mmol) and [3 H]-(R)-(+)-7-chloro-8-hydroxy-3-methyl-1-phenyl-2,3,4,5-tetrahydro-1H-3-benzazepine ([3 H]SCH23390, specific activity of 83.2 Ci/mmol) were purchased from PerkinElmer (Groningen, The Netherlands). xCELLigence PET E-plates 96 (ACEA Biosciences, San Diego, CA, USA) were purchased from Bioké (Leiden, The Netherlands). All other chemicals were of analytical grade and obtained from standard commercial sources.

3.4.2 – Stable JumpIn-DAT cell line generation

After thawing Jump In T-REx HEK 293 (JumpIn) cells were split twice a week in growth medium containing 200 μ g/ml hygromycin B and 5 μ g/ml blasticidin. A codon optimized ORF (Addgene #132160) for the human dopamine transporter (SLC6A3, ORF: NM_001044) was cloned into a Gateway-compatible expression vector which was generated by inserting Twin-Strep-tag epitopes followed by the human influenza hemagglutinin (HA)-tag downstream of the AttR2 gateway site in the original pJTI R4 DEST CMV TO pA vector. This vector therefore allows expression of SLC6A3 with a C-terminal Twin-Strep-HA tag. Of note, the plasmid contains two tetracycline operator 2 (TO) sites under a cytomegalovirus immediate-early (CMV) promoter to allow inducible expression of the gene of interest in the presence of doxycycline (dox). JumpIn cells were transfected with the expression vector using Lipofectamine in medium without antibiotics according to the manufacturer's protocol (ThermoFisher Scientific). Successfully transfected cells were selected in medium containing 2 mg/ml Geneticin (G418) and 5 μ g/ml blasticidin for 2 to 4 weeks. Resistant clones were pooled after selection and used for all further experiments.

3.4.3 – Cell culture

JumpIn-DAT cells were grown as adherent cells in culture medium consisting of DMEM (high glucose) supplemented with 10% (v/v) fetal calf serum (FCS), 2 mM Glutamax, 100

µg/ml streptomycin and 100 IU/ml penicillin at 37°C and 7% CO₂. After thawing, recovered cells were maintained up to one week in culture medium supplemented with 2 mg/ml G418 and 5 µg/ml blasticidin to select transfected clones. After this round of selection, cells were switched back to regular culture medium at least 24 h before the next experiment. Cells were subcultured twice a week at ratios of 1:8 – 1:16 in 10 cm plates.

U2OS cells were grown as adherent cells in culture medium consisting of DMEM (high glucose) supplemented with 10% (v/v) newborn calf serum (NCS), 2 mM Glutamax, 100 µg/ml streptomycin and 100 IU/ml penicillin at 37°C and 7% CO₂. Cells were subcultured twice a week at ratios of 1:8 – 1:12 in 10 cm plates.

3.4.4 – Transient U2OS-DAT cell line generation

For transient transfection of U2OS cells, empty pcDNA3.1(+) plasmid (mock cDNA), as well as cDNA encoding the human DAT (SLC6A3, ORF: NM_001044) containing a C-terminal FLAG-tag cloned into a pcDNA3.1(+) plasmid (DAT cDNA) were purchased from GenScript (Piscataway, NJ, USA). cDNA was transformed into DH5α competent cells (Invitrogen, Carlsbad, CA, USA) in the presence of 100 µg/ml ampicillin and was purified using a QIAGEN Plasmid Midi Kit (QIAGEN, Hilden, Germany). Quality and concentration of the cDNA were measured using a NanoDrop 2000 (Thermo Fisher Scientific, Waltham, MA, USA).

U2OS cells were transiently transfected using polyethyleneimine (PEI) as a transfection vector⁵⁶. 24 h before transfection, cells were seeded in 10 cm plates to achieve 50–70% confluence on the day of transfection. Prior to transfection, medium was switched to culture medium without penicillin/streptomycin. A mix of 15 µg/ml PEI and 5 µg total cDNA (mock or DAT) in 1 ml Opti-MEM was incubated at room temperature for 30 min. Per 10 cm plate, 1 ml PEI-cDNA complex was added and cells were incubated for 24 h at 37°C and 7% CO₂ before membrane preparation or use in TRACT or ELISA assays.

3.4.5 – Whole-cell FLAG-tag ELISA

Transiently transfected U2OS cells were detached from 10 cm plates 24 h post-transfection using phosphate-buffered saline (PBS)/EDTA. Cells were counted and seeded in a sterile 96-well flat bottom plate in culture medium at 80,000 cells/well in the presence of 5 mM sodium butyrate to enhance DAT expression⁵⁷ and incubated at 37°C and 7% CO₂ for 24 h (100 µl total volume). All subsequent handlings were performed at room temperature. After incubation, cells were washed with PBS and fixed with 3.7% formaldehyde for 10 min. Cells were washed with Tris-buffered saline (TBS) and subsequently blocked with TBS containing 2% (w/v) bovine serum albumin (BSA) and 0.2% (w/v) saponin for 30 min. Saponin was included in all subsequent incubation steps to facilitate membrane permeabilization⁵⁸ to allow the primary and secondary antibodies to reach the intracellular C-terminal FLAG-tag of DAT. After blocking, cells were incubated with 1:2500 mouse anti-FLAG M2 monoclonal antibody (Sigma Aldrich) for 2 h. Subsequently, cells were incubated with 1:10,000 rabbit anti-mouse horse radish peroxidase (HRP)-conjugated IgG antibody (Sigma Aldrich) for 1 h. To visualize immunoreactivity, HRP substrate 3,3',5,5'-tetramethylbenzidine (TMB)

was added to cells and incubated for 5 min. The reaction was quenched with 1 M H_3PO_4 . Absorbance at 450 nm was measured using a Wallac EnVision multimode plate reader (PerkinElmer, Groningen, The Netherlands).

3.4.6 – Whole-cell HA-tag ELISA

JumpIn-DAT cells were grown in culture medium to 80% confluence. Cells were trypsinized, counted and seeded in a sterile 96-well flat bottom plate in culture medium at 60,000 cells/well in the presence of increasing amounts (1 pg/ml – 1 µg/ml) of dox (100 µl total volume). Cells were incubated at 37°C and 7% CO_2 for 24 h. All subsequent handlings were performed at room temperature. After incubation, cells were washed with PBS and fixed with 3.7% formaldehyde for 10 min. Cells were washed with DMEM and blocked with DMEM containing 2% (w/v) BSA and 0.2% (w/v) saponin for 1 h. After blocking, cells were incubated with 1:2500 rabbit anti-HA polyclonal antibody (Invitrogen, Carlsbad, CA, USA) for 30 min. Subsequently, cells were washed with DMEM containing 25 mM HEPES and incubated with 1:3000 goat anti-rabbit HRP-conjugated IgG antibody (Brunschwig Chemie, Amsterdam, The Netherlands) for 30 min. Immunoreactivity was visualized and measured as described in **Section 3.4.5**.

3.4.7 – Membrane preparation

Transiently transfected U2OS-DAT cells were treated with 5 mM sodium butyrate 24 h post-transfection to enhance protein expression. U2OS-DAT cells were grown to 50–70% confluence in 10 cm plates and harvested 48 h post-transfection by scraping in PBS and pelleted by centrifugation for 5 min at 1400 x g. Non-transfected U2OS cells were grown to 90% confluence prior to scraping in PBS and centrifugation. Pellets were suspended in ice-cold Tris buffer (50 mM Tris-HCl, pH 7.4) and homogenized using an Ultra Turrax homogenizer (IKA-Werke GmbH & Co.KG, Staufen, Germany). Membranes were separated from the cytosolic fraction by centrifugation at 31,000 x g using an Optima LE-80K Ultracentrifuge (Beckman Coulter, Fullerton, CA, USA) for 20 min at 4°C. Pellets were suspended in ice-cold Tris buffer, homogenized and centrifuged once more. Final pellets were suspended in ice-cold Tris buffer, aliquoted and stored at –80°C. Protein amount of the membranes was determined using a bicinchoninic acid protein determination⁵⁹.

3.4.8 – [^3H]WIN35,428 and [^3H]SCH23390 saturation binding assays

U2OS-DAT or non-transfected U2OS membranes (20 µg per well) were incubated in assay buffer (50 mM Tris-HCl, pH 7.4, and 100 mM NaCl) containing [^3H]WIN35,428 or [^3H]SCH23390, respectively, for 120 min at 25°C to ensure equilibrium binding was reached at all tested radioligand concentrations. Total binding (TB) was determined in the presence of increasing concentrations of [^3H]WIN35,428 (2–150 nM) or [^3H]SCH23390 (0.1–10 nM). Non-specific binding (NSB) was determined at three concentrations of [^3H]WIN35,428 (2, 80, 150 nM) in the presence of 100 µM GBR12909, or [^3H]SCH23390 (0.1, 4, 10 nM) in the presence of 10 µM (+)-butaclamol. Amounts of dimethylsulfoxide (DMSO) in all wells were kept at 1%. Membrane incubation was terminated by rapid filtration through a 96-well GF/B filter plate using a FilterMate 96-well plate harvester (PerkinElmer, Groningen, The

Netherlands). Filters were washed 10 times with ice-cold assay buffer and dried completely. Filter-bound radioactivity was measured in the presence of 25 µl/well Microscint scintillation cocktail using a MicroBeta² 2450 microplate scintillation counter (PerkinElmer, Groningen, The Netherlands).

3.4.9 – TRACT assays (xCELLigence)

Label-free whole-cell TRACT assays were performed using the xCELLigence real-time cell analyzer (RTCA) system as described in previous publications^{22,43}. In principle, xCELLigence RTCA measures the impedance that is generated by cells that adhere to the gold-coated electrodes and cover the bottom of microtiter E-plates. Any change in adhesion, cell number, proliferation rate and morphology (e.g., as a result of pharmacological perturbations) is measured as an increase or decrease of impedance over time. Impedance values, which are measured continuously at a frequency of 10 kHz, for each well are converted by the RTCA software to the dimensionless parameter Cell Index (CI) using the following formula:

$$CI = \frac{(Z_i - Z_0)\Omega}{15\Omega}$$

where Z_i is the impedance at any given time point and Z_0 is the baseline impedance that is measured at the start of each experiment¹⁶.

All assays were performed at 37°C and 5% CO₂ in 96-well E-plates in a total volume of 100 µl per well. Depending on the amount of compound additions during an experiment, background impedance at the start of each experiment was measured in 45 µl (1 addition) or 40 µl (2 additions) culture medium. Cells were seeded manually in the wells in a volume of 50 µl. Compounds were added in 5 µl per addition using a VIAFLO 96 handheld electronic 96 channel pipette (INTEGRA Biosciences, Tokyo, Japan).

3.4.9.1 – Cell preparation and monitoring

To demonstrate reproducibility of the TRACT experiments, cells were used from at least two different cell batches. In addition, cells were used at different passage numbers, ranging from p2 to p11. U2OS-mock or U2OS-DAT cells grown to 50–70% confluence were detached 24 h post-transfection from 10 cm plates with PBS/EDTA. Background impedance in 96-well E-plates was measured using culture medium containing a final concentration of 5 mM sodium butyrate. Subsequently, cells were seeded at 40,000 cells/well in culture medium. The E-plate was left at room temperature for 30 min and placed in the recording station. Impedance was measured overnight every 15 min. Cells were treated 17–19 h after seeding based on previous reports^{12,22}.

JumpIn-DAT cells grown to 70–80% confluence were briefly trypsinized from 10 cm plates prior to use in the assay. Baseline impedance was measured using culture medium containing dox (1 pg/ml – 1 µg/ml) or vehicle (milliQ water). Subsequently, cells were seeded at 60,000 cells/well in culture medium. The E-plate was left at room temperature for 30 min and placed in the recording station. Impedance was measured overnight every 15 min. Cells

were treated 22–24 h after seeding as dox-induced protein expression is optimal after 24 h according to the JumpIn cells manufacturer's protocol (Thermo Fisher Scientific).

3.4.9.2 – Cell pretreatment

In antagonist experiments, cells were pretreated by the addition of a GPCR antagonist (1 μ M; SCH23390, raclopride, doxazosin, yohimbine, propranolol). In TRACT assays, cells were pretreated with a DAT inhibitor (10 μ M or increasing concentrations (100 pM – 10 μ M); GBR12909, cocaine) or a vehicle control (0.1% DMSO in PBS). Final amounts of DMSO in each well were kept at 0.1%. Impedance was measured every minute after the addition for 60 min.

3.4.9.3 – Cell stimulation

Cells were stimulated by the addition of dopamine (concentration depending on type of assay) or a vehicle control (1 mM ascorbic acid in PBS). Note, ascorbic acid was used in the presence of dopamine to prevent its oxidation in culture medium. In antagonist experiments, cells were stimulated with a submaximal (EC_{80}) concentration of dopamine. In TRACT assays to determine the inhibitory potency of DAT inhibitors, cells were stimulated with a submaximal (EC_{20}) concentration of dopamine. Impedance was measured initially every 15 seconds after the addition for 25 min, then every minute for 10 min, every 5 minutes for 50 min and finally every 15 minutes. For U2OS-mock and U2OS-DAT cells, impedance was measured for 120 min after stimulation. For JumpIn-DAT cells, impedance was measured for 30 min after stimulation.

3.4.10 – Data analysis

3.4.10.1 – Radioligand saturation binding

To calculate B_{max} values, disintegrations per minute (DPM) values of each data point obtained from saturation binding experiments were converted to pmol/mg protein using the specific activity of the radioligand and overall membrane protein concentration. Resulting data were analyzed using GraphPad Prism v8.1.1 (GraphPad Software, San Diego, CA, USA). The equilibrium dissociation constant (K_D) and total amount of specific binding sites (B_{max}) of [3 H]WIN35,438 and [3 H]SCH23390 were determined by fitting the data with non-linear regression to an exponential one site – total and non-specific binding equation. Specific binding was visualized by subtracting linear non-specific binding from total binding and fitting the data with a one site – specific binding equation.

3.4.10.2 – xCELLigence

Experimental data was recorded using RTCA Software v2.0 or v2.1.1 (ACEA Biosciences). CI values were normalized to the first time point prior to cell stimulation to obtain normalized CI (nCI) values. Raw nCI data were exported using RTCA Software and all subsequent analyses were performed using GraphPad Prism v8.1.1. In all experiments, nCI values of vehicle-only conditions were subtracted from all other data points to correct for vehicle-induced, ligand-independent effects. Vehicle-corrected nCI responses were analyzed

by taking the absolute net area under the curve (AUC) of the first 120 min (U2OS-mock, U2OS-DAT) or 30 min (JumpIn-DAT) after agonist stimulation to make concentration-effect curves and bar graphs. Apparent potency values of dopamine (pEC_{50}) and inhibitory potency values of DAT inhibitors (pIC_{50}) were obtained by fitting the AUC data with non-linear regression to a sigmoidal concentration-effect curve with a pseudo-Hill slope of 1 or a variable pseudo-Hill slope.

3.4.10.3 – Statistics

Data are shown as the mean \pm standard error of the mean (SEM) of at least three separate experiments each performed in duplicate, unless stated otherwise. Significant difference between two mean potency values was determined by an unpaired two-tailed Student's t-test. Comparison of multiple mean values to a vehicle control was done using a one-way ANOVA with Dunnett's post-hoc test. Differences were considered statistically significant when p-values were below 0.05.

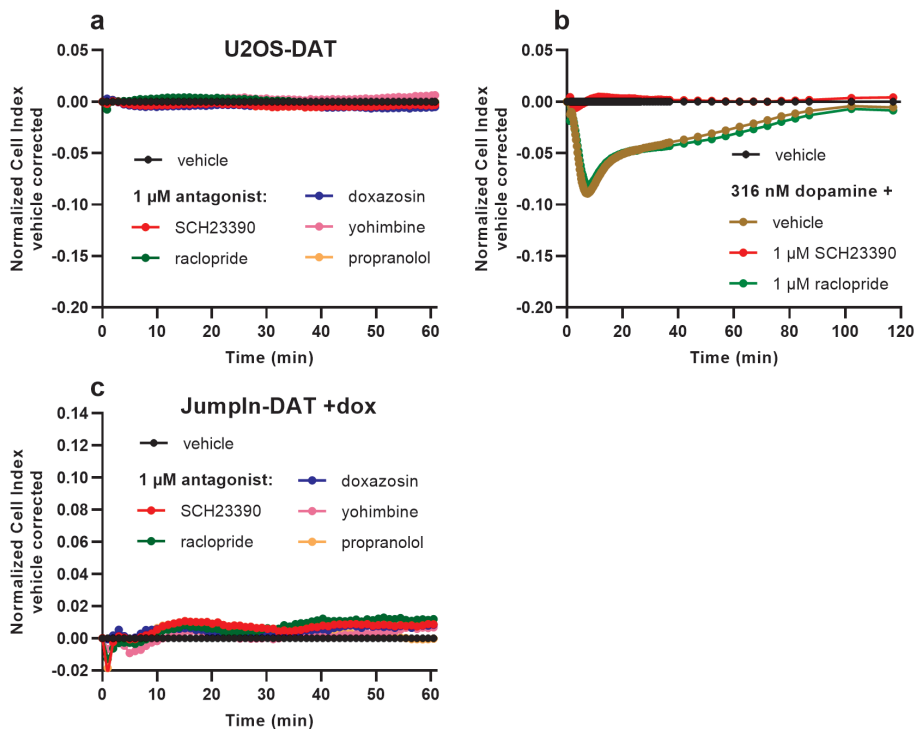
References

1. Hediger, M. A., Cléménçon, B., Burrier, R. E. & Bruford, E. A. (2013) The ABCs of membrane transporters in health and disease (SLC series): Introduction. *Mol. Aspects Med.* **34**, 95–107.
2. Lin, L., Yee, S. W., Kim, R. B. & Giacomini, K. M. (2015) SLC transporters as therapeutic targets: Emerging opportunities. *Nat. Rev. Drug Discov.* **14**, 543–560.
3. Wang, W. W., Gallo, L., Jadhav, A., Hawkins, R. & Parker, C. G. (2020) The druggability of solute carriers. *J. Med. Chem.* **63**, 3834–3867.
4. Volpe, D. A. (2016) Transporter assays as useful in vitro tools in drug discovery and development. *Expert Opin. Drug Discov.* **11**, 91–103.
5. Brouwer, K. L. R. *et al.* (2013) In vitro methods to support transporter evaluation in drug discovery and development. *Clin. Pharmacol. Ther.* **94**, 95–112.
6. César-Razquin, A. *et al.* (2015) A call for systematic research on solute carriers. *Cell* **162**, 478–487.
7. Mason, J. N. *et al.* (2005) Novel fluorescence-based approaches for the study of biogenic amine transporter localization, activity, and regulation. *J. Neurosci. Methods* **143**, 3–25.
8. Zheng, W., Spencer, R. H. & Kiss, L. (2004) High throughput assay technologies for ion channel drug discovery. *Assay Drug Dev. Technol.* **2**, 543–552.
9. Schroeder, K. S. & Neagle, B. D. (1996) FLIPR: A new instrument for accurate, high throughput optical screening. *J. Biomol. Screen.* **1**, 75–80.
10. Grewer, C., Gameiro, A., Mager, T. & Fendler, K. (2013) Electrophysiological characterization of membrane transport proteins. *Annu. Rev. Biophys.* **42**, 95–120.
11. Scott, C. W. & Peters, M. F. (2010) Label-free whole-cell assays: Expanding the scope of GPCR screening. *Drug Discov. Today* **15**, 704–716.
12. Hillger, J. M. *et al.* (2015) Whole-cell biosensor for label-free detection of GPCR-mediated drug responses in personal cell lines. *Biosens. Bioelectron.* **74**, 233–242.
13. Atienza, J. M., Yu, N., Wang, X., Xu, X. & Abassi, Y. (2006) Label-free and real-time cell-based kinase assay for screening selective and potent receptor tyrosine kinase inhibitors using microelectronic sensor array. *J. Biomol. Screen.* **11**, 634–643.
14. Xi, B. *et al.* (2011) Functional cardiotoxicity profiling and screening using the xCELLigence RTCA cardio system. *J. Lab. Autom.* **16**, 415–421.
15. Krebs, K. M. *et al.* (2018) Label-free whole cell biosensing for high-throughput discovery of activators and inhibitors targeting G protein-activated inwardly rectifying potassium channels. *ACS Omega* **3**, 14814–14823.
16. Yu, N. *et al.* (2006) Real-time monitoring of morphological changes in living cells by electronic cell sensor arrays: an approach to study G protein-coupled receptors. *Anal. Chem.* **78**, 35–43.
17. Fang, Y., Ferrie, A. M., Fontaine, N. H., Mauro, J. & Balakrishnan, J. (2006) Resonant waveguide grating biosensor for living cell sensing. *Biophys. J.* **91**, 1925–1940.
18. Doijen, J. *et al.* (2019) Advantages and shortcomings of cell-based electrical impedance measurements as a GPCR drug discovery tool. *Biosens. Bioelectron.* **137**, 33–44.
19. Halai, R. & Cooper, M. A. (2012) Using label-free screening technology to improve efficiency in drug discovery. *Expert Opin. Drug Discov.* **7**, 123–131.
20. Nederpelt, I., Vergroesen, R. D., IJzerman, A. P. & Heitman, L. H. (2016) Persistent GnRH receptor activation in pituitary α T3-1 cells analyzed with a label-free technology. *Biosens. Bioelectron.* **79**, 721–727.
21. Schröder, R. *et al.* (2010) Deconvolution of complex G protein-coupled receptor signaling in live cells using dynamic mass redistribution measurements. *Nat. Biotechnol.* **28**, 943–949.
22. Vlachodimou, A., IJzerman, A. P. & Heitman, L. H. (2019) Label-free detection of transporter activity via GPCR signalling in living cells: a case for SLC29A1, the equilibrative nucleoside transporter 1. *Sci. Rep.* **9**, 13802.
23. Kristensen, A. S. *et al.* (2011) SLC6 neurotransmitter transporters: Structure, function, and regulation. *Pharmacol. Rev.* **63**, 585–640.
24. Faraone, S. V. (2018) The pharmacology of amphetamine and methylphenidate: Relevance to the neurobiology of attention-deficit/hyperactivity disorder and other psychiatric comorbidities. *Neurosci. Biobehav. Rev.* **87**, 255–270.
25. Volkow, N. D. *et al.* (2009) Effects of modafinil on dopamine and dopamine transporters in the male human brain clinical implications. *J. Am. Med. Assoc.* **301**, 1148–1154.
26. Reith, M. E. A. *et al.* (2015) Behavioral, biological, and chemical perspectives on atypical agents targeting the dopamine transporter. *Drug Alcohol Depend.* **147**, 1–19.
27. Schmitt, K. C. & Reith, M. E. A. (2010) Regulation of the dopamine transporter: Aspects relevant to psychostimulant drugs of abuse. *Ann. N. Y. Acad. Sci.* **1187**, 316–340.
28. Hashimoto, M., Girardi, E., Eichner, R. & Superti-Furga, G. (2018) Detection of chemical engagement of solute carrier proteins by a cellular thermal shift assay. *ACS Chem. Biol.* **13**, 1480–1486.

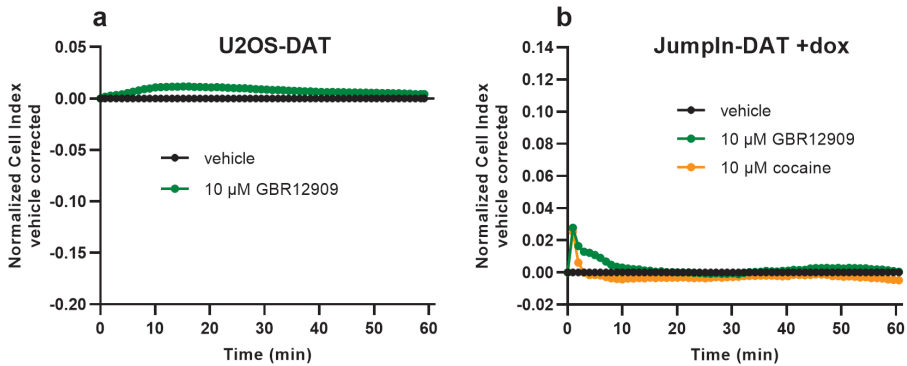
29. Neiens, P. *et al.* (2018) Development and validation of an LC-ESI-MS/MS method for the quantification of D-84, reboxetine and citalopram for their use in MS binding assays addressing the monoamine transporters hDAT, hSERT and hNET. *Biomed. Chromatogr.* **32**, e4231.
30. Bailey, T. L., Nieto, A. & McDonald, P. H. (2019) A nonradioactive high-throughput screening-compatible cell-based assay to identify inhibitors of the monocarboxylate transporter protein 1. *Assay Drug Dev. Technol.* **17**, 275–284.
31. Wong, S.-H., Gao, A., Ward, S., Henley, C. & Lee, P. H. (2012) Development of a label-free assay for sodium-dependent phosphate transporter NaPi-IIb. *J. Biomol. Screen.* **17**, 829–834.
32. Thul, P. J. *et al.* (2017) A subcellular map of the human proteome. *Science* **356**, eaal3321.
33. Peters, M. F. & Scott, C. W. (2009) Evaluating cellular impedance assays for detection of GPCR pleiotropic signaling and functional selectivity. *J. Biomol. Screen.* **14**, 246–255.
34. Zhang, Z., Guan, N., Li, T., Mais, D. E. & Wang, M. (2012) Quality control of cell-based high-throughput drug screening. *Acta Pharm. Sin. B* **2**, 429–438.
35. Courtot, M. D. S. *et al.* (2019) Biosamples database: An updated sample metadata hub. *Nucleic Acids Res.* **47**, D1172–D1178.
36. Sánchez-Soto, M. *et al.* (2018) $\alpha 2$ A- and $\alpha 2$ C-adrenoceptors as potential targets for dopamine and dopamine receptor ligands. *Mol. Neurobiol.* **55**, 8438–8454.
37. Torres, G. E., Gainetdinov, R. R. & Caron, M. G. (2003) Plasma membrane monoamine transporters: Structure, regulation and function. *Nat. Rev. Neurosci.* **4**, 13–25.
38. Giros, B., Jaber, M., Jones, S. R., Wightman, R. M. & Caron, M. G. (1996) Hyperlocomotion and indifference to cocaine and amphetamine in mice lacking the dopamine transporter. *Nature* **379**, 606–612.
39. Kenakin, T. P. (1985) Schild regressions as indicators of non-equilibrium steady-states and heterogeneous receptor populations. *Trends Pharmacol. Sci.* **6**, 68–71.
40. Kenakin, T. P. (Elsevier, 2014). *A Pharmacology Primer: Techniques for More Effective and Strategic Drug Discovery*. Academic Press vol. 38.
41. Hovde, M. J., Larson, G. H., Vaughan, R. A. & Foster, J. D. (2019) Model systems for analysis of dopamine transporter function and regulation. *Neurochem. Int.* **123**, 13–21.
42. Jacobsen, L. B., Calvin, S. A. & Lobenhofer, E. K. (2009) Transcriptional effects of transfection: the potential for misinterpretation of gene expression data generated from transiently transfected cells. *Biotechniques* **47**, 617–624.
43. Vlachodimou, A., Konstantinopoulou, K., Ijzerman, A. P. & Heitman, L. H. (2020) Affinity, binding kinetics and functional characterization of draflazine analogues for human equilibrative nucleoside transporter 1 (SLC29A1). *Biochem. Pharmacol.* **172**, 113747.
44. Vaughan, R. A. & Foster, J. D. (2013) Mechanisms of dopamine transporter regulation in normal and disease states. *Trends Pharmacol. Sci.* **34**, 489–496.
45. Pristupa, Z., Wilson, J., Hoffman, D., Kish, S. & Niznik, H. (1994) Pharmacological heterogeneity of the cloned and native human dopamine transporter: disassociation of [3 H]WIN 35,428 and [3 H]GBR 12,935 binding. *Mol. Pharmacol.* **45**, 125–135.
46. Andersen, P. H. (1989) The dopamine uptake inhibitor GBR 12909: selectivity and molecular mechanism of action. *Eur. J. Pharmacol.* **166**, 493–504.
47. Han, Y., Han, M., Shin, D., Song, C. & Hahn, H. G. (2012) Exploration of novel 3-substituted azetidine derivatives as triple reuptake inhibitors. *J. Med. Chem.* **55**, 8188–8192.
48. Storch, A., Ludolph, A. C. & Schwarz, J. (1999) HEK-293 cells expressing the human dopamine transporter are susceptible to low concentrations of 1-methyl-4-phenylpyridine (MPP $^{+}$) via impairment of energy metabolism. *Neurochem. Int.* **35**, 393–403.
49. Quizon, P. M. *et al.* (2016) Molecular mechanism: the human dopamine transporter histidine 547 regulates basal and HIV-1 Tat protein-inhibited dopamine transport. *Sci. Rep.* **6**, 39048.
50. Giros, B. *et al.* (1992) Cloning, pharmacological characterization, and chromosome assignment of the human dopamine transporter. *Mol. Pharmacol.* **42**, 383–390.
51. Brüss, M., Wieland, A. & Bönisch, H. (1999) Molecular cloning and functional expression of the mouse dopamine transporter. *J. Neural Transm.* **106**, 657–662.
52. Volpe, D. A., Hamed, S. S. & Zhang, L. K. (2014) Use of different parameters and equations for calculation of IC $_{50}$ values in efflux assays: Potential sources of variability in IC $_{50}$ determination. *AAPS J.* **16**, 172–180.
53. Aggarwal, S. & Mortensen, O. V. (2017) In vitro assays for the functional characterization of the dopamine transporter (DAT). *Curr. Protoc. Pharmacol.* **79**, 12.17.1-12.17.21.
54. Wang, K. H., Penmatsa, A. & Gouaux, E. (2015) Neurotransmitter and psychostimulant recognition by the dopamine transporter. *Nature* **521**, 322–327.
55. Steele, T. W. E. & Eltit, J. M. (2019) Using Ca $^{2+}$ -channel biosensors to profile amphetamines and cathinones at monoamine transporters: electro-engineering cells to detect potential new psychoactive substances. *Psychopharmacology* **236**, 973–988.

56. Boussif, O. *et al.* (1995) A versatile vector for gene and oligonucleotide transfer into cells in culture and in vivo: Polyethylenimine. *Proc. Natl. Acad. Sci. U. S. A.* **92**, 7297–7301.
57. Gorman, C. M., Howard, B. H. & Reeves, R. (1983) Expression of recombinant plasmids in mammalian cells is enhanced by sodium butyrate. *Nucleic Acids Res.* **11**, 7631–7648.
58. Jacob, M. C., Favre, M. & Bensa, J.-C. (1991) Membrane cell permeabilisation with saponin and multiparametric analysis by flow cytometry. *Cytometry* **12**, 550–558.
59. Smith, P. K. *et al.* (1985) Measurement of protein using bicinchoninic acid. *Anal. Biochem.* **150**, 76–85.

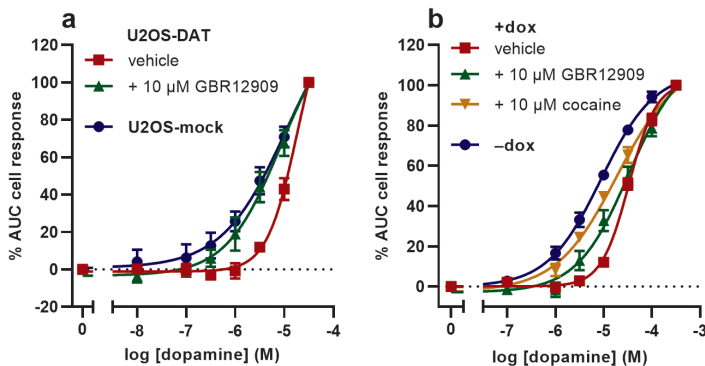
Supplementary Information



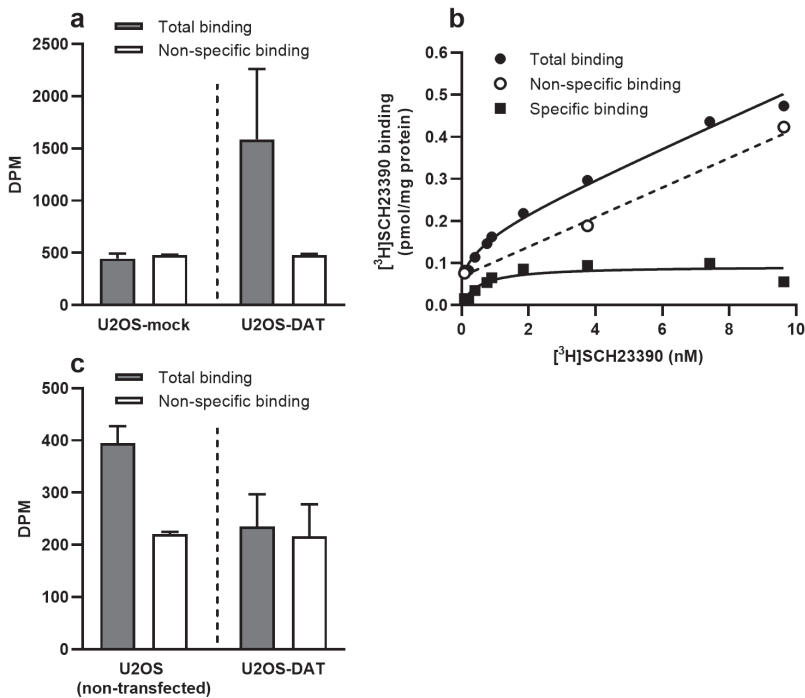
Supplementary Figure 3.S1 – Representative vehicle-corrected xCELLigence traces of GPCR antagonists in three cell lines. **(a)** Pretreatment of U2OS-DAT cells with 1 μ M antagonist for 1 h. **(b)** Stimulation of non-transfected U2OS cells with 316 nM dopamine after pretreatment with vehicle, 1 μ M SCH23390 or raclopride for 1 h. **(c)** Pretreatment of JumpIn-DAT cells in the presence of 1 μ g/ml dox (+dox) with 1 μ M antagonist for 1 h. Data are shown as the mean of a representative graph of at least three separate experiments each performed in duplicate.



Supplementary Figure 3.S2 – Representative vehicle-corrected xCELLigence traces of DAT inhibitors in two cell lines. **(a)** Pretreatment of U2OS-DAT cells with 10 μM GBR12909 for 1 h. **(b)** Pretreatment of JumpIn-DAT cells in the presence of 1 μg/ml dox (+dox) with 10 μM GBR12909 or cocaine for 1 h. Data are shown as the mean of a representative graph of at least three separate experiments performed with 16 replicates.



Supplementary Figure 3.S3 – Dose-response curves of dopamine on **(a)** U2OS-DAT, U2OS-mock and **(b)** JumpIn-DAT cells with or without 1 μg/ml dox (\pm dox). Data are shown as the net AUC of the first 120 minutes (U2OS) or 30 minutes (JumpIn-DAT) after stimulation normalized to the cell response of 31.6 μM (U2OS) or 316 μM (JumpIn-DAT) dopamine. U2OS-DAT and dox-treated JumpIn-DAT cells were pretreated with 10 μM GBR12909, 10 μM cocaine (dox-treated JumpIn-DAT only) or vehicle. Data were fitted with non-linear regression to a sigmoidal dose-response curve with a variable slope. Data are shown as mean \pm SEM of three to nine separate experiments each performed in duplicate.



Supplementary Figure 3.S4 – Radioligand binding experiments. **(a)** Binding of ~10 nM [³H]WIN35,428 to 40 µg U2OS-mock or U2OS-DAT membranes. Total binding and non-specific binding were determined in the absence or presence of 100 µM GBR12909, respectively. **(b)** Representative saturation binding curve of [³H]SCH23390 to D₁R on non-transfected U2OS membranes. Total binding (●) and non-specific binding (○) were determined in the absence or presence of 10 µM (+)-butaclamol, respectively. Specific binding (■) was obtained by linear subtraction of non-specific binding from total binding. **(c)** Binding of ~0.8 nM [³H]SCH23390 to 40 µg U2OS-DAT or non-transfected U2OS membranes. Total binding and non-specific binding were determined in the absence or presence of 10 µM (+)-butaclamol. Data are shown as mean ± SD of two experiments (**a,c**) or as the mean of a representative graph of three separate experiments (**b**) each performed in triplicate. DPM = disintegrations per minute.

Supplementary Table 3.S1 – Apparent potency values (pEC_{50}) of dopamine and pseudo-Hill slopes of the concentration-effect curves on U2OS-mock, U2OS-DAT or Jumpln-DAT (\pm dox) cells in TRACT assays using a non-linear regression analysis model with a variable slope.

Cell line	Compound	$pEC_{50} \pm SEM$	slope $\pm SEM$	<i>n</i>
U2OS-mock	Dopamine	5.4 (5.2, 5.5) ^a	0.9 (1.0, 0.8) ^a	2
U2OS-DAT	Dopamine	4.7 \pm 0.2	1.5 \pm 0.1	5
	Dopamine + 10 μ M GBR12909	5.0 \pm 0.4	0.9 \pm 0.1 ^{##}	4
Jumpln-DAT –dox	Dopamine	5.1 \pm 0.1	0.8 \pm 0.1	7
	Dopamine	4.5 \pm 0.0 ^{†††}	1.5 \pm 0.1 ^{***}	9
Jumpln-DAT +dox	Dopamine + 10 μ M GBR12909	4.5 \pm 0.1	0.8 \pm 0.1 ^{&&&}	4
	Dopamine + 10 μ M cocaine	4.7 \pm 0.1	0.7 \pm 0.1 ^{&&&}	4

^a Mean (individual values) of two individual experiments each performed in duplicate

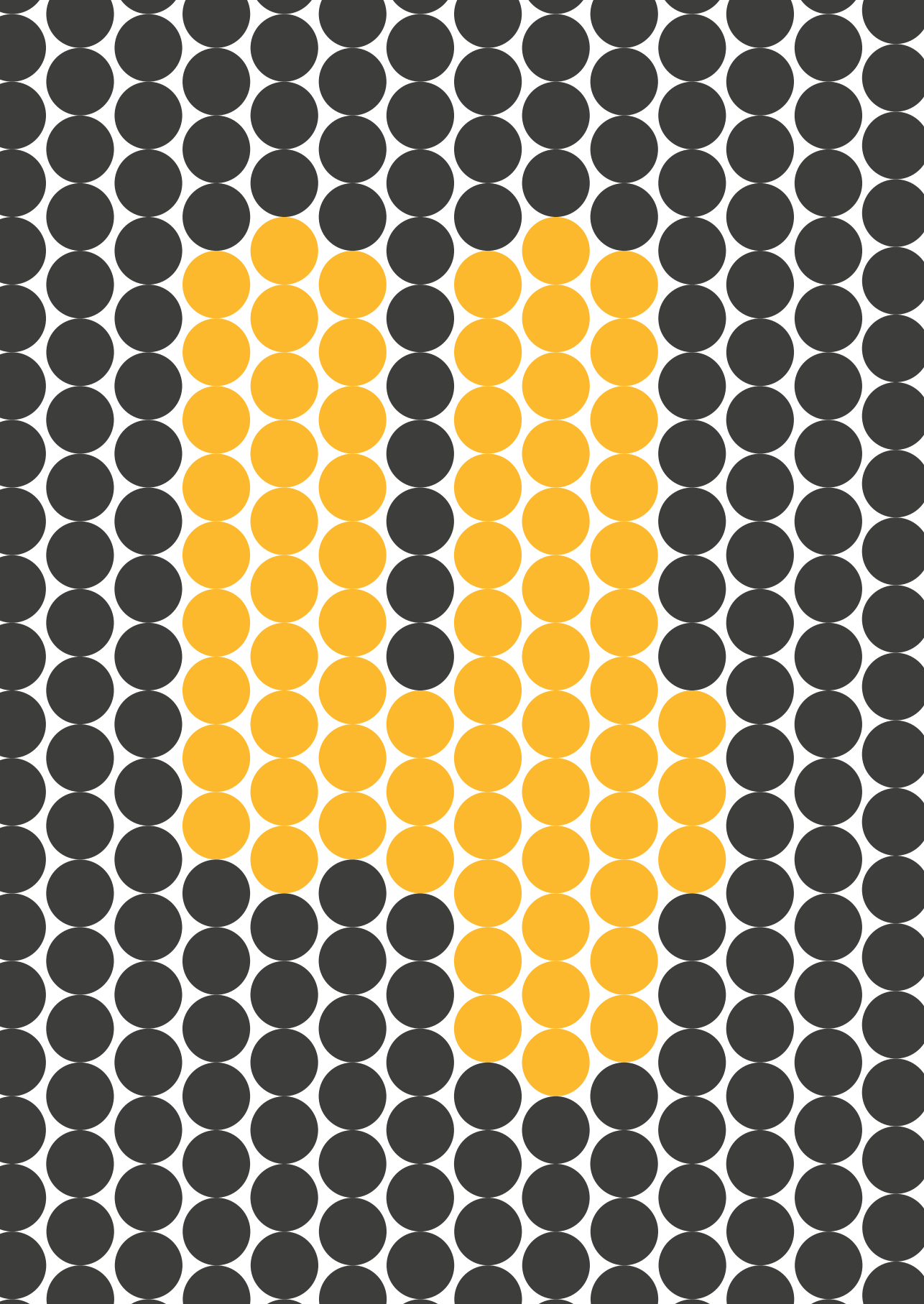
Values are reported as the mean \pm SEM of three to nine individual experiments performed in duplicate, unless stated otherwise. Significant difference between two mean potency values was determined by unpaired two-tailed Student's t-test.

^{†††} $p < 0.001$ (compared to Jumpln-DAT (–dox)/dopamine); ^{##} $p < 0.01$ (compared to U2OS-DAT/dopamine);

^{***} $p < 0.001$ (compared to Jumpln-DAT (–dox)/dopamine).

Comparison of multiple mean values to vehicle control was done using a one-way ANOVA with Dunnett's post-hoc test.

^{&&&} $p < 0.001$ (compared to Jumpln-DAT (+dox)/dopamine).



CHAPTER 4

Label-free high-throughput screening assay for the identification of norepinephrine transporter inhibitors

Hubert J. Sijben
Wieke M. van Oostveen
Peter B.R. Hartog
Laura Stucchi
Andrea Rossignoli
Giovanna Maresca
Lia Scarabottolo
Adriaan P. IJzerman
Laura H. Heitman

The human norepinephrine transporter (NET) is an established drug target for a wide range of psychiatric disorders. Conventional methods that are used to functionally characterize NET inhibitors are based on the use of radiolabeled or fluorescent substrates. These methods are highly informative, but pose limitations to either high-throughput screening (HTS) adaptation or physiologically accurate representation of the endogenous uptake events. In **Chapter 3**, we developed a label-free functional assay based on the activation of G protein-coupled receptors by a transported substrate, termed the TRACT assay. In the current chapter, the TRACT assay technology was applied to NET expressed in a doxycycline-inducible HEK293-JumpIn cell line. Three endogenous substrates of NET – norepinephrine (NE), dopamine (DA) and epinephrine (EP) – were compared in the characterization of the reference NET inhibitor nisoxetine. The resulting assay, using NE as a substrate, was validated in a manual HTS set-up with a $Z' = 0.55$. The inhibitory potencies of several reported NET inhibitors from the TRACT assay showed positive correlation with those from an established fluorescent substrate uptake assay. These findings demonstrate the suitability of the TRACT assay for HTS characterization and screening of NET inhibitors and provide a basis for investigation of other solute carrier transporters with label-free biosensors.

4.1 – Introduction

The uptake of neurotransmitters in and around the synaptic cleft by dedicated membrane transport proteins is a key process in the regulation of neurotransmitter signaling¹. As such, transporter dysfunction and aberrant levels of synaptic neurotransmitters have been linked to the manifestation of an array of psychiatric disorders including depression, anxiety and attention-deficit hyperactive-disorder². Monoamine transporters of the solute carrier transporter family 6 (SLC6) mediate the rapid clearance of released monoamine neurotransmitters (e.g., dopamine, norepinephrine, serotonin) and are therefore considered major drug targets for the aforementioned psychiatric disorders^{3,4}.

The norepinephrine transporter (NET, SLC6A2) facilitates sodium- and chloride-dependent uptake of norepinephrine, with overlapping substrate specificity for dopamine and epinephrine^{1,5}. NET is mainly expressed at synaptic terminals in the nervous system where it is a regulator of noradrenergic signaling, which affects physiological processes such as mood, behavior, heart rate and blood pressure⁶. Currently, NET is a therapeutic target of tricyclic antidepressants (TCAs), selective norepinephrine reuptake inhibitors (NRIs) and serotonin-norepinephrine reuptake inhibitors (SNRIs) for the treatment of depression^{2,3,7}. In addition, NET is targeted by radiolabeled “theranostics” for imaging and treatment of neuroendocrine tumors^{8,9}, as well as drugs of abuse (e.g., cocaine, amphetamine) which are known to inhibit NET^{3,10}. The continuing clinical use of (S)NRIs to treat anxiety and depression as well as the recent developments of NET inhibitors as potential treatment for incontinence¹¹, excessive sleepiness¹² and neuropathic pain^{13,14} still warrant the discovery of novel NET inhibitors.

Conventionally, *in vitro* methods to functionally characterize NET inhibitors are based on inhibition of uptake of a radiolabeled substrate (e.g., [³H]norepinephrine^{15,16}) or a fluorescent substrate^{17,18}. While these methods generally provide reliable IC₅₀ values for NET inhibitors, the use of labeled substrates has practical downsides such as high costs, waste management, safety precautions and availability of suitable (fluorescent) substrates, limiting the broad implementation of these principles for drug screening¹⁹. Recently, our group developed a novel functional ‘transport activity through receptor activation’ (TRACT) assay (**Figure 1.4, Chapter 1**) based on a label-free impedance-based technology for the equilibrative nucleoside transporter 1 (ENT1, SLC29A1)^{20,21} and the dopamine transporter (DAT, SLC6A3, see **Chapter 3**)²². In this bioassay a transporter that shares its substrate (e.g., adenosine, dopamine) with a G protein-coupled receptor (GPCR) is expressed in live cells together with a cognate GPCR. Uptake of substrate by the transporter decreases its local extracellular concentration, thereby limiting the ability of the substrate to activate the GPCR. Conversely, pharmacological inhibition of the transporter augments the substrate-induced GPCR response, providing an assay window for identification of transporter modulators. So far, the TRACT assay principle has been demonstrated in a low-throughput setting, while the screening potential of the assay has not yet been investigated.

In this chapter, a label-free TRACT assay was developed and validated for the human NET using an impedance-based biosensor, xCELLigence^{23–25}. To develop the assay we

used a modified human embryonic kidney (HEK)-293 cell line with doxycycline-inducible overexpression of NET and endogenous expression of adrenergic receptors (JumpIn-NET). Endogenous substrates of NET (norepinephrine, dopamine and epinephrine) were used to explore the substrate specificity of NET inhibitors and to maximize the assay window. Following optimization, the assay was validated in a manual 96-well high-throughput screening (HTS) set-up, demonstrating an “excellent assay” window, according to definition by Zhang²⁶. Several reference NET inhibitors were tested for their inhibitory potencies, which showed a strong correlation with potencies from an established fluorescent substrate uptake assay¹⁸. These results render the TRACT assay suitable for characterization of NET inhibitors and demonstrate that the assay is amenable to HTS. The detailed read-out, physiological setting and label-free nature of the method make the TRACT assay a meaningful alternative to conventional label-based assays for SLCs.

4.2 – Results

4.2.1 – Presence of NET attenuates substrate-induced cellular responses

In order to detect NET function in a label-free TRACT assay, a JumpIn cell line with dox-inducible expression of NET (JumpIn-NET) was generated. Suitable substrates for the TRACT assay were selected based on the criteria that the substrate should both be transported by NET and activate the cognate GPCR. Besides norepinephrine (NE), which is the most common endogenous substrate of NET, there are at least two other endogenous substrates known to be transported by NET and act as GPCR agonists, namely dopamine (DA) and epinephrine (EP). To evaluate which substrate was the most applicable for use in the TRACT assay for NET, all three substrates were extensively assessed for their ability to

Table 4.1 – Apparent potency values (pEC_{50}) and pseudo-Hill slopes (n_H) of norepinephrine (NE), dopamine (DA) and epinephrine (EP) in the absence (–) or presence of 1 μ M nisoxetine on JumpIn-NET cells treated with vehicle (–dox) or doxycycline (+dox) in TRACT assays.

Substrate	Pretreatment	$pEC_{50} \pm SEM^a$	slope (n_H) $\pm SEM^a$	<i>n</i>
Norepinephrine (NE)	–dox	–	6.4 ± 0.1	7
	–dox	Nisoxetine	6.5 ± 0.0	5
	+dox	–	$5.2 \pm 0.1^{***}$	8
	+dox	Nisoxetine	$6.3 \pm 0.1^{###}$	6
Dopamine (DA)	–dox	–	5.1 ± 0.1	3
	+dox	–	$4.7 \pm 0.0^{**}$	7
	+dox	Nisoxetine	$4.4 \pm 0.1^{\#}$	4
Epinephrine (EP)	–dox	–	6.4 ± 0.2	3
	+dox	–	$5.4 \pm 0.1^{***}$	6
	+dox	Nisoxetine	$6.3 \pm 0.1^{###}$	3

^a Mean \pm SEM of three to eight individual experiments performed in duplicate.

^b Significant difference between two mean potency values was determined by an unpaired two-tailed Student's t-test.

^{**} $p < 0.01$, ^{***} $p < 0.001$, compared to vehicle-treated (–dox) cells in the absence (–) of 1 μ M nisoxetine using the same substrate. [#] $p < 0.05$, ^{###} $p < 0.001$, compared to doxycycline-treated (+dox) cells in the absence (–) of 1 μ M nisoxetine using the same substrate.

induce a cellular response on the JumpIn-NET cells and for their suitability to characterize the reference NET inhibitor nisoxetine. In the following sections we describe the results for each of the three substrates separately.

4.2.1.1 – Norepinephrine (NE)

To assess the substrate-induced cellular response in cells without and with NET in the TRACT assay, JumpIn-NET cells were cultured for 22–24 h in E-plates in the absence (vehicle-treated, –dox) or presence (dox-treated, +dox) of 1 $\mu\text{g}/\text{ml}$ dox, respectively. Cells were pretreated for 1 h with vehicle prior to stimulation with increasing concentrations of substrate. Upon stimulation of vehicle-treated cells with NE, the vehicle-corrected normalized Cell Index (nCI) transiently decreased within the first 2 minutes after stimulation followed initially by a rapid ascent of the nCI to a peak around 5 minutes and then a more prolonged increase in nCI leading to a plateau between 20 and 30 minutes (Figure 4.1a). In dox-treated cells, NE induced a comparable response in the first 4 minutes after stimulation, however, at NE concentrations at or below 10 μM the nCI stabilized or gradually decreased

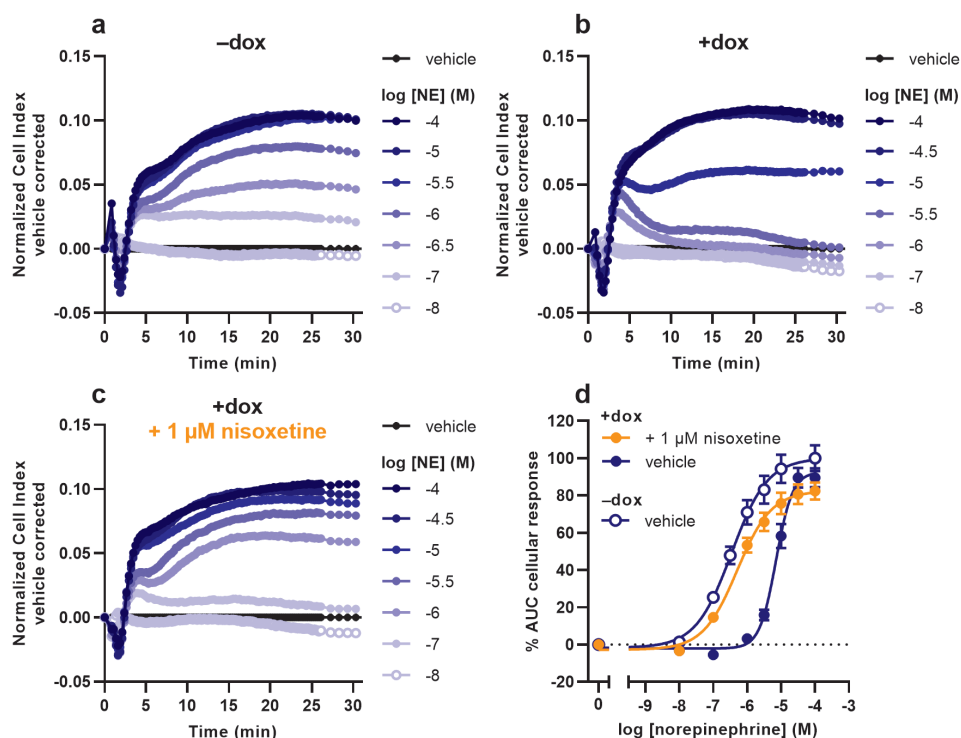


Figure 4.1 – Characterization of the norepinephrine (NE) response on JumpIn-NET cells in the TRACT assay. (a–c) Representative vehicle-corrected normalized Cell Index traces of vehicle-pretreated JumpIn-NET cells (a) in the absence (–dox) or (b) in the presence of 1 $\mu\text{g}/\text{ml}$ dox (+dox). (c) Dox-treated cells were pretreated for 1 h with 1 μM nisoxetine prior to stimulation with NE. (d) Combined concentration-effect curves of NE on vehicle- or dox-treated JumpIn-NET cells. Cellular response is expressed as the net AUC of the first 30 minutes after stimulation. Data are normalized to the response of 100 μM NE on vehicle-treated (–dox) cells. Data are shown as the mean \pm SEM of three to eight individual experiments each performed in duplicate.

back to baseline after 30 minutes (**Figure 4.1b**). The apparent potency of NE was 18-fold lower and the pseudo-Hill slope was more than 2-fold higher in dox-treated cells ($pEC_{50} = 5.2 \pm 0.1$, $n_H = 2.1 \pm 0.2$) compared to vehicle-treated cells ($pEC_{50} = 6.4 \pm 0.1$, $n_H = 0.8 \pm 0.1$), indicating the presence of NET leads to removal of extracellular NE (**Figure 4.1d**; **Table 4.1**).

4.2.1.2 – Dopamine (DA)

Stimulation of vehicle-treated cells with DA resulted in an initial rapid increase in nCI peaking at 5 min followed by a more gradual increase until a plateau was reached between 15 and 30 minutes (**Figure 4.2a**). In dox-treated cells, the magnitude and extent of DA responses at concentrations greater than 10 μ M was similar to vehicle-treated cells (**Figure 4.2b**). However, at DA concentrations of 10 μ M and lower the nCI slightly peaked at 5 min and gradually returned to baseline within 30 minutes. In contrast to NE, the apparent potency of DA was only 2-fold lower with an increased pseudo-Hill slope in dox-treated cells ($pEC_{50} = 4.7 \pm 0.0$, $n_H = 1.5 \pm 0.1$) compared to vehicle-treated cells ($pEC_{50} = 5.1 \pm$

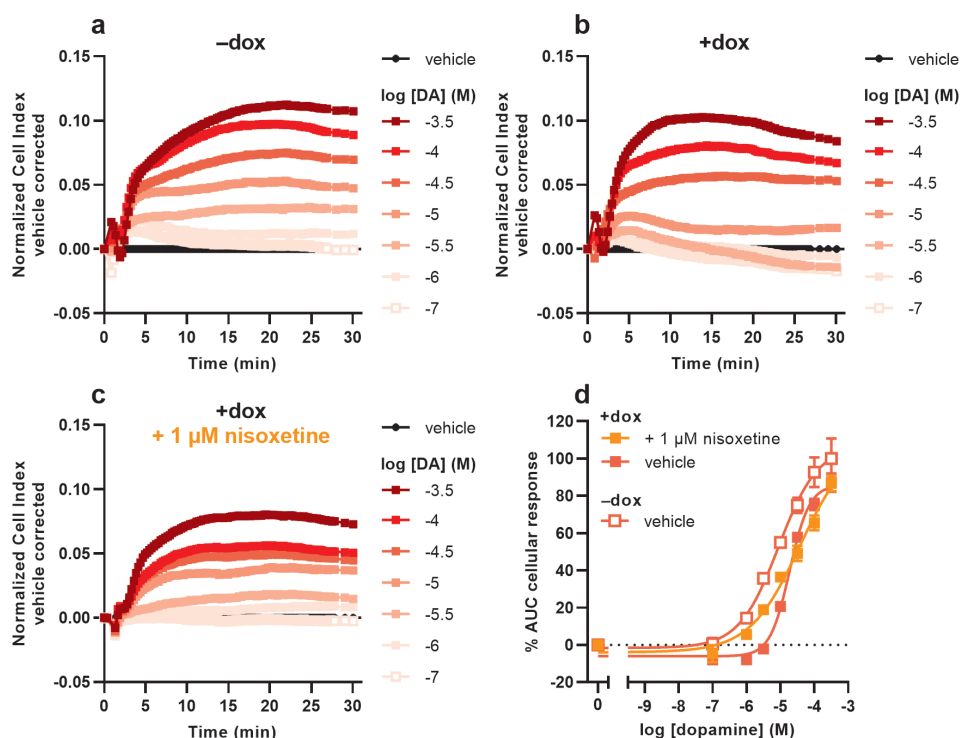


Figure 4.2 – Characterization of the dopamine (DA) response on Jumpln-NET cells in the TRACT assay. (a–c) Representative vehicle-corrected normalized Cell Index traces of vehicle-pretreated Jumpln-NET cells (a) in the absence (–dox) or (b) in the presence of 1 μ g/ml dox (+dox). (c) Dox-treated cells were pretreated for 1 h with 1 μ M nisooxetine prior to stimulation with DA. (d) Combined concentration-effect curves of DA on vehicle- or dox-treated Jumpln-NET cells. Cellular response is expressed as the net AUC of the first 30 minutes after stimulation. Data are normalized to the response of 316 μ M DA on vehicle-treated (–dox) cells. Data are shown as the mean \pm SEM of three to seven individual experiments each performed in duplicate.

0.1, $n_H = 0.8 \pm 0.1$) (**Figure 4.2d, Table 4.1**). This indicates that DA is less potent than NE on JumpIn-NET cells and that the presence of NET leads to a slight potency shift of DA.

4.2.1.3 – Epinephrine (EP)

Addition of EP to vehicle-treated JumpIn-NET cells lead to a brief decrease in nCI in the first 2 minutes after stimulation, then a sharp increase in nCI that peaked at 4 minutes (**Figure 4.3a**). The rise in nCI then temporarily halted before gradually surging to a plateau within 30 minutes. Cells pretreated with dox demonstrated a similar response to EP within the first 4 minutes (**Figure 4.3b**). At concentrations of EP lower than 10 μM the nCI briefly dropped followed by a plateau or a steady decline back to baseline between 7 and 30 minutes. The apparent potency of EP was decreased 10-fold with no change in the pseudo-Hill slope in dox-treated cells ($pEC_{50} = 5.4 \pm 0.1$, $n_H = 0.8 \pm 0.1$) compared to vehicle-treated cells ($pEC_{50} = 6.4 \pm 0.2$, $n_H = 0.6 \pm 0.0$) (**Figure 4.3d, Table 4.1**), indicating that extracellular levels of EP are lowered in the presence of NET.

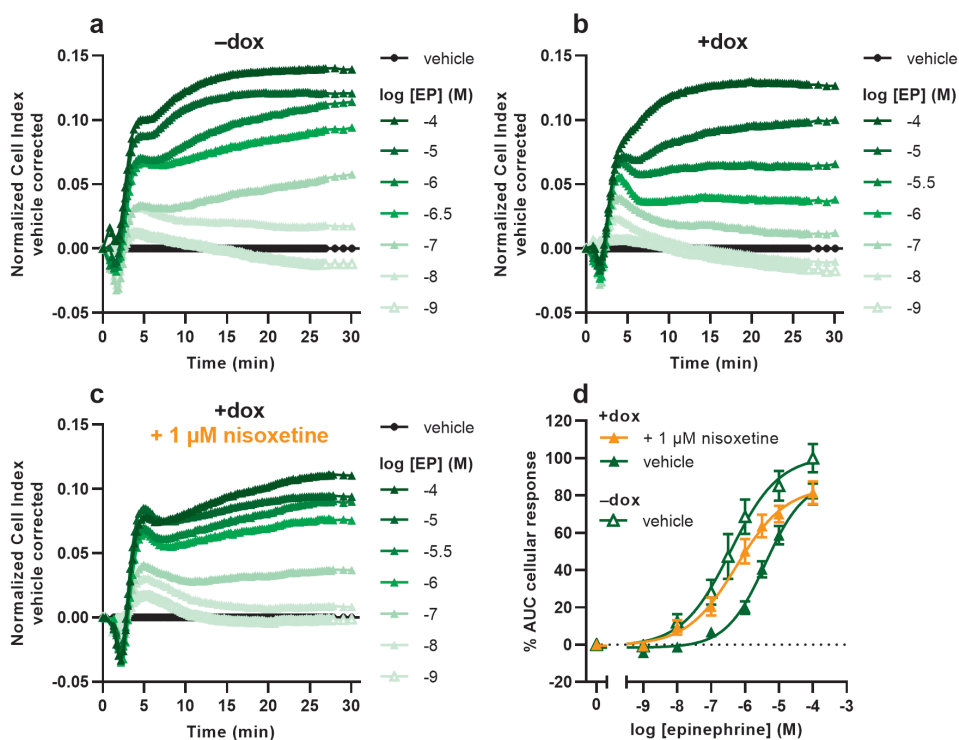


Figure 4.3 – Characterization of the epinephrine (EP) response on JumpIn-NET cells in the TRACT assay. (a–c) Representative vehicle-corrected normalized Cell Index traces of vehicle-pretreated JumpIn-NET cells (a) in the absence (–dox) or (b) in the presence of 1 $\mu\text{g/ml}$ dox (+dox). (c) Dox-treated cells were pretreated for 1 h with 1 μM nisoxetine prior to stimulation with EP. (d) Combined concentration-effect curves of EP on vehicle- or dox-treated JumpIn-NET cells. Cellular response is expressed as the net AUC of the first 30 minutes after stimulation. Data are normalized to the response of 100 μM EP on vehicle-treated (–dox) cells. Data are shown as the mean \pm SEM of three to six individual experiments each performed in duplicate.

4.2.2 – Substrate-induced responses are mainly caused by alpha-2 receptor activation

To validate whether activation of GPCRs on JumpIn-NET cells was related to substrate-induced cellular responses in the TRACT assay, dox-treated cells were pretreated for 1 h with two different monoamine GPCR antagonists prior to stimulation with a submaximal concentration (EC_{80}) of substrate (**Figure 4.4**). Involvement of alpha-2 adrenergic receptors (α_2 ARs) was assessed in the presence of 1 μ M yohimbine, while 1 μ M propranolol was used as a non-selective beta adrenergic receptor (β AR) antagonist. In the presence of yohimbine, the overall NE-induced cellular response significantly decreased ($p < 0.001$) by 92% compared to vehicle-pretreated cells (**Figure 4.4a,d**). The transient decrease in nCI 2 minutes after NE stimulation was more negative in the presence of yohimbine, but the response kinetics of this part of the trace were not altered (**Figure 4.4a**). However, this negative peak did not occur when cells were pretreated with propranolol, suggesting that this early-phase response is β AR-mediated. To assess the contribution of β AR activation to the overall NE-induced cellular response, yohimbine and propranolol were used simultaneously. Dual antagonist pretreatment prevented the early negative peak response, but did not cause a further decrease in the overall cellular response (**Figure 4.4a,d**).

When dox-treated cells were stimulated with DA, yohimbine was able to significantly reduce ($p < 0.001$) the DA-induced response by 68% compared to vehicle-pretreated cells (**Figure 4.4b,e**). Neither propranolol alone nor a combination of yohimbine and propranolol could further reduce the cellular response.

Similar to NE, pretreatment with yohimbine significantly reduced ($p < 0.001$) the overall EP-induced cellular response compared to vehicle-pretreated cells, whereas the rapid nCI decrease in the first 2 minutes after stimulation was more negative (**Figure 4.4c,f**). In the presence of the β AR antagonist the initial negative peak was abolished, but the overall cellular response was not affected. Pretreatment with both yohimbine and propranolol slightly elevated the cellular response compared to yohimbine alone, albeit not significantly ($p = 0.203$). Overall, these data demonstrate that the substrates used in this chapter mainly exert their observed effects in the TRACT assay through activation of α_2 ARs.

4.2.2 – Nisoxetine rescues apparent potency of NE and EP, but not DA

To determine whether pharmacological inhibition of NET leads to altered substrate responsiveness in the TRACT assay, dox-treated JumpIn-NET cells were pretreated for 1 h with the selective NET inhibitor nisoxetine (1 μ M, final concentration) prior to addition of increasing concentrations of substrate. Addition of 1 μ M nisoxetine itself did not affect the nCI during the 1 h pre-treatment (**Supplementary Figure 4.S1j**). Moreover, nisoxetine pretreatment did not change the apparent potency of NE in vehicle-treated cells ($pEC_{50} = 6.5 \pm 0.0$, $n_H = 0.9 \pm 0.1$; **Table 4.1**), which demonstrates that NE signaling is not affected by nisoxetine in the absence of NET. In dox-treated cells, stimulation with NE after nisoxetine pretreatment generated nCI traces with a shape comparable to those observed in vehicle-treated cells (compare **Figure 4.1c** and **4.1a**, respectively), resulting in a complete restoration of the pseudo-Hill slope and apparent potency of NE ($pEC_{50} = 6.3 \pm 0.1$, $n_H = 0.9 \pm 0.1$; **Figure 4.1d**, **Table 4.1**). A similar trend was observed in dox-treated cells

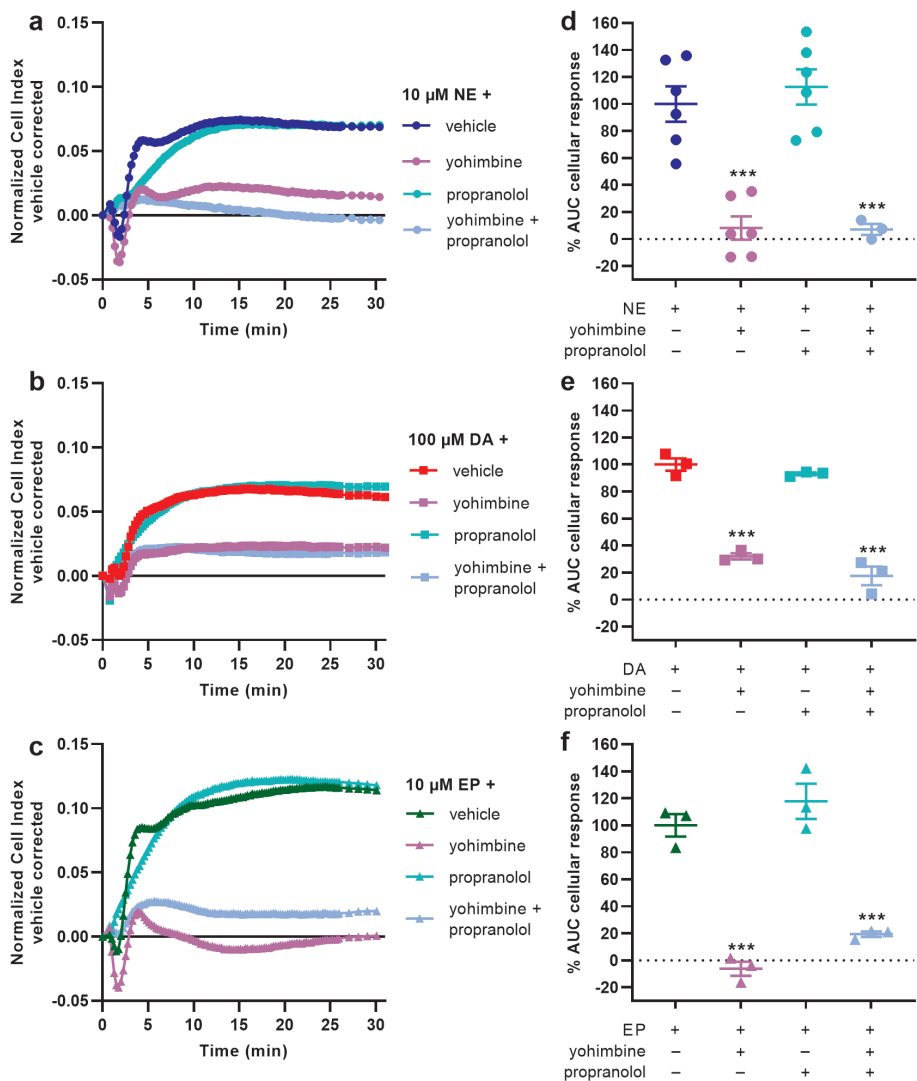


Figure 4.4 – Assessment of GPCR involvement in substrate-specific cellular responses on dox-treated JumpIn-NEt cells. Prior to stimulation with substrate, dox-treated cells were pretreated for 1 h with vehicle or 1 μ M antagonist for α_2 ARs (yohimbine; purple) or β ARs (propranolol; mint green) or a 1:1 mixture of both antagonists (light blue). Subsequently, cells were stimulated with an EC₈₀ of either (a,d) norepinephrine (NE, 10 μ M; blue ●), (b,e) dopamine (DA, 100 μ M; red ■), or (c,f) epinephrine (EP, 10 μ M; green ▲). (a–c) Representative vehicle-corrected normalized Cell Index traces of substrate-induced cellular responses. (d–f) Net AUC of the first 30 minutes after stimulation. Data are shown as mean \pm SEM of three to six individual experiments each performed in duplicate. Comparison of multiple mean values to vehicle control was done using a one-way ANOVA with Dunnett’s post-hoc test. *** p<0.001 compared to substrate only.

stimulated with EP (compare **Figure 4.3c** and **4.3a**, respectively), for which the apparent potency of EP was significantly ($p = 0.0008$) enhanced in the presence of nisoxetine ($pEC_{50} = 6.3 \pm 0.1$, $n_H = 0.6 \pm 0.1$; **Figure 4.3d**, **Table 4.1**) compared to vehicle-pretreated cells. Interestingly, pretreatment of dox-treated cells with nisoxetine enhanced DA responses at concentrations of 10 μM or less, but not at higher DA concentrations (**Figure 4.2c**), resulting in a slight decrease in apparent potency of DA and a decreased pseudo-Hill slope ($pEC_{50} = 4.4 \pm 0.1$, $n_H = 0.6 \pm 0.0$; **Figure 4.2d**, **Table 4.1**). This suggests the magnitude and extent of the restoration of substrate-induced cellular responses by pharmacological inhibition of NET depends on the substrate used.

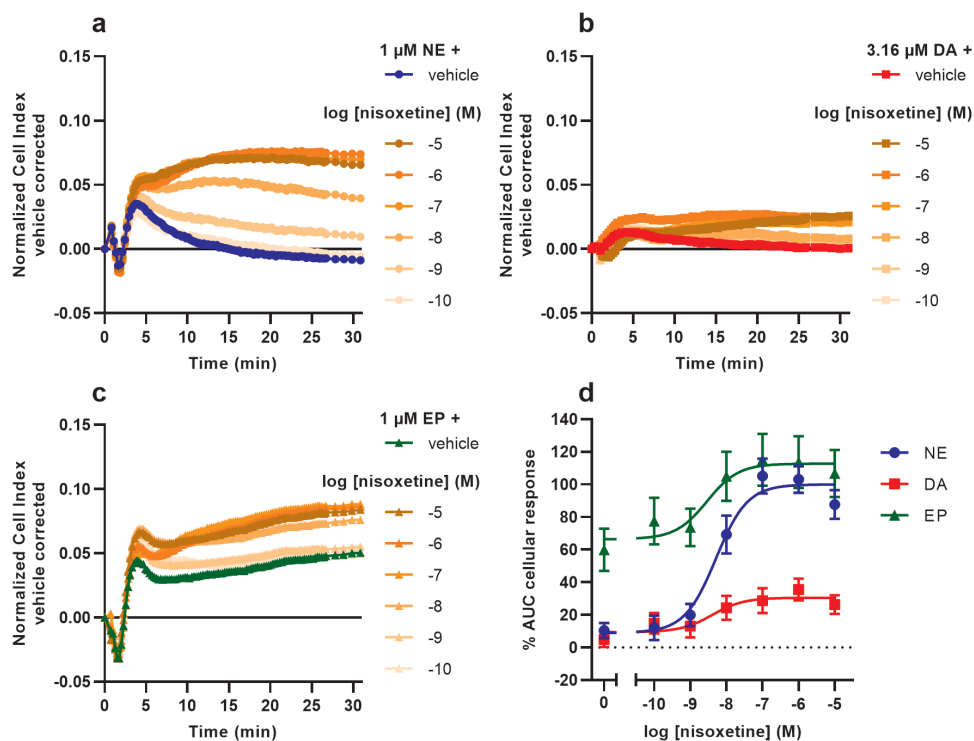


Figure 4.5 – Nisoxetine potentiates substrate-induced cellular response in dox-treated Jumln-NET cells in the TRACT assay. Representative vehicle-corrected normalized Cell Index traces are shown of dox-treated cells pretreated for 1 h with increasing concentrations of nisoxetine (orange), stimulated with a submaximal (EC_{20}) concentration of (a) norepinephrine (NE, 1 μM ; ●), (b) dopamine (DA, 3.16 μM ; ■), or (c) epinephrine (EP, 1 μM ; ▲). (d) Combined concentration-inhibition curve of nisoxetine upon stimulation with either NE, DA or EP. Cellular response is expressed as the net AUC of the first 30 minutes after stimulation. To demonstrate the assay window for each substrate, data are normalized to the response of 1 μM NE in the presence of 1 μM nisoxetine (set at 100%) and the vehicle response (set at 0%). Data are shown as mean \pm SEM of four to seven individual experiments performed in duplicate.

4.2.4 – NE provides the largest assay window for the determination of NET inhibitor potency

The main purpose of the TRACT assay is to identify transporter inhibitors and, subsequently, determine their inhibitory potency (IC₅₀) values. After characterization of the various substrate-induced cellular responses in JumpIn-NET cells, we assessed which substrate was most suitable to determine the inhibitory potencies of NET inhibitors in the TRACT assay (Figure 4.5). Dox-treated cells were pretreated for 1 h with increasing concentrations of the reference NET inhibitor nisoxetine and subsequently stimulated with a suboptimal concentration of substrate. For each substrate, a submaximal concentration (EC₂₀) was selected as this resulted in the largest possible assay window to detect NET inhibition.

Nisoxetine was able to dose-dependently augment the cellular response for all three substrates (Figure 4.5). However, the largest assay window, i.e., the relative difference between the vehicle response and the maximum response was obtained with NE as a substrate (Figure 4.5a,d). Specifically, nisoxetine enhanced the cellular response of EP to the same maximum as when NE was used (Figure 4.5c,d), but since the basal response of EP in vehicle-pretreated cells was approximately 60% higher than that of NE this resulted in a smaller assay window compared to NE. With DA as a substrate the maximum enhancement in cellular response that was attained within the concentration range of nisoxetine was roughly 25% of the maximum NE response, resulting in the least favorable assay window (Figure 4.5b,d). The IC₅₀ values for nisoxetine that were determined in the TRACT assay using the various substrates (NE: pIC₅₀ = 8.3 ± 0.1, DA: pIC₅₀ = 8.4 ± 0.4, EP: pIC₅₀ = 8.8 ± 0.3) were not significantly different from each other (p = 0.37), showing that the inhibitory potency of nisoxetine was not dependent on the type of substrate used.

Table 4.2 – Inhibitory potency (pIC₅₀) values of NET inhibitors determined in the TRACT assay and fluorescent substrate uptake assay.

Inhibitor	pIC ₅₀ ^a			
	TRACT assay ^b	n	Fluorescent substrate uptake assay ^c	n
Amitriptyline	6.7 ± 0.1	4	7.2 ± 0.1	5
Atomoxetine	7.7 ± 0.1	4	8.6 ± 0.0	3
Benztropine	6.5 ± 0.1	3	6.1 ± 0.1	3
Bupropion	4.9 ± 0.1	3	5.5 ± 0.0	3
Cocaine	6.2 ± 0.1	4	n.d. ^d	–
Desipramine	8.2 ± 0.1	3	8.6 ± 0.1	5
GBR12909	6.1 ± 0.2	3	6.0 ± 0.1	3
Maprotiline	7.3 ± 0.1	4	7.4 ± 0.1	3
Milnacipran	7.3 ± 0.2	4	7.8 ± 0.0	3
Nisoxetine	8.3 ± 0.1	7	8.4 ± 0.1	5
Nortriptyline	7.4 ± 0.1	5	8.0 ± 0.1	5
Reboxetine	8.3 ± 0.1	5	8.8 ± 0.0	5

^a The mean pIC₅₀ values found in the TRACT assay were on average 0.3 log-units lower than in the fluorescent substrate uptake assay (p = 0.016, paired two-tailed Student's t-test).
^b Mean ± SEM of three to seven individual experiments performed in duplicate.
^c Mean ± SEM of three to five individual experiments each performed in quadruplicate.
^d Not determined

4.3.5 – HTS assay validation and comparison with an orthogonal assay

After defining the optimal assay conditions, the TRACT assay was assessed and validated for its high-throughput screening (HTS) compatibility. Reproducibility and robustness of the assay window were assessed by running three individual 96 E-plates each day for three consecutive days. In this test run E-plates comprised of wells in an interleaved format producing high (1 μ M nisoxetine + 1 μ M NE), mid (10 nM nisoxetine + 1 μ M NE) and low (vehicle + 1 μ M NE) cellular responses. The test run resulted in a signal window (SW) of 7.7 ± 1.2 and a Z' factor (Z') of 0.55 ± 0.04 (Figure 4.6a).

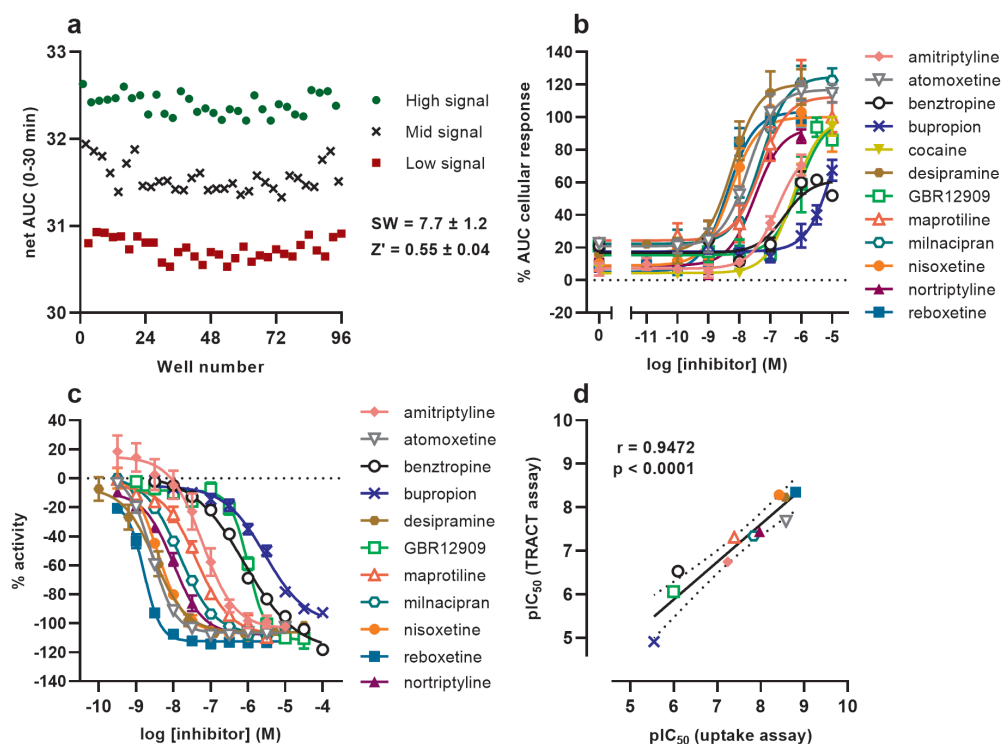


Figure 4.6 – TRACT assay HTS validation and characterization of NET inhibitors in the TRACT assay and the fluorescent substrate uptake assay. **(a)** Validation of the reproducibility and robustness of the TRACT assay. Representative graph of a 96-well E-plate (row-oriented) with wells producing high (1 μ M nisoxetine + 1 μ M NE), mid (10 nM nisoxetine + 1 μ M NE) and low (vehicle + 1 μ M NE) cellular responses. Data is presented as the net AUC of the raw nCl traces of the first 30 min after NE stimulation. Each data point in the graph represents a single well. Signal window (SW) and Z' factor (Z') are shown as mean \pm S.E.M. and were calculated according to the formulas in **section 4.4.7.2**. **(b)** Concentration-inhibition curves of NET inhibitors in the TRACT assay. Cells are pretreated for 1 h with vehicle or one of six increasing concentrations of inhibitor, then stimulated with 1 μ M NE or vehicle. Data were normalized to the average top and bottom values of the nisoxetine concentration-effect curve. Data are shown as mean \pm SEM of three to seven individual experiments each performed in duplicate. **(c)** Concentration-inhibition curves of NET inhibitors in the fluorescent substrate uptake assay. Cells were pretreated for 1 h with vehicle or one of ten increasing concentrations of inhibitor, followed by addition of loading dye solution for 1 h. Data were normalized according to the formula in **section 4.4.7.3**. Data are shown as the mean \pm SEM of three to five individual experiments each performed in quadruplicate. **(d)** Correlation plot between pIC_{50} values obtained in the TRACT assay and the fluorescent substrate uptake assay. The Pearson's r coefficient and the corresponding p -value of the linear correlation (solid line) are shown. The dotted line represents the 95% confidence interval.

Next, we determined the inhibitory potency of several reference NET inhibitors in the TRACT assay (**Figure 4.6b**, **Table 4.2**) and in an orthogonal fluorescent substrate uptake assay (**Figure 4.6c**, **Table 4.2**). The inhibitors were selected to represent a wide range of inhibitory potencies on NET. Due to strict local regulations cocaine could only be assessed in the TRACT assay; likewise amphetamines could not be tested in either of the two assays. In the TRACT assay the inhibitors generally did not affect the nCI on their own during the 1 h pretreatment (**Supplementary Figure 4.S1**). Upon stimulation with 1 μ M NE, all inhibitors demonstrated dose-dependent enhancement of the NE response indicating inhibition of NET (**Figure 4.6b**). Inhibitory potencies of NET inhibitors in the TRACT assay ranged over more than 3 log-units (**Table 4.2**). Moreover, a strong correlation (Pearson's $r = 0.9472$, $p < 0.0001$) was observed when comparing the pIC_{50} values to a more conventional fluorescent substrate uptake assay (**Figure 4.6d**). Of note, the TRACT assay produced on average 0.3 log-unit lower inhibitory potencies when compared to the fluorescent substrate uptake assay, which was found to be significant ($p = 0.016$, paired two-tailed Student's t-test, **Table 4.2**). Taken together, these results indicate that the TRACT assay is a suitable method to characterize and screen potential NET inhibitors.

4.3 – Discussion

The functional characterization of inhibitors for neurotransmitter transporters, such as NET, is conventionally done by performing radioligand or fluorescent substrate uptake assays, which can also be used to derive kinetic parameters (K_m , V_{max}) of substrates for a specific transporter^{15,17,18}. However, radioligand uptake assays are generally labor-intensive, end-point measurements and restricted to low-throughput screening due to practical limitations in handling of radioactive materials^{15,19}. Fluorescent substrate uptake assays, on the other hand, overcome these limitations by allowing one-step, real-time measurements in live cells and have the potential for high-throughput screens^{17,18,27}. Despite this, a fluorescent substrate first needs to be designed, synthesized and thoroughly validated. Moreover, the chemical modification of a substrate in order to generate a fluorescent readout could influence the observed response when regarding the native substrate(s) of the transporter²⁸. The TRACT assay presented in this chapter demonstrates that GPCR activation can be used as a readout to infer NET transport function, allowing functional characterization of NET inhibitors in live cells using unmodified, endogenous substrates.

The TRACT assay principle assumes that the substrate of the transporter is able to induce a cellular response (e.g., by activation of a cell surface GPCR), where the transporter activity (i.e., uptake of substrate) indirectly affects the magnitude of the substrate-induced response, as has been shown recently²⁰. Besides its main substrate, NE, NET is known to transport the catecholamines DA and EP^{29,30} as well as other amines and substances such as tyramine, phenylethylamine and MPP⁺⁶. Since NE, DA and EP are reported endogenous agonists for adrenergic and/or dopamine GPCRs^{31–33}, it was hypothesized that these could be used as substrates in the TRACT assay. Indeed, all three substrates were able to induce concentration-dependent cellular responses in JumpIn-NET cells (**Figures 4.1–4.3**), which

were mainly attributed to the activation of α_2 ARs (**Figure 4.4**). Cellular responses to these catecholamines in unmodified HEK293 cells have previously been observed using a label-free optical biosensor, indicating that adrenergic receptors are commonly expressed in these cells³⁴. Notably, a comparable observation was made in the TRACT assay for the dopamine transporter (DAT) using a similar JumpIn cell line, in which the substrate DA activated α_2 ARs (**Chapter 3**)²².

The suitability of each substrate to measure NET activity was dependent on the apparent potency of the substrate for the GPCR. In the TRACT assay the apparent potency of DA was not significantly increased by nisoxetine in the presence of NET (**Figure 4.2d**), most likely due to the poor potency of DA on α_2 ARs. A possible alternative to increase the substrate sensitivity and inhibitory assay window could be to co-express a high affinity dopamine receptor (e.g., D₁ or D₂ dopamine receptor^{22,35}). This could lead to a more leftward-shifted concentration-response curve in cells lacking NET (–dox) or cells expressing NET (+dox) in presence of a NET inhibitor. In the TRACT assay for DAT (**Chapter 3**), U2OS cells with endogenous D₁ receptor expression displayed a slightly higher DA potency and shift compared to α_2 AR-expressing JumpIn-DAT cells²², although this might be further improved by heterologous expression of high affinity receptors. This matching of transporter substrate and receptor potency could be optimized for each TRACT assay.

When using NE and EP in the TRACT assay a rapid, transient negative nCI peak was observed upon substrate addition, which was likely related to activation of beta adrenergic receptors on the JumpIn cells (**Figure 4.4a,c**). However, this part of the substrate response was not affected in the presence of a NET inhibitor nor did it substantially contribute to the overall AUC. This indicates that a complex impedance signal comprised of more than one (GPCR) signaling event can be used to define a TRACT assay window³⁶. Although receptor activation provides a sensitive readout in this assay, caution is warranted when interpreting the data since NET inhibitors could potentially display activity at the same (adrenergic) receptors³⁷. If a compound would be a receptor agonist as well this could be observed as an impedance change during pretreatment, whereas a receptor antagonist would lead to a reduction rather than enhancement of the substrate-induced response. In both cases receptor-related activity would be observed in both cells lacking (–dox) and expressing (+dox) NET, whereas selective NET inhibitors only display activity in NET-expressing cells. Most of the inhibitors that were tested in the TRACT assay did not substantially affect the impedance during pretreatment, indicating a lack of GPCR-related effects of the inhibitors (**Supplementary Figure 4.S1**). A transient increase in nCI was observed at the highest tested concentration (10 μ M) of atomoxetine, bupropion, maprotiline and nisoxetine, although these impedance changes could not directly be attributed to receptor activation or other off-target effects. To correct for any inhibitor-induced impedance changes during the pretreatment the CI data was normalized prior to substrate (NE) addition.

While all three substrates induced GPCR-mediated cellular responses, differences were observed between the substrates regarding concentration-effect curves of non-induced and dox-induced cells (**Figure 4.1–4.3**, **Table 4.1**). Interestingly, dox-treated cells produced a considerable increase in steepness of the pseudo-Hill slope for NE ($n_H = 2.1 \pm 0.2$) and

DA ($n_H = 1.5 \pm 0.1$), but not for EP ($n_H = 0.8 \pm 0.1$), which is in line with the observation of increased slopes of DA in cells expressing DAT (**Chapter 3**)²². This finding fits with previously reported pharmacological experiments on innervated nictitating membranes (expressing NET) of pithed cats, where it was demonstrated that concentration-effect curves of sympathomimetic amines (e.g., norepinephrine, epinephrine) were steeper and right-shifted compared to membranes in the presence of cocaine or in denervated membranes (i.e. lacking NET)³⁸. Specifically, the slopes were dependent on the affinity (K_m) and maximum uptake rate (V_{max}) of the substrate, whereas the horizontal curve shift was related to the potency (EC_{50}) of the substrate^{38,39}. Whereas these findings may in part explain the observed changes in slope and horizontal shift of concentration-effect curves for NE and DA in this chapter, we could not rationalize the lack of a change in slope for EP. Nevertheless, the steep slope for NE provides a rationale that the largest window for NET inhibition by nisoxetine is found when NE is used as a substrate. A more detailed analysis of the curve shifts and slope changes in the TRACT assays in this thesis is provided based in **Chapter 8**.

In this chapter, it was demonstrated that the TRACT assay can be used to accurately determine inhibitory potency values of NET inhibitors, as a direct comparison to a commercially available fluorescent substrate uptake assay¹⁸ resulted in similar values that were highly correlated (**Figure 4.6d**). While the rank order of potencies for both assays were comparable, the pIC_{50} values were generally found to be lower in the TRACT assay than in the fluorescent substrate uptake assay ($p = 0.016$, **Table 4.2**). A possible reason for this inter-assay discrepancy might be that the assays use a different substrate to determine inhibitory potency, which may affect binding affinity or kinetics of the inhibitor⁴⁰. Although the substrate identity and concentration in the fluorescent substrate uptake assay were not disclosed by the supplier, a reasonable explanation could be that the transporter occupancy by NE is higher than the fluorescent substrate leading to increased inhibitor competition and thus lower pIC_{50} values in the TRACT assay. Alternatively, the uptake process might be rapidly saturated in the TRACT assay in presence of relatively high concentrations of NE, which could lead to an underestimation of the potency of inhibitors⁴¹. Although information on uptake kinetics could provide a more substantiated explanation to this, a drawback of the TRACT assay is that it cannot be used to directly measure the substrate uptake kinetics (e.g., K_m , V_{max}). Nevertheless, the inhibitory potency values of all tested inhibitors were in line with previously reported values from both fluorescent substrate uptake assays^{17,18,42,43} and radioligand uptake assays^{16–18,44–47} indicating that the TRACT assay can be reliably used for NET inhibitor characterization.

The TRACT assay for NET was validated in a manual HTS set-up to assess the assay robustness. Over a three day period, an average Z' of 0.55 ± 0.04 was obtained which generally indicates an “excellent assay”^{26,48}. This score is comparable to previous high-throughput analyses of fluorescent substrate uptake assays by Jørgensen *et al.* ($Z' = 0.43^{18}$), Haunso *et al.* ($Z' = 0.64–0.79^{17}$) and Wagstaff *et al.* ($Z' = 0.61–0.63^{42}$). While this Z' value can be considered acceptable, the overall robustness could be further optimized. For example, standardization of cell and compound handling can improve the overall performance and decrease intra-plate and inter-plate variability⁴⁸. Other considerations for optimization of

the assay window and robustness are the consistency in confluence and homogeneity of cells, cell density, inhibitor pretreatment duration, buffer/medium composition and DMSO tolerability (generally <1% final concentration in live cell assays)^{48–50}. In this chapter, three E-plates were manually run per day, which would not be considered “high-throughput” and as such the work-flow should be optimized if the TRACT assay is to be used on a larger scale⁵¹. For instance, impedance measurements could be taken over time for 30 min (using the AUC for analysis) or impedance can be measured once 30 min after stimulation, effectively making the assay a single-point measurement. With proper automation and plate handling systems, the potential throughput per RTCA station would increase from two E-plates per hour (measurement over time) to approximately 30 E-plates per hour (single-point measurement). In the latter case, the amount of plates that could be run per day (360 plates, assuming a 12-hour shift) would compare to the estimated throughput of a FLIPR^{TETRA} system⁴². Scale-up of the assay to a multi-plate xCELLigence station that can hold up to six 96-well E-plates simultaneously, or 384-well E-plate format is also an option, but in all cases adjusting the plate format or data acquisition method would necessitate additional optimization of the assay conditions to ensure a robust assay window.

In summary, this chapter demonstrates the potential of the recently described TRACT assay to be utilized as a high-throughput screening platform for inhibitors of NET. The inhibitory potencies of several well-known NET inhibitors could be accurately determined and the robustness and reproducibility of the assay was validated. Hence, this work makes a case for the TRACT assay as a viable alternative to conventional uptake assays and underpins the breadth of possibilities of using label-free biosensor technologies in drug discovery.

4.4 – Materials & Methods

4.4.1 – Chemicals and reagents

Jump In T-REx HEK 293 cells modified for doxycycline-inducible overexpression of the wild-type human norepinephrine transporter (JumpIn-NET) were provided by CeMM (Research Center for Molecular Medicine, Medical University of Vienna, Austria). These cells were used in the TRACT and the fluorescent substrate uptake assays to allow a good comparison. Benztropine mesylate, desipramine hydrochloride, Dulbecco’s Modified Eagle’s Medium (DMEM), dopamine hydrochloride, doxycycline hyclate, (–)-epinephrine (+)-bitartrate salt, L-(–)-norepinephrine (+)-bitartrate salt monohydrate and (±)-propranolol hydrochloride were purchased from Sigma Aldrich (St. Louis, MO, USA). Nisoxetine hydrochloride, maprotiline hydrochloride and yohimbine hydrochloride were purchased from Santa Cruz Biotechnology (Dallas, TX, USA). GBR12909 dihydrochloride and reboxetine mesylate were purchased from Toronto Research Chemicals (Toronto, ON, Canada). Amitriptyline hydrochloride, atomoxetine hydrochloride, bupropion hydrochloride, milnacipran hydrochloride and nortriptyline hydrochloride were purchased from Tebu-Bio (Heerhugowaard, The Netherlands). Cocaine hydrochloride was purchased from Duchefa Farma (Haarlem, The Netherlands), where Leiden University has been certified for its use

in pharmacological experiments. All other chemicals were of analytical grade and obtained from standard commercial sources.

4.4.2 – *JumpIn-NET cell line generation*

Jump In T-REx HEK 293 (JumpIn) cells were cultured and transfected according to the manufacturer's protocol (ThermoFisher Scientific) and as described previously (see **Chapter 3**)²². Cells were split twice a week in growth medium containing 200 µg/ml hygromycin B and 5 µg/ml blasticidin. For transfection, a codon optimized ORF (Addgene #131891) for the human norepinephrine transporter (SLC6A2, ORF: NM_001043.3) was cloned into a Gateway-compatible pJTI R4 DEST CMV TO pA expression vector. This allows doxycycline (dox)-inducible expression of NET in successfully transfected cells. Cells were selected in medium containing 2 mg/ml geneticin (G418) and 5 µg/ml blasticidin for 2 to 4 weeks and resistant clones were pooled for use in all further experiments.

4.4.3 – *Cell culture*

JumpIn-NET cells were grown as adherent cells in high glucose DMEM supplemented with 10% (v/v) fetal calf serum (FCS), 2 mM Glutamax, 100 IU/ml penicillin and 100 µg/ml streptomycin (culture medium) at 37°C and 7% CO₂. Upon thawing, cells were cultured in regular culture medium for 1–2 passages. Then, cells were cultured up to one week in culture medium supplemented with 2 mg/ml G418 and 5 µg/ml blasticidin to select only the transfected clones. Cells were subsequently switched to regular culture medium, waiting at least 24 h before performing an experiment. Cell cultures were split twice a week at ratios of 1:8 – 1:16 in 10 cm plates.

4.4.4 – *TRACT assays*

Label-free TRACT assays were performed using the xCELLigence real-time cell analysis (RTCA) technology as reported previously (see **Chapter 3**)²². Impedance values, which are measured continuously at a frequency of 10 kHz, for each well are converted by the RTCA software to the dimensionless parameter Cell Index (CI) using the following formula:

$$CI = \frac{(Z_i - Z_0)\Omega}{15\Omega}$$

where Z_i is the impedance at any given time point and Z_0 is the baseline impedance that is measured at the start of each experiment⁵².

Assays were performed at 37°C and 5% CO₂ in 96-well E-plates in a final volume of 100 µl per well. Background impedance was measured in 45 µl (one compound addition) or 40 µl (two compound additions) culture medium prior to cell seeding. Compounds were added in 5 µl per addition using a VIAFLO 96 handheld electronic 96 channel pipette (INTEGRA Biosciences, Tokyo, Japan). All conditions were tested in duplicate on each plate.

4.4.4.1 – Cell preparation and monitoring

JumpIn-NET cells were grown to 70–80% confluence on the day of the experiment. Baseline impedance was measured using culture medium with or without 1 µg/ml doxycycline (dox). Cells were seeded in E-plates at 60,000 cells/well in culture medium. Cells were left to sink to the bottom for 30 minutes at room temperature before placing the E-plate in the recording station at 37°C. Cells were left to grow overnight for 22–24 hr while recording impedance every 15 minutes.

4.4.4.2 – Cell pretreatment

In GPCR antagonist experiments, cells were pretreated by the addition of a single concentration (1 µM) of yohimbine (alpha-2 adrenergic receptor antagonist), propranolol (non-selective beta adrenergic receptor antagonist) or a 1:1 mix of both antagonists in DMSO. In TRACT assays, cells were pretreated with either a single concentration (1 µM) of nisoxetine (high affinity NET inhibitor⁵³) or six increasing concentrations of a NET inhibitor. Due to strict local regulations, cocaine could only be tested in the TRACT assay and not in the fluorescent substrate uptake assay. For all pretreatments DMSO was kept at 0.1% per well and impedance was measured for 1 h prior to substrate addition.

4.4.4.3 – Cell stimulation

Cells with or without pretreatment were stimulated by the addition of either norepinephrine (NE), dopamine (DA) or epinephrine (EP) as a substrate dissolved in 1mM ascorbic acid in PBS. Note, ascorbic acid was used as an antioxidant for the monoamine neurotransmitter substrates⁵⁴. In antagonist experiments cells were stimulated with a submaximal concentration (EC_{80}) of substrate (i.e. 10 µM NE; 100 µM DA; 10 µM EP). In TRACT assays cells were stimulated with seven increasing concentrations of substrate to determine substrate potency. To determine the inhibitory potencies of NET inhibitors, cells were stimulated with a submaximal (EC_{20}) concentration of substrate (i.e. 1 µM NE; 3.16 µM DA; 1 µM EP). For a total of 30 min after stimulation, impedance was measured initially every 15 seconds for 25 minutes and then every minute.

4.4.5 – TRACT assay HTS validation

The TRACT assay was assessed for reproducibility, robustness and amenability to high-throughput screening (HTS) according to methods described previously in assay guidance manuals⁴⁸. Three 96-well E-plates were run consecutively per day on three separate days. Cells were induced with 1 µg/ml dox at the start of each experimental run. After cell seeding, E-plates were left at room temperature for 30 min and subsequently placed inside an incubator for 22 h. Each E-plate had an alternating interleaved layout consisting of high, mid and low signals for which cells were pretreated with either 1 µM nisoxetine, 10 nM nisoxetine or vehicle (DMSO), respectively. After 1 h pretreatment, all wells were stimulated with a submaximal (EC_{20}) concentration (1 µM) of NE. Impedance was recorded for 30 min after substrate addition. Immediately after recording the NE response the next E-plate was inserted in the RTCA recording station. Compound additions were done using a VIAFLO

96 handheld electronic 96 channel pipette. All other handlings were performed manually.

4.4.6 – Fluorescent substrate uptake assay

Fluorescent substrate uptake assays were performed using the Neurotransmitter Transporter Uptake Assay Kit (Molecular Devices, San Jose, CA, USA) following the supplier's protocol. JumpIn-NET cells were seeded at 20,000 cells/well in culture medium in presence of 1 µg/ml dox in clear-bottom, black-walled 384 microtiter plates pre-coated with poly-D-lysine (Twin Helix, Milan, Italy) at 37°C and 5% CO₂. After 24 h medium was removed and 20 µl/well of Standard Tyrode's buffer (130 mM NaCl, 5 mM KCl, 2 mM CaCl₂, 1 mM MgCl₂, 5 mM NaHCO₃, 20 mM HEPES, pH 7.4) was added. Cells were pretreated by addition of 10 µl/well NET inhibitor (increasing concentrations), inhibitor control (30 µM desipramine) or vehicle control (buffer only) in Standard Tyrode's buffer at 0.1% DMSO (final concentration) for 1 h. Subsequently, cells were treated with 15 µl/well loading dye solution in Standard Tyrode's buffer. Cells were incubated for 1 h, after which the fluorescence was measured for 60 seconds using a FLIPR^{TETRA} plate reader (Molecular Devices, San Jose, CA, USA). All conditions were tested in quadruplicate on each plate except the vehicle and inhibitor controls, which each had 16 replicates per plate.

4.4.7 – Data analysis

4.4.7.1 – TRACT assay

Experimental data was recorded using RTCA Software v2.0 or v2.1.1 (ACEA Biosciences). For analysis of substrate-induced responses CI values were normalized to the time point prior to substrate addition to obtain normalized CI (nCI) values. Data were exported from RTCA Software and all subsequent analyses were performed in GraphPad Prism v8.1.1 (GraphPad Software, San Diego, CA, USA). The nCI values of vehicle-only controls were subtracted from all other data points to baseline-correct for any substrate-independent effects. Substrate-induced responses were quantified by taking the net area under the curve (AUC) of the first 30 min after substrate addition. The apparent potency values of NET substrates and the inhibitory potency values of NET inhibitors were obtained by fitting the AUC data with non-linear regression to a sigmoidal concentration-effect curve with a variable pseudo-Hill slope.

4.4.7.2 – TRACT assay HTS validation

For intra-plate variability tests, the net AUC of non-corrected nCI values were used to determine the signal window (SW, indicating dynamic range of the signal) using the following formula⁴⁸:

$$SW = \frac{\left(\text{AVG}_{\text{high}} - \frac{3SD_{\text{high}}}{\sqrt{n}} \right) - \left(\text{AVG}_{\text{low}} + \frac{3SD_{\text{low}}}{\sqrt{n}} \right)}{\frac{SD_{\text{high}}}{\sqrt{n}}}$$

where n is the number of technical replicates per compound in the intended screening assay (e.g., for duplicate measurements $n = 2$), AVG is the average and SD is the standard deviation of the AUC of the high or low signal.

Similarly, the Z' factor (Z' , indicating separation of the high and low signals) is calculated using the following formula^{26,48}:

$$Z' = \frac{\left(\text{AVG}_{\text{high}} - \frac{3\text{SD}_{\text{high}}}{\sqrt{n}} \right) - \left(\text{AVG}_{\text{low}} + \frac{3\text{SD}_{\text{low}}}{\sqrt{n}} \right)}{(\text{AVG}_{\text{high}} - \text{AVG}_{\text{min}})}$$

The reported SW and Z' are the mean \pm SEM of all nine E-plates. According to Iversen *et al.*⁴⁸, the recommended acceptance criterion for an HTS amenable assay is a $\text{SW} \geq 2$ or $Z' \geq 0.4$.

4.4.7.3 – Fluorescent substrate uptake assay

Fluorescence data was collected using the FLIPR^{TETRA} plate reader. The fluorescent substrate uptake was quantified by taking the AUC over 60 seconds of the fluorescence signals that were recorded 1 h after addition of the loading dye solution. The AUC values were normalized to percentage activity by the following formula:

$$\% \text{ activity} = \frac{X - \text{VC}}{\text{IC} - \text{VC}} \times -100\%$$

where X is the AUC of the tested condition, VC is the AUC of the vehicle control (buffer only) and IC is the AUC of the inhibitor control (30 μM desipramine). Here, a negative value of -100% indicates complete inhibition of NET. The inhibitory potency values of NET inhibitors were obtained in Genedata Screener software v16.0.6 (Genedata, Basel, Switzerland) by fitting the normalized activity data with non-linear regression to a sigmoidal concentration-effect curve with a variable pseudo-Hill slope.

4.4.7.4 – Statistics

Data are shown as mean \pm standard error of the mean (SEM) of at least three separate experiments each performed in duplicate, unless stated otherwise. Significant difference between two mean potency values was determined by an unpaired two-tailed Student's t -test. Significant difference between the mean potencies found in two assays was determined by a paired two-tailed Student's t -test. Comparison of multiple mean values to each other or a vehicle control was done using a one-way ANOVA with Tukey's post-hoc test or Dunnett's post-hoc test, respectively. Differences were considered statistically significant when p -values were below 0.05.

References

- Gether, U., Andersen, P. H., Larsson, O. M. & Schousboe, A. (2006) Neurotransmitter transporters: molecular function of important drug targets. *Trends Pharmacol. Sci.* **27**, 375–383.
- Rudnick, G., Krämer, R., Blakely, R. D., Murphy, D. L. & Verrey, F. (2014) The SLC6 transporters: perspectives on structure, functions, regulation, and models for transporter dysfunction. *Pflügers Arch. - Eur. J. Physiol.* **466**, 25–42.
- Kristensen, A. S. *et al.* (2011) SLC6 neurotransmitter transporters: Structure, function, and regulation. *Pharmacol. Rev.* **63**, 585–640.
- Navratna, V. & Gouaux, E. (2019) Insights into the mechanism and pharmacology of neurotransmitter sodium symporters. *Curr. Opin. Struct. Biol.* **54**, 161–170.
- Bröer, S. & Gether, U. (2012) The solute carrier 6 family of transporters. *Br. J. Pharmacol.* **167**, 256–278.
- Bönisch, H. & Brüss, M. (Springer Berlin Heidelberg, 2006). The norepinephrine transporter in physiology and disease. in *Neurotransmitter Transporters. Handbook of Experimental Pharmacology* (eds. Sitte, H. H. & Freissmuth, M.) vol. 175 485–524.
- Xue, W. *et al.* (2018) Recent advances and challenges of the drugs acting on monoamine transporters. *Curr. Med. Chem.* **25**, 1–42.
- Pandit-Taskar, N. & Modak, S. (2017) Norepinephrine transporter as a target for imaging and therapy. *J. Nucl. Med.* **58**, 39S–53S.
- Zhang, H., Xie, F., Cheng, M. & Peng, F. (2019) Novel meta-iodobenzylguanidine-based copper thiosemicarbazide-1-guanidinomethylbenzyl anticancer compounds targeting norepinephrine transporter in neuroblastoma. *J. Med. Chem.* **62**, 6985–6991.
- Han, D. D. & Gu, H. H. (2006) Comparison of the monoamine transporters from human and mouse in their sensitivities to psychostimulant drugs. *BMC Pharmacol.* **6**, 6.
- Mizutani, H., Sakakibara, F., Komuro, M. & Sasaki, E. (2018) TAS-303, a novel selective norepinephrine reuptake inhibitor that increases urethral pressure in rats, indicating its potential as a therapeutic agent for stress urinary incontinence. *J. Pharmacol. Exp. Ther.* **366**, 322–331.
- Baladi, M. G. *et al.* (2018) Characterization of the neurochemical and behavioral effects of soliamfetol (JZP-110), a selective dopamine and norepinephrine reuptake inhibitor. *J. Pharmacol. Exp. Ther.* **366**, 367–376.
- Zajackowska, R. *et al.* (2018) Tapentadol – A representative of a new class of MOR-NRI analgesics. *Pharmacol. Reports* **70**, 812–820.
- Kremer, M., Salvat, E., Muller, A., Yalcin, I. & Barrot, M. (2016) Antidepressants and gabapentinoids in neuropathic pain: mechanistic insights. *Neuroscience* **338**, 183–206.
- Sucic, S. & Bönisch, H. (Humana Press, 2016). Classical radioligand uptake and binding methods in transporter research: an emphasis on the monoamine neurotransmitter transporters. in *Neurotransmitter Transporters: Neuromethods* (eds. Bönisch, H. & Sitte, H. H.) vol. 118 1–21.
- Decker, A. M. & Blough, B. E. (2018) Development of norepinephrine transporter reuptake inhibition assays using SK-N-BE(2)C cells. *Heliyon* **4**, e00633.
- Haunsø, A. & Buchanan, D. (2007) Pharmacological characterization of a fluorescent uptake assay for the noradrenaline transporter. *J. Biomol. Screen.* **12**, 378–384.
- Jørgensen, S., Nielsen, E. Ø., Peters, D. & Dyhring, T. (2008) Validation of a fluorescence-based high-throughput assay for the measurement of neurotransmitter transporter uptake activity. *J. Neurosci. Methods* **169**, 168–176.
- Wang, W. W., Gallo, L., Jadhav, A., Hawkins, R. & Parker, C. G. (2020) The druggability of solute carriers. *J. Med. Chem.* **63**, 3834–3867.
- Vlachodimou, A., IJzerman, A. P. & Heitman, L. H. (2019) Label-free detection of transporter activity via GPCR signalling in living cells: a case for SLC29A1, the equilibrative nucleoside transporter 1. *Sci. Rep.* **9**, 13802.
- Vlachodimou, A., Konstantinopoulou, K., IJzerman, A. P. & Heitman, L. H. (2020) Affinity, binding kinetics and functional characterization of drafazine analogues for human equilibrative nucleoside transporter 1 (SLC29A1). *Biochem. Pharmacol.* **172**, 113747.
- Sijben, H. J., van den Berg, J. J. E., Broekhuis, J. D., IJzerman, A. P. & Heitman, L. H. (2021) A study of the dopamine transporter using the TRACT assay, a novel in vitro tool for solute carrier drug discovery. *Sci. Rep.* **11**, 1312.
- Ke, N., Wang, X., Xu, X. & Abassi, Y. A. (Humana Press, 2011). The xCELLigence system for real-time and label-free monitoring of cell viability. in *Mammalian Cell Viability: Methods in Molecular Biology* (ed. Stoddart, M. J.) vol. 1 33–43.
- Doornbos, M. L. J. & Heitman, L. H. (Academic Press, 2019). Label-free impedance-based whole cell assay to study GPCR pharmacology. in *Methods in Cell Biology* (ed. Shukla, A. K.) vol. 149 179–194.
- Doijen, J. *et al.* (2019) Advantages and shortcomings of cell-based electrical impedance measurements as a GPCR drug discovery tool. *Biosens. Bioelectron.* **137**, 33–44.
- Zhang, J.-H., Chung, T. D. Y. & Oldenburg, K. R. (1999) A simple statistical parameter for use in evaluation and validation of high throughput screening assays. *J. Biomol. Screen.* **4**, 67–73.

27. Liao, J., Sportsman, R., Harris, J. & Stahl, A. (2005) Real-time quantification of fatty acid uptake using a novel fluorescence assay. *J. Lipid Res.* **46**, 597–602.
28. Toseland, C. P. (2013) Fluorescent labeling and modification of proteins. *J. Chem. Biol.* **6**, 85–95.
29. Apparsundaram, S., Moore, K. R., Malone, M. D., Hartzell, H. C. & Blakely, R. D. (1997) Molecular cloning and characterization of an l-epinephrine transporter from sympathetic ganglia of the bullfrog, *Rana catesbeiana*. *J. Neurosci.* **17**, 2691–2702.
30. Raffel, D. M. *et al.* (2013) Radiotracers for cardiac sympathetic innervation: transport kinetics and binding affinities for the human norepinephrine transporter. *Nucl. Med. Biol.* **40**, 331–337.
31. Lei, S. (2014) Cross interaction of dopaminergic and adrenergic systems in neural modulation. *Int. J. Physiol. Pathophysiol. Pharmacol.* **6**, 137–142.
32. Cornil, C. A. & Ball, G. F. (2008) Interplay among catecholamine systems: dopamine binds to α 2-adrenergic receptors in birds and mammals. *J. Comp. Neurol.* **511**, 610–627.
33. Sánchez-Soto, M. *et al.* (2018) α 2A- and α 2C-adrenoceptors as potential targets for dopamine and dopamine receptor ligands. *Mol. Neurobiol.* **55**, 8438–8454.
34. Ferrie, A. M., Sun, H., Zaytseva, N. & Fang, Y. (2015) Divergent label-free cell phenotypic pharmacology of ligands at the overexpressed β 2-adrenergic receptors. *Sci. Rep.* **4**, 3828.
35. Klein Herenbrink, C. *et al.* (2016) The role of kinetic context in apparent biased agonism at GPCRs. *Nat. Commun.* **7**, 10842.
36. Schröder, R. *et al.* (2010) Deconvolution of complex G protein-coupled receptor signaling in live cells using dynamic mass redistribution measurements. *Nat. Biotechnol.* **28**, 943–949.
37. Cottingham, C., Percival, S., Birky, T. & Wang, Q. (2014) Tricyclic antidepressants exhibit variable pharmacological profiles at the α 2A adrenergic receptor. *Biochem. Biophys. Res. Commun.* **451**, 461–466.
38. Langer, S. Z. & Trendelenburg, U. (1969) The effect of a saturable uptake mechanism on the slopes of dose-response curves for sympathomimetic amines and on the shifts of dose-response curves produced by a competitive antagonist. *J. Pharmacol. Exp. Ther.* **167**, 117–142.
39. Kenakin, T. P. (Elsevier, 2014). *A Pharmacology Primer: Techniques for More Effective and Strategic Drug Discovery*. Academic Press vol. 38.
40. Tsuruda, P. R. *et al.* (2010) Influence of ligand binding kinetics on functional inhibition of human recombinant serotonin and norepinephrine transporters. *J. Pharmacol. Toxicol. Methods* **61**, 192–204.
41. Brouwer, K. L. R. *et al.* (2013) In vitro methods to support transporter evaluation in drug discovery and development. *Clin. Pharmacol. Ther.* **94**, 95–112.
42. Wagstaff, R., Hedrick, M., Fan, J., Crowe, P. D. & DiSepio, D. (2007) High-throughput screening for norepinephrine transporter inhibitors using the FLIPRTetra. *J. Biomol. Screen.* **12**, 436–441.
43. Zwartsen, A. *et al.* (2017) Measuring inhibition of monoamine reuptake transporters by new psychoactive substances (NPS) in real-time using a high-throughput, fluorescence-based assay. *Toxicol. Vitro.* **45**, 60–71.
44. Pacholczyk, T., Blakely, R. D. & Amara, S. G. (1991) Expression cloning of a cocaine- and antidepressant-sensitive human noradrenaline transporter. *Nature* **350**, 350–354.
45. Owens, M. J., Morgan, W. N., Plott, S. J. & Nemeroff, C. B. (1997) Neurotransmitter receptor and transporter binding profile of antidepressants and their metabolites. *J. Pharmacol. Exp. Ther.* **283**, 1305–22.
46. Sørensen, L. *et al.* (2012) Interaction of antidepressants with the serotonin and norepinephrine transporters: mutational studies of the S1 substrate binding pocket. *J. Biol. Chem.* **287**, 43694–43707.
47. Eshleman, A. J. *et al.* (1999) Characteristics of drug interactions with recombinant biogenic amine transporters expressed in the same cell type. *J. Pharmacol. Exp. Ther.* **289**, 877–885.
48. Iversen, P. W. *et al.* (Eli Lilly & Company and the National Center for Advancing Translational Sciences, 2004). HTS assay validation. in *Assay Guidance Manual [Internet]* (eds. Sittampalam, G. S., Grossman, A. & Brimacombe, K.) 1–26.
49. Larsson, P. *et al.* (2020) Optimization of cell viability assays to improve replicability and reproducibility of cancer drug sensitivity screens. *Sci. Rep.* **10**, 5798.
50. Bailey, T. L., Nieto, A. & McDonald, P. H. (2019) A nonradioactive high-throughput screening-compatible cell-based assay to identify inhibitors of the monocarboxylate transporter protein 1. *Assay Drug Dev. Technol.* **17**, 275–284.
51. Entzeroth, M., Flotow, H. & Condron, P. (2009) Overview of high-throughput screening. *Curr. Protoc. Pharmacol.* **44**, 1–27.
52. Yu, N. *et al.* (2006) Real-time monitoring of morphological changes in living cells by electronic cell sensor arrays: an approach to study G protein-coupled receptors. *Anal. Chem.* **78**, 35–43.
53. Tejani-Butt, S. M. (1992) [3 H]nisoxetine: a radioligand for quantitation of norepinephrine uptake sites by autoradiography or by homogenate binding. *J. Pharmacol. Exp. Ther.* **260**, 427–36.
54. Hughes, I. E. & Smith, J. A. (1978) The stability of noradrenaline in physiological saline solutions. *J. Pharm. Pharmacol.* **30**, 124–126.

Supplementary Information

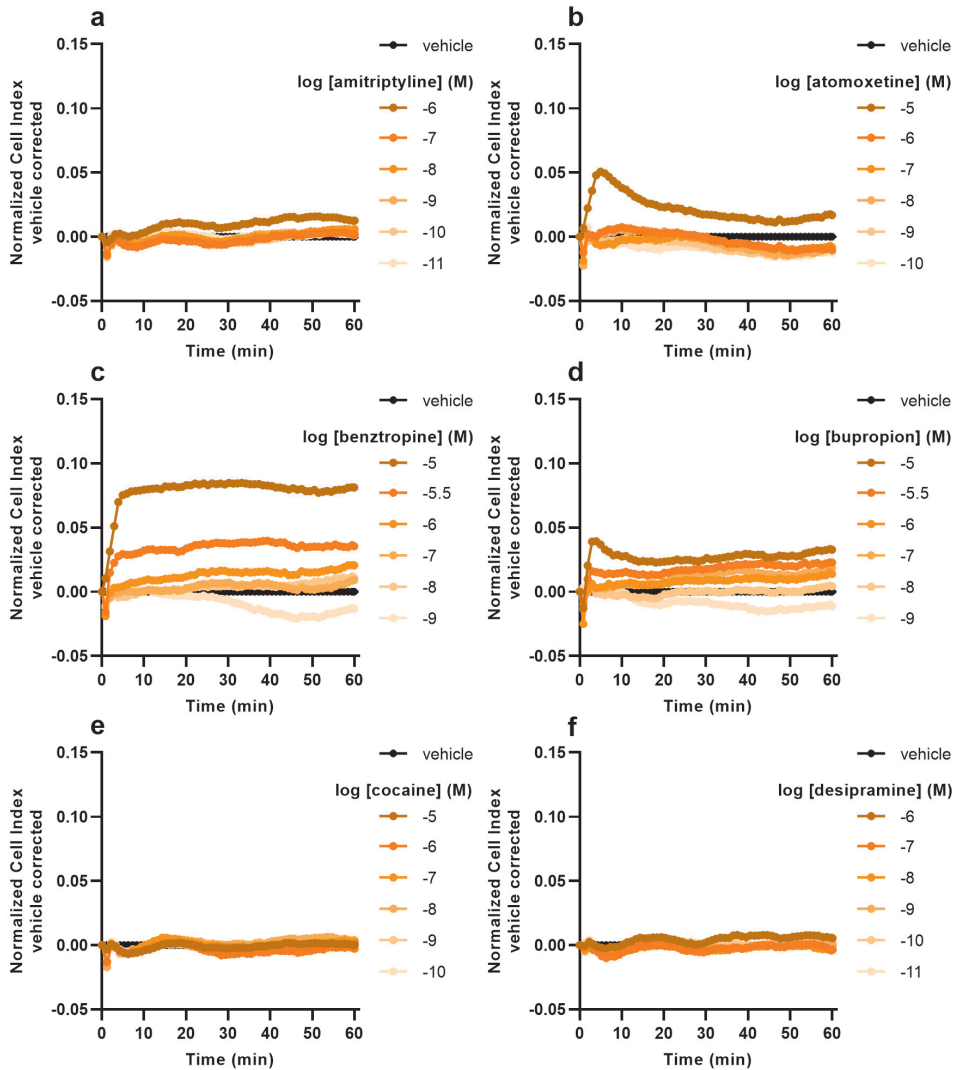


Figure 4.S1 – Representative vehicle-corrected xCELLigence traces of NET inhibitors in doxycycline-treated (+dox) JumpIn-NET cells. (a) amitriptyline, (b) atomoxetine, (c) benztropine, (d) bupropion, (e) cocaine, (f) desipramine (g–i are shown on the next page). Graphs show the effect of increasing concentration of the inhibitor on the normalized Cell Index (nCI) during the 1 h pretreatment. Data are normalized to the time point prior to addition of the inhibitor (= 0 min). Data are shown as the mean of a representative graph of at least three separate experiments each performed in duplicate.

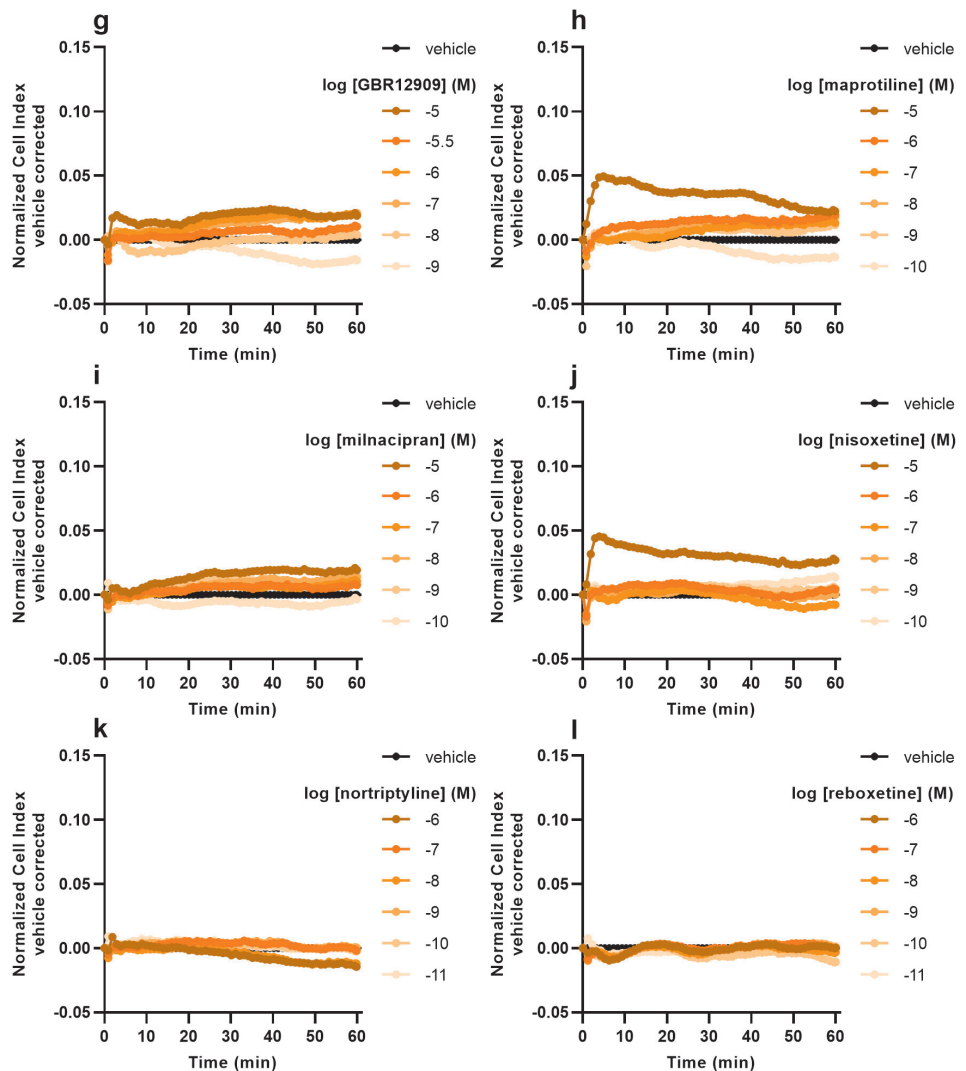
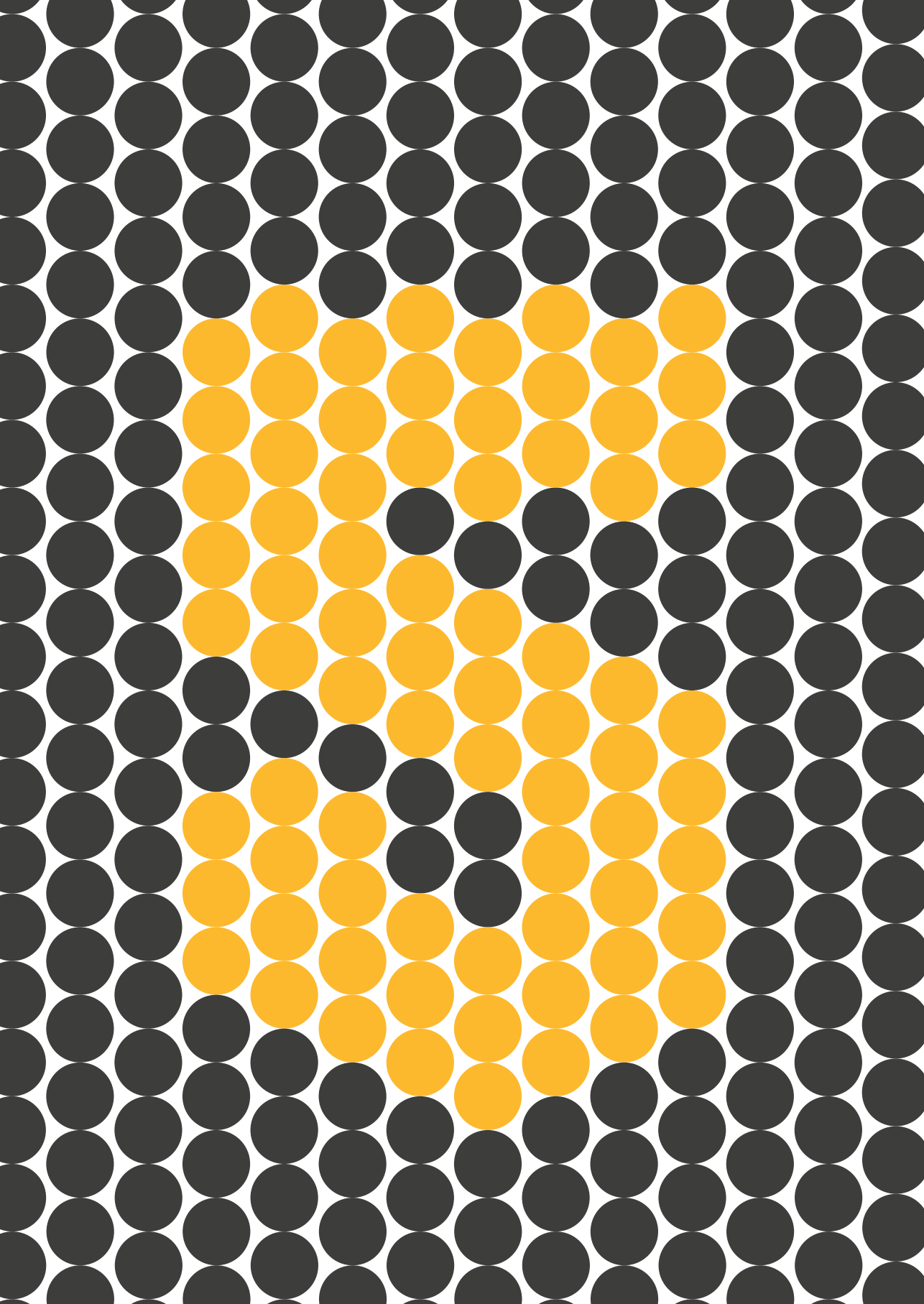


Figure 4.S1 – Representative vehicle-corrected xCELLigence traces of NET inhibitors in doxycycline-treated (+dox) JumpIn-NET cells. (**a–f** are shown on the previous page). (**g**) GBR12909, (**h**) maprotiline, (**i**) milnacipran, (**j**) nisoxetine, (**k**) nortriptyline, (**l**) reboxetine. Graphs show the effect of increasing concentration of the inhibitor on the normalized Cell Index (nCI) during the 1 h pretreatment. Data are normalized to the time point prior to addition of the inhibitor (= 0 min). Data are shown as the mean of a representative graph of at least three separate experiments each performed in duplicate.



CHAPTER 5

Proteochemometric modeling identifies chemically diverse norepinephrine transporter inhibitors

Brandon J. Bongers [†]

Hubert J. Sijben [†]

Peter B.R. Hartog

Adriaan P. IJzerman

Laura H. Heitman

Gerard J.P. van Westen

Solute carriers (SLCs) are a relatively underexplored protein family compared to other major protein families such as kinases and G protein-coupled receptors (GPCRs). However, the SLC family and their role in a diverse array of diseases is known and of interest. One such SLC is the high-affinity norepinephrine transporter (NET/SLC6A2), which in contrast to most other SLCs has been relatively well studied, resulting in a large defined chemical space. Due to the low diversity of this chemical space it is challenging to identify ligands that are chemically novel. In this chapter, we aimed to find new NET inhibitors using a computational modeling screening pipeline. We applied multiple optimization steps during dataset creation, including similarity networks and stepwise feature selection, to end up with an optimal training set for our model, which was created by using proteochemometrics and stacking of several machine learning techniques. The model was applied to a large virtual database of Enamine, from which 22,000 of the 600 million predicted compounds were clustered to end up with 46 chemically diverse candidates. Of these candidates, 32 were synthesized and tested using the impedance-based TRACT assay that was developed in **Chapter 4**. We identified five hit compounds with submicromolar inhibitory potencies towards NET, which are promising for follow-up experimental research. This chapter demonstrates a comprehensive computational pipeline to predict new potential ligands for NET, which could be applied to any protein that has enough interaction data available.

Manuscript submitted

[†] These authors have contributed equally

5.1 – Introduction

Solute carriers (SLCs) are a divergent class of transporters and understudied compared to some of the other major receptor families, such as kinases and G protein-coupled receptors (GPCRs)¹. Yet SLCs can play a critical role in complex diseases and as such several SLCs are interesting drug targets^{2–4}. To further characterize SLCs, recently the RESOLUTE consortium was founded to develop and distribute biochemical tools and assays for *in vitro* and *in vivo* study of these transporters⁵. SLC subfamilies recognize highly divergent natural substrates and their sequence identity is low compared to other superfamilies such as kinases or GPCRs⁶. Hence, from a drug discovery perspective it is challenging to design family-wide studies to find new ligands that interact with SLCs. Instead, the focus lies on single subfamilies, or even a single SLC, to identify novel compounds.

The norepinephrine transporter (NET / SLC6A2) is involved in the rapid re-uptake of the neurotransmitter norepinephrine (NE) from the synaptic clefts of noradrenergic neurons in the peripheral and central nervous system⁷. As one of the most well characterized transporters, NET is an established drug target for depression, chronic pain and narcolepsy, with several marketed drugs available. Despite the abundance of pharmacological data on NET ligand binding, there is a need for the development of novel inhibitors with improved affinity and selectivity over other monoamine transporters⁸. Despite more structures becoming available, for NET structure-based work there is still no option for structure-based design of ligands due to the absence of a crystal or cryo-EM structure^{9,10}.

Computational studies such as statistical modeling and ligand docking have increased in popularity over the last decades, yet application to SLCs has been limited so far^{11,12}. A 3D structure (crystal, cryo-EM or homology modeling based) of sufficient quality is required to perform structure-based drug discovery¹³. However, crystallization of SLCs is difficult given their membrane bound nature analogous to GPCRs. Hence, only limited amounts of structures are available for this family, with the promise of cryo-EM increasing that amount in the near future. While advances in cryo-EM and machine learning, such as AlphaFold, are expected to significantly increase the available structures and alleviate some of these issues, their application in virtual screening has still to be demonstrated^{14,15}.

In the absence of structural information virtual screening can also be performed ligand-based using 2D chemical structures or *via* proteochemometrics (PCM), using ligand and protein information¹⁶. In both cases machine learning is used to identify correlation between bioactivity and structural features. Here, we will use PCM which allows us to create a comprehensive model of ligand structures of multiple proteins. This allows us to not only use the ligand space for NET, but also the most structurally related proteins, such as the dopamine and serotonin transporters. We then train these models on publically available data from ChEMBL, which contains a large amount of ligand-receptor interaction information for all ligands/proteins^{17,18}.

In this chapter, we applied PCM modeling to identify new chemotypes for the NET. While this transporter has been relatively well characterized compared to other SLCs, there still is a need for novel ligands that effectively, efficiently and selectively target NET^{19,20}. We used

similarity networks as an approach to determine the optimal number of targets to include in our PCM model. After completion of our PCM model it was applied to the Enamine REAL database to identify novel ligands. Interestingly, the REAL database does not consist of on-the-shelf compounds but instead contains over 600 million make-on-demand molecules. These molecules can be synthesized *via* well-validated parallel synthesis protocols using a large number of building blocks. After virtual screening, the activity of our identified hits were validated experimentally with a hit rate of 5 out of 32 (16%).

5.2 – Results

5.2.1 – Dataset optimization by employing similarity networks and phylogenetic trees

The whole set derived from ChEMBL (All SLCs) was too large for model training, hence a selection of the data was made using sequence-based similarity networks (SNs). These SNs were used to highlight clusters with a pBLAST similarity to NET above a given threshold (Figure 5.1). Subsequently the clustered sets were used for PCM model training

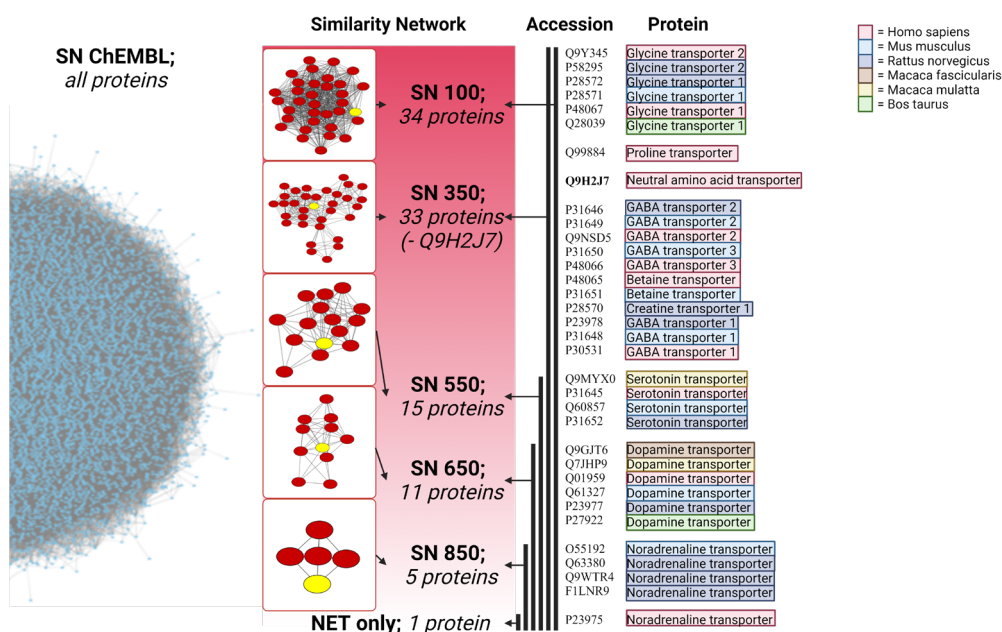


Figure 5.1 – Sequence based similarity networks obtained from SLCs in ChEMBL. Displayed are similarity networks wherein each node represents a single protein and each connection a pBLAST similarity above the chosen cutoff. Nodes in yellow denote human NET. SN25 resulted into one large cluster of almost all proteins and was discarded (left hand). From there, the following thresholds were used for the Similarity networks: Similarity network SN100 (34 proteins), including NET and related proteins from several animal species. SN350 (33 proteins), showing a smaller network with a section appearing to nearly dissociate. SN550 (15 proteins), containing the serotonin and dopamine transporters together with NET. SN650 (11 proteins) drops the serotonin transporters and the minimum viable similarity network SN850 (and all SNs above this threshold) contains solely NET from human and other species.

to determine the optimal number of related proteins for our model. A pBLAST threshold of 25 (smallest) led to a large network including all proteins (and was discarded), a threshold of 850 (largest) led to a network only including NET proteins between several species. Between these extremes several networks were obtained at intervals of 100, 350, 550, and 650, leading to a total of 6 data sets. Identification of a viable subset was also approached using phylogenetic trees calculated from protein sequence similarity.

Related proteins to NET could be identified if they were found on the same layer of the tree (**Figure 5.2**). Both the similarity networks and phylogenetic layers would then be selected for testing by modelling (up to an including layers 5, 6, and 7). In the phylogenetic approach, layer two represented the SN850 network, including three overlapped with the SN650 network, and including four represented SN550 network. Hence no separate models were trained for these groups (**Figure 5.3**).

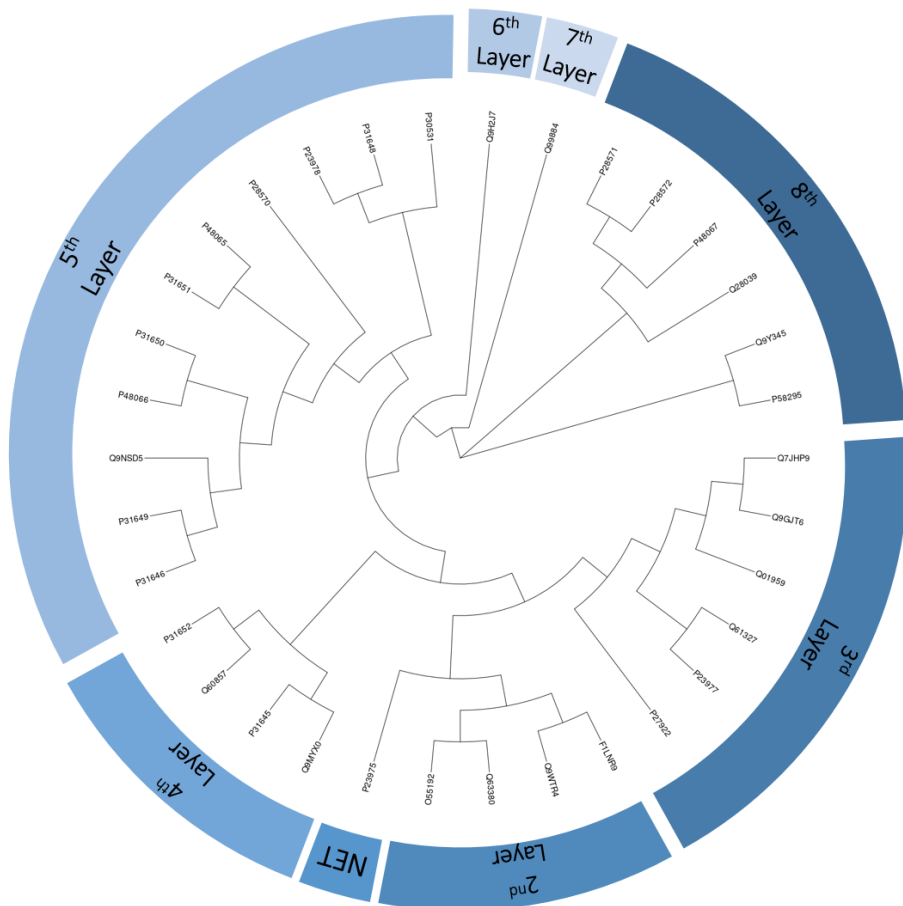


Figure 5.2 – Phylogenetic tree of maximal viable similarity network (SN100) reveals 8 individual layers. Displayed is the phylogenetic tree of the proteins (Uniprot codes) analyzed and colored with the various layers (defined as splits from the root of the tree defined by NET). This resulted in eight layers (including NET as the first layer).

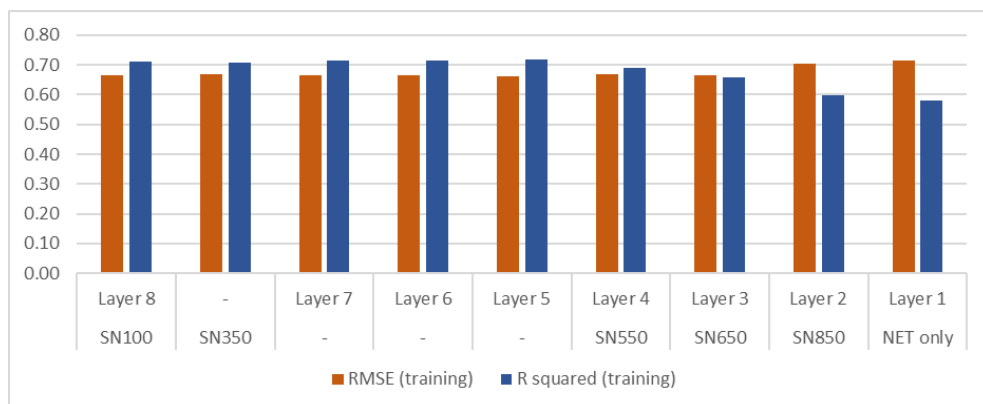


Figure 5.3 – Differences in cross validated R squared (R^2) and RMSE from models trained of the different subsets. Displayed is a plot of the R^2 and RMSE values generated during the dataset selection process. A high value for R^2 and a low value for RMSE were desired. SN100 was eventually preferred due to this due to its RMSE and R^2 values. It was preferred over layers 5, 6, 7 and SN350 as SN100 contained more data to model with.

5.2.2 – Final dataset was chosen from best scoring similarity networks

Both selection methods led to a total of nine subsets that were empirically tested to find the optimal training set. To do this, a random forest model was created and cross-validated to assess the R^2 and RMSE (**Figure 5.3**). Subsets Layer 5, 6, 7, SN350, and SN100 all scored comparatively with a R^2 of 0.71–0.72 and a RMSE of 0.66–0.67. The other sets all scored lower with R^2 0.58–0.62 and RMSE 0.66–0.75. Out of these five comparable sets, SN100 was chosen in the end as this contained the most data and produced top performing models.

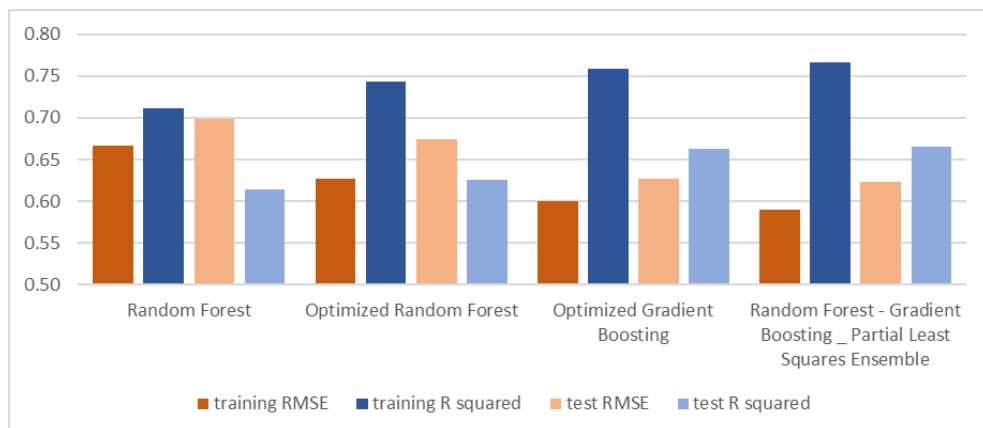


Figure 5.4 – Overview of performance of selected modeling approaches. Displayed are the internal (training, cross validation) and external (testing 30% holdout) statistics. Shown are three intermediate models, a Random Forest, an optimized Random Forest and Gradient Boosting model, with a final model consisting of a Random Forest plus Gradient Boosting ensemble with a stacked Partial Least Squares ensemble as second step. Each model improves performance over the last one, with the last being best. This optimization was applied to every combination possible, but these are not shown for brevity.

5.2.3 – Several machine learning techniques were used to create an optimized model

After selection of the optimal data subset, an optimal choice of machine learning method (ML) was determined. Three different methods were used: Random Forest (RF), Gradient Boosting (GB) and Partial Least Squares (PLS). Moreover, these methods were also further optimized and tested in an ensemble approach. Optimization was performed by both a backwards stepwise feature selection and a parameter optimization using grid search, with the best scoring model of each method continued for further analysis. Performance was determined using the R^2 and RMSE from a 30% (random based) holdout set of all NET interactions in the dataset.

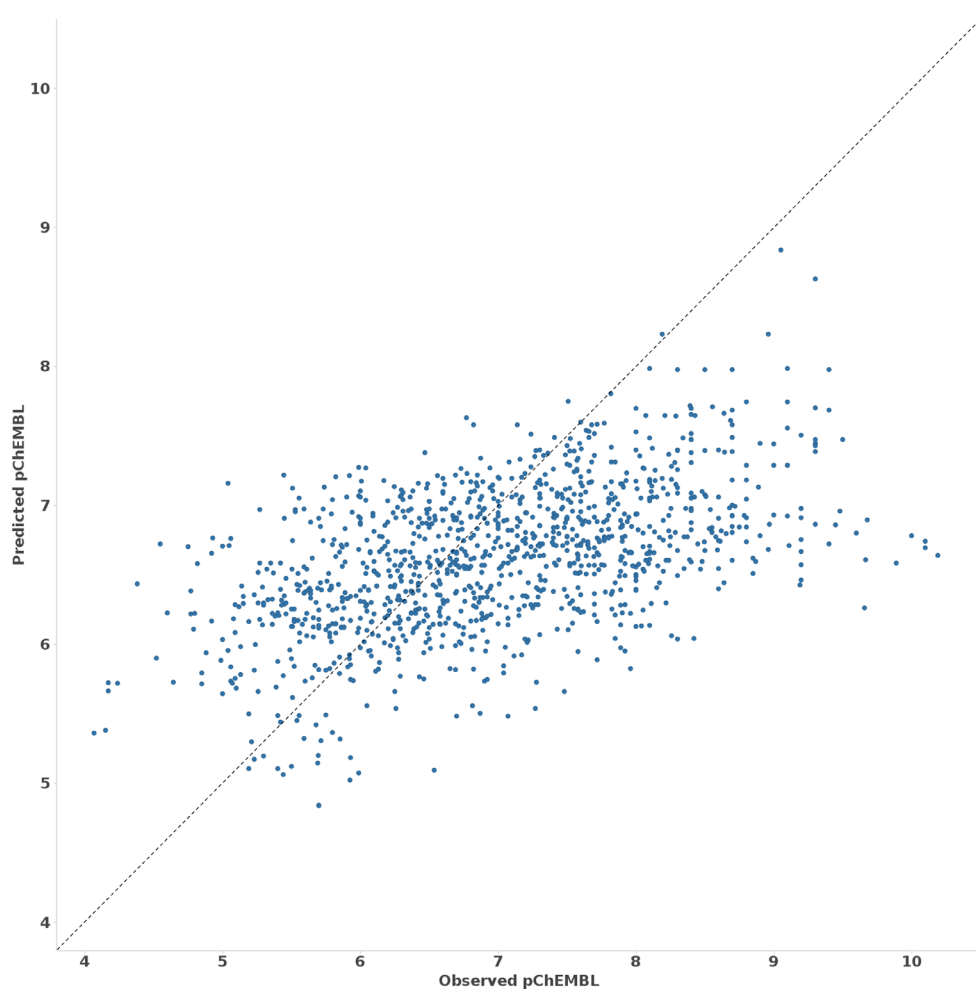


Figure 5.5 – Predicted pChEMBL values of temporal split correlated to the observed values. Temporal split prediction where all known interactions of ChEMBL of 2010 and before were used as training set (15,106 data points) and those of 2011 and later (5,083 data points) were used as the test set. R^2 was 0.24 and RMSE was 1.02.

Without optimization, PLS (R^2 : 0.28; RMSE: 0.93) was underperforming compared to RF (R^2 : 0.61; RMSE: 0.70) and GB (R^2 : 0.65; RMSE: 0.62). Next, stepwise feature selection and parameter optimization using a grid search were performed to fine-tune the models. Optimization of both the RF and GB models showed an increase in R^2 (0.62; 0.66) and a decrease in RMSE (0.67; 0.62) (**Figure 5.4**). There was another small increase in performance when PLS was stacked as a second model after the RF and GB models. The ensemble of optimized RF and GB models, of which predictions became the descriptors for a PLS model, performed the best and will be referred to as the NET model from now on.

5.2.4 – External validation shows the robustness of the NET model

To check whether the created NET model would meet the standards of a robust model, an external validation was performed with ChEMBL data (**Figure 5.5**). This validation was a temporal split, with the training set containing data from literature published before and in 2010, and the test set 2011 and later. This resulted in a R^2 of 0.24 and a RMSE of 1.02, in line with our previous examples of a temporal split¹⁸. Given the challenging nature of this approach (different chemotypes that are removed from the training set) and our prior experience with expected performance of models trained on temporal split ChEMBL data, it was concluded that the NET model was robust enough to continue forward.

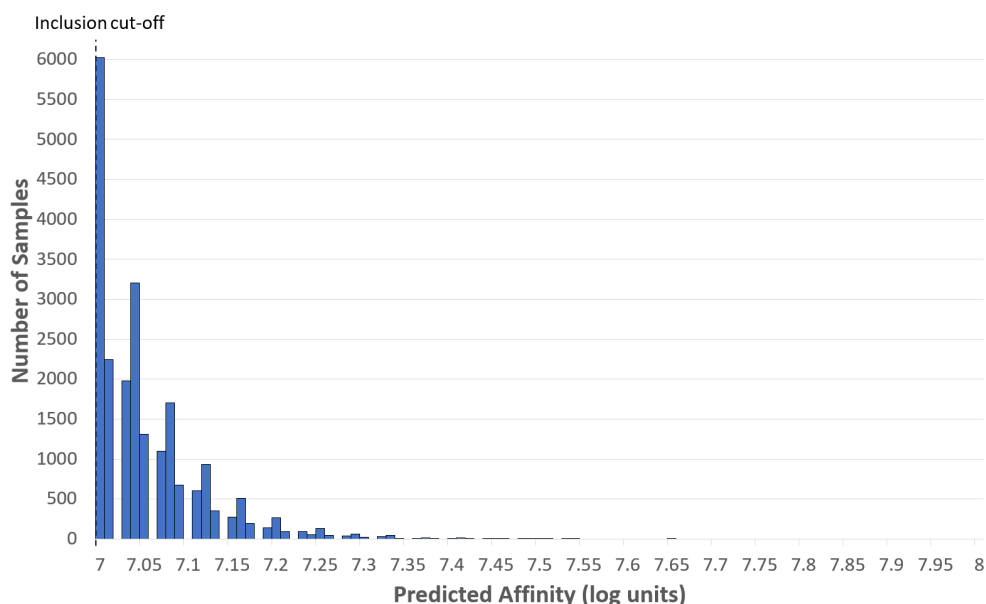


Figure 5.6 – Distribution of all predictions with affinity above 100 nM. Displayed is a histogram plot of the predicted affinities for the NET virtual screening of the Enamine compound database. Only those affinities which were predicted to have values lower than 100 nM were included (22,206 compounds).

5.2.5 – The NET model predicted 46 groups of compounds as viable candidates

The Enamine database was virtually screened with the NET model to predict the bioactivity of compounds for NET. Subsequently through several filtering steps a final selection was made as the initial database contained around 700 million compounds. In the first step only compounds with a predicted affinity towards NET better than 100 nM (7.00 log units) were considered (**Figure 5.6**). This threshold resulted in 22,206 compounds remaining, with the highest predicted affinity to reach 7.65 log units.

Subsequently compounds were clustered using HDBSCAN and visualized with t-SNE using a 1024 bit ECFP₆ fingerprint (**Figure 5.7**). HDBSCAN produced 46 clusters, with each

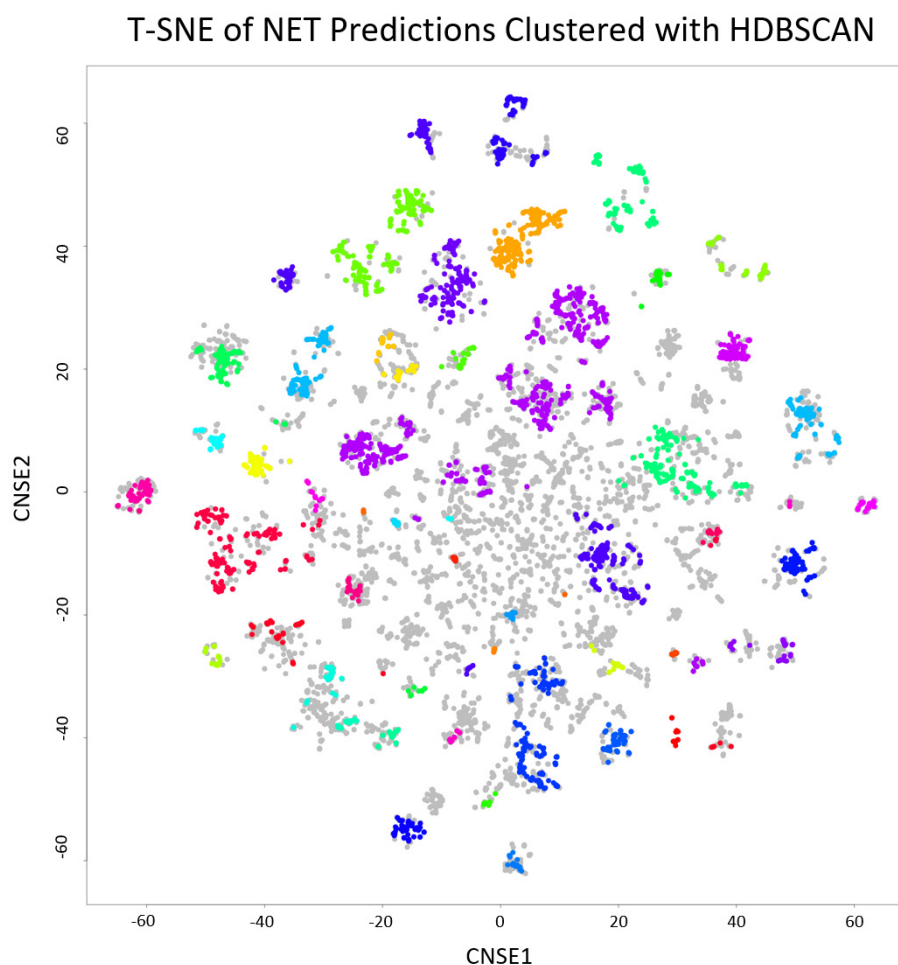


Figure 5.7 – t-SNE of the 22,206 predictions with HDBSCAN designated clusters. The t-SNE displayed was created using 1024 bits of FCFP₆. The HDBSCAN shows 46 distinct clusters with different colors. Grey points were filtered out as too similar (<90%) or too unsimilar (>50%) by HDBSCAN. The member of each cluster with the highest predicted activity was used as representative of that cluster in the prospective validation.

cluster representing structurally similar compounds. Compounds were first filtered (colored grey) by similarity to the training set, removing entries that shared either a 90% or higher similarity or a 50% or lower similarity. This was to ensure novelty and to increase the chance on NET activity in our final selection, respectively. Then, of each cluster, the compound with the highest predicted affinity was selected for a final suggested list of potential NET inhibitors. Of the 46 compounds, 32 were purchased and tested for NET activity in a label-free impedance-based assay.

5.2.6 – Experimental validation

To validate whether the predicted molecules from the NET model showed biological activity on NET, we used an impedance-based ‘transport activity through receptor activation’ (TRACT) assay as described in **Chapter 3 and 4**^{21,22}. In this assay a HEK293 cell line with inducible expression of NET was used and the activation of endogenously expressed alpha-2 adrenergic receptors by norepinephrine (NE) was measured as a cellular response. A compound was considered a NET inhibitor if the compound was able to significantly enhance the NE-induced cellular response in a concentration-dependent manner. A single-point primary screen was performed with 10 μ M test compound, using the reference NET inhibitor nisoxetine as a positive control (**Figure 5.8a**). Five of the 32 tested compounds were able to enhance the NE-induced response to a similar level as nisoxetine, which indicated that the compounds inhibited NET with a decent potency. None of the five compounds showed modulation of the NE response in cells lacking NET (**Supplementary Figure 5.S1**), confirming that the enhanced NE-induced response was specific to NET.

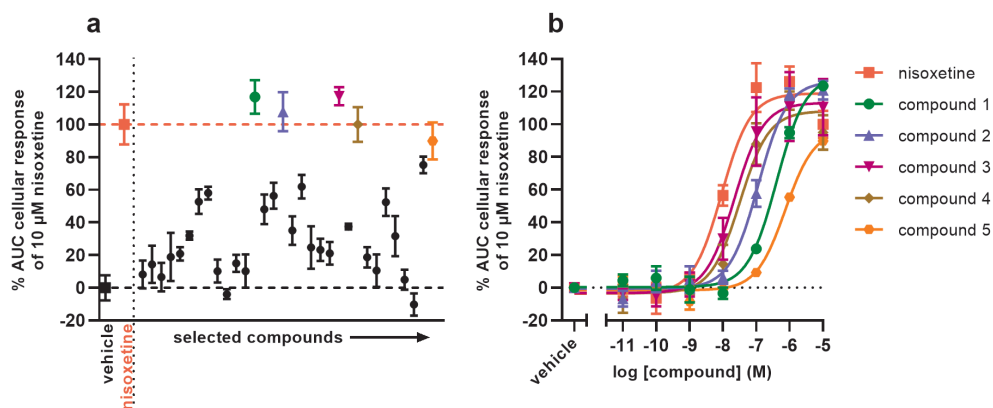
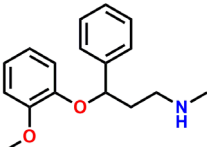
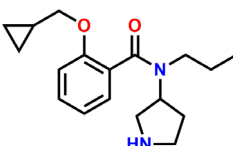
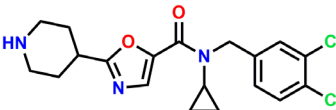
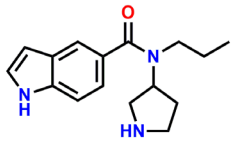
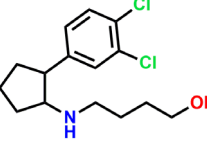
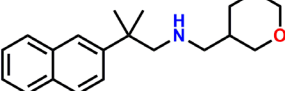


Figure 5.8 – *In vitro* functional validation of hits in a label-free impedance-based TRACT assay. **(a)** Single point screen of 32 hit compounds and **(b)** full-range concentration-inhibition curves of the top five compounds from the single point screen. Doxycycline-induced JumpIn-NET cells were pretreated for 1 h with either vehicle or **(a)** 10 μ M or **(b)** increasing concentrations of nisoxetine or hit compound. Subsequently, cells were stimulated with 1 μ M norepinephrine (NE) and Cell Index (CI) was measured for 30 min. Cellular responses are expressed as the net area under the curve (AUC) of the first 30 minutes after stimulation with NE. Data were normalized to the response of NE only (vehicle, 0%) and the response of NE in the presence of 10 μ M nisoxetine (100%). Data are shown as the mean \pm SEM of three separate experiments each performed in duplicate.

To further characterize the most potent inhibitors, full-range concentration-inhibition curves were obtained for the top five compounds and inhibitory potency (pIC_{50}) values were determined (**Figure 5.8b**, **Table 5.1**). The compounds on their own did not induce substantial cellular responses during pretreatment (**Supplementary Figure 5.S2**). All tested compounds showed concentration-dependent enhancement of the NE response with submicromolar inhibitory potencies (**Supplementary Figure 5.S3**, **Figure 5.8b**). Compounds 3 and 4 showed the highest pIC_{50} values (7.6 ± 0.1 and 7.5 ± 0.2 , respectively), which were in the range of the pIC_{50} of nisoxetine (8.0 ± 0.0) (**Table 5.1**). Taken together, these results demonstrate that at least five of the 32 tested compounds were biologically active NET inhibitors in a label-free TRACT assay.

Table 5.1 – Inhibitory potency (pIC_{50}) values of tested compounds as determined in the impedance-based TRACT assay. Data are reported as the mean \pm SEM of three individual experiments each performed in duplicate.

Compound	Molecular structure	$\text{pIC}_{50} \pm \text{SEM}$
Nisoxetine		8.0 ± 0.0
Compound 1		6.4 ± 0.1
Compound 2		6.9 ± 0.1
Compound 3		7.6 ± 0.1
Compound 4		7.5 ± 0.2
Compound 5		6.1 ± 0.1

5.3 – Discussion

Major depressive disorder is one of the main causes of disability, and an increasing trend in the worldwide incidence and prevalence of depression has been observed in recent years^{23,24}. Selective serotonin reuptake inhibitors (SSRIs), serotonin-norepinephrine reuptake inhibitors (SNRIs) and selective norepinephrine reuptake inhibitors (sNRIs) are established classes of prescription drugs for the first-line treatment of depression⁸. Although these drugs improve on the polypharmacological profile of tricyclic antidepressants, the current generation of reuptake inhibitors suffer from partial or non-responsiveness, relatively low remission rates, slow onset of action, and risk of adverse effects²⁵. Thus, the identification of novel norepinephrine transporter (NET) inhibitors could improve on the efficacy of current antidepressants, as well as provide scaffolds for the development of (fluorescent) probes for *in vitro* imaging²⁶. In this chapter, we have developed a machine learning model for the identification of novel inhibitors for human NET. After virtual screening of the Enamine database with this predictive model, we filtered out 46 compounds by clustering for experimental validation. Using the live-cell, impedance-based TRACT assay that was validated in **Chapter 4**, we identified five novel inhibitors for NET. Here, we will discuss the opportunities and limitations of this approach.

The bioactivity data that was used for training our models was obtained from ChEMBL25. However, machine learning models work best using more data and hence complementary data from ExCAPE-DB can be included in future work²⁷. Moreover, we recently released a comprehensive dataset called Papyrus that combines several datasets, that is annotated and standardized for compatibility²⁸. In future applications of this pipeline, we would switch to this dataset to increase our training set size while still retaining high quality and open source data. As said, having more data improves model performance and it is known that PCM models often demonstrate better performance than single target models due to the inclusion of more data. Here we have shown that we can empirically determine an optimal set of related proteins to include in a PCM model. This is a relevant finding as prior work in the area has primarily focused on small conserved families or very large protein superfamilies^{29,30}. We argue that the optimal number of included similar sequences is dependent on the (mean) similarity, the chemical variation, and the amount of data points per sequence and therefore data set dependent. Hence, good practice is to optimize this number when creating optimized models.

We used both phylogenetic trees and similarity networks to identify the optimal selection of proteins. Here, similarity networks proved to be a useful tool compared to the phylogenetic trees, as optimizing the pBLAST score threshold allowed us to vary the data set size and hence model performance. Conversely, while the trees are often used in metabolic pathway studies^{31,32}, here they were less useful than the networks due to the inability to tune the threshold as is the case with the networks. Similarity networks have also been used in comparative research, for example to visualize enzyme function using protein sequence, to visualize relationships between protein superfamilies, or to find similarities using gene ontology databases^{33–35}. Whereas these studies mainly focused on functional similarity, we

used sequence similarity, and thus including this functional similarity used in other work to our networks could potentially create a higher quality network that could predict more accurately.

When optimizing our prediction models for R^2 and RMSE, we concluded that the ensemble-stacking model containing all three methods (Random Forest, Gradient Boosting and Partial Least Squares) performed the best. However, the values for R^2 and RMSE between different combinations of these methods were very close, including some single models. We decided to use the ensemble-stacking model, since we concluded in earlier work that these models tend to work better compared to single models¹⁸. Deep learning could likely improve our model even further, as was demonstrated in our earlier work, however this was deemed outside the scope of this chapter³⁶.

To perform our clustering we had to trim down from our initial predictions to only include compounds that had a predicted affinity of 100 nM or better (resulting in a set of 22,206 compounds). Lower thresholds resulted in a clustering that was too large and would not converge. In follow up work, by increasing the amount of computational power we should be able to include more compounds, which subsequently could reveal new interesting clusters. Next, in order to only include novel candidates, we filtered for similarity between the set of 22,206 predicted compounds compared to our initial training set. Compounds that had higher than 90% similarity were excluded, as they would be too similar to existing inhibitors. Compounds that had a similarity of 50% or lower would be discarded as well, to increase the confidence in model predictions for the compound. The thresholds were chosen arbitrarily and could be subject to another optimization finding, but this was deemed out of scope of the current work. To further limit the amount of candidates, the minimal amount of points in a cluster was set to 19; so any smaller clusters were not taken further. From each cluster the most potent compound was then selected. Finally, as not all 46 candidates could be synthesized readily we eventually obtained final set of 32 compounds that were available for experimental validation. Note, potentially exploring (analogs of) the 14 cut candidates, or centers from the smaller clusters could hence result in more hits.

After clustering, 32 compounds were initially screened for their activity on NET using the impedance-based TRACT assay that was developed in **Chapter 4**. This assay has been used previously to characterize well-known inhibitors of NET, showing a similar rank order of inhibitory potencies compared to a more traditional fluorescent substrate uptake assay. In addition, the assay was validated for screening purposes and taking into account our experience with this platform we favored the use of the TRACT assay over traditional assays. Eleven out of the 32 compounds displayed at 10 μ M more than 50% enhancement of the NE-induced response, which is substantial considering that these compounds are structurally distinct from each other. This was also apparent from the five hit compounds, which all display submicromolar potencies towards NET. Although all compounds contain structural elements that are key to interacting with the sub-pockets of the norepinephrine binding site, such as a secondary amine and a substituted aromatic moiety, the scaffolds vary significantly in the substitution and size of aliphatic groups or the presence of an

amide moiety (Table 2)³⁷. Thus, these scaffolds could provide a starting point for the design and synthesis of derivatives, quantitative structure-activity relationships and subsequent hit optimizations of novel NET inhibitors.

Here, we have demonstrated an approach to identify novel protein inhibitors using a combination of machine learning techniques. In contrast to prior work which focused on a single model created from only NET interaction data, the optimal set of related targets for the PCM model was determined dynamically based on data analysis and subsequent modeling, stressing the fact that multiple SLC families were investigated for model inclusion. We applied this approach to identify novel NET inhibitors, which were found by virtually screening a database containing virtual molecules that were synthesized on demand. The complete computational pipeline can be applied to other protein families with relative ease, with the same provided data, or potentially be improved on with either larger datasets or more in-depth machine learning techniques.

5.4 – Materials and methods

5.4.1 – Software

Proteochemometric modeling, data curation, feature extraction, and cluster analysis was performed in Pipeline Pilot (version 18³⁸). Machine learning was performed using R (version 3.5.2) as integrated in Pipeline Pilot. Similarity network construction was done with Cytoscape (version 3.7.1³⁹) in RStudio (version 3.6.0⁴⁰). Any seeds used in randomization or model creation/prediction was set to ‘12345’.

5.4.2 – Interaction data

Interactions were gathered from the ChEMBL database (version 25.0⁴¹). Properties included were canonical SMILES for the compounds, amino acid sequence for the proteins, pChEMBL value representing the affinity (in $-\log M$). If there was more than one pChEMBL unit assigned to a data point (combination of chemical structure and protein) the highest of the following ranked units were chosen: $K_i > IC_{50} > EC_{50} > K_d$. Any duplicate pChEMBL values left were averaged so that only a single data point for each interaction remained.

5.4.3 – Compound standardization

Pipeline Pilot was used to convert canonical SMILES to structures. Compounds were standardized as in the statistical section of Burggraaff *et al*⁴². These steps included removing salts, standardizing stereoisomers/charges, and (de)protonation based on a pH 7.0.

5.4.4 – Compound descriptors

Physicochemical properties were calculated using Pipeline Pilot built-in components. Several fingerprints were calculated Estate keys/counts, MDL fingerprints, and a selection of extended-connectivity fingerprints⁴³. A full list of these compound descriptors can be found in **Supplementary Table 5.S1**, and an explanation of the letter system for the

extended-connectivity fingerprints can be found in the related article. All these descriptors were used during the feature selection process to sample which ones performed optimally.

5.4.5 – Protein descriptors

Three classes of protein descriptors were tested. The first set of protein descriptors was generated using the PROFEAT interface⁴⁴, which are alignment agnostic. Secondly, three alignment-based protein descriptors were included as used previously (Z-scores, FASGAI and BLOSUM)⁴⁵. Finally, a third set of protein descriptors was prepared using an in-house algorithm that included a selection of protein descriptor generators and returned an autocross correlated (ACC) version⁴⁶. An overview can be found in **Supplementary Table 5.S1**. Like the compound descriptors, these were also used in the feature selection part of the process.

5.4.6 – Similarity networks

Similarity networks were created using RStudio and package ‘Rcy3’ in Cytoscape, while displayed using ‘yFiles’. 9,131 proteins were extracted from ChEMBL, with 5,142 proteins used in the similarity investigations as these had interactions with compounds detailed. Proteins were first analyzed using pBLAST, resulting in an all-versus-all similarity matrix. Networks were then created using a varying pBLAST threshold, a higher threshold resulting in a higher required similarity for inclusion and hence less proteins included for the network. Two networks representing the extremes: a maximum viable similarity network (required similarity ≥ 100) representing multiple solute carriers; and a minimum viable similarity network (required similarity ≥ 800) containing only NET homologs.

5.4.7 – Phylogenetic tree formation

Phylogenetic trees were created using R packages ‘msa’, ‘seqinr’ and ‘ape’. Alignment was performed using the ‘msa’ implementation of ClustalW. Phylogenetic tree formation ended at the maximum viable similarity network (pBLAST ≥ 100), as it proved unfeasible to create a tree with all 5,142 proteins (pBLAST ≥ 25) with the available resources. Tree layers were created upwards from the minimum viable layer (NET only), with each layer above it including the previous layer. Tree creation was stopped when it reached the maximum viable similarity network. Modeling performance on the data using selected similarity networks as filter was then obtained using a 70/30 target based data split. This split was done with PCA assisted K-means, this was to ensure as much homogeneity between the datasets when validating. The R^2 and Residual Mean Squared Error (RMSE) were then calculated from a 10-fold cross validation.

5.4.8 – Feature selection

Stepwise feature selection was performed during model optimization. The maximum number of iterations were set at 25 and the number of iterations without model improvement was set to 3. Model improvement was defined as an increase in 5-fold cross validated R^2 .

Table 5.2 – Grids used during the parameter optimization procedure. Models are found on the left hand side with their respective R package. Parameter grids are separated per model.

Model	Parameter Grids	
Random Forest (ranger)	Number of Trees	100, 250, 500, 1000
	Number of Descriptors	Sqrt(D)*, Log2(D)*, Fraction: 10%, 50%, 90%
	Minimum Node Size	1, 5, 7
	Maximum Depth	5, 7, no max
Gradient Boosting (xgboost)	Maximum number of Trees	100, 250, 500, 1000
	Learning Rate	0.1, 0.3, 0.5
	Gamma	0, 0.3, 0.5
	Maximum Depth	5, 7
	Data Fraction	0.1, 0.5, 1.0
	Descriptor Fraction	0.5, 0.7
Partial Least Squares (pls)	Number of Variables	100, 200, 300

* D represents number of descriptors.

5.4.9 – Parameter optimization

Parameter optimization was performed using a simple full grid search. Model improvement was defined as an increase in 5-fold cross validated R^2 . Parameter grids are separated per model as shown in **Table 5.2**.

5.4.10 – Final validation / clustering

Clustering was used to select a diverse set of compounds for external validation. As an additional step after clustering, an identity filter was applied that removed points that had a 90% or higher identity or a 50% or lower identity with compounds found in the training data. This was to ensure that compounds were novel compared to existing compounds, but did not stray too far from the known interactions. Clustering was performed using R package ‘hdbscan’. Clusters were visualized in Pipeline Pilot, including the coloring of the different clusters. Grey points were filtered out automatically as noise, and thus discarded in the final selection. Finally, these clusters were ranked based on predicted NET affinity, and the top ranked compounds were chosen for further experimental validation.

5.4.11 – Chemicals and reagents

Jump In T-REx HEK 293 cells modified for doxycycline-inducible overexpression of the wild-type human norepinephrine transporter (JumpIn-NET) were provided by CeMM (Research Center for Molecular Medicine, Medical University of Vienna, Austria) and generated as described in **Chapter 4**. Doxycycline hyclate was purchased from Sigma Aldrich (St. Louis, MO, USA). Nisoxetine hydrochloride was purchased from Santa Cruz Biotechnology (Dallas, TX, USA). The 32 selected predicted active molecules were synthesized and provided by Enamine. All other chemicals were of analytical grade and obtained from standard commercial sources.

5.4.12 – Cell culture

JumpIn-NET cells were grown as adherent cells in culture medium (high glucose Dulbecco's Modified Eagle's Medium (DMEM) supplemented with 10% (v/v) fetal calf serum (FCS), 2 mM Glutamax, 100 IU/ml penicillin and 100 µg/ml streptomycin) at 37°C and 7% CO₂. Cryopreserved cells were thawed and cultured for 1–2 passages in culture medium. Cells were then cultured up to one week in culture medium supplemented with 2 mg/ml G418 and 5 µg/ml blasticidin before switching back to culture medium at least 24 h prior to an experiment. Cell cultures were split twice per week at ratios of 1:8 – 1:16 in 10 cm plates.

5.4.13 – TRACT assay

Label-free TRACT assays were performed using the xCELLigence real-time cell analysis (RTCA) platform as described in **Chapter 4**. In short, cells grown on gold-coated electrodes of 96-well E-plates impede the electric current that is generated on the electrodes. Impedance is measured at 10 kHz and is converted to the dimensionless parameter Cell Index (CI) using the following formula:

$$CI = \frac{(Z_i - Z_0)\Omega}{15\Omega}$$

where Z_i is the impedance at any given time and Z_0 is the baseline impedance measured at the start of each experiment.

Assays were performed at 37°C and 5% CO₂ in 96-well E-plates in a total volume of 100 µl. Background impedance was measured in 40 µl culture medium. JumpIn-NET cells were seeded in 50 µl at 60,000 cells/well in the presence of 1 µg/ml doxycycline (or no doxycycline for the counterscreen). The E-plate was left at room temperature for 30 min before placement in the recording station. Cells were grown for 22 hr prior to inhibitor pretreatment. All compound additions were done using a VIAFLO 96 handheld electronic 96 channel pipette (INTEGRA Biosciences, Tokyo, Japan). After 22 h, cells were pretreated for 1 h with either a single concentration (single-point primary screen, 10 µM) or increasing concentrations (full-range concentration-inhibition curves, ranging from 10 pM to 10 µM) of compound or nioxetine (positive control). Dilutions of compounds were first made in DMSO, then in phosphate-buffered saline (PBS). Vehicle-pretreated cells received only DMSO in PBS. Final amounts of DMSO were kept at 0.1% per well. After 1 h inhibitor pretreatment, cells were stimulated with either vehicle or 1 µM norepinephrine in PBS containing 1 mM ascorbic acid (final concentration). Impedance was then measured every 15 seconds for 30 minutes.

5.4.14 – Data analysis

Raw data from TRACT assays were recorded using RTCA Software v2.0 or v2.1.1 (ACEA Biosciences). For analysis of NE-induced cellular responses CI values were normalized to the time point prior to substrate addition to obtain normalized CI (nCI) values. Data were exported from RTCA Software and analyzed in GraphPad Prism v8.1.1 (GraphPad

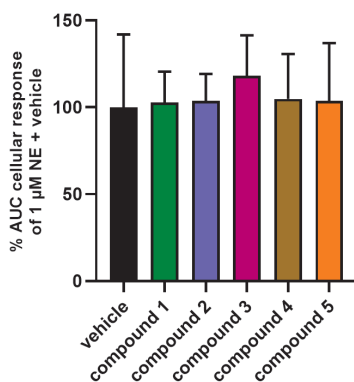
Software, San Diego, CA, USA). Per E-plate, nCI values of vehicle-pretreated and vehicle-stimulated cells were subtracted from all other data points to correct for any inhibitor and substrate-independent effects. NE-induced cellular responses were quantified by taking the net area under the curve (AUC) of the first 30 min after NE stimulation. Inhibitory potency (pIC_{50}) values of compounds are reported as a concentration-dependent enhancement of the NE-induced response by fitting the AUC data with non-linear regression to a sigmoidal concentration-inhibition curve with a fixed pseudo-Hill slope of 1. Data are shown as mean \pm standard error of the mean (SEM) of three separate experiments each performed in duplicate.

References

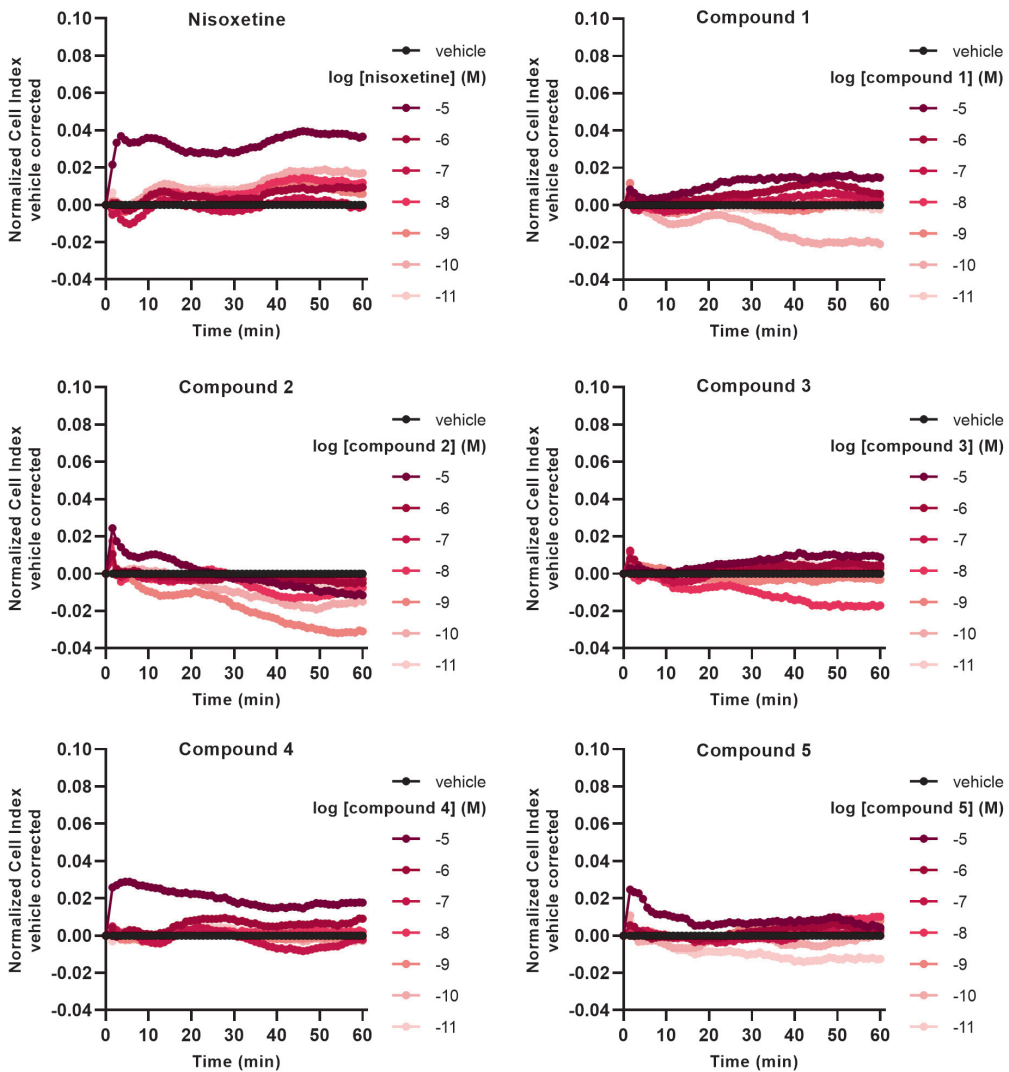
1. César-Razquin, A. *et al.* (2015) A call for systematic research on solute carriers. *Cell* **162**, 478–487.
2. Rask-Andersen, M., Masuram, S., Fredriksson, R. & Schiöth, H. B. (2013) Solute carriers as drug targets: Current use, clinical trials and prospective. *Mol. Aspects Med.* **34**, 702–710.
3. Girardi, E. *et al.* (2020) A widespread role for SLC transmembrane transporters in resistance to cytotoxic drugs. *Nat. Chem. Biol.* **16**, 469–478.
4. Okabe, M. *et al.* (2008) Profiling SLCO and SLC22 genes in the NCI-60 cancer cell lines to identify drug uptake transporters. *Mol. Cancer Ther.* **7**, 3081–3091.
5. Superti-Furga, G. *et al.* (2020) The RESOLUTE consortium: unlocking SLC transporters for drug discovery. *Nat. Rev. Drug Discov.* **19**, 429–430.
6. Höglund, P. J., Nordström, K. J. V., Schiöth, H. B. & Fredriksson, R. (2011) The solute carrier families have a remarkably long evolutionary history with the majority of the human families present before divergence of Bilaterian species. *Mol. Biol. Evol.* **28**, 1531–1541.
7. Bönisch, H. & Brüss, M. (Springer Berlin Heidelberg, 2006). The norepinephrine transporter in physiology and disease. in *Neurotransmitter Transporters: Handbook of Experimental Pharmacology* (eds. Sitte, H. H. & Freissmuth, M.) vol. 175 485–524.
8. Xue, W. *et al.* (2018) Recent advances and challenges of the drugs acting on monoamine transporters. *Curr. Med. Chem.* **25**, 1–42.
9. Coleman, J. A., Green, E. M. & Gouaux, E. (2016) X-ray structures and mechanism of the human serotonin transporter. *Nature* **532**, 334–339.
10. Penmatsa, A., Wang, K. H. & Gouaux, E. (2013) X-ray structure of dopamine transporter elucidates antidepressant mechanism. *Nature* **503**, 85–90.
11. Rognan, D. (2007) Chemogenomic approaches to rational drug design. *Br. J. Pharmacol.* **152**, 38–52.
12. Schlessinger, A. (Springer Berlin Heidelberg, 2014). Characterizing the structure, function, and evolution of human solute carrier (SLC) transporters using computational approaches. in *Membrane Transport Mechanism: Springer Series in Biophysics* (eds. Krämer, R. & Ziegler, C.) vol. 17 23–57.
13. Maia, E. H. B., Assis, L. C., de Oliveira, T. A., da Silva, A. M. & Taranto, A. G. (2020) Structure-based virtual screening: From classical to artificial intelligence. *Front. Chem.* **8**, 343.
14. Lee, Y. *et al.* (2019) Cryo-EM structure of the human L-type amino acid transporter 1 in complex with glycoprotein CD98hc. *Nat. Struct. Mol. Biol.* **26**, 510–517.
15. Tunyasuvunakool, K. *et al.* (2021) Highly accurate protein structure prediction for the human proteome. *Nature* **596**, 590–596.
16. Van Westen, G. J. P., Wegner, J. K., IJzerman, A. P., Van Vlijmen, H. W. T. & Bender, A. (2011) Proteochemometric modeling as a tool to design selective compounds and for extrapolating to novel targets. *Medchemcomm* **2**, 16–30.
17. Bento, A. P. *et al.* (2014) The ChEMBL bioactivity database: An update. *Nucleic Acids Res.* **42**, 1083–1090.
18. Lenselink, E. B. *et al.* (2017) Beyond the hype: deep neural networks outperform established methods using a ChEMBL bioactivity benchmark set. *J. Cheminform.* **9**, 1–14.
19. Wong, E. H. F. *et al.* (2000) Reboxetine: A pharmacologically potent, selective, and specific norepinephrine reuptake inhibitor. *Biol. Psychiatry* **47**, 818–829.
20. Zhou, J. (2004) Norepinephrine transporter inhibitors and their therapeutic potential. *Drugs Future* **29**, 1235–1244.
21. Sijben, H. J., van den Berg, J. J. E., Broekhuis, J. D., IJzerman, A. P. & Heitman, L. H. (2021) A study of the dopamine transporter using the TRACT assay, a novel in vitro tool for solute carrier drug discovery. *Sci. Rep.* **11**, 1312.
22. Sijben, H. J. *et al.* (2021) Label-free high-throughput screening assay for the identification of norepinephrine transporter (NET/SLC6A2) inhibitors. *Sci. Rep.* **11**, 12290.
23. Moreno-Agostino, D. *et al.* (2021) Global trends in the prevalence and incidence of depression: a systematic review and meta-analysis. *J. Affect. Disord.* **281**, 235–243.
24. James, S. L. *et al.* (2018) Global, regional, and national incidence, prevalence, and years lived with disability for 354 diseases and injuries for 195 countries and territories, 1990–2017: A systematic analysis for the Global Burden of Disease Study 2017. *Lancet* **392**, 1789–1858.
25. Artigas, F. (2013) Future directions for serotonin and antidepressants. *ACS Chem. Neurosci.* **4**, 5–8.
26. Camacho-Hernandez, G. A. *et al.* (2021) Illuminating the norepinephrine transporter: fluorescent probes based on nisoxetine and talopram. *RSC Med. Chem.* **12**, 1174–1186.
27. Sun, J. *et al.* (2017) ExCAPE-DB: An integrated large scale dataset facilitating Big Data analysis in chemogenomics. *J. Cheminform.* **9**, 1–9.
28. Béquignon, O. J. *et al.* (2021) Papyrus – A large scale curated dataset. *ChemRxiv preprint*, 1–26.
29. Van Westen, G. J. P. *et al.* (2012) Identifying novel adenosine receptor ligands by simultaneous proteochemometric modeling of rat and human bioactivity data. *J. Med. Chem.* **55**, 7010–7020.

30. Lapins, M. & Wikberg, J. E. S. (2010) Kinome-wide interaction modelling using alignment-based and alignment-independent approaches for kinase description and linear and non-linear data analysis techniques. *BMC Bioinformatics* **11**, 339.
31. Oh, S. J., Joung, J. G., Chang, J. H. & Zhang, B. T. (2006) Construction of phylogenetic trees by kernel-based comparative analysis of metabolic networks. *BMC Bioinformatics* **7**, 1–12.
32. Zhou, T., Chan, K. C. C. & Wang, Z. (Springer Berlin Heidelberg, 2008). TopEVM: Using co-occurrence and topology patterns of enzymes in metabolic networks to construct phylogenetic trees. in *Pattern Recognition in Bioinformatics: Lecture Notes in Computer Science* (eds. Chetty, M., Ngom, A. & Ahmad, S.) vol. 5265 225–236.
33. Gerlt, J. A. *et al.* (2015) Enzyme function initiative-enzyme similarity tool (EFI-EST): A web tool for generating protein sequence similarity networks. *Biochim. Biophys. Acta - Proteins Proteomics* **1854**, 1019–1037.
34. Atkinson, H. J., Morris, J. H., Ferrin, T. E. & Babbitt, P. C. (2009) Using sequence similarity networks for visualization of relationships across diverse protein superfamilies. *PLoS One* **4**, e4345.
35. Pesquita, C. *et al.* (2008) Metrics for GO based protein semantic similarity: A systematic evaluation. *BMC Bioinformatics* **9**, 1–16.
36. Koutsoukas, A., Monaghan, K. J., Li, X. & Huan, J. (2017) Deep-learning: Investigating deep neural networks hyper-parameters and comparison of performance to shallow methods for modeling bioactivity data. *J. Cheminform.* **9**, 1–13.
37. Pidathala, S., Mallela, A. K., Joseph, D. & Penmatsa, A. (2021) Structural basis of norepinephrine recognition and transport inhibition in neurotransmitter transporters. *Nat. Commun.* **12**, 2199.
38. <http://accelrys.com/products/collaborative-science/biovia-pipeline-pilot/> BIOVIA Pipeline Pilot | Scientific Workflow Authoring Application for Data Analysis (accessed 15-12-2015).
39. Su, G., Morris, J. H., Demchak, B. & Bader, G. D. (2014) Biological network exploration with Cytoscape 3. *Curr. Protoc. Bioinforma.* **2014**, 8.13.1–8.13.24.
40. <https://support.rstudio.com/hc/en-us/articles/206212048-Citing-RStudio/> RStudio: Integrated Development for R. (accessed 31-05-2017).
41. Mendez, D. *et al.* (2019) ChEMBL: Towards direct deposition of bioassay data. *Nucleic Acids Res.* **47**, D930–D940.
42. Burggraaff, L. *et al.* (2019) Identification of novel small molecule inhibitors for solute carrier SGLT1 using proteochemometric modeling. *J. Cheminform.* **11**, 15.
43. Rogers, D. & Hahn, M. (2010) Extended-connectivity fingerprints. *J. Chem. Inf. Model.* **50**, 742–754.
44. Chrszon, P., Dubslaff, C., Klüppelholz, S. & Baier, C. (2018) ProFeat: feature-oriented engineering for family-based probabilistic model checking. *Form. Asp. Comput.* **30**, 45–75.
45. van Westen, G. J. *et al.* (2013) Benchmarking of protein descriptor sets in proteochemometric modeling (part 2): modeling performance of 13 amino acid descriptor sets. *J. Cheminform.* **5**, 42.
46. Wold, S., Jonsson, J., Sjöström, M., Sandberg, M. & Rännar, S. (1993) DNA and peptide sequences and chemical processes multivariately modelled by principal component analysis and partial least-squares projections to latent structures. *Anal. Chim. Acta* **277**, 239–253.

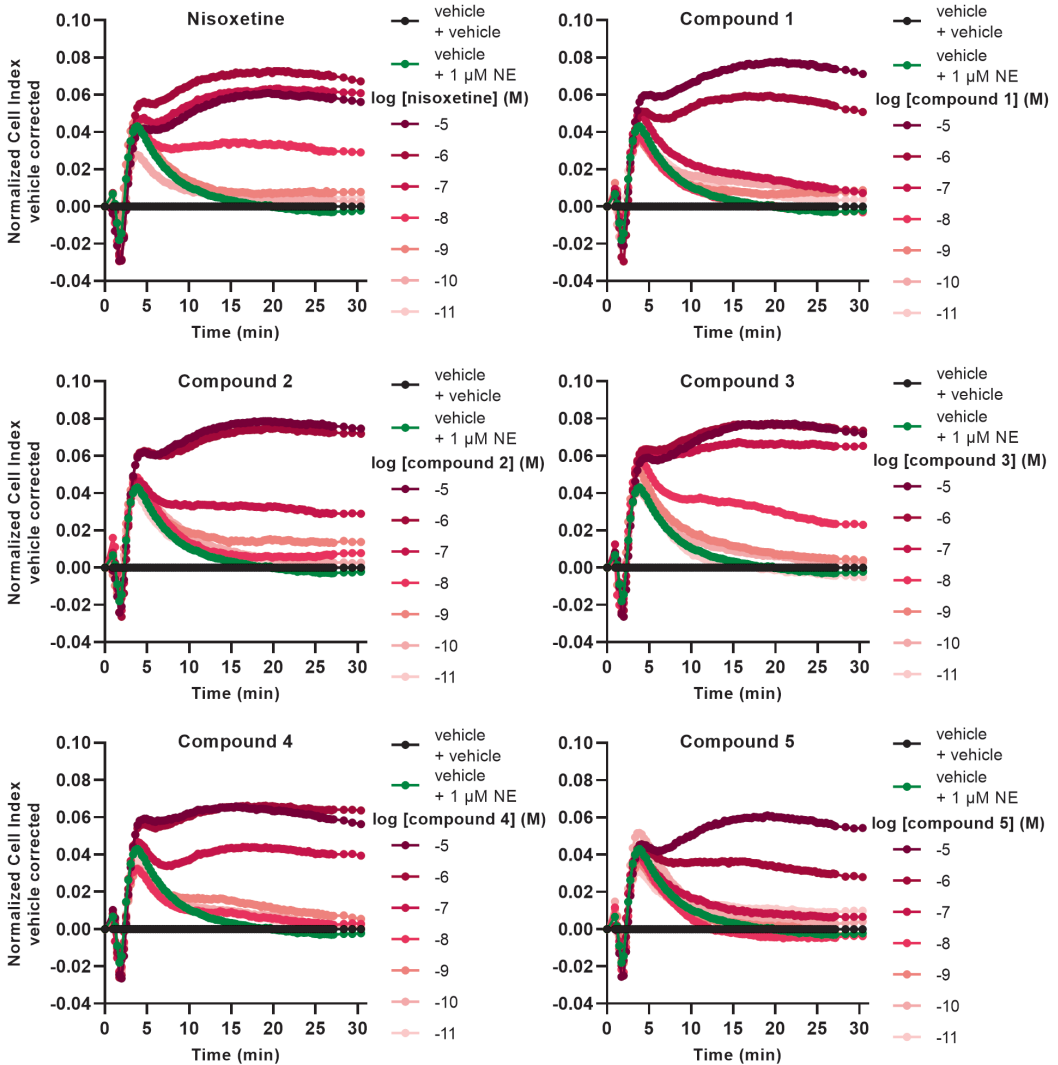
Supplementary Information



Supplementary Figure 5.S1 – Counterscreen of the five hit compounds in a label-free impedance-based TRACT assay. JumpIn-NET were not induced with doxycycline and as such did not express NET. Cells were pretreated for 1 h with either vehicle or 10 μ M of the hit compound. Subsequently, cells were stimulated with 1 μ M norepinephrine (NE) and Cell Index (CI) was measured for 30 min. Cellular responses are expressed as the net area under the curve (AUC) of the first 30 minutes after stimulation with NE. Data were normalized to the response of NE only (vehicle, 100%). Data are shown as the mean \pm SD of two separate experiments each performed in duplicate.



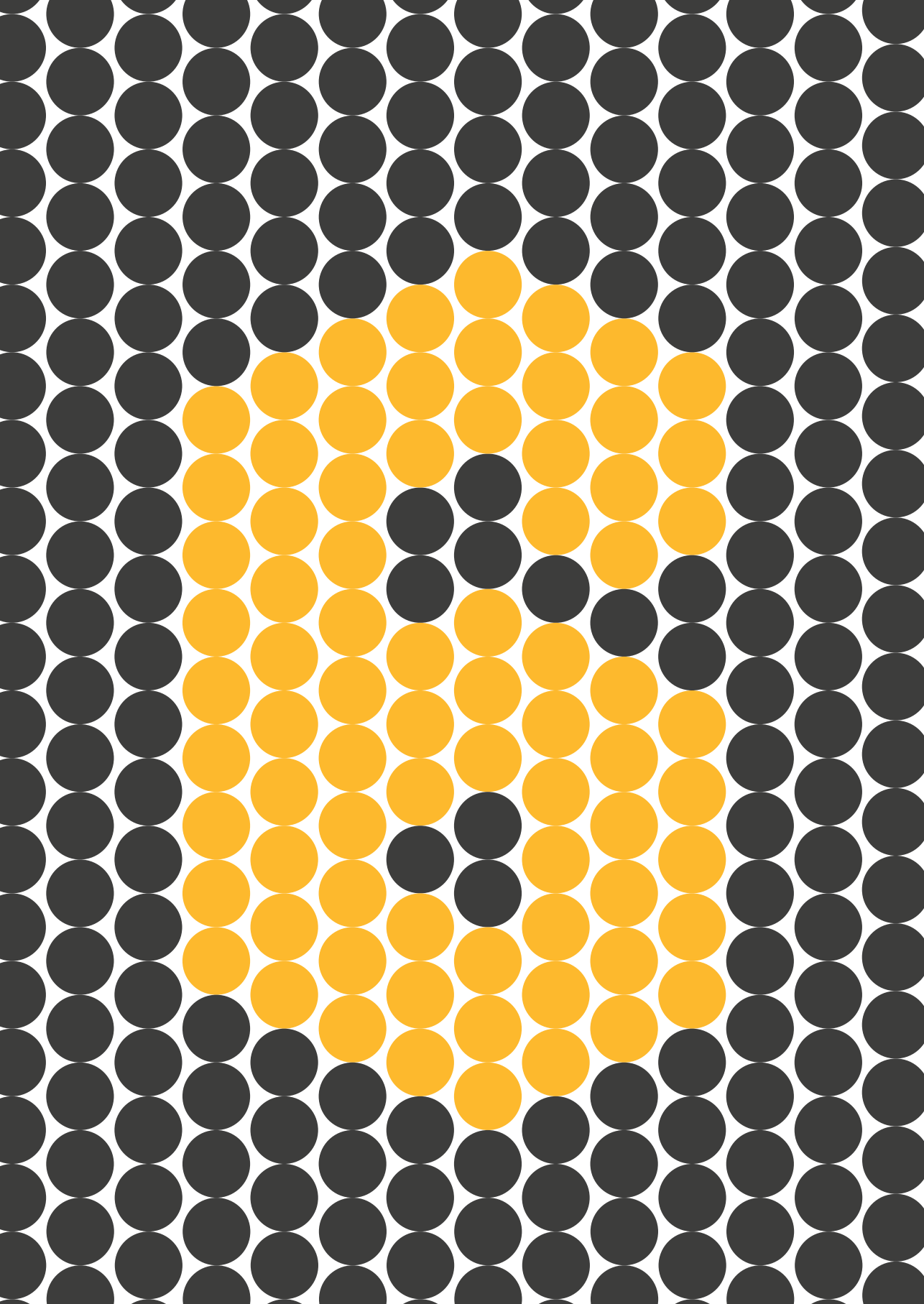
Supplementary Figure 5.S2 – Representative xCELLigence traces of JumpIn-NET cells during inhibitor pretreatment in a label-free impedance-based TRACT assay. Cells were pretreated for 1 h with either vehicle or increasing concentrations of nisoxetine or hit compound. Cell Index was normalized to the time point prior to inhibitor addition (t = 0 min). Data are shown as the mean of a representative experiment.



Supplementary Figure 5.S3 – Representative xCELLigence traces of JumpIn-NET cells during norepinephrine (NE) stimulation in a label-free impedance-based TRAC assay. Cells were pretreated for 1 h with either vehicle or increasing concentrations of nisoxetine or hit compound, and subsequently stimulated with vehicle or 1 μ M NE. Cell Index was normalized to the time point prior to NE addition ($t = 0$ min). Data are shown as the mean of a representative experiment.

Supplementary Table 5.S1 – Descriptors used throughout the model building process.

Molecular Descriptors		Protein Descriptors	
ALogP	SCFC 6	Amino Acid Composition	ACC c scales
Molecular Weight	FPFC 6	Dipeptide Composition	ACC DPPS
Number of Hydrogen Donors	EPFC 6	Auto Correlation Descriptors	ACC E scales
Number of Hydrogen Acceptors	LPFC 6	Composition Transition Distribution	ACC G scales
Number of Rotatable Bonds	SPFC 6	Quasi Sequence Order Descriptors	ACC HESH
Number of Bridge Bonds	FEFC 6	Pseudo Amino Acid Composition	ACC HSEHPCSV
Number of Atoms	EEFC 6	Amphiphilic Pseudo Amino Acid Composition	ACC Norinder
Number of Rings	LEFC 6	Total Amino Acid Properties	ACC Kidera
Number of Aromatic Rings	SEFC 6	Aligned Z scales Sandberg	ACC P scales
Number of Fragments	FHFC 6	Aligned FASGAI	ACC QCP
N Plus O Count	EHFC 6	Aligned BLOSUM	ACC Sneath
Molecular Solubility	LHFC 6	ACC Z scales Hellberg	ACC SVEEVA
Molecular Surface Area	SHFC 6	ACC Z scales Jonsson	ACC SVHEHS
Molecular Polar Surface Area	FCFP 6	ACC Z scales Sandberg	ACC SVRG
Molecular Polar Solvent-Accessible Surface Area (SASA)	ECFP 6	ACC Z scales binary	ACC SVWG
Estate Keys	LCFP 6	ACC T scales	ACC V scales
Estate Counts	SCFP 6	ACC ST scales	ACC VSGETAWAY
MDLPublicKeys	FPFP 6	ACC VHSE	ACC VSTPV
MDL2DKeys960	EPFP 6	ACC ISA ECI	ACC VSW
MDL2DKeys166	LPFP 6	ACC GRID t-score	ACC VTSA
PHFP 2-4	SPFP 6	ACC VSTV	ACC SVGER
PHRFP 2-4	FEFP 6	ACC MSWHIM	ACC PSM
PHPFP 2-4	EEFP 6	ACC_FASGAI	ACC SSIA AM1
PHFC 2-4	LEFP 6	ACC_BLOSUM	ACC SSIA PM3
PHPFC 2-4	SEFP 6	ACC_VARIMAX	ACC SSIA HF
PHRFC 2-4	FHFP 6	ACC Protein fingerprint numerical	ACC SSIA DFT
FCFC 6	EHFP 6	ACC Protein fingerprint hash	
ECFC 6	LHFP 6		
LCFC 6	SHFP 6		



CHAPTER 6

Impedance-based phenotypic readout of transporter function: a case for glutamate transporters

Hubert J. Sijben
Laura Dall' Acqua
Rongfang Liu
Abigail Jarret
Eirini Christodoulaki
Svenja Onstein
Gernot Wolf
Simone J. Verburgt
Sylvia E. Le Dévédec
Tabea Wiedmer
Giulio Superti-Furga
Adriaan P. IJzerman
Laura H. Heitman

Excitatory amino acid transporters (EAAT/SLC1) mediate Na⁺-dependent uptake of extracellular glutamate and are potential drug targets for neurological disorders. Conventional methods to assess glutamate transport *in vitro* are based on radiolabels, fluorescent dyes or electrophysiology, which potentially compromise the cell's physiology and are generally less suited for primary drug screens. Here, we describe a novel label-free method to assess human EAAT function in living cells, i.e. without the use of chemical modifications to the substrate or cellular environment. In adherent HEK293 cells overexpressing EAAT1, stimulation with glutamate or aspartate induced cell spreading, which was detected in real-time using an impedance-based biosensor. This change in cell morphology was prevented in the presence of the Na⁺/K⁺-ATPase inhibitor ouabain and EAAT inhibitors, which suggests the substrate-induced response was ion-dependent and transporter-specific. A mechanistic explanation for the phenotypic response was substantiated by actin cytoskeleton remodeling and changes in the intracellular levels of the osmolyte taurine, which suggests that the response involves cell swelling. In addition, substrate-induced cellular responses were observed for cells expressing other EAAT subtypes, as well as in a breast cancer cell line (MDA-MB-468) with endogenous EAAT1 expression. These findings allowed the development of a label-free high-throughput screening assay, which could be beneficial in early drug discovery for EAATs and holds potential for the study of other transport proteins that modulate cell shape.

6.1 – Introduction

Glutamate is the main excitatory amino acid in the human central nervous system. Its release from neurons is essential for the activation of ionotropic and metabotropic (mGluR) glutamate receptors in the close vicinity of the release site¹. Extracellular concentrations of glutamate are tightly regulated by vesicular release and dedicated solute carrier (SLC) transport proteins that are found on neurons and neighboring glia². The excitatory amino acid transporters (EAAT/SLC1) are the main facilitators of Na⁺-dependent glutamate uptake, with EAAT1 and EAAT2 accounting for roughly 90% of all glutamate uptake in the human central nervous system³. EAAT1 and EAAT2 are mainly expressed on astroglia⁴, whereas neuronal cells express EAAT3⁴, EAAT4 (cerebellar Purkinje cells)⁵ and EAAT5 (retina)⁶. Aberrant function or expression of glutamate transporters has been linked to an extensive list of neurological and psychological disorders, including Alzheimer's disease⁷, Parkinson's disease⁸, epilepsy⁹, schizophrenia¹⁰ and depression¹¹. Moreover, excessive extracellular concentrations of glutamate are generally linked to excitotoxicity caused by overactivation of glutamate receptors¹.

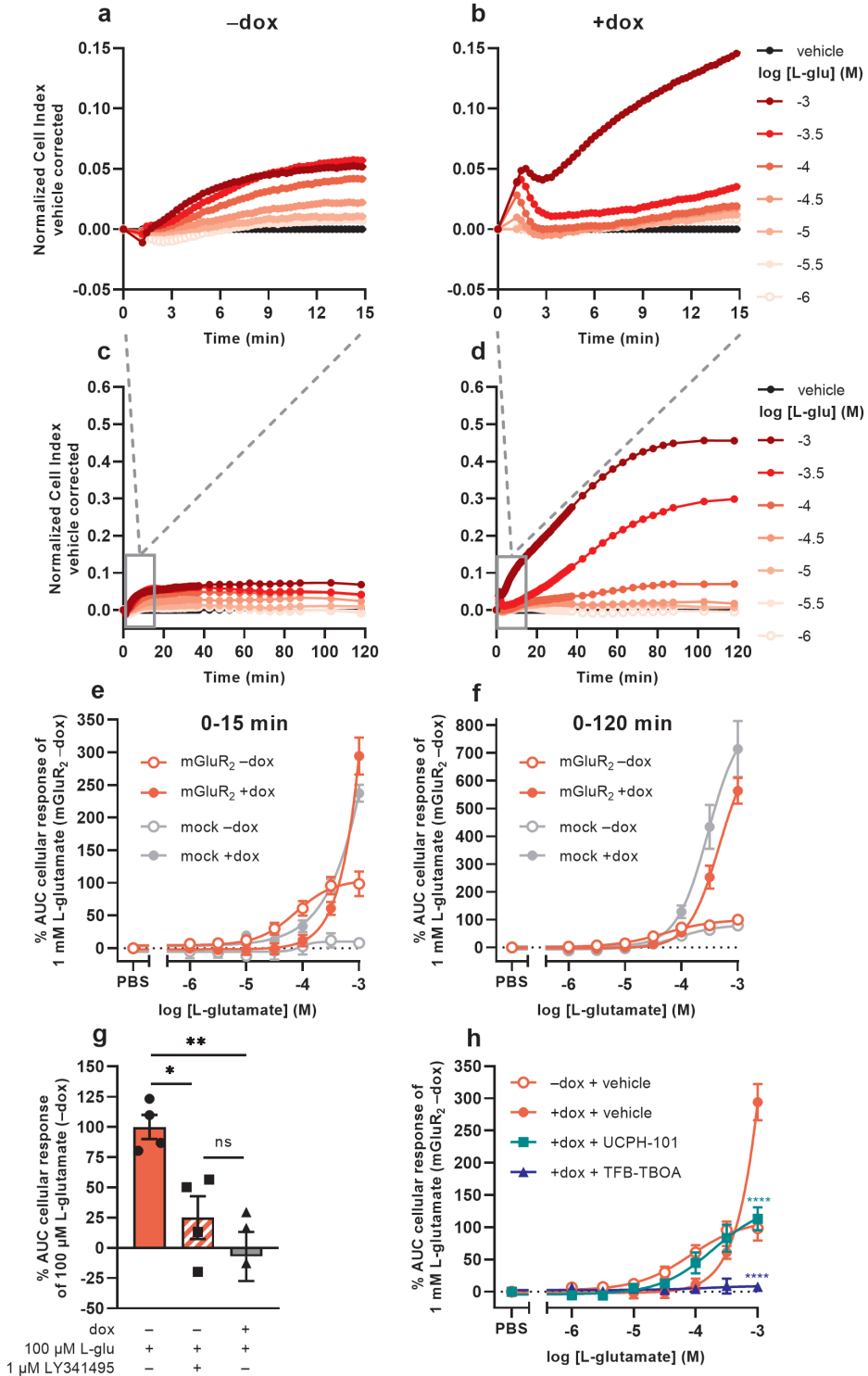
Under most conditions, pharmacological EAAT inhibition leads to highly elevated and detrimental glutamate levels, which refrains this class of modulators from widespread therapeutic applications. As such, most EAAT inhibitors have been mainly developed as probes for mechanistic studies and protein structure elucidations^{12–14}. However, in instances of severe ischemic stroke glutamate transport can be reversed as a result of a disrupted Na⁺/K⁺ balance, effectively increasing the extracellular glutamate levels in which cases EAAT inhibition could be a viable therapeutic strategy^{15,16}. Furthermore, a missense mutation of EAAT1 (P290R) that was identified in a patient with episodic ataxia type 6 shows a gain-of-function of the anion conductivity of EAAT, which contributes to severe ataxia symptoms and cerebellar degeneration^{17,18}. Another EAAT1 variant (E219D) associated with Tourette's syndrome has increased plasma membrane insertion probability and elevated glutamate uptake rates¹⁹. Thus, EAAT1 inhibition in patients with gain-of-function mutations could be an attractive approach to treat disease. Although so far no EAAT inhibitors have made it into clinical trials, the search for subtype selective modulators that alter the function or expression levels of EAATs is ongoing²⁰. Indeed, allosteric enhancers of EAAT2, which increase glutamate uptake, were recently discovered using a hybrid structure-based approach, and could be a potential treatment for excitotoxicity-related diseases²¹. Moreover, the first truly selective EAAT3 inhibitors were described only recently²², indicating that the development of small molecule tools for EAATs is still ongoing and considered an important endeavor.

Several *in vitro* methods are available to screen for EAAT active molecules in endogenous cell lines or cells with heterologous EAAT expression (**Chapter 1, Table 1.1**). Traditional electrophysiology approaches are accurate and present kinetic insight in transporter ion fluxes, but are tedious and labor-intensive, which makes them unsuitable for large compound screens²³. Automated electrophysiology-based methods on solid-supported membranes vastly increase throughput and have been used to study EAAT3 function^{24,25}. Another direct method, uptake of radiolabeled substrate by EAAT-expressing cells provides a rapid and

sensitive readout of transporter function and inhibition²⁶, although the use and handling of radioactivity may be a drawback to use this method. Alternatively, indirect assays based on fluorescent probes and reporters such as membrane potential dyes²⁷, glutamate sensors²⁸ and intracellular anion sensors²⁹ have proven successful to infer glutamate transport activity, although they require the introduction of non-physiological chemical labels. Previously, we reported on a label-free impedance-based method to assess activity and inhibition of nucleoside³⁰, dopamine³¹ (**Chapter 3**) and norepinephrine transporters³² (**Chapter 4**) *via* activation of congruent G protein-coupled receptors (GPCRs) by their endogenous substrate in live cells, termed the TRACT assay (**Chapter 1, Figure 1.4**). Importantly, impedance-based biosensors have the advantage to record any changes in cellular morphology upon cell perturbation, such as receptor activation and acute cytotoxicity³³, which opens a broader application of label-free assays to study transport proteins.

Here, we used an impedance biosensor system, xCELLigence, to study the function of EAATs in a HEK293 cell line with inducible heterologous expression of either one of the five human EAAT subtypes. An in-depth analysis of EAAT1-expressing cells revealed two distinct effects: 1) in cells transfected with the metabotropic glutamate receptor type 2 (mGluR₂), EAAT1 reduced the apparent potency of glutamate on mGluR₂, whereas 2) in cells lacking mGluR₂ glutamate induced EAAT1-mediated, receptor-independent cellular responses. Live-cell imaging revealed that the cells spread upon substrate stimulation, most likely initiated by EAAT1-mediated cell swelling. Substantial transporter-mediated responses were also observed for EAAT2 and EAAT3, but not for EAAT4 and EAAT5, likely due to poor expression of the latter two proteins. In addition, substrate-induced responses could be measured in a cell line with endogenous EAAT1 expression, which together indicate that this phenotypic assay is highly sensitive and applicable to multiple EAAT subtypes. With this method we demonstrate a completely novel approach to study glutamate transporters, effectively expanding the toolbox for mechanistic and drug discovery purposes.

→ **Figure 6.1** – L-glutamate induces distinct mGluR₂- and EAAT1-mediated responses in a TRACT assay. (**a,b,d,e**) Vehicle-corrected normalized Cell Index (nCI) traces of the first 15 min (**a,b**) or 120 min (**d,e**) after stimulation of cells with vehicle (PBS) or L-glutamate (L-glu) in the absence (–dox) (**a,d**) or presence (+dox) (**b,e**), of doxycycline, shown as the mean of a representative experiment performed in duplicate. (**c,f**) Combined concentration-response curves of L-glu on Jumpln-EAAT1-mGluR₂ cells (±dox, red) and mock-transfected Jumpln-EAAT1 cells (mock) (±dox, grey). (**g**) Cellular response of 100 µM L-glu on Jumpln-EAAT1-mGluR₂ cells (±dox) pretreated for 1 h with vehicle (PBS/DMSO) or 1 µM LY341495. (**h**) Combined concentration-response curves of L-glu on Jumpln-EAAT1-mGluR₂ cells (±dox) pretreated for 1 h with vehicle (PBS/DMSO) (data derived from **Figure 6.1e**), 10 µM UCPH-101 or 10 µM TFB-TBOA. Cellular response is expressed as the net AUC of the first 15 min (**c,g,h**) or 120 min (**f**) after L-glu stimulation. Data are normalized to the response of 1 mM (**c,f,h**) or 100 µM (**g**) L-glu on Jumpln-EAAT1-mGluR₂ (–dox) cells. Data are shown as the mean ± SEM of three or four individual experiments each performed in duplicate. ns = not significant, * p < 0.05, ** p < 0.01, *** p < 0.001, **** p < 0.0001; one-way ANOVA with Tukey's post-hoc test (**g**) or two-way ANOVA with Šídák's post-hoc test compared to vehicle-treated +dox cells (**h**).



6.2 – Results

6.2.1 – *L*-glutamate induces distinct mGluR₂- and EAAT1-mediated responses in a TRACT assay

Initial attempts to set up a functional method for EAATs were focused on the use of an impedance-based TRACT assay, i.e., using receptor activation as a measure of transporter activity^{31,32}. To validate this approach we used a modified HEK293 cell line with doxycycline (dox)-inducible overexpression of EAAT1 (JumpIn-EAAT1) that was transiently transfected with a plasmid encoding metabotropic glutamate receptor type 2 (mGluR₂) (JumpIn-EAAT1-mGluR₂). In the TRACT assay, the changes in electrical impedance are reported as the unitless parameter Cell Index (CI), which increases or decreases as the electrode coverage by cells increases or decreases, respectively. In non-induced (–dox) cells *L*-glutamate (*L*-glu) induced a concentration-dependent increase of the normalized Cell Index (nCI) within 15 min after stimulation ($pEC_{50} = 4.1 \pm 0.1$) (**Figure 6.1a,e, Table 6.1**), where a plateau was maintained for at least 120 min (**Figure 6.1c**). The early-phase *L*-glu response was attributed to mGluR₂ activation, as the response of a submaximal concentration of *L*-glu could be significantly blocked ($p = 0.0265$) by the mGluR₂-specific antagonist LY341495 (**Figure 6.1g**). No distinct early-phase response was observed in non-induced, mock-transfected cells (**Figure 6.1e**).

In cells with dox-induced EAAT1 expression (+dox) stimulation with *L*-glu resulted in a sharp nCI increase within two minutes followed by a brief decrease and a subsequent gradual increase in nCI in the first 15 minutes ($pEC_{50} < 3.0$) reaching a plateau after approximately 120 min that was 6-fold higher than in non-induced cells (**Figure 6.1b,d,e,f, Table 6.1**). Interestingly, 1 mM *L*-glu produced a vastly elevated nCI response within the first 15 min in dox-induced cells (**Figure 6.1b**), whereas at concentrations between 10 and 316 μ M the *L*-glu response was lower than in non-induced cells (**Figure 6.1e**), indicating that EAAT1 lowers the extracellular *L*-glu concentration leading to reduced mGluR₂ activation. In dox-induced mock-transfected cells the *L*-glu response over 120 min was in line with JumpIn-EAAT1-mGluR₂ (**Figure 6.1e,f**), which suggests that the *L*-glu response was comprised of two distinct phases: an early mGluR₂-dependent phase (0–15 min) and a late EAAT1-mediated phase (0–120 min).

The role of EAAT1 in the early-phase mGluR₂ response was confirmed using the non-competitive selective EAAT1 inhibitor UCPH-101¹⁴ and competitive non-selective EAAT inhibitor TFB-TBOA¹³ in JumpIn-EAAT1-mGluR₂ cells (**Figure 6.1h**). Of note, addition of TFB-TBOA on its own resulted in a peak nCI after 15 min in both non-induced and dox-induced cells, whereas UCPH-101 induced a response in non-induced cells only (**Supplementary Figure 6.S1a–d**). In dox-induced cells UCPH-101 substantially enhanced the apparent potency of *L*-glu ($pEC_{50} = 3.7 \pm 0.2$) compared to vehicle pretreated cells, indicating that EAAT1 inhibition potentiates mGluR₂ activation (**Figure 6.1h, Table 6.1**). The maximal response of 1 mM *L*-glu was significantly ($p < 0.0001$) reduced by 62% in the presence of UCPH-101, confirming that this part of the response is EAAT1-mediated. Strikingly, TFB-TBOA completely blocked 316 μ M ($p = 0.0769$) and 1 mM *L*-glu ($p <$

0.0001) responses. Since differential effects of the two EAAT1 inhibitors on the mGluR₂ response complicated data interpretation, which is impractical for a screening assay, we did not pursue optimization of the TRACT assay. Rather, we further explored the late-phase EAAT1-mediated L-glu response.

Table 6.1 – List of (–log) potency (pEC₅₀) and inhibitory potency (pIC₅₀) values of EAAT substrates and inhibitors on various cell lines in the TRACT and phenotypic assays. Potencies were determined on non-induced (–) or doxycycline (dox)-induced (+) cells in the absence (–) or presence of an inhibitor by analyzing the net area under the curve (AUC) of the first 120 min after substrate stimulation (unless stated otherwise).

Assay	Cell line	Dox	Substrate	Inhibitor	pEC ₅₀ ± SEM pIC ₅₀ ± SEM	n
TRACT assay	Substrate pEC ₅₀ ± SEM (AUC = 0–15 min)					
	JumpIn-EAAT1-mGluR ₂	–	L-glutamate	–	4.1 ± 0.1	6
		+		–	< 3.0	7
				UCPH-101 ^a	3.7 ± 0.2	3
				TFB-TBOA ^a	N.D.	3
	JumpIn-EAAT1-mock	–	–	N.D.	3	
		+	–	< 3.0	3	
	Substrate pEC ₅₀ ± SEM (AUC = 0–120 min)					
	JumpIn-EAAT1-mGluR ₂	–	L-glutamate	–	4.3 ± 0.1	6
		+		–	3.3 ± 0.1	7
	JumpIn-EAAT1-mock	–	–	4.0 ± 0.1	3	
		+	–	3.5 ± 0.0	3	
Phenotypic assay	Substrate pEC ₅₀ ± SEM					
	JumpIn-EAAT1	–	L-glutamate	–	4.2 ± 0.3	8
		–		3.4 ± 0.0	10	
		+	D-glutamate	–	< 3.0	5
			L-aspartate	–	3.4 ± 0.0	6
			D-aspartate	–	3.4 ± 0.1	5
	JumpIn-EAAT2	–		–	3.8 ± 0.1	6
		+		–	3.6 ± 0.0	6
	JumpIn-EAAT3	–	L-glutamate	–	N.D.	6
		+		–	3.9 ± 0.0	6
	MDA-MB-468 ^d	–	–	4.0 ± 0.2 ^b	3	
	Inhibitor pIC ₅₀ ± SEM (M)					
	JumpIn-EAAT1	+	L-glutamate	Ouabain	7.2 ± 0.0 ^c	3
				UCPH-101	5.2 ± 0.1 ^c	7
					6.7 ± 0.1 ^c	6
	JumpIn-EAAT2		TFB-TBOA	7.1 ± 0.0 ^d	3	
	JumpIn-EAAT3			6.1 ± 0.2 ^d	3	

^a 10 μM inhibitor;

^b AUC = 0–180 min;

^c stimulated with 1 mM L-glutamate;

^d stimulated with 316 μM L-glutamate

N.D. = not determined

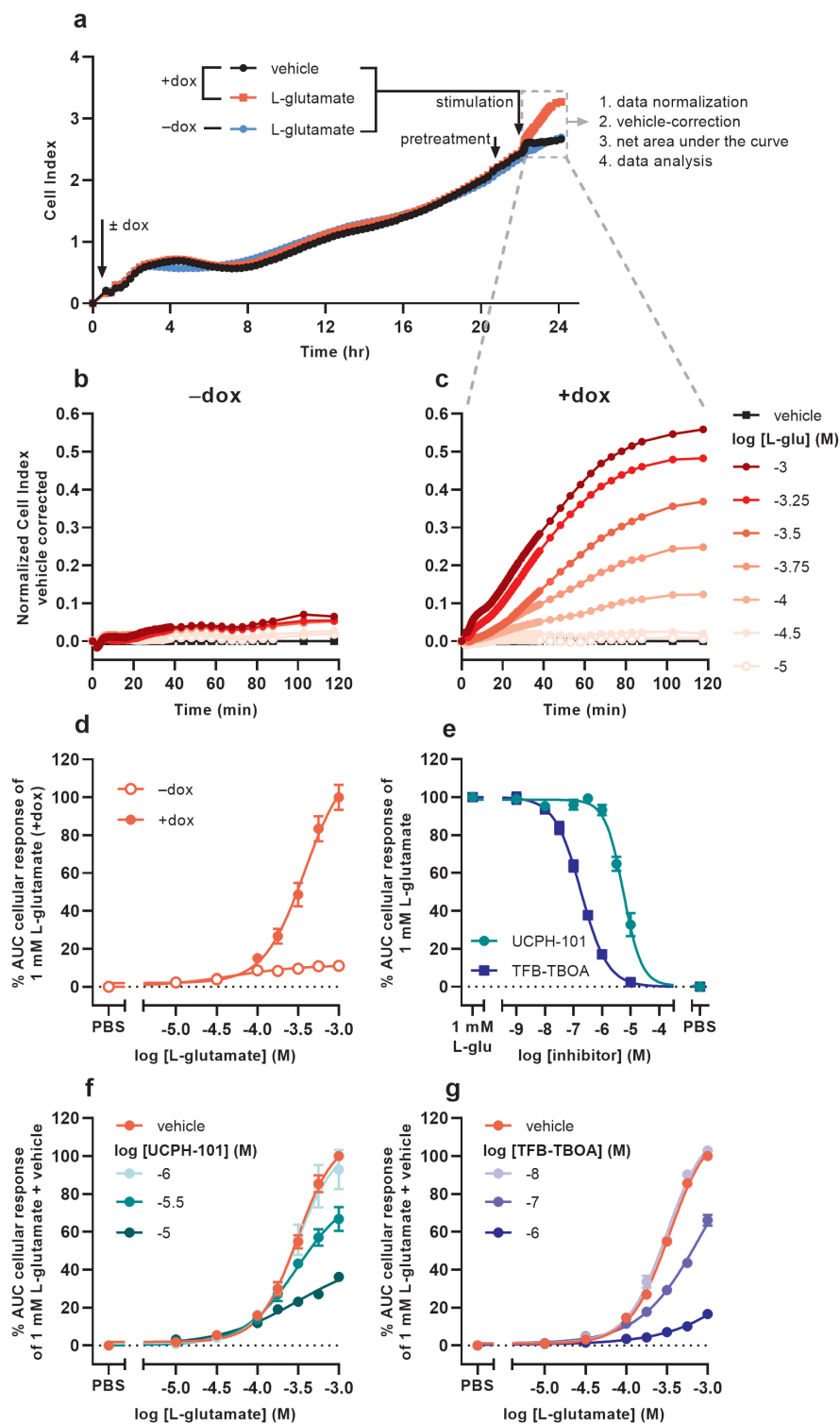
6.2.2 – EAAT1-specific L-glutamate-induced cellular responses are blocked by UCPH-101 and TFB-TBOA

Receptor-independent cellular responses by L-glu were assessed in non-transfected JumpIn-EAAT1 cells in the absence (–dox) or presence (+dox) of doxycycline. Incubation with doxycycline did not affect the growth of the cells prior to pretreatment or stimulation (**Figure 6.2a**). L-glu induced a gradual concentration-dependent increase in nCI in non-induced cells ($pEC_{50} = 4.2 \pm 0.3$), whereas in dox-induced cells L-glu produced a drastically elevated nCI ($pEC_{50} = 3.4 \pm 0.0$) reaching a 10-fold higher plateau after 120 min (**Table 6.1**, **Figure 6.2b–d**). Similar L-glu potencies were measured at 120 min in the TRACT assay on both non-induced and dox-induced JumpIn-EAAT1-mGluR₂ and JumpIn-EAAT1-mock cells (**Table 6.1**). This indicates that the L-glu-induced cellular response is largely EAAT1-mediated. Unless stated otherwise, all further experiments were conducted on dox-induced cells.

To confirm the specific role of EAAT1 in the L-glu response we assessed the pharmacological properties of UCPH-101 and TFB-TBOA. No substantial changes in nCI were observed during the 1 h pretreatment with 10 μ M of either inhibitor (**Supplementary Figure 6.S1e,f**). Both UCPH-101 ($pIC_{50} = 5.2 \pm 0.1$) and TFB-TBOA ($pIC_{50} = 6.7 \pm 0.1$) blocked the response of 1 mM L-glu in a concentration-dependent manner (**Table 6.1**, **Figure 6.2e**). To assess the reproducibility and robustness of the inhibitory assay window, a semi-manual high-throughput screening (HTS) validation was performed using a low (10 μ M TFB-TBOA), mid (0.2 μ M TFB-TBOA) and high (vehicle) signal upon stimulation with 1 mM L-glu (**Supplementary Figure 6.S2a**). The assay produced a Z' of 0.85 ± 0.01 and a signal window (SW) of 25.1 ± 1.3 , which indicates an “excellent” assay^{34,35} that is suitable for single-point detection of EAAT1 inhibition (**Supplementary Figure 6.2b**).

The mechanism of inhibition by UCPH-101 and TFB-TBOA was demonstrated by pretreating cells with three different concentrations of inhibitor prior to stimulation with increasing concentrations of L-glu (**Figure 6.2f,g**). Since not all L-glu concentration-response curves reached a plateau within the tested concentration range, no formal Schild analysis was performed. Nevertheless, UCPH-101 reduced the maximum response of L-glu (**Figure 6.2f**) without much affecting the potency of L-glu, whereas the presence of TFB-

→ **Figure 6.2** – L-glutamate induces EAAT1-specific cellular responses on JumpIn-EAAT1 cells. **(a)** Experimental layout of an xCELLigence growth curve, the subsequent assay course and data analysis. Shown are traces of two separate wells from a representative experiment. **(b,c)** Vehicle-corrected nCI traces of cells in the absence (–dox) **(b)** or presence (+dox) **(c)** of doxycycline stimulated with vehicle (PBS) or L-glutamate (L-glu), shown as the mean of a representative experiment performed in duplicate. **(d)** Combined concentration-response curves of L-glu on JumpIn-EAAT1 cells (\pm dox). **(e)** Combined concentration-inhibition curves of TFB-TBOA and UCPH-101 on +dox cells pretreated for 1 h with vehicle (PBS/DMSO) or increasing concentrations of TFB-TBOA or UCPH-101 and subsequently stimulated with a submaximal concentration (1 mM) of L-glu. **(f)** Combined concentration-response curves of L-glu on +dox cells pretreated for 1 h with vehicle (PBS/DMSO), 1 μ M, 3.16 μ M or 10 μ M UCPH-101. **(g)** Combined concentration-response curves of L-glu on +dox cells pretreated for 1 h with vehicle (PBS/DMSO), 10 nM, 100 nM or 1 μ M TFB-TBOA. Cellular response is expressed as the net AUC of the first 120 min after L-glu stimulation. Data are normalized to the response of 1 mM L-glu on +dox cells. Data are shown as the mean \pm SEM of three to ten individual experiments each performed in duplicate.



TBOA produced an apparent right-ward shift of the L-glu curve (**Figure 6.2g**), indicating a non-competitive and competitive mode of inhibition, respectively.

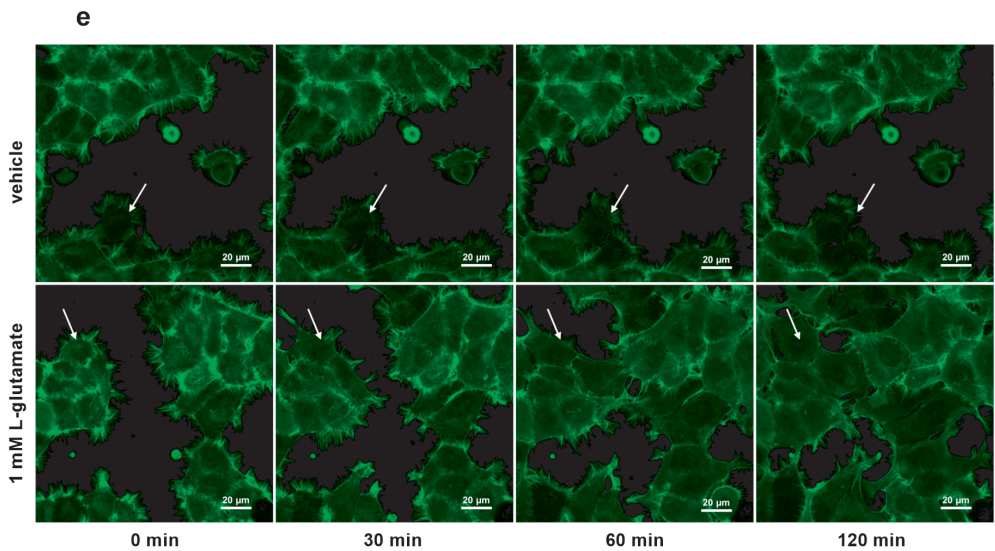
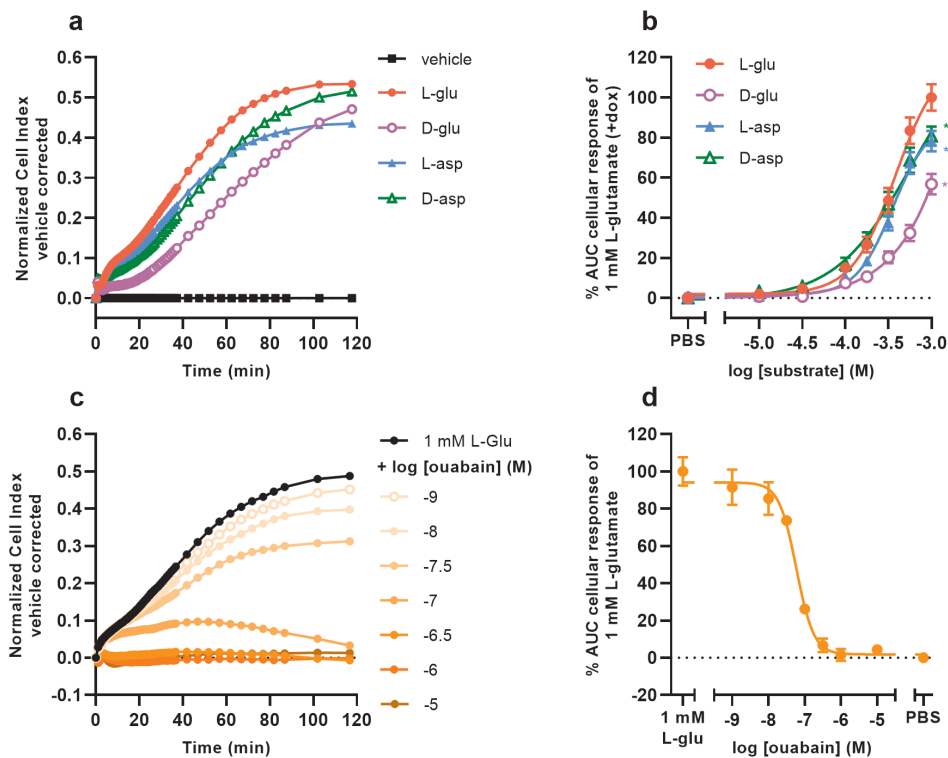
6.2.3 – Substrate-specific uptake via EAAT1 induces Na^+/K^+ -ATPase (NKA)-dependent cell spreading

To investigate whether the cellular responses were L-glu specific, three additional EAAT1 substrates were tested. Similar to L-glu, stimulation of cells with D-glutamate (D-glu), L-aspartate (L-asp) and D-aspartate (D-asp) induced a substantial nCI increase within 120 min (**Figure 6.3a**). L-asp and D-asp had potencies ($\text{pEC}_{50} = 3.4 \pm 0.0$ and 3.4 ± 0.1 , respectively) that were comparable to L-glu, whereas the potency of D-glu was substantially lower ($\text{pEC}_{50} < 3.0$) (**Table 6.1, Figure 6.3b**). The maximal responses of 1 mM L-asp ($p = 0.0005$), D-asp ($p = 0.0054$) and D-glu ($p < 0.0001$) were significantly lower than L-glu (**Figure 6.3b**), which was attributed to a lower nCI plateau (L-asp) or slower onset of the nCI increase (D-asp, D-glu) (**Figure 6.3a**). These data suggest that the cellular responses are substrate-specific and likely emanate from a shared mechanism.

To assess the role of Na^+/K^+ -ATPase (NKA) in the L-glu-induced cellular response, cells were pretreated for 1 h with increasing concentrations of the NKA inhibitor ouabain and stimulated with 1 mM L-glu (**Figure 6.3c**). During pretreatment with ouabain the nCI gradually decreased in a concentration-dependent manner (**Supplementary Figure 6.S1g**), which was corrected for during substrate stimulation by including vehicle controls for each concentration of ouabain. Upon L-glu stimulation ouabain showed concentration-dependent inhibition of the cellular response ($\text{pIC}_{50} = 7.2 \pm 0.0$) (**Table 6.1, Figure 6.3d**). This validates that the Na^+ gradient and NKA activity are crucial for proper EAAT1-mediated L-glu uptake and the subsequent cellular responses.

To determine whether changes in cell morphology underlie the L-glu-induced cellular responses, JumpIn-EAAT1 cells were transduced with a LifeAct-GFP actin lentiviral plasmid (JumpIn-EAAT1-LifeAct-GFP) and visualized during an L-glu stimulation using confocal microscopy (**Figure 6.3e**). Dox-induced cells did not show substantial changes in morphology within 2 h after vehicle stimulation. Strikingly, cells stimulated with 1 mM L-glu

→ **Figure 6.3** – Substrate-dependent uptake via EAAT1 mediates Na^+/K^+ -ATPase (NKA)-dependent cell spreading. **(a)** Vehicle-corrected nCI traces of +dox cells stimulated with vehicle (PBS), 1 mM of L-glutamate (L-glu), D-glutamate (D-glu), L-aspartate (L-asp) or D-aspartate (D-asp), shown as the mean of a representative experiment performed in duplicate. **(b)** Combined concentration-response curves of L-glu (derived from **Figure 6.2d**), D-glu, L-asp and D-asp on +dox cells. **(c)** Vehicle (PBS)-corrected nCI traces of +dox cells pretreated for 1 h with vehicle (PBS/DMSO, black) or increasing concentrations of ouabain and subsequently stimulated with 1 mM L-glu, shown as the mean of a representative experiment performed in duplicate. **(d)** Combined concentration-inhibition curves of ouabain in +dox cells. Vehicle (PBS)-induced responses were subtracted from L-glu-induced responses for each concentration of ouabain. Cellular response is expressed as the net AUC of the first 120 min after substrate stimulation. Data are normalized to the response of 1 mM L-glu. Data are shown as the mean \pm SEM of three to six individual experiments each performed in duplicate. **(e)** Representative confocal images of JumpIn-EAAT1-LifeAct-GFP (green) cells 0, 30, 60 and 120 min after stimulation with vehicle (PBS) or 1 mM L-glu, scale bar = 20 μm . Stills were selected from a representative live imaging movie from two independent experiments each performed in triplicate. White arrow indicates representative behavior of a single cell, showing increased cell spreading over time.



appeared to drastically extend their actin cytoskeleton outward within 2 h after stimulation, producing protrusions that stretch towards neighboring cells effectively expanding their surface area and thus well coverage (**Figure 6.3e**). When cells were pretreated with 1 μ M ouabain, stimulation with vehicle or 1 mM L-glu did not induce cell spreading, but rather a slight reduction of the cell surface area (**Supplementary Figure 6.S3**). Since the onset of cell spreading concurs with the nCI increases that were observed in xCELLigence experiments (**Figure 6.2c**), this implies that these distinct L-glu-induced morphological changes are at the basis of EAAT1-mediated cellular responses.

6.2.4 – EAAT1-mediated uptake of L-glu and L-asp affect intracellular metabolite levels

Since glutamate and aspartate may be metabolized in the cell upon entering the cytosol *via* EAAT1, we investigated whether changes in intracellular metabolite levels could provide an explanation for the observed cellular responses. Non-induced and dox-induced cells were stimulated for 2 h with 1 mM L-glu or L-asp in the presence or absence of 10 μ M TFB-TBOA and lysates were subsequently analyzed using targeted metabolomics. Intracellular levels of 131 predefined metabolites were screened and visualized in volcano plots to highlight significant increases or decreases after 2 h (**Supplementary Figure 6.S4**). Based on these plots, we focused on intracellular metabolites that were significantly increased or decreased for both L-glu and L-asp in order to reveal a common mechanism (**Figure 6.4**). Firstly, metabolite levels were generally not affected in non-induced (–dox) cells. Secondly, in dox-induced (+dox) cells, stimulation with L-glu and L-asp resulted in a respective 5-fold and a 60-fold increases of glutamate and aspartate, respectively, which confirms that both substrates entered the cells *via* EAAT1. Thirdly, all observed changes in metabolite levels (except hydroxyglutamate) were significantly prevented in the presence of TFB-TBOA (**Figure 6.4, hatched bars**), indicating that these were the result of EAAT1-mediated substrate influx.

The levels of glutamine, a product of glutamate metabolism, were not significantly altered by either substrate, indicating that this metabolite is not involved in the cellular response. Interestingly, the tricyclic acid (TCA) cycle intermediates (alpha-ketoglutarate, dimethyl succinate, hydroxyglutamate, hydroxyglutarate, succinate and aconitate) were oppositely increased or decreased for each substrate, which suggests that L-glu and L-asp are differentially metabolized in the cell and that the TCA cycle does not contribute to the cellular response. Moreover, products of L-asp metabolism (argininosuccinate, adenosine monophosphate (AMP), inosine monophosphate (IMP) and malate) were increased upon stimulation with L-asp, but to a lesser extent by L-glu. Strikingly, the organic osmolyte taurine, which is not a product of L-glu or L-asp metabolism and is involved in cell volume regulation, was significantly reduced upon stimulation with both L-glu and L-asp, which suggests that substrate uptake *via* EAAT1 may result in taurine efflux. Taken together, these data imply that the cellular response in the impedance-based assay is likely not driven by substrate metabolism, but is rather associated with changes in cell volume.

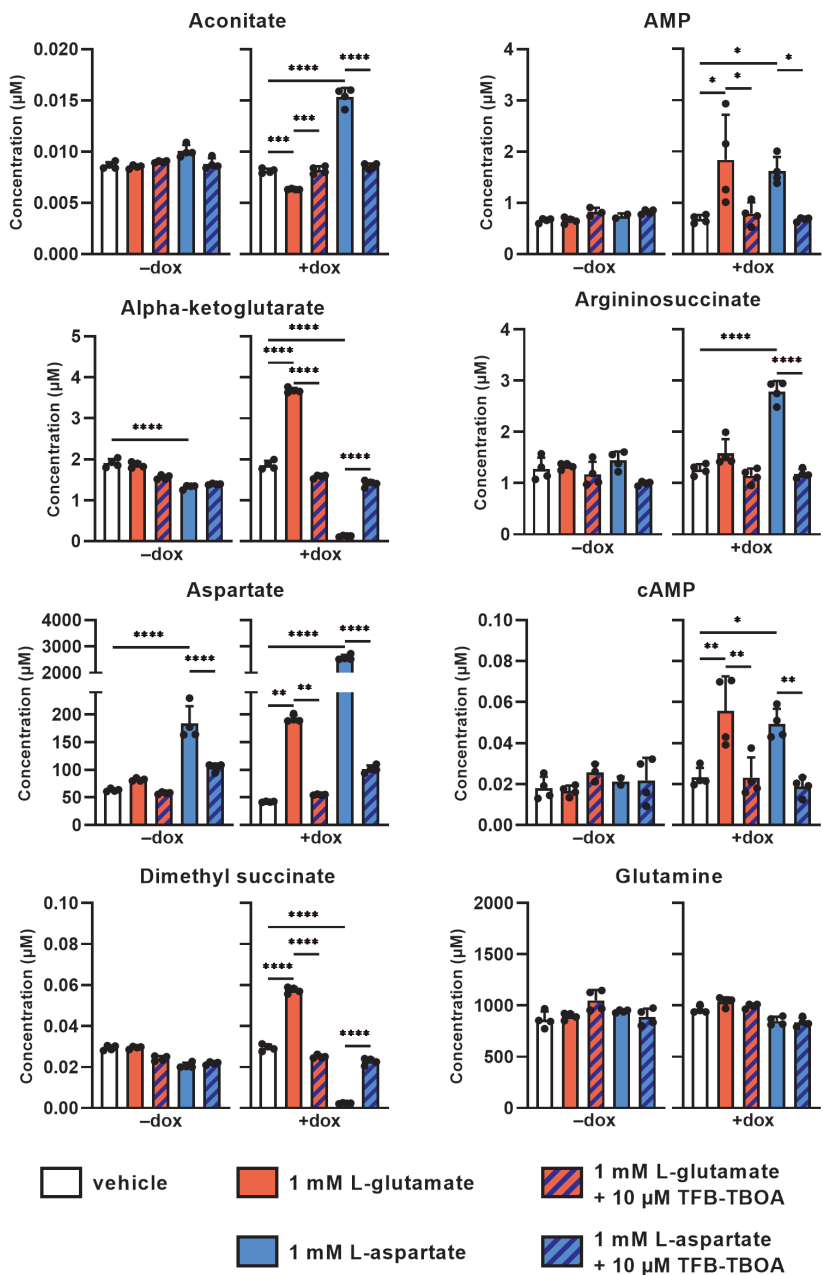
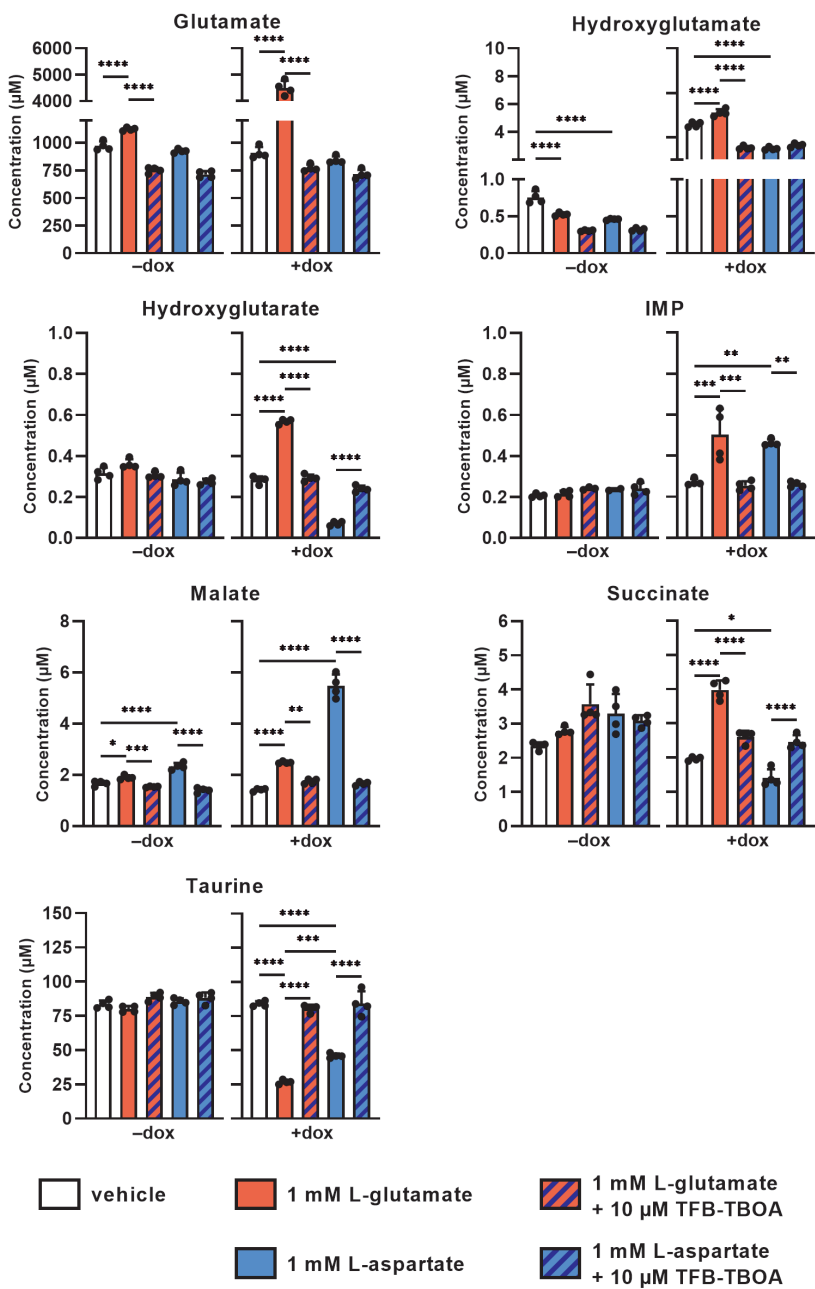


Figure 6.4 – Changes in intracellular metabolite levels upon substrate stimulation of JumpIn-EAAT1 cells. Targeted metabolomics was used to measure the concentrations of several metabolites in the absence (-dox) or presence (+dox) of doxycycline. AMP, adenosine monophosphate; cAMP, cyclic AMP; IMP, inosine monophosphate. Cells were pretreated for 1 h with vehicle (PBS/DMSO, plain bars) or 10 μM TFB-TBOA (hatched bars) prior to stimulation with vehicle (PBS, white bars), 1 mM L-glutamate (red bars) or L-aspartate (blue bars). Data are shown as the mean concentration (in μM) \pm SD of four replicate experiments. * $p < 0.05$, ** $p < 0.01$, *** $p < 0.001$, **** $p < 0.0001$; one-way ANOVA with Tukey's post-hoc test. (see next page)



6.2.5 – MDA-MB-468 cells with endogenous EAAT1 expression show substrate-induced cellular responses

To assess whether EAAT1-mediated cellular responses were not exclusive to JumpIn-EAAT1 cells, we selected two cell lines with high or low endogenous EAAT1 expression. Transcriptomics analyses indicated that the human breast cancer cell line MDA-MB-468 has a high endogenous expression of EAAT1 (BioSamples database: SAMN11893674, SAMN11893681, SAMN11893688), whereas the human astrocytoma cell line (1321N1) lacked endogenous EAAT1 expression (BioSamples database: SAMN11893671, SAMN11893678, SAMN11893685). In line with the expression data, MDA-MB-468 cells showed a gradual and concentration-dependent nCI increase upon stimulation with L-glu ($pEC_{50} = 4.0 \pm 0.2$) that reached a plateau after 180 min (**Figure 6.5a,c**). In contrast,

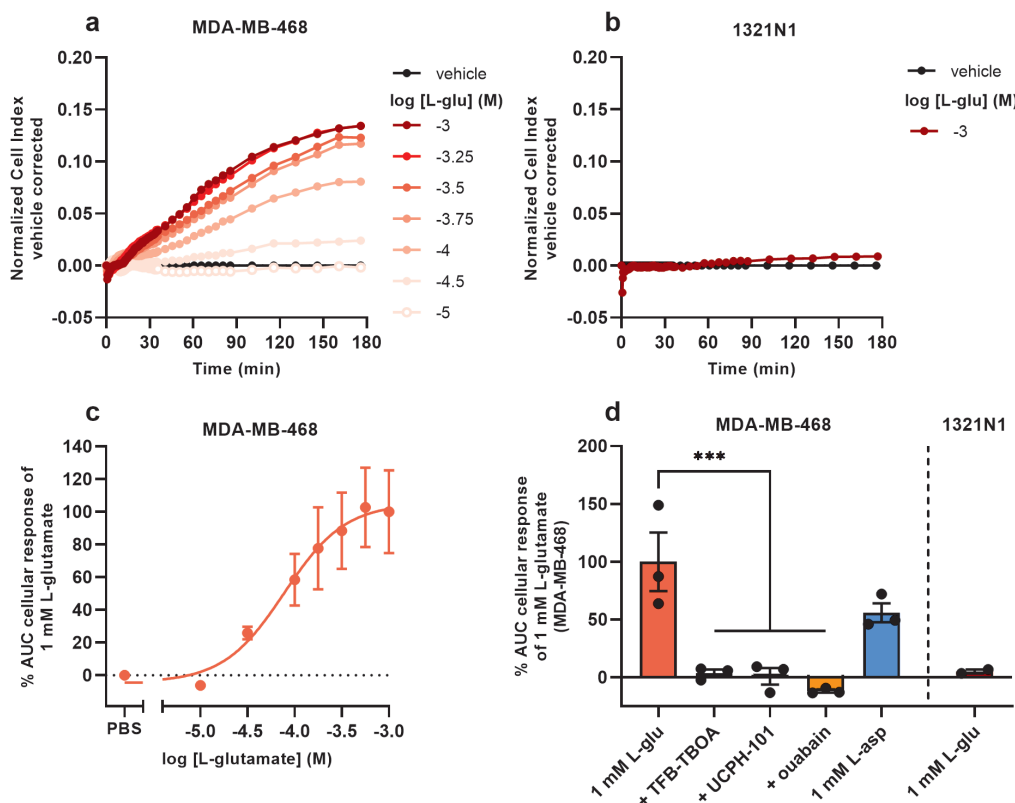
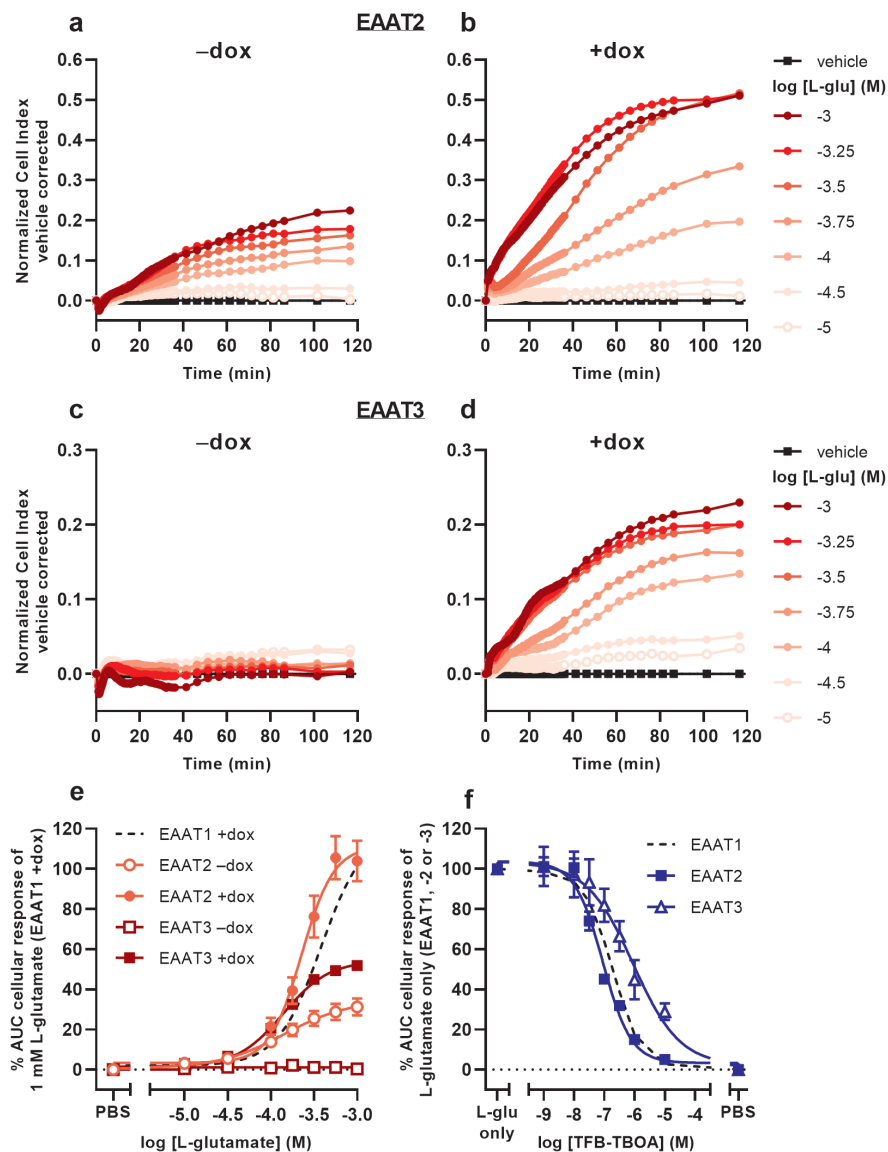


Figure 6.5 – L-glutamate induces cellular responses on MDA-MB-468 cells with endogenous EAAT1 expression. (a,b) Vehicle-corrected nCI traces of MDA-MB-468 (a) and 1321N1 (b) cells stimulated with L-glutamate (L-glu), shown as the mean of a representative experiment performed in duplicate. (c) Combined concentration-response curve of L-glu on MDA-MB-468 cells. (d) Cellular response of L-glu or L-aspartate (L-asp) on MDA-MB-468 and 1321N1 cells. MDA-MB-468 cells were pretreated for 1 h with vehicle (PBS/DMSO), 10 μ M TFB-TBOA, 10 μ M UCPH-101 or 1 μ M ouabain prior to stimulation with vehicle (PBS), 1 mM L-glu or L-asp. Data are shown as the mean \pm SEM of three (MDA-MB-468) or SD of two (1321N1) individual experiments each performed in duplicate. *** $p < 0.001$; one-way ANOVA with Dunnett's post-hoc test.

1321N1 cells did not show a substantial cellular response upon stimulation with 1 mM L-glu within 180 min (**Figure 6.5b,d**). The response of 1 mM L-glu on MDA-MB-468 cells was completely blocked in the presence of 10 μ M TFB-TBOA and 10 μ M UCPH-101, which suggested that the cellular response was EAAT1-mediated (**Figure 6.5d**). Similar to JumpIn-EAAT1 cells the cellular responses were substrate- and Na⁺-dependent, which was demonstrated by an L-asp response and inhibition of the L-glu response by ouabain, respectively. These data suggest that EAAT1 function can be assessed in cells with endogenous EAAT1 expression.



6.2.6 – L-glutamate induces cellular responses via EAAT2 and EAAT3, but not EAAT4 and EAAT5

To investigate whether the phenotypic assay could be used to assess activity of other glutamate transporters, we used JumpIn cell lines with dox-inducible overexpression of EAAT2, EAAT3, EAAT4 and EAAT5 (**Figure 6.6**). Non-induced (–dox) JumpIn-EAAT2 cells responded to L-glu stimulation in a concentration-dependent manner ($pEC_{50} = 3.8 \pm 0.1$), whereas no substantial L-glu response was observed in non-induced JumpIn-

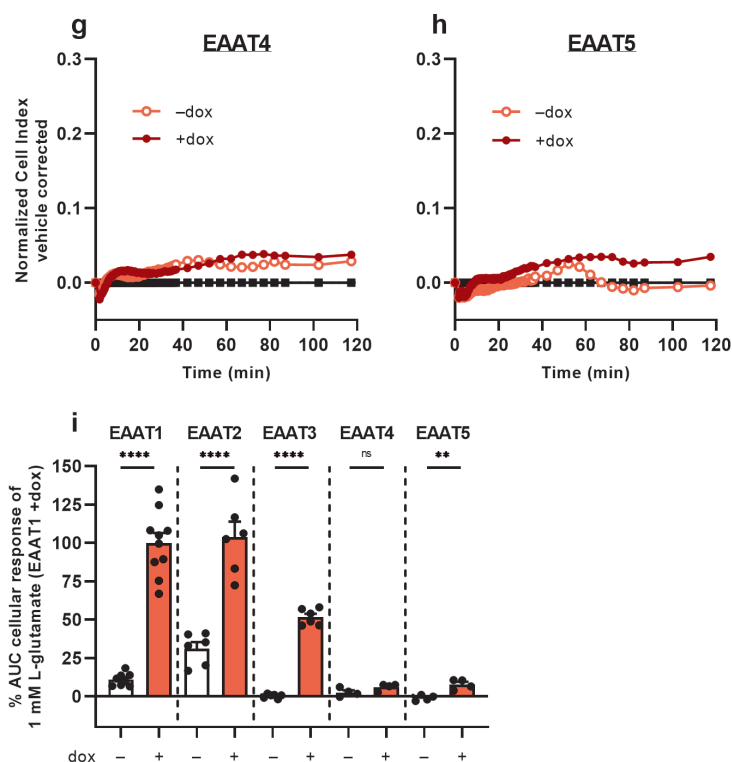


Figure 6.6 – L-glutamate-induced cellular responses on JumpIn-EAAT2 and JumpIn-EAAT3 cells. (**a–d,g,h**) Vehicle-corrected nCi traces of JumpIn-EAAT2 (**a,b**), JumpIn-EAAT3 (**c,d**), JumpIn-EAAT4 (**g**) and JumpIn-EAAT5 (**h**) cells in the absence (–dox) or presence (+dox) of doxycycline stimulated with vehicle (PBS) or L-glutamate (L-glu), shown as the mean of a representative experiment performed in duplicate. (**e**) Combined concentration-response curves of L-glu on JumpIn-EAAT2 and JumpIn-EAAT3 cells (\pm dox). Data are normalized to the response of 1 mM L-glu on JumpIn-EAAT1 +dox cells (data is derived from **Figure 6.2d** and shown as a black dotted line). (**f**) Combined concentration-inhibition curves of TFB-TBOA on +dox JumpIn-EAAT2 and JumpIn-EAAT3 cells pretreated for 1 h with vehicle (PBS/DMSO) or increasing concentrations of TFB-TBOA and subsequently stimulated with a submaximal concentration (316 μ M) of L-glu. Data are normalized to the response of 1 mM L-glu (JumpIn-EAAT1, data is derived from **Figure 6.2e** and shown as a black dotted line) or 316 μ M L-glu (JumpIn-EAAT2 and -EAAT3). (**i**) Cellular response of 1 mM L-glu on –dox and +dox JumpIn cells for all EAAT subtypes. Data on JumpIn-EAAT1, -EAAT2 and -EAAT3 cells were derived from **Figure 6.2d** and **Figure 6.6e**. Cellular response is expressed as the net AUC of the first 120 min after substrate stimulation. Data are shown as the mean \pm SEM of at least three individual experiments each performed in duplicate. ns = not significant, ** $p < 0.01$, **** $p < 0.0001$; unpaired two-tailed Student's t-test.

EAAT3 cells (**Figure 6.6a,c, Table 6.1**). Similar to JumpIn-EAAT1 cells, L-glu induced concentration-dependent nCI increases reaching a plateau after 120 min on dox-induced (+dox) JumpIn-EAAT2 ($pEC_{50} = 3.6 \pm 0.0$) and JumpIn-EAAT3 cells ($pEC_{50} = 3.9 \pm 0.0$) (**Figure 6.6b,d,e, Table 6.1**). The responses of a submaximal concentration (316 μ M) of L-glu could be inhibited in a concentration-dependent manner by TFB-TBOA in JumpIn-EAAT2 ($pIC_{50} = 7.1 \pm 0.0$) and JumpIn-EAAT3 ($pIC_{50} = 6.1 \pm 0.2$) cells, which indicates that the cellular responses were transporter-specific (**Figure 6.6f**).

The L-glu-induced responses in dox-induced JumpIn-EAAT4 (**Figure 6.6g**) and JumpIn-EAAT5 cells (**Figure 6.6h**) were substantially lower than for cells overexpressing EAAT1, EAAT2 or EAAT3 (**Figure 6.6i**). L-glu induced a significantly higher response in dox-induced JumpIn-EAAT5 cells than in non-induced cells ($p = 0.0032$), whereas in JumpIn-EAAT4 this difference was not significant ($p = 0.093$). Immunoblotting of JumpIn-EAAT cell lysates indicates that the relative expression of EAAT4 and EAAT5 was considerably lower than EAAT1, EAAT2 and EAAT3 (**Supplementary Figure 6.S5**), which indicates that the transporter expression level could be related to the magnitude of the cellular response. Taken together, these data confirm that the phenotypic impedance-based assay allows pharmacological assessment of at least three Na^+ -dependent glutamate transporters.

6.3 – Discussion

In recent years the pleas for invigoration of fundamental SLC drug research have led to an ever-growing wealth of innovative molecular tools and technologies that enable functional investigation of transport proteins^{23,36,37}. In efforts to expand the SLC toolbox, we demonstrate a novel method to detect activity of glutamate transporters in living cells without the use of labels or biochemical reporters. Impedance-based biosensors can detect in real-time the temporal cytoskeleton rearrangements that result from GPCR activation in live cells^{38,39}, making this an ideal functional readout. As such, we initially attempted to set up a TRACT assay, as previously reported by our lab^{30–32}, for EAAT1 by using a cell line with inducible overexpression of EAAT1 and transient expression of mGluR₂. However, in the absence of mGluR₂, we observed that JumpIn-EAAT1 cells start spreading as a result of EAAT1-mediated L-glu uptake (**Figure 6.3e**), which was reflected by the increased cellular response in the impedance assay (**Figure 6.2**). This phenotypic response suggests a very different mechanism by which transport activity of EAAT1 can be assessed.

The interpretation of cellular impedance data requires an initial mechanistic understanding of the subcellular events that underlie the major changes in cell morphology as a response to applied external stimuli⁴⁰. Since the cellular response in JumpIn-EAAT1 cells did not arise from GPCR activation in the absence of mGluR₂, we sought to investigate the possible triggers that induced cell spreading. Initially, we hypothesized that increased intracellular levels of L-glu may lead to conversion of L-glu to glutamine or tricarboxylic acid (TCA) cycle intermediates, which could possibly be associated with ATP synthesis and changes in cell morphology⁴¹. However, in line with initial pharmacological characterizations of EAAT1^{4,27}, both L- and D-isomers of glutamate and aspartate induced cellular responses

of comparable magnitude (**Figure 6.3a,b**). Since these substrates have divergent metabolic fates, this suggests that it is unlikely that the cellular response is the result of intracellular substrate metabolism. Indeed, upon stimulation with L-glu or L-asp we observed opposite changes in the levels of the tricarboxylic acid (TCA) cycle intermediates and related metabolites, which either increased (L-glu) or decreased (L-asp) (**Figure 6.4**). This suggests that L-glu and L-asp differentially feed into the TCA cycle⁷ and as such it is unlikely that this metabolic route underlies the observed phenotypic response of both substrates. Interestingly, intracellular aspartate was increased 60-fold upon stimulation with L-asp, but only 5-fold with L-glu. Pathways that are associated with L-asp metabolism, such as purine nucleotide synthesis (AMP, IMP), the urea cycle (AMP, argininosuccinate) and the malate-aspartate shuttle (malate) also showed increased metabolite levels⁴². However, since L-asp induces a slightly lower cellular response in the impedance-based assay compared to L-glu, it is unlikely that these changes in L-asp metabolite levels explain the changes in cell morphology. It should be noted that some metabolite levels (e.g. hydroxyglutamate) could have been altered as a consequence of the presence of doxycycline rather than the induced expression of the transporter, for these types of antibiotics have been reported to induce mitochondrial stress responses⁴³. Nevertheless, any non-specific metabolite changes upon L-glu or L-asp stimulation were identified by the absence of substrate-specific regulation and/or a lack of inhibition by TFB-TBOA. Although metabolomics provides a wealth of information on the intracellular fates of transporter-mediated substrate uptake, we conclude that substrate metabolism is not the main driver behind the substrate-induced cellular responses.

As such, we ascribed the cellular responses to the initial changes in intracellular ionic concentrations and cell volume following EAAT-mediated substrate uptake. The continuous Na^+ -driven uptake of substrate *via* EAAT leads to an accumulation of intracellular Na^+ and substrate with release of 1 K^+ with each transport cycle. The Na^+ gradient-restoring activity of NKA leads to subsequent elevation of intracellular K^+ ⁴⁴. The net increase of the intracellular positive charges with each transport cycle is compensated by the influx of Cl^- *via* the uncoupled anion conductance of EAAT or other Cl^- -coupled transporters⁴⁵, which leads to an increased osmolarity that evokes water flux into the cytosol and causes cell swelling^{46,47}. The resulting cell volume increase causes the formation of membrane protrusions that extend towards regions with high extracellular substrate concentrations (**Figure 6.3e**), commencing a transmembrane ionic cycle that drives cell swelling and spreading at the leading edges of the cell membrane similar to a migrating cell^{48,49}. It should be noted that we did not measure the actual swelling of the cells in this chapter, and as such the specific contribution of cell swelling to the observed cellular responses remains to be experimentally verified. Nevertheless, our hypothesis is in agreement with previous reports of glutamate- and aspartate-induced cell swelling in astrocytes^{50–56}, which have related swelling to EAAT-mediated cytosolic accumulation of Na^+ , K^+ and Cl^- ions. In line with this, inhibition of NKA by ouabain disrupts the Na^+ gradient across the membrane and prevents substrate uptake and cellular responses *via* EAAT (**Figure 6.3d**). However, reduced NKA activity does not block, but may rather enhance the Cl^- conductance of EAAT⁵⁷. Thus, it is likely that the entry of large quantities of Na^+ *via* EAAT upon substrate

stimulation, and not primarily the uncoupled Cl^- flux, is the major trigger for cell volume changes and subsequent cell spreading.

To compensate for increased osmolarity, high intracellular ion levels are eventually dissipated *via* the release of K^+ and Cl^- as well as organic osmolytes through volume-sensitive channels^{46,58}. Indeed, in L-glu- and L-aspartate-stimulated JumpIn-EAAT1 cells we observed a significant decrease of the intracellular concentration of taurine (**Figure 6.4**), which is an osmolyte that is released in response to cell swelling to decrease cell volume^{47,59}. In addition to increased osmolarity, cell swelling is accompanied by increased cytosolic Ca^{2+} concentrations, which together with mechanical cell stress evoke the release of adenosine triphosphate (ATP) from the cell^{60,61}. Autocrine activation of metabotropic P2Y purinergic receptors by ATP can in turn lead to increased cytosolic cyclic AMP (cAMP) levels, further Ca^{2+} elevations, activation of Ca^{2+} -dependent K^+ and Cl^- channels, cytoskeleton remodeling and increased efflux of Cl^- and taurine *via* volume-regulated anion channels (VRAC)^{53,62–64}. Of note, we observed significant elevations of cAMP levels in JumpIn-EAAT1 cells upon stimulation with L-glu and L-aspart (**Figure 6.4**), which suggests that GPCR activation is involved in the cellular response⁶⁴. In general, reorganization of the actin cytoskeleton is a common consequence of cell volume regulation and the mechanisms driving these

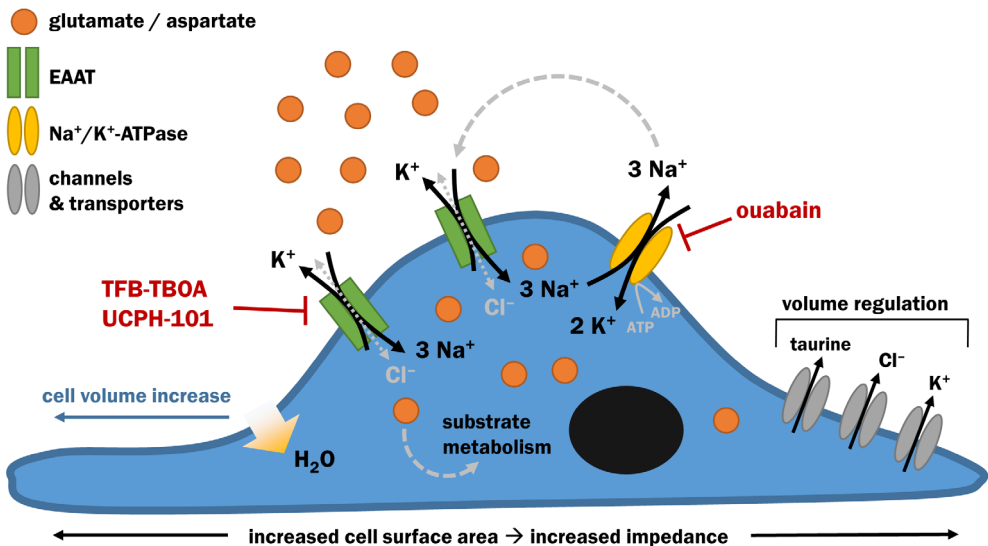


Figure 6.7 – Proposed mechanism of the phenotypic impedance-based assay. Cells (over)expressing excitatory amino acid transporters (e.g., EAAT1) are stimulated with exogenous substrate (e.g., glutamate). The substrate is taken up into the cell through EAAT together with 3 Na^+ in exchange for 1 K^+ . Cl^- enters the cells *via* uncoupled Cl^- -conductivity of EAAT or other Cl^- influx mechanisms, counterbalancing the increase in intracellular Na^+ . The Na^+/K^+ -ATPase (NKA) restores the transmembrane Na^+ gradient by ATP-dependent efflux of 3 Na^+ in exchange for 2 K^+ . Over time, the intracellular concentrations of substrate, Na^+ , K^+ and Cl^- ions initially rise, increasing cell osmolarity. Subsequent cell swelling, *via* influx of H_2O into the cytosol, triggers cell spreading, which increases the surface area of the E-plate that is covered by cells. Regulatory mechanisms lead to dissipation of the high intracellular ion concentrations *via* channels and/or transporters that mediate efflux of Cl^- , K^+ and osmolytes such as taurine, effectively reducing cell volume over time.

events have been extensively described in literature^{47,60,62,65–67}. Based on our observations, we conclude that the phenotypic responses in the impedance assay are likely initiated by EAAT-mediated cell swelling (**Figure 6.7**).

The phenotypic assay was used to assess functionality of various EAAT subtypes in overexpressing cells, as well as EAAT1 function in cells endogenously expressing the transport protein. Interestingly, the potencies of L-glu for EAAT1–3 that we found in the phenotypic assay were substantially lower than the reported steady-state affinities (K_m) of L-glu (around 20 μ M) for these transporters^{4,68}. It should be noted that the impedance-based method does not provide information on uptake kinetics, as it is not a direct measure of substrate uptake and as such the potencies found here should be compared to literature with caution. Nevertheless, a high transporter density has been shown to affect the buffering capacity of the substrate, resulting in a reduced affinity for the substrate⁶⁹. Indeed, dox-induced JumpIn-EAAT1 cells had a lower L-glu potency than MDA-MB-468 cells with endogenous EAAT1 expression, likely due to a higher transporter density in the former cell line. Of note, a higher L-glu potency was observed in non-induced JumpIn-EAAT cells, which could indicate low levels of endogenous EAAT or “leaky” heterologous transporter expression in the absence of dox⁷⁰, although this was not apparent from Western blots of –dox cell lysates (**Supplementary Figure 6.S5**). Moreover, the differences in L-glu potency between EAAT1–3 could be attributed to their dissimilar substrate turnover rate, which is 2- to 10-fold higher for EAAT3 than EAAT2 and EAAT1, respectively⁷¹. Besides discrepancies in L-glu potency, we also observed a difference in the maximal response of L-glu between the various EAAT subtypes (**Figure 6.6i**). A likely explanation for the lack of a specific L-glu response for EAAT4 and EAAT5 is the poor expression of these subtypes compared to EAAT1–3, although a small fraction of these transporters appears to be expressed (**Supplementary Figure 6.S5**). Alternatively, the absence of a substantial substrate responses for EAAT4 and EAAT5 may be related to slow turnover rates⁷¹ and their predominant chloride conductivity function^{5,72,73}.

One of the applications of the phenotypic assay is to screen for potential EAAT modulators. We have validated the EAAT specificity of the substrate-induced cellular response by using TFB-TBOA and UPCH-101, which are widely used tool compounds for EAATs^{13,14}. Strikingly, the inhibitory potency values that were found in the cell swelling assay were roughly 10-fold lower than in radioligand uptake assays^{13,14,74}. Although these assays use different readouts, one explanation for this discrepancy might be the high competing concentrations of substrate in the cell swelling assay, which are 100–10,000 times higher than in radioligand uptake assays²⁶. Alternatively, dox-induced overexpression of EAATs could create a pool of “spare” transporters on the plasma membrane that effectively buffers the extracellular concentration of inhibitor, resulting in a rightward shift of the concentration-inhibition curve and a lower apparent inhibitory potency⁷⁵. Although the transporter expression levels and substrate concentrations should be thoroughly considered in further assay development, our impedance-based assay showed a robust window for the detection of transporter inhibitors.

In summary, this chapter presents a novel application of a label-free biosensor to study function and pharmacology of a transport protein family. It provides an alternative to existing radioactive- or fluorescence-based methods and opens up new venues to study other Na⁺-coupled transporters or, in fact, any transporter of which the activity is intrinsically linked to cytoskeletal changes upon perturbation. In addition, we demonstrated that this method is sensitive enough to detect EAAT1 activity in an endogenous cell line, which could further expand the possibilities to investigate disease-relevant cell lines. Moreover, a semi-manual HTS validation demonstrates an “excellent” assay window³⁵, which renders this phenotypic assay applicable for drug discovery screens. Ultimately, this method is a novel addition to the continuously expanding drug discovery toolbox for SLC transporters.

6.4 – Materials & methods

6.4.1 – Chemicals and reagents

Jump In T-REx HEK 293 (JumpIn) overexpressing human EAAT1/2/3/4/5 (see **section 6.4.2**), MDA-MB-468 and 1321N1 cells were kindly provided by the RESOLUTE consortium (Research Center for Molecular Medicine, Medical University of Vienna, Austria). L-glutamic acid monosodium salt monohydrate (L-glu), L-aspartic acid monosodium salt monohydrate (L-asp), D-glutamic acid (D-glu), D-aspartic acid (D-asp), doxycycline hyclate and ouabain octahydrate were purchased from Sigma Aldrich (St. Louis, MO, USA). 2-amino-4-(4-methoxyphenyl)-7-(naphthalen-1-yl)-5-oxo-5,6,7,8-tetrahydro-4H-chromene-3-carbonitrile (UCPH-101) was purchased from Santa Cruz Biotechnology (Dallas, TX, USA). (2S,3S)-3-[3-[4-(trifluoromethyl)benzoylamino]benzyloxy] aspartate (TFB-TBOA) was purchased from Axon Medchem (Groningen, The Netherlands). (2S)-2-amino-2-[(1S,2S)-2-carboxycycloprop-1-yl]-3-(xanth-9-yl) propanoic acid (LY341495) was purchased from Cayman Chemical (Ann Arbor, MI, USA). xCELLigence PET E-plates 96 (ACEA Biosciences, San Diego, CA, USA) were purchased from Bioké (Leiden, The Netherlands). cDNA encoding the human metabotropic glutamate receptor 2 (GRM2, ORF: NM_000839) containing an N-terminal FLAG-tag cloned in a pcDNA3.1(+) plasmid (mGluR₂ cDNA), as well as empty pcDNA3.1(+) plasmid (mock cDNA) were purchased from GenScript (Piscataway, NJ, USA). The lentiviral GFP-LifeAct cDNA expression vector was provided by Dr. Olivier Pertz (University of Basel, Basel, Switzerland). Puromycin was purchased from Acros Organics/Fisher Scientific (Landsmeer, The Netherlands). PNGaseF was purchased from New England Biolabs (Ipswich, MA, USA). Pierce ECL Western blotting substrate was purchased from Thermo Fisher Scientific (Waltham, MA, USA). All other chemicals were of analytical grade and obtained from standard commercial sources.

6.4.2 – *JumpIn-EAAT cell line generation*

JumpIn cells with doxycycline (dox)-inducible transgene overexpression were generated for either one of the five human EAAT subtypes by the RESOLUTE consortium. JumpIn cells were cultured and transfected as described previously^{31,32}. In short, cells were cultured in culture medium supplemented with 200 µg/ml hygromycin B and 5 µg/ml blasticidin.

For transfection, a codon-optimized ORF for either human EAAT1 (*SLC1A3*, Addgene #131889), EAAT2 (*SLC1A2*, Addgene #131901), EAAT3 (*SLC1A1*, Addgene #131878), EAAT4 (*SLC1A6*, Addgene #131986) or EAAT5 (*SLC1A7*, Addgene #131998) was cloned into a Gateway-compatible pJTI R4 DEST CMV TO pA expression vector with a C-terminal Twin-Strep-tag followed by an HA-tag. Successfully transfected cells were selected in culture medium supplemented with 2 mg/ml geneticin (G418) and 5 µg/ml blasticidin and were subsequently pooled for use in further experiments. Expression of the transgene was induced by incubating the cells for 24 h in presence of 1 µg/ml dox.

6.4.3 – Cell culture

JumpIn-EAAT cells were cultured as adherent cells in high glucose Dulbecco's Modified Eagle's Medium (DMEM) containing 10% (v/v) fetal calf serum (FCS), 2 mM Glutamax, 100 IU/ml penicillin and 100 µg/ml streptomycin (culture medium) at 37 °C and 5% CO₂. Cells were thawed and split for 1–2 passages in culture medium before switching to selection medium (culture medium supplemented with 2 mg/ml G418 and 5 µg/ml blasticidin) for up to one week. Subsequently, the cells were maintained in culture medium at least 24 h prior to performing an experiment. Cells were split twice weekly at 1:8 – 1:16 ratios in 10 cm culture dishes.

MDA-MB-468 cells were cultured as adherent cells in DMEM containing 10% (v/v) FCS, 2 mM Glutamax, 100 IU/ml penicillin and 100 µg/ml streptomycin (culture medium) at 37 °C and 5% CO₂. Cells were split twice weekly at 1:3 – 1:4 ratios in 10 cm culture dishes.

6.4.4 – Transient transfection of JumpIn-EAAT1 cells

JumpIn-EAAT1 cells were transiently transfected using 25 kDa linear polyethyleneimine (PEI) as a transfection reagent⁷⁶. Cells were split in 10 cm dishes to achieve ~60% confluence on the day of transfection. A mix of 7.5 µg/ml PEI and 2.5 µg total cDNA (mock or mGluR₂) in 1 ml Opti-MEM was incubated at room temperature for 30 min. Subsequently, cells were refreshed in penicillin/streptomycin-free culture medium before adding the PEI:DNA mix to each dish. Cells were incubated for 24 h at 37 °C and 5% CO₂ prior to use in the TRACT assay.

6.4.5 – JumpIn-EAAT1-LifeAct-GFP cell line generation

For visualization of the actin cytoskeleton, JumpIn-EAAT1 cells were transduced with a lentiviral GFP-LifeAct cDNA expression vector and were maintained in culture medium containing 2 µg/ml puromycin to select for successfully transduced cells.

6.4.6 – xCELLigence assays

6.4.6.1 – General

Label-free whole-cell assays, based on cell-induced changes in impedance, were performed using the xCELLigence real-time cell analyzer (RTCA) system (ACEA Biosciences, San Diego, CA, USA) as described previously^{30–32}. In short, cells are cultured in medium on gold-

plated electrodes in microwell E-plates. Per well impedance is continuously measured at 10 kHz and is converted to the unitless parameter Cell Index (CI) by the following formula:

$$CI = \frac{(Z_i - Z_0)\Omega}{15\Omega}$$

where Z_i is the impedance at any given time point and Z_0 is the baseline impedance measured at the start of each experiment⁴⁰.

Assays were performed at 37 °C and 5% CO₂ in 96-well PET E-plates in a total volume of 100 µl per well. Prior to cell seeding, the baseline impedance (Z_0) was measured in the recording station in 40 µl (two compound additions) or 45 µl (one compound addition) medium in the presence (+) or absence (–) of 1 µg/ml dox. All compounds were diluted in phosphate-buffered saline (PBS) and added in 5 µl per addition using a VIAFLO 96 handheld electronic 96 channel pipette (INTEGRA Biosciences, Tokyo, Japan). When DMSO was used as a solvent for a compound, the final amount of DMSO was kept at 0.1% per well and was included in the vehicle (PBS/DMSO). All conditions were tested at two technical replicates per plate.

6.4.6.2 – Assay procedures

On the day of the experiment, JumpIn-EAAT cells grown to 70–80% confluence were trypsinized (0.25% trypsin in PBS/EDTA), counted and seeded in the E-plate in a volume of 50 µl at 60,000 cells/well. Transiently transfected JumpIn-EAAT1 cells were detached using only PBS/EDTA. The E-plate was left to rest at room temperature for 30 min prior to replacement in the recording station at 37 °C and 5% CO₂. Cell growth was recorded overnight for 22 hr. If a pretreatment was required for the experiment, the cells were pretreated after 22 h with either a concentration of inhibitor or vehicle (PBS/DMSO) and cells were monitored for 60 min. For GPCR antagonist experiments, a maximum concentration of LY341495 (1 µM) was used. For EAAT inhibition experiments increasing concentrations (1 nM – 10 µM) of UCPH-101 and TFB-TBOA were used. After the pretreatment, cells were stimulated with substrate or vehicle (PBS). For GPCR antagonist and EAAT inhibition experiments, cells were stimulated with a submaximal concentration of L-glu, i.e. 100 µM L-glu with mGluR₂ antagonist, 1 mM L-glu for EAAT1 inhibition and 316 µM L-glu for EAAT2 and EAAT3 inhibition. After stimulation the impedance was measured for at least 2 h. Following each experiment, the cells were washed from the E-plates using sterile H₂O and 70% ethanol and the plates were sterilized for 1 h under UV light^{77,78}. Properly washed plates were re-used up to two times.

6.4.6.3 – HTS validation

The impedance-based phenotypic assay for JumpIn-EAAT1 cells was assessed for reproducibility and robustness in a semi-manual high-throughput screening (HTS) validation as described previously³². Briefly, three 96-well E-plates were run consecutively on one day for three days in a row. Each plate consisted of alternating columns of wells producing a high, mid or low signal, which were JumpIn-EAAT1 cells pretreated with either vehicle

(PBS/DMSO), 0.2 μM or 10 μM TFB-TBOA, respectively. After 1 h pretreatment, cells were stimulated with 1 mM L-glutamate. The assay procedure was the same as for the regular xCELLigence assays.

6.4.7 – Automated microscopy

JumpIn-EAAT1-LifeAct-GFP cells were seeded at 20,000 cells/well on a SCREENSTAR black-walled clear-bottom 96-well culture plate in 90 μL culture medium and grown for 24 h at 37 °C and 5% CO_2 . Cells were pretreated for 1 h with PBS/DMSO and subsequently stimulated with vehicle (PBS) or 1 mM L-glutamate upon which cells were immediately imaged using automated microscopy. Microscopy was performed on a Nikon Eclipse Ti2 C2+ confocal microscope (Nikon, Amsterdam, The Netherlands). This system was equipped with a 37 °C incubation chamber, an automated xy-stage, an integrated Perfect Focus System (PFS) and 408, 488 and 561 nm lasers. The system was controlled by Nikon's NIS software. All images were acquired using a Plan-Apochromat 20x objective with 0.75 NA, at a resolution of 512x512 pixels.

6.4.8 – Targeted metabolomics

6.4.8.1 – Metabolite extraction

JumpIn-EAAT1 cells were plated at 150,000 cells/well in 24 well poly-L-lysine coated plates in culture medium in the absence (–dox) or presence (+dox) of 1 $\mu\text{g/mL}$ doxycycline and grown at 37°C and 5% CO_2 . After 24h, the medium was refreshed and cells were pretreated with vehicle (PBS/DMSO) or 10 μM TFB-TBOA. After 1 h pretreatment, cells were stimulated for 2 h with vehicle (PBS) or 1 mM L-glutamate or L-aspartate. For lysis, cells were first gently washed with room temperature bicarbonate buffer (91 mM NH_4HCO_3 , pH 7.4). Then, cells were transferred to ice where 300 μL /well of ice-cold 80:20 MeOH:H₂O containing a mixture of isotopically labeled internal standards (Metabolite Yeast Extract (U-13C, 98%), ISOTopic Solutions, Vienna, Austria) was added to each well. The cells were then scraped and transferred to a pre-cooled Eppendorf tube and immediately snap frozen in liquid nitrogen. Samples were thawed on ice before being centrifuged at 16,000 $\times g$ for 10 min at 4°C. The clarified metabolite-containing supernatants were moved into a high-performance liquid chromatography vial and stored at –80°C until LC-MS/MS analysis.

6.4.8.2 – LC-MS/MS analysis

Cell extracts were dried using a nitrogen evaporator. The dry residue was reconstituted in 16 μL H₂O and 4 μL of sample extract was used for LC-MS/MS analysis. A 1290 Infinity II UHPLC system (Agilent Technologies) coupled to a 6470 triple quadrupole mass spectrometer (Agilent Technologies) was used for the LC-MS/MS analysis. The chromatographic separation for samples was carried out on a ZORBAX RRHD Extend-C18, 2.1 \times 150 mm, 1.8 μm analytical column (Agilent Technologies). The column was maintained at a temperature of 40 °C and 4 μL of sample was injected per run. The mobile phase A was 3% MeOH (v/v), 10 mM tributylamine, 15 mM acetic acid in H₂O, and mobile phase B was 10 mM tributylamine, 15 mM acetic acid in MeOH. The gradient elution with a flow rate

0.25 mL/min was performed for a total time of 24 min. Afterward, a back flushing of the column using a 6 port 2-position divert valve was carried out for 8 min using acetonitrile, followed by 8 min of column equilibration with 100% mobile phase A. The triple quadrupole mass spectrometer was operated in an electrospray ionization negative mode, spray voltage 2 kV, gas temperature 150 °C, gas flow 1.3 L/min, nebulizer 45 psi, sheath gas temperature 325 °C, and sheath gas flow 12 L/min. The metabolites of interest were detected using a dynamic Multiple Reaction Monitoring (MRM) mode. The MassHunter 10.0 software (Agilent Technologies) was used for the data processing. Ten-point linear calibration curves with internal standardization were constructed for the quantification of metabolites.

6.4.9 – Western blot analysis

JumpIn-EAAT cells were grown at 1×10^6 cells/well on a 6-well culture plate for 24 h in the presence or absence of 1 µg/ml doxycycline at 37 °C and 5% CO₂. Cells were lysed in lysis buffer (50 mM HEPES (pH 7.4), 250 mM NaCl, 5 mM EDTA, 1% NP-40, 1 tablet complete EDTA-free protease inhibitor cocktail (Roche) per 50 ml) for 30 min on ice and centrifuged at 20,800 x g, 4 °C for 15 min. Protein concentration was measured using the bicinchoninic acid (BCA) protein assay⁷⁹. Lysates were either treated or not treated with PNGaseF overnight at 37 ° and samples were subsequently denatured and separated by SDS-PAGE, then transferred to nitrocellulose membranes. The membranes were blocked in 5% milk + TBS-T for 1 h and cut at 25 kDa. The top membranes (>25 kDa) were incubated with horse radish peroxidase (HRP)-conjugated anti-HA-7 (Sigma, H6533, 1:7000) and bottom membranes (<25 kDa) with cyclophilin B antibody (Abcam, ab178397, 1:5000) in 5% milk + TBS-T overnight at 4 °C. The bottom membrane was subsequently incubated with HRP-conjugated anti-rabbit IgG (Jackson ImmunoResearch, 111-035-003, 1:5000) in 5% milk + TBS-T for 1 h at 4 °C. Both membranes were visualized using Pierce ECL substrate.

6.4.10 – Data analysis

6.4.10.1 – xCELLigence

Experimental data was recorded using RTCA Software v2.0 or v2.1.1 (ACEA Biosciences). In the RTCA Software CI values were normalized to the time point prior to substrate/agonist stimulation resulting in normalized Cell Index (nCI) values. The nCI data were exported and subsequent analyses and data visualizations were done using GraphPad Prism v9 (GraphPad Software, San Diego, CA, USA). In all experiments, nCI values of vehicle-only conditions were subtracted from all other conditions to correct for vehicle-induced, substrate-independent effects. The resulting nCI responses were quantified by taking the net area under the curve (AUC) of the first 120 min after substrate/agonist stimulation, unless stated otherwise. The potency values of substrates and inhibitory potencies of EAAT inhibitors were determined by fitting the net AUC data to a sigmoidal concentration-effect curve with a variable slope.

6.4.10.2 – HTS validation

For intra-plate variability tests, the net AUC of non-corrected nCI values were used to determine the signal window (SW, indicating dynamic range of the signal) using the following formula³⁴:

$$SW = \frac{\left(AVG_{high} - \frac{3SD_{high}}{\sqrt{n}} \right) - \left(AVG_{low} + \frac{3SD_{low}}{\sqrt{n}} \right)}{\frac{SD_{high}}{\sqrt{n}}}$$

where n is the number of technical replicates per compound in the intended screening assay (e.g., for duplicate measurements $n = 2$), AVG is the average and SD is the standard deviation of the AUC of the high or low signal. Similarly, the Z' factor (Z' , indicating separation of the high and low signals) is calculated using the following formula^{34,35}:

$$Z' = \frac{\left(AVG_{high} - \frac{3SD_{high}}{\sqrt{n}} \right) - \left(AVG_{low} + \frac{3SD_{low}}{\sqrt{n}} \right)}{(AVG_{high} - AVG_{min})}$$

The reported SW and Z' are the mean \pm SEM of all nine E-plates. According to Iversen *et al.*³⁴, the recommended acceptance criterion for an HTS amenable assay is a $SW \geq 2$ or $Z' \geq 0.4$.

6.4.10.3 – Targeted metabolomics

Volcano plots were generated to visualize the significant up- or downregulation of intracellular metabolite concentrations. The log₂ fold change upon substrate addition is plotted against the $-\log_{10}$ adjusted p-value. A Benjamini-Hochberg correction⁸⁰ was used to reduce the false discovery rate to obtain the adjusted p-value.

6.4.10.4 – Statistics

Data are shown as mean \pm standard error of the mean (SEM) of at least three separate experiments each performed in duplicate, unless stated otherwise. Significant difference between two mean potency values was determined by an unpaired two-tailed Student's t-test. Comparison of multiple mean values to each other or a vehicle control was done using a one-way ANOVA with Tukey's post-hoc test or Dunnett's post-hoc test, respectively. Comparison of multiple mean values between two data sets was done using a two-way ANOVA with Šídák's post-hoc test. Differences were considered statistically significant when p-values were below 0.05.

References

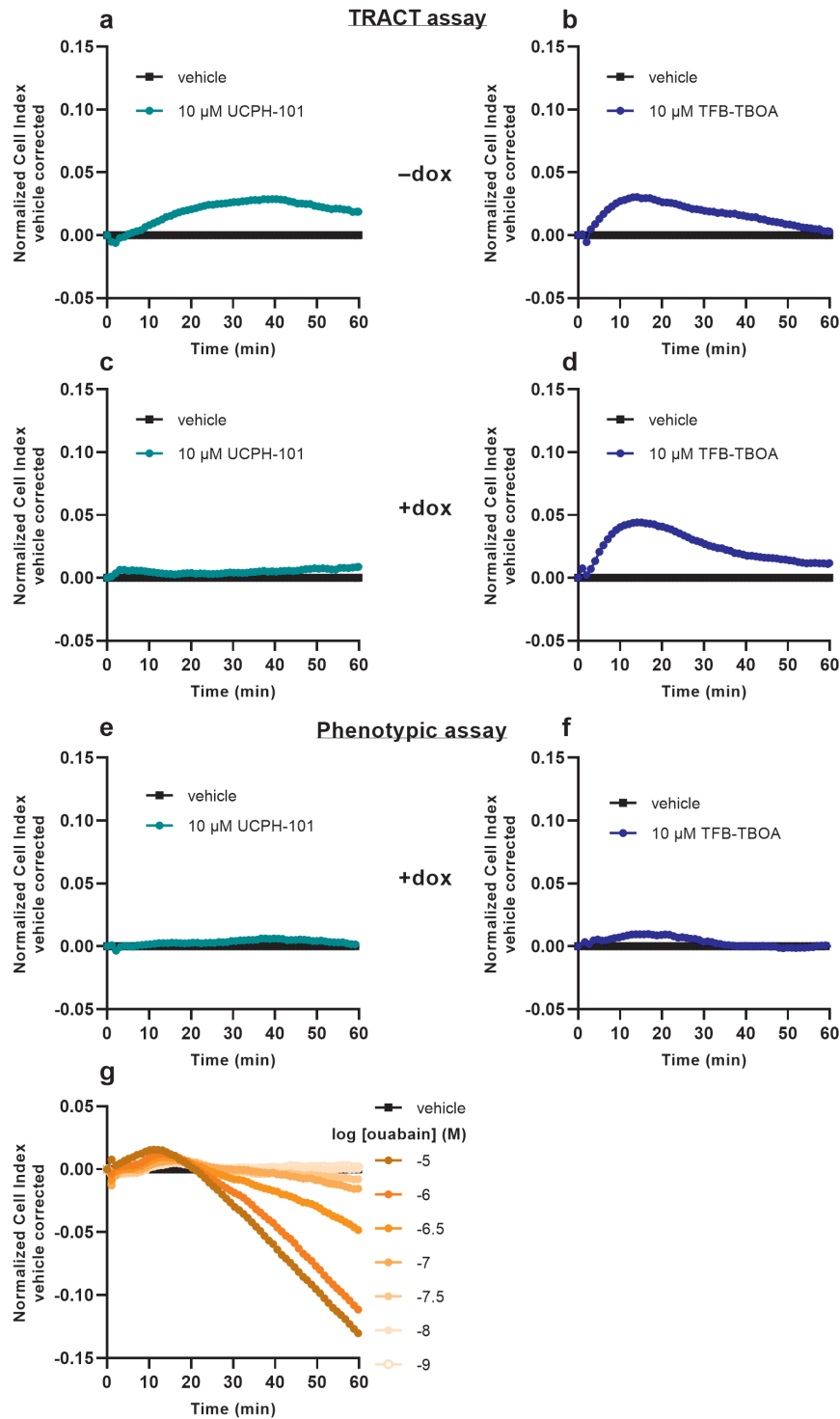
1. Danbolt, N. C. (2001) Glutamate uptake. *Prog. Neurobiol.* **65**, 1–105.
2. Zhou, Y. & Danbolt, N. C. (2013) GABA and glutamate transporters in brain. *Front. Endocrinol. (Lausanne)*. **4**, 1–14.
3. Martínez-Lozada, Z. & Ortega, A. (2015) Glutamatergic transmission: A matter of three. *Neural Plast.* **2015**, 1–11.
4. Arriza, J. *et al.* (1994) Functional comparisons of three glutamate transporter subtypes cloned from human motor cortex. *J. Neurosci.* **14**, 5559–5569.
5. Fairman, W. A., Vandenberg, R. J., Arriza, J. L., Kavanaugh, M. P. & Amara, S. G. (1995) An excitatory amino-acid transporter with properties of a ligand-gated chloride channel. *Nature* **375**, 599–603.
6. Arriza, J. L., Eliassof, S., Kavanaugh, M. P. & Amara, S. G. (1997) Excitatory amino acid transporter 5, a retinal glutamate transporter coupled to a chloride conductance. *Proc. Natl. Acad. Sci.* **94**, 4155–4160.
7. Andersen, J. V. *et al.* (2021) Glutamate metabolism and recycling at the excitatory synapse in health and neurodegeneration. *Neuropharmacology* **184**, 108719.
8. Li, X., Wang, W., Yan, J. & Zeng, F. (2021) Glutamic acid transporters: Targets for neuroprotective therapies in parkinson's disease. *Front. Neurosci.* **15**, 678154.
9. Peterson, A. R. & Binder, D. K. (2020) Astrocyte glutamate uptake and signaling as novel targets for antiepileptogenic therapy. *Front. Neurol.* **11**, 1006.
10. Parkin, G. M., Udawela, M., Gibbons, A. & Dean, B. (2018) Glutamate transporters, EAAT1 and EAAT2, are potentially important in the pathophysiology and treatment of schizophrenia and affective disorders. *World J. Psychiatry* **8**, 51–63.
11. Lang, U. E. & Borgwardt, S. (2013) Molecular mechanisms of depression: perspectives on new treatment strategies. *Cell. Physiol. Biochem.* **31**, 761–777.
12. Dunlop, J. *et al.* (2005) Characterization of novel aryl-ether, biaryl, and fluorene aspartic acid and diaminopropionic acid analogs as potent inhibitors of the high-affinity glutamate transporter EAAT2. *Mol. Pharmacol.* **68**, 974–982.
13. Shimamoto, K. *et al.* (2004) Characterization of novel L-threo- β -Benzyloxyaspartate derivatives, potent blockers of the glutamate transporters. *Mol. Pharmacol.* **65**, 1008–1015.
14. Jensen, A. A. *et al.* (2009) Discovery of the first selective inhibitor of excitatory amino acid transporter subtype 1. *J. Med. Chem.* **52**, 912–915.
15. Mahmoud, S., Gharagozloo, M., Simard, C. & Gris, D. (2019) Astrocytes maintain glutamate homeostasis in the CNS by controlling the balance between glutamate uptake and release. *Cells* **8**, 184.
16. Rossi, D. J., Oshima, T. & Attwell, D. (2000) Glutamate release in severe brain ischaemia is mainly by reversed uptake. *Nature* **403**, 316–321.
17. Winter, N., Kovermann, P. & Fahlke, C. (2012) A point mutation associated with episodic ataxia 6 increases glutamate transporter anion currents. *Brain* **135**, 3416–3425.
18. Kovermann, P. *et al.* (2020) Increased glutamate transporter-associated anion currents cause glial apoptosis in episodic ataxia 6. *Brain Commun.* **2**, 1–17.
19. Adamczyk, A. *et al.* (2011) Genetic and functional studies of a missense variant in a glutamate transporter, SLC1A3, in Tourette syndrome. *Psychiatr. Genet.* **21**, 90–97.
20. Fontana, A. C. K. K. (2015) Current approaches to enhance glutamate transporter function and expression. *J. Neurochem.* **134**, 982–1007.
21. Kortagere, S. *et al.* (2018) Identification of novel allosteric modulators of glutamate transporter EAAT2. *ACS Chem. Neurosci.* **9**, 522–534.
22. Wu, P., Björn-Yoshimoto, W. E., Staudt, M., Jensen, A. A. & Bunch, L. (2019) Identification and structure–activity relationship study of imidazo[1,2-a]pyridine-3-amines as first selective inhibitors of excitatory amino acid transporter subtype 3 (EAAT3). *ACS Chem. Neurosci.* **10**, 4414–4429.
23. Dvorak, V. *et al.* (2021) An overview of cell-based assay platforms for the solute carrier family of transporters. *Front. Pharmacol.* **12**, 1–31.
24. Krause, R., Watzke, N., Kelety, B., Dörner, W. & Fendler, K. (2009) An automatic electrophysiological assay for the neuronal glutamate transporter mEAAC1. *J. Neurosci. Methods* **177**, 131–141.
25. Qiu, B., Matthies, D., Fortea, E., Yu, Z. & Boudker, O. (2021) Cryo-EM structures of excitatory amino acid transporter 3 visualize coupled substrate, sodium, and proton binding and transport. *Sci. Adv.* **7**, eabf5814.
26. Fontana, A. C. K. (2018) Protocols for measuring glutamate uptake: dose-response and kinetic assays in *in vitro* and *ex vivo* systems. *Curr. Protoc. Pharmacol.* **82**, 1–26.
27. Jensen, A. A. & Bräuner-Osborne, H. (2004) Pharmacological characterization of human excitatory amino acid transporters EAAT1, EAAT2 and EAAT3 in a fluorescence-based membrane potential assay. *Biochem. Pharmacol.* **67**, 2115–2127.
28. Armbruster, M., Dulla, C. G. & Diamond, J. S. (2020) Effects of fluorescent glutamate indicators on neurotransmitter diffusion and uptake. *Elife* **9**, 1900–1930.

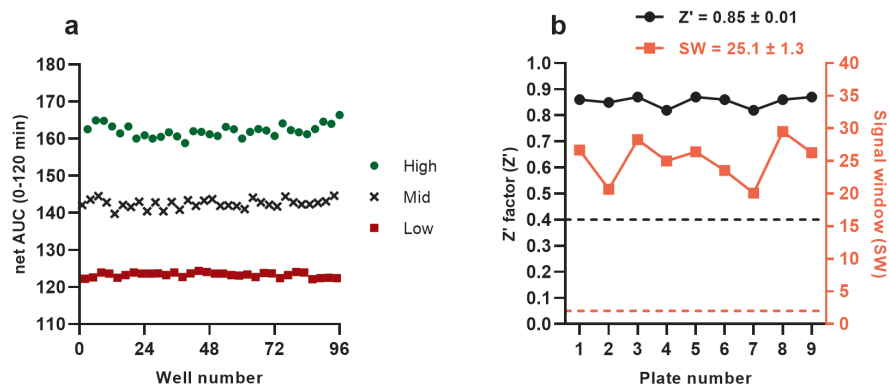
29. Zielewicz, L. & Grever, C. (2019) Genetically encoded halide sensor-based fluorescent assay for rapid screening of glutamate transport and inhibition. *ACS Sensors* **4**, 2358–2366.
30. Vlachodimou, A., IJzerman, A. P. & Heitman, L. H. (2019) Label-free detection of transporter activity via GPCR signalling in living cells: a case for SLC29A1, the equilibrative nucleoside transporter 1. *Sci. Rep.* **9**, 13802.
31. Sijben, H. J., van den Berg, J. J. E., Broekhuis, J. D., IJzerman, A. P. & Heitman, L. H. (2021) A study of the dopamine transporter using the TRACT assay, a novel in vitro tool for solute carrier drug discovery. *Sci. Rep.* **11**, 1312.
32. Sijben, H. J. *et al.* (2021) Label-free high-throughput screening assay for the identification of norepinephrine transporter (NET/SLC6A2) inhibitors. *Sci. Rep.* **11**, 12290.
33. Lundstrom, K. (2017) Cell-impedance-based label-free technology for the identification of new drugs. *Expert Opin. Drug Discov.* **12**, 335–343.
34. Iversen, P. W. *et al.* (Eli Lilly & Company and the National Center for Advancing Translational Sciences, 2004). HTS assay validation. in *Assay Guidance Manual [Internet]* (eds. Sittampalam, G. S., Grossman, A. & Brimacombe, K.) 1–26.
35. Zhang, J.-H., Chung, T. D. Y. & Oldenburg, K. R. (1999) A simple statistical parameter for use in evaluation and validation of high throughput screening assays. *J. Biomol. Screen.* **4**, 67–73.
36. Superti-Furga, G. *et al.* (2020) The RESOLUTE consortium: unlocking SLC transporters for drug discovery. *Nat. Rev. Drug Discov.* **19**, 429–430.
37. César-Razquin, A. *et al.* (2015) A call for systematic research on solute carriers. *Cell* **162**, 478–487.
38. Doijen, J. *et al.* (2019) Advantages and shortcomings of cell-based electrical impedance measurements as a GPCR drug discovery tool. *Biosens. Bioelectron.* **137**, 33–44.
39. Hillger, J. M., Lieuw, W.-L., Heitman, L. H. & IJzerman, A. P. (2017) Label-free technology and patient cells: from early drug development to precision medicine. *Drug Discov. Today* **22**, 1808–1815.
40. Kho, D. *et al.* (2015) Application of xCELLigence RTCA biosensor technology for revealing the profile and window of drug responsiveness in real time. *Biosensors* **5**, 199–222.
41. Magi, S. *et al.* (2013) Glutamate-induced ATP synthesis: Relationship between plasma membrane Na⁺/Ca²⁺ exchanger and excitatory amino acid transporters in brain and heart cell models. *Mol. Pharmacol.* **84**, 603–614.
42. Arinze, I. J. (2005) Facilitating understanding of the purine nucleotide cycle and the one-carbon pool. Part I: The purine nucleotide cycle. *Biochem. Mol. Biol. Educ.* **33**, 165–168.
43. Moullan, N. *et al.* (2015) Tetracyclines disturb mitochondrial function across eukaryotic models: a call for caution in biomedical research. *Cell Rep.* **10**, 1681–1691.
44. Rose, E. M. *et al.* (2009) Glutamate transporter coupling to Na⁺/K⁺-ATPase. *J. Neurosci.* **29**, 8143–8155.
45. Grever, C. & Rauen, T. (2005) Electrogenic glutamate transporters in the CNS: molecular mechanism, pre-steady-state kinetics, and their impact on synaptic signaling. *J. Membr. Biol.* **203**, 1–20.
46. Rungta, R. L. *et al.* (2015) The cellular mechanisms of neuronal swelling underlying cytotoxic edema. *Cell* **161**, 610–621.
47. Hoffmann, E. K., Lambert, I. H. & Pedersen, S. F. (2009) Physiology of cell volume regulation in vertebrates. *Physiol. Rev.* **89**, 193–277.
48. Schwab, A., Nechyporuk-Zloy, V., Fabian, A. & Stock, C. (2006) Cells move when ions and water flow. *Pflügers Arch. - Eur. J. Physiol.* **453**, 421–432.
49. Morishita, K., Watanabe, K. & Ichijo, H. (2019) Cell volume regulation in cancer cell migration driven by osmotic water flow. *Cancer Sci.* **110**, 2337–2347.
50. Schneider, G. H., Baethmann, A. & Kempfski, O. (1992) Mechanisms of glial swelling induced by glutamate. *Can. J. Physiol. Pharmacol.* **70**, S334–S343.
51. Bender, A. S., Schousboe, A., Reichelt, W. & Norenberg, M. D. (1998) Ionic mechanisms in glutamate-induced astrocyte swelling: Role of K⁺ influx. *J. Neurosci. Res.* **52**, 307–321.
52. Hansson, E. *et al.* (2000) Astroglia and glutamate in physiology and pathology: aspects on glutamate transport, glutamate-induced cell swelling and gap-junction communication. *Neurochem. Int.* **37**, 317–329.
53. Wilson, C. S. & Mongin, A. A. (Academic Press, 2018). Cell volume control in healthy brain and neuropathologies. in *Current Topics in Membranes* (eds. Levitan, I., Delpire, E. & Rasgado-Flores, H.) vol. 81 385–455.
54. Koyama, Y. *et al.* (2000) Transient treatments with L-glutamate and threo-β-hydroxyaspartate induce swelling of rat cultured astrocytes. *Neurochem. Int.* **36**, 167–173.
55. Staub, F. *et al.* (1993) Swelling of glial cells in lacticidosis and by glutamate: significance of Cl⁻ transport. *Brain Res.* **610**, 69–74.
56. Chan, P. H., Chu, L. & Chen, S. (1990) Effects of MK-801 on glutamate-induced swelling of astrocytes in primary cell culture. *J. Neurosci. Res.* **25**, 87–93.
57. Kovermann, P., Engels, M., Müller, F. & Fahlke, C. (2022) Cellular physiology and pathophysiology of EAAT anion channels. *Front. Cell. Neurosci.* **15**, 815279.

58. Schober, A. L. & Mongin, A. A. (2015) Intracellular levels of glutamate in swollen astrocytes are preserved via neurotransmitter reuptake and de novo synthesis: implications for hyponatremia. *J. Neurochem.* **135**, 176–185.
59. Lambert, I. H., Kristensen, D. M., Holm, J. B. & Mortensen, O. H. (2015) Physiological role of taurine – from organism to organelle. *Acta Physiol.* **213**, 191–212.
60. Okada, Y. *et al.* (2001) Receptor-mediated control of regulatory volume decrease (RVD) and apoptotic volume decrease (AVD). *J. Physiol.* **532**, 3–16.
61. Boudreault, F. & Grygorczyk, R. (2004) Cell swelling-induced ATP release is tightly dependent on intracellular calcium elevations. *J. Physiol.* **561**, 499–513.
62. Jakab, M. *et al.* (2002) Mechanisms sensing and modulating signals arising from cell swelling. *Cell. Physiol. Biochem.* **12**, 235–258.
63. Jentsch, T. J. (2016) VRACs and other ion channels and transporters in the regulation of cell volume and beyond. *Nat. Rev. Mol. Cell Biol.* **17**, 293–307.
64. Franco, R., Panayiotidis, M. I. & Ochoa de la Paz, L. D. (2008) Autocrine signaling involved in cell volume regulation: The role of released transmitters and plasma membrane receptors. *J. Cell. Physiol.* **216**, 14–28.
65. Jakab, M. & Ritter, M. (2006) Cell volume regulatory ion transport in the regulation of cell migration. *Contrib. Nephrol.* **152**, 161–180.
66. Lang, F. *et al.* (1998) Functional significance of cell volume regulatory mechanisms. *Physiol. Rev.* **78**, 247–306.
67. Lang, F. (2007) Mechanisms and significance of cell volume regulation. *J. Am. Coll. Nutr.* **26**, 613S–623S.
68. Tzingounis, A. V. & Wadiche, J. I. (2007) Glutamate transporters: confining runaway excitation by shaping synaptic transmission. *Nat. Rev. Neurosci.* **8**, 935–947.
69. Sun, W., Shchepakina, D., Kalachev, L. V. & Kavanaugh, M. P. (2014) Glutamate transporter control of ambient glutamate levels. *Neurochem. Int.* **73**, 146–151.
70. Costello, A. *et al.* (2019) Leaky expression of the TEET-On system hinders control of endogenous miRNA abundance. *Biotechnol. J.* **14**, 1800219.
71. Vandenberg, R. J. & Ryan, R. M. (2013) Mechanisms of glutamate transport. *Physiol. Rev.* **93**, 1621–1657.
72. Ryan, R. M., Ingram, S. L. & Scimemi, A. (2021) Regulation of glutamate, GABA and dopamine transporter uptake, surface mobility and expression. *Front. Cell. Neurosci.* **15**, 670346.
73. Lukasiewicz, P. D., Bligard, G. W. & DeBrecht, J. D. (2021) EAAT5 glutamate transporter-mediated inhibition in the vertebrate retina. *Front. Cell. Neurosci.* **15**, 662859.
74. Abrahamsen, B. *et al.* (2013) Allosteric modulation of an excitatory amino acid transporter: the subtype-selective inhibitor UCPH-101 exerts sustained inhibition of EAAT1 through an intramonomeric site in the trimerization domain. *J. Neurosci.* **33**, 1068–1087.
75. Belo do Nascimento, I. *et al.* (2021) Pharmacological evidence for the concept of spare glutamate transporters. *Neurochem. Int.* **149**, 105142.
76. Boussif, O. *et al.* (1995) A versatile vector for gene and oligonucleotide transfer into cells in culture and in vivo: Polyethylenimine. *Proc. Natl. Acad. Sci. U. S. A.* **92**, 7297–7301.
77. Stefanowicz-Hajduk, J., Adamska, A., Bartoszewski, R. & Ochocka, J. R. (2016) Reuse of E-plate cell sensor arrays in the xCELLigence real-time cell analyzer. *Biotechniques* **61**, 117–122.
78. Xu, Z. *et al.* (2017) A general method to regenerate arrayed gold microelectrodes for label-free cell assay. *Anal. Biochem.* **516**, 57–60.
79. Smith, P. K. *et al.* (1985) Measurement of protein using bicinchoninic acid. *Anal. Biochem.* **150**, 76–85.
80. Benjamini, Y. & Hochberg, Y. (1995) Controlling the false discovery rate: a practical and powerful approach to multiple testing. *J. R. Stat. Soc. Ser. B* **57**, 289–300.

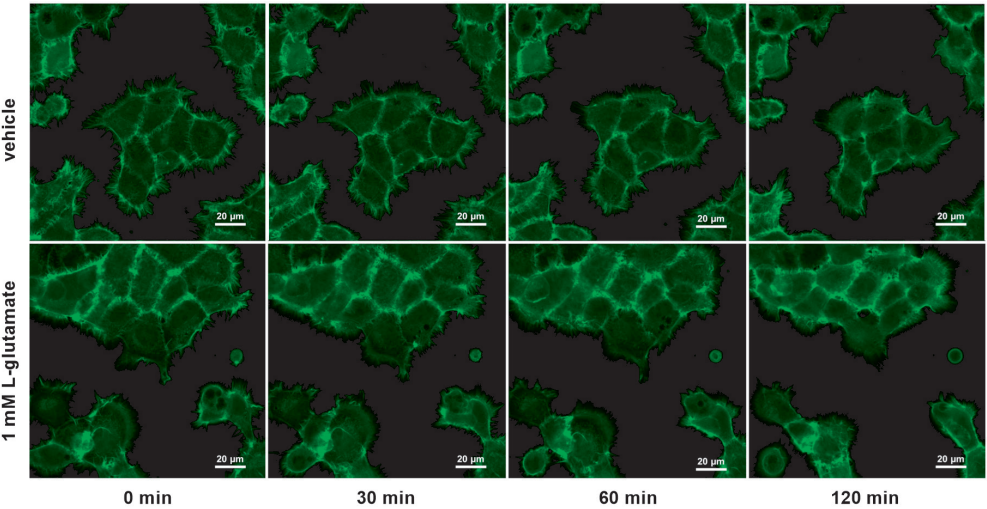
→ **Supplementary Figure 6.S1** – Vehicle-corrected nCI traces during pretreatment of cells. **(a–d)** In the TRACT assay, JumpIn-EAAT1-mGluR₂ cells were pretreated for 1 h with vehicle (PBS/DMSO), 10 μM UCPH-101 **(a)** or 10 μM TFB-TBOA **(b)** in the absence (–dox) **(a,b)** or presence (+dox) **(c,d)** of doxycycline. **(e,g)** In the phenotypic assay, JumpIn-EAAT1 +dox cells were pretreated for 1 h with vehicle (PBS/DMSO), 10 μM UCPH-101 **(e)**, 10 μM TFB-TBOA **(f)** or increasing concentrations of ouabain **(g)**. Data are shown as the mean of a representative experiment performed with four or eight replicates.

Supplementary Information

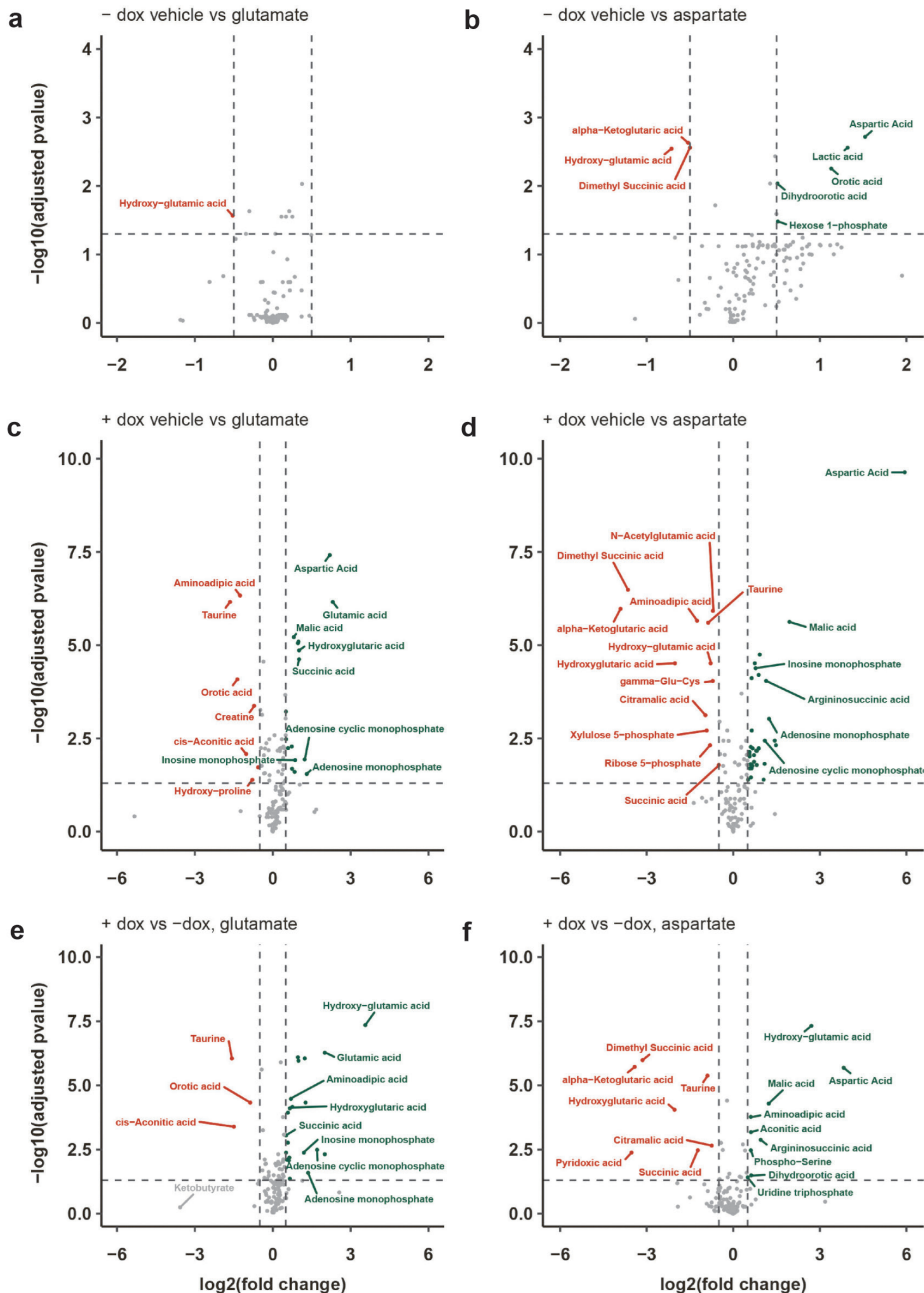




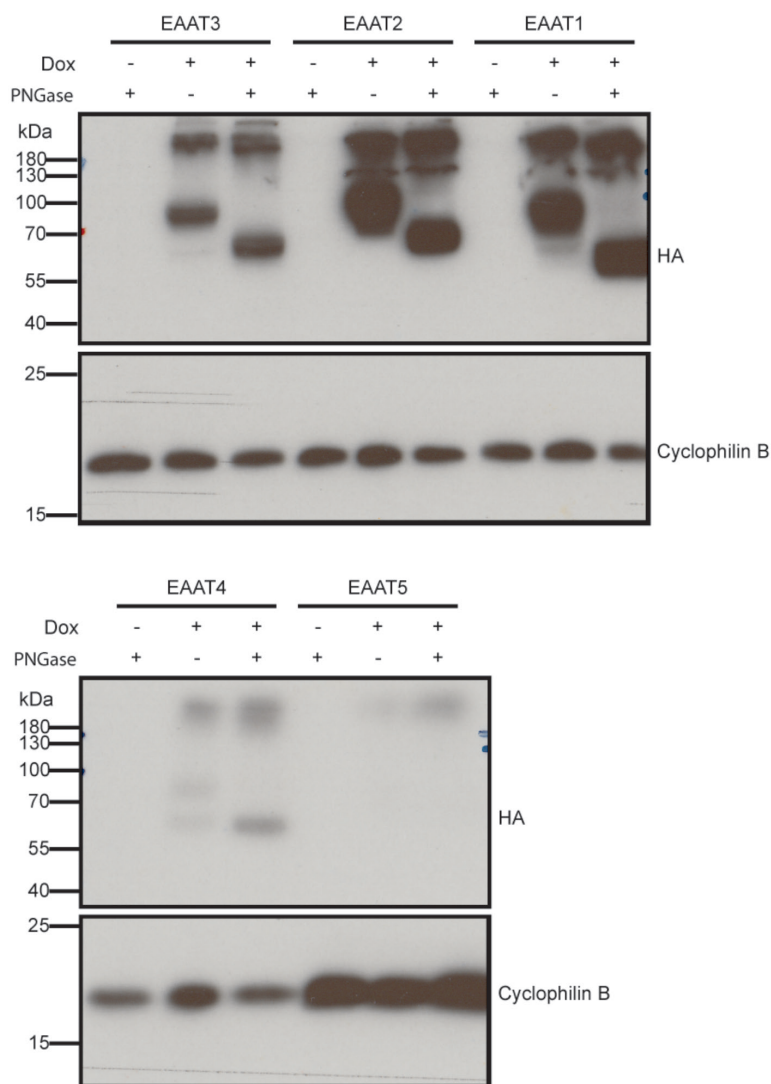
Supplementary Figure 6.S2 – HTS validation of the phenotypic impedance-based assay on JumpIn-EAAT1 cells. **(a)** Representative row-oriented graph of a 96-well E-plate contain high (vehicle + 1 mM L-glu), mid (0.2 μ M TFB-TBOA + 1 mM L-glu) and low (10 μ M TFB-TBOA + 1 mM L-glu) signal wells. Data is shown as the net AUC of the non-corrected nCI traces of the first 120 min after L-glu stimulation. Each data point represents a single well. **(b)** Stability of the Z' factor (Z') and signal window (SW) for each of the 96-well E-plates in the HTS validation. Three plates were run consecutively per day for three days in a row. Z' and SW are calculated according to the formulas in the STAR methods and presented as the mean \pm SEM of all nine plates.



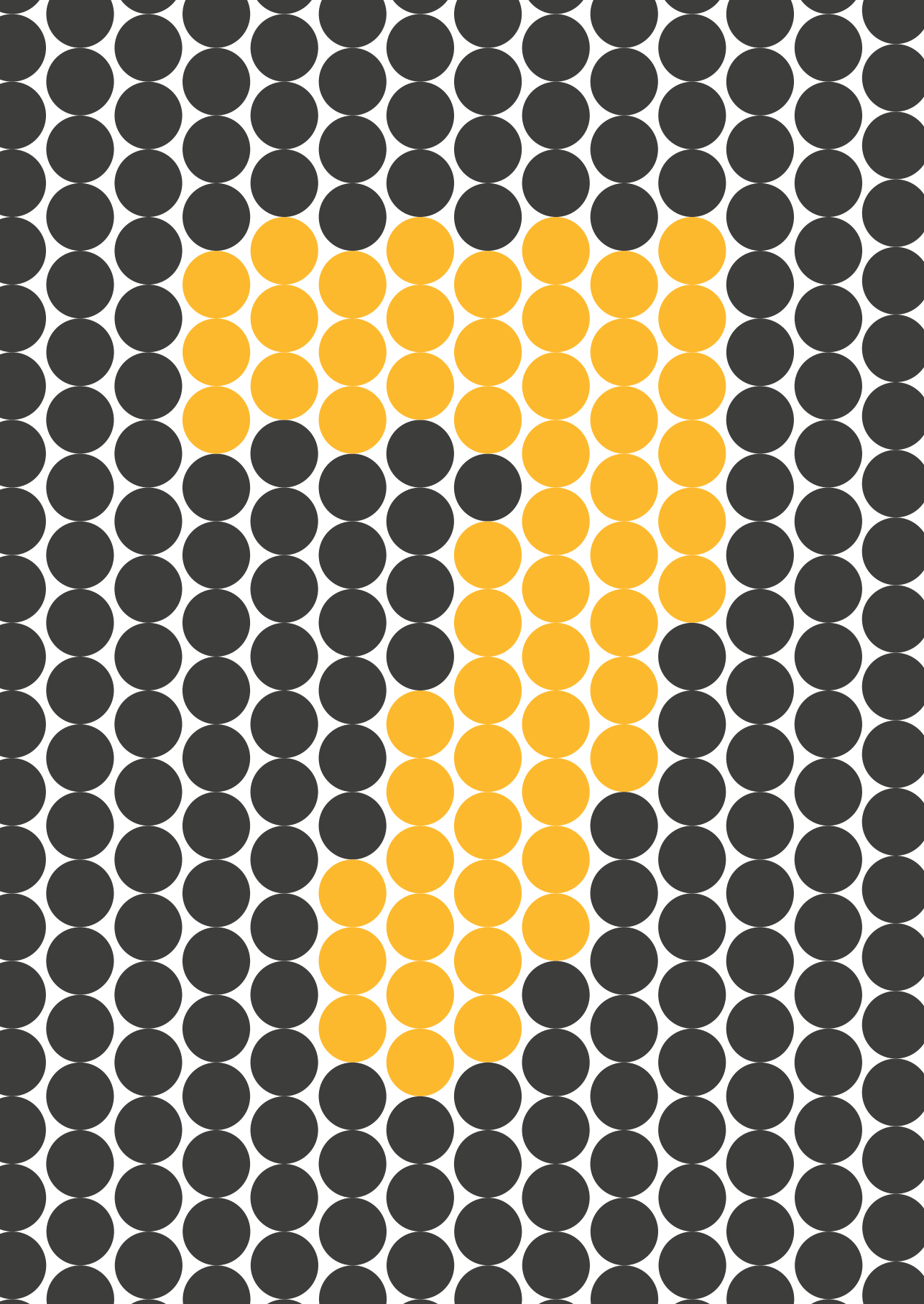
Supplementary Figure 6.S3 – NKA inhibition with ouabain does not increase L-glutamate-induced cell spreading. Representative confocal images of JumpIn-EAAT1-LifeAct-GFP (green) cells pretreated for 60 min with 1 μ M ouabain. Images were taken 0, 30, 60 and 120 min after stimulation with vehicle (PBS) or 1 mM L-glu, scale bar = 20 μ m. Stills were selected from a representative live imaging movie from two independent experiments each performed in triplicate.



Supplementary Figure 6.S4 – Volcano plots showing the \log_2 fold change of 131 metabolites plotted against the $-\log_{10}$ adjusted p-value. The change in metabolite levels is calculated for (a,b) non-induced (–dox) and (c,d) dox-induced (+dox) Jmpln-EAAT1 cells as the difference between vehicle treated cells and (a,c) L-glutamate or (b,d) L-aspartate treated cells. In addition, a comparison is made between (e,f) non-induced and dox-induced cells stimulated with (e) L-glutamate or (f) L-aspartate. Changes in metabolite levels were considered substantial and significant when the \log_2 fold change ≤ -0.5 or ≥ 0.5 , and the p-value < 0.05 ($-\log_{10} > 1.3$).



Supplementary Figure 6.S5 – Western blots of lysed JumoIn cells expressing hemagglutinin (HA)-tagged EAAT1-5. Cells were incubated for 24 h in the presence or absence of 1 μ g/ml doxycycline (dox) prior to cell lysis. Where indicated, cell lysates were treated with PNGase to deglycosylate the protein. The expected molecular weights of deglycosylated protein are: EAAT1, ~67 kDa; EAAT2, ~70 kDa; EAAT3, ~65 kDa; EAAT4, ~69 kDa; EAAT5, ~68 kDa. Cyclophilin B was used as a protein loading control. Blots are shown as a representative of two replicate experiments.



CHAPTER 7

Molecular insights into disease-associated glutamate transporter variants using *in silico* and *in vitro* approaches

Marina Gorostiola González †
Hubert J. Sijben †
Laura Dall'Acqua
Rongfang Liu
Adriaan P. IJzerman
Gerard J.P. van Westen
Laura H. Heitman

Glutamate is an essential excitatory neurotransmitter and an intermediate for energy metabolism. Depending on the tumor site, cancer cells have increased or decreased expression of excitatory amino acid transporter 1 or 2 (EAAT1/2, SLC1A3/2) to regulate glutamate uptake for the benefit of tumor growth. Thus, EAAT1/2 may be an attractive target for therapeutic intervention. Genetic variation of EAAT1 has been associated with rare cases of episodic ataxia, but the occurrence and functional contribution of EAAT1 mutants in other diseases, such as cancer, is poorly understood. In this chapter, we identified 105 unique somatic EAAT1 mutations in cancer patients from the Genomic Data Commons dataset. Using EAAT1 crystal structures and *in silico* simulations, we selected eight mutations based on their close proximity to the orthosteric or allosteric ligand binding sites and the predicted change in ligand binding affinity. *In vitro* functional assessment in the live-cell, impedance-based phenotypic assay described in **Chapter 6** demonstrated that these mutants differentially affect L-glutamate and L-aspartate transport, as well as the inhibitory potency of an orthosteric (TFB-TBOA) and allosteric (UCPH-101) inhibitor. Moreover, two episodic ataxia-related mutants displayed functional responses that were in line with literature, which confirmed the validity of our assay. We demonstrate the application of a robust *in vitro* method to functionally characterize EAAT1 variants, which could substantiate mechanistic studies and aid drug discovery efforts.

Manuscript in preparation

† These authors have contributed equally

7.1 – Introduction

Glutamate is an abundant endogenous amino acid that acts as the major excitatory neurotransmitter in the central nervous system and serves as a key metabolite in energy homeostasis¹. In the synaptic cleft glutamate is transported across the cell membrane *via* excitatory amino acid transporters (EAATs), which belong to subfamily 1 of the solute carrier (SLC) transporters². Glutamate transport is thermodynamically coupled to the transport of three Na⁺ ions and one proton, and the counter-transport of one K⁺ ion, where binding of Na⁺ and/or substrate activates an uncoupled Cl⁻ conductive state³. Deregulated glutamate levels have been associated with a plethora of neurological diseases^{4,5} and more recently with cancer^{6,7}. As a result, pharmacological modulation of EAATs may be a promising therapeutic strategy for conditions that are associated with altered glutamate levels^{8,9}.

Depending on the location of the tumor, cancerous cells have been shown to exploit the uptake, metabolism and signaling properties of glutamate as well as aspartate as fuel for tumor proliferation and a key advantage for expansion. Healthy glia cells abundantly express EAAT1 and EAAT2 to mediate the majority of glutamate clearance². However, expression levels of EAAT2 are vastly reduced in gliomas, which combined with increased efflux *via* the glutamate/cystine antiporter (xCT, SLC7A11) leads to elevated glutamate levels surrounding the glioma that induce cell death and allow further growth of the tumor^{10,11}. Moreover, EAAT1 was found to be overexpressed and cause glutamate efflux in aggressive glioblastomas, which indicates selective EAAT1 inhibitors as a potential treatment option for glioma¹². In several instances of cancer in peripheral tissues EAAT1 expression has been linked to a poor disease prognosis. Under hypoxia or conditions that starve the tumor of glutamine, some cancer cells promote EAAT1 or EAAT2 expression to drive uptake of aspartate or glutamate which rescues cancer cell growth^{13–15}. As such, EAAT expression in such tumors could be a predictive biomarker and pharmacological modulation of glutamate transporter expression or activity could be of therapeutic interest.

Despite the clear advantages for tumor cells to regulate EAAT expression, little is known about human genetic variations of these transporters in cancer, although several mutations have been associated with other diseases. Thus far, reports have linked seven missense mutations in the coding region of EAAT1 to the etiology of extremely rare cases of episodic ataxia type 6 (EA6)¹⁶. These mutants vary in their degree of loss- or gain-of-function of substrate transport and/or anion conductivity¹⁶. Moreover, several other EAAT1 mutations and duplications have been associated with other neurological disorders including migraine, ADHD, autism, and Tourette's syndrome^{17–19}. To the best of our knowledge, there have been no reports so far that associate mutations of EAAT1 to the development and progression of cancer.

Over the last fifteen years, a growing number of 3D structures have been published for the archaeal glutamate transporter orthologues Glt_{ph}²⁰ and Glt_{tk}²¹, as well as human EAAT1^{22,23}, EAAT2²⁴ and EAAT3²⁵, in complex with the endogenous substrate L-aspartate, Na⁺ ions and/or inhibitors. Glutamate transporters assemble in obligate homo-trimers of which the protomers operate independently of each other. Each protomer consists of a rigid

trimerization or scaffold domain (scaD) and a dynamic transport domain (tranD) that engages with the substrate and co-transported Na^+ ions²². Structures covering inward-facing, intermediate, and outward-facing conformations provide information on the movement of individual transmembrane helices (TMs). Specifically, the flexible helical hairpin 2 (HP2) in tranD controls the access of ligands to the substrate binding site and is an essential ‘gate’ that upon opening and closing regulates the ‘elevator-like’ translocation of tranD. Thus, these structures may be used to gain mechanistic insight into the effects of genetic variability on transport function, as was previously demonstrated by mapping genetic variants of glucose (GLUT1) and nucleoside (ENT1) transporters to their respective crystal structures²⁶.

In this chapter, we characterize a series of EAAT1 somatic mutations that were identified from biopsy material of cancer patients represented in the Genomic Data Commons (GDC) dataset²⁷. Using the reported ligand-bound crystal structures of EAAT1^{22,23}, predictions were made on which variants would most likely impact binding of substrates (L-glutamate and L-aspartate). To determine whether these mutants would affect the binding of potential pharmacological modulators, we included the ‘orthosteric’ inhibitor TFB-TBOA²⁸ and the ‘allosteric’ inhibitor UCPH-101⁹, which have both been co-crystallized in EAAT1²². The selected eight mutations, together with two EA6-associated mutants (M128R, T318A), were tested *in vitro* for substrate uptake and inhibition using the impedance-based phenotypic assay that was developed in **Chapter 6**. Mutants displayed divergent effects on EAAT1 function, which was apparent from an altered substrate and/or inhibitor potency. Taken together, the results in this work demonstrate 1) the suitability of the label-free phenotypic method to assess functional variation of EAAT1 mutants and 2) the opportunity of using *in silico* techniques to rationalize the *in vitro* phenotype of disease-relevant mutants.

7.2 – Results

7.2.1 – Cancer-related mutations are widespread across the EAAT1 structure

Somatic mutations in EAAT1 are found in cancer patients suffering from different cancer types. Across all cancer types in the Genomic Data Commons (GDC)²⁷, we identified 105 unique EAAT1 mutations primarily located in uterine cancer (29 mutations) followed by lung cancer and melanoma (21 mutations each) and colon cancer (11 mutations). The frequency of these unique mutations is comparable to natural variance occurrence (1.18% vs. 1.75%, respectively), and they are widespread across the EAAT1 structure without any specific mutational pattern observed per cancer type (**Supplementary Figure 7.S1a,b**). However, most EAAT1 mutations found in cancer patients are not present in natural variance, and some of them are found in structural domains in which conformational rearrangements could lead to transport function impairment. For example, there are mutations located in the vicinity of the binding sites occupied by the substrate and coordinating Na^+ ions, as well as in the HP2 domain (**Supplementary Figure 7.S1a,b**). Moreover, certain mutations found in cancer patients are located in the binding pockets occupied by orthosteric and allosteric EAAT1 inhibitors, which could lead to changes in their binding affinity and potency. We shortlisted 12 mutations not present in natural variance that were found in the

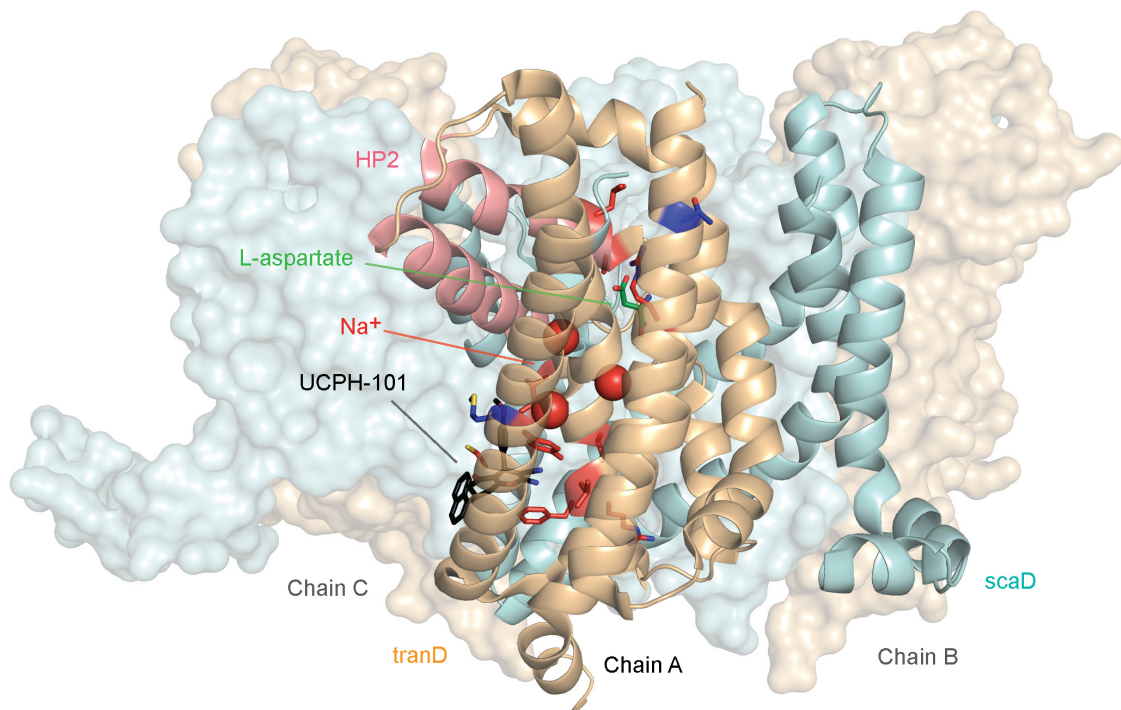


Figure 7.1 – EAAT1 mutations presented in this study. Structural distribution of cancer- and ataxia-related mutants in EAAT1 functionally relevant domains presented in this study. Cancer-related mutations (Y127C, V247F, C252F, R388K, F389L, V390M, P392L, I397V, A446E, A446V, L448Q, and R479W) are mapped in red onto chain A of the EAAT1 trimer (PDB 7AWM). Ataxia-related mutations (M128R and T318A) are mapped in dark blue onto chain A. Chains B and C are represented as surfaces. Protein domains are color-coded as follows: tranD domain (orange), scaD domain (cyan), helical hairpin 2 (HP2) domain (red). The co-crystallized substrate, L-aspartate, is represented in green sticks in chain A. The three coordinated Na⁺ ions are represented as red spheres in chain A. The allosteric inhibitor UCPH-101 is represented in black sticks.

functional and binding domains mentioned above (Y127C, V247F, C252F, R388K, F389L, V390M, P392L, I397V, A446E, A446V, L448Q, and R479W) to characterize their effect with a combination of *in silico* and *in vitro* methods (**Figure 7.1**).

7.2.2 – EAAT1 mutants are predicted to have a local effect on substrate and inhibitor binding affinity

The effect on ligand binding affinity of cancer-related mutants found in the orthosteric and allosteric binding sites of EAAT1 was tested *in silico* to prioritize mutations for *in vitro* testing. We calculated changes in binding energy $\Delta\Delta G_{\text{bind}}$ for two endogenous substrates (L-aspartate and L-glutamate), one competitive “orthosteric” inhibitor (TFB-TBOA), and one non-competitive “allosteric” inhibitor UCPH-101 (**Table 7.1**). Since the method employed short-range Monte Carlo sampling, we restricted our analysis to mutants in the vicinity of the ligand of interest and classified the mutants as “orthosteric” (V247F, P392L,

Table 7.1 – Binding energy changes ($\Delta\Delta G_{\text{bind}}$) predicted in ICM-Pro for EAAT1 orthosteric and allosteric mutants.

	Orthosteric mutants			Allosteric mutants	
	$\Delta\Delta G_{\text{bind}}$ (kcal/mol) ^a			$\Delta\Delta G_{\text{bind}}$ (kcal/mol) ^b	
	L-aspartate	L-glutamate	TFB-TBOA	UCPH-101	
V247F ^c	0.52	0.08	-0.70	Y127C	5.82
P392L	0.04	-0.01	-0.70	V247F ^c	0.68
A446E	6.39	-0.90	1.86	C252F	-0.49
A446V	0.58	-1.73	2.23	R388K	-0.05
L448Q	-0.35	-1.88	1.79	F389L	3.83
R479W	7.13	6.42	42.19	V390M	-0.76
				I397V	-0.62

^a $\Delta\Delta G_{\text{bind}}$ was calculated for the endogenous substrates L-aspartate and L-glutamate and for the competitive inhibitor TFB-TBOA for orthosteric EAAT1 mutants. The systems used were chain A of PDB 5LLU (with L-aspartate co-crystallized and L-glutamate docked), and chain A of PDB 5MJU (with TFB-TBOA co-crystallized).

^b For the allosteric mutants, $\Delta\Delta G_{\text{bind}}$ was calculated for the allosteric inhibitor UCPH-101 in Chain A of PDB 5MJU.

^c V247F is situated between the orthosteric and allosteric site

A446E, A446V, L448Q, and R479W, **Figure 7.2a,b**) and “allosteric” (Y127C, V247F, C252F, R388K, F389L, V390M, and I397V, **Figure 7.2c,d**). A positive $\Delta\Delta G_{\text{bind}}$ over 1 kcal/mol can be interpreted as a significant decrease in binding affinity, while a negative $\Delta\Delta G_{\text{bind}}$ below -1 kcal/mol can be interpreted as a significant increase in binding affinity (**Table 7.1**)²⁹.

Within the orthosteric mutants, we observed a substantial increase in $\Delta\Delta G_{\text{bind}}$ values in mutant R479W for both endogenous substrates and especially for the inhibitor TFB-TBOA, which indicates highly unfavorable binding of these ligands. V247F and P392L did not show significant changes as these residues are further away from the substrate’s binding site, but an incipient increased binding affinity towards TFB-TBOA was observed. A446V and L448Q, and to a lesser extent A446E, showed an increased binding affinity towards L-glutamate. Interestingly, while both A446 mutants displayed a reduced TFB-TBOA affinity, A446E and A446V showed a different profile for the two endogenous substrates. A substantial loss of binding affinity towards L-aspartate was observed in A446E, but not A446V. Within the allosteric mutants, Y127C and F389L showed a significant decrease in binding affinity towards UCPH-101. V390M showed the biggest increase in binding affinity, although this change in $\Delta\Delta G_{\text{bind}}$ was not significant..

Based on these results, we selected five orthosteric (P392L, A446E, A446V, L448Q, and R479W) and two allosteric mutants (Y127C and V390M) for *in vitro* testing based on their differential $\Delta\Delta G_{\text{bind}}$ profiles. Moreover, we included V247F in the selection since it was considered to be at the interface of both binding pockets. Of the selected residues, Y127, V390, P392, A446, L448 and R479 are fully conserved in mammalian EAATs, as well as the archaeal glutamate transporter homolog Glt_{ph} (except V390 and L448), which suggests the relative importance of these residues in protein function (**Supplementary Figure 7.S2**). To validate the *in vitro* assay, we selected two additional EA6-associated EAAT1 mutations that have been reported to either completely abolish glutamate transport (M128R) or have unaltered transport (T318A). Neither of these two residues are conserved in other

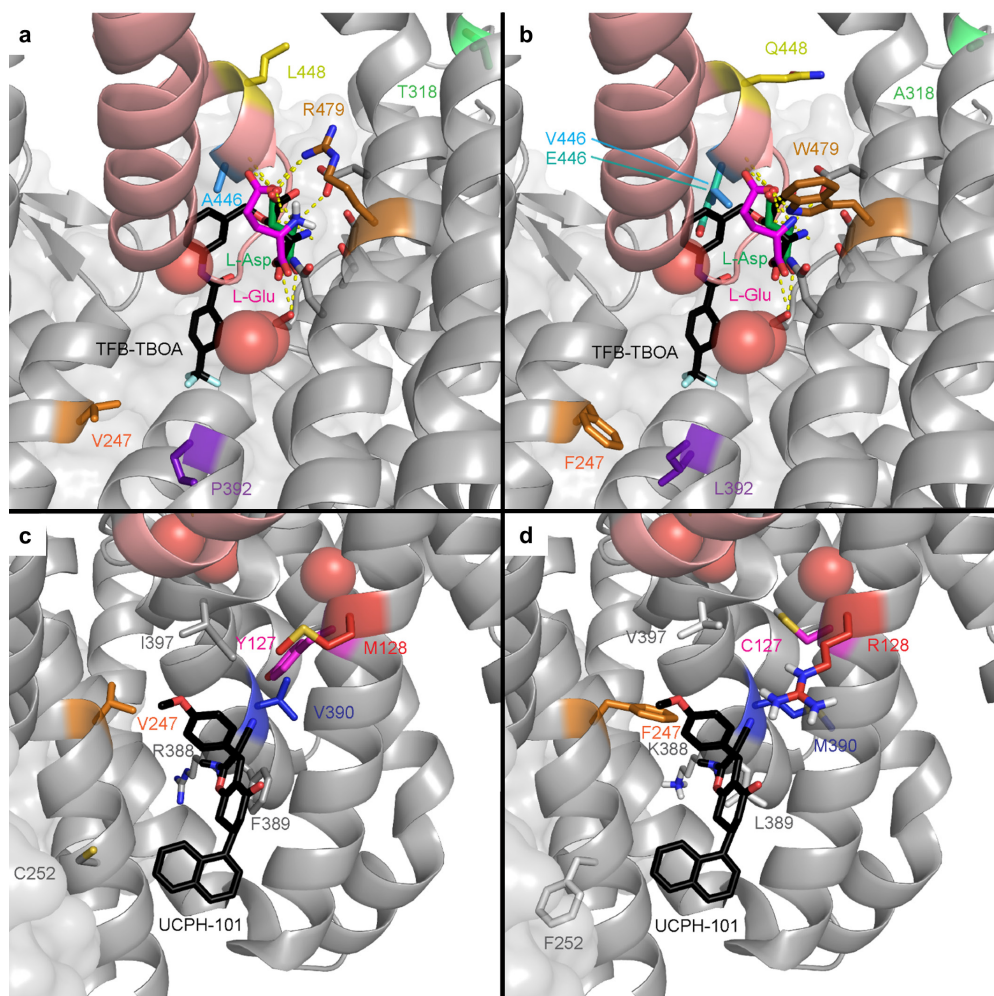


Figure 7.2 – EAAT1 disease-related mutations in the orthosteric and allosteric binding sites. Mutations are mapped onto chain A of PDB 7AWM. Thermostabilizing mutations C252V and T318M were reverted in 7AWM for $\Delta\Delta G_{\text{bind}}$ calculation and visualization purposes. For spatial reference, the helical hairpin 2 (HP2) domain helices are colored salmon. The three coordinated Na⁺ ions are represented as red spheres. (a) Wild-type residues where mutations have been found in cancer in the orthosteric binding site of EAAT1. Ataxia-related reference mutation T318A is visualized in light green. The co-crystallized substrate, L-aspartate, is represented as green sticks. The docked substrate, L-glutamate, is represented in magenta. The competitive inhibitor TFB-TBOA is represented as black sticks and superimposed to the 7AWM structure from its position in PDB 5MJU. Polar contacts between the substrate and EAAT1 are represented as dashed yellow lines. (b) Mutated residues in the orthosteric binding site of EAAT1. (c) Wild-type residues where mutations have been found in cancer in the allosteric binding site of EAAT1. Ataxia-related reference mutation M128R is visualized in red. The co-crystallized allosteric inhibitor UCPH-101 is represented as black sticks. (d) Mutated residues in the allosteric binding site of EAAT1.

glutamate transporters (**Supplementary Figure 7.S2**). M128 is adjacent to Y127 and in close proximity to the binding site of UCPH-101, whereas T318 is not in the vicinity of ligand binding sites (**Figure 7.2**).

7.2.3 – EAAT1 mutants respond differentially to substrates in a phenotypic assay

To assess the selected mutants for their function *in vitro*, we generated a series of HEK293 JumpIn cell lines that were modified to stably express either wild-type (EAAT1_{WT}) or mutant EAAT1 upon induction with 1 µg/ml doxycycline for 24 h. None of the ten mutants showed either a decreased or increased expression of the HA-tagged EAAT1 compared to EAAT1_{WT} after doxycycline treatment, indicating that the mutations did not affect translation of the transgene (**Supplementary Figure 7.S3**).

To assess whether the EAAT1 mutants affect transporter functionality, we used the impedance-based phenotypic assay that was developed in **Chapter 6**. In this set-up, adherent cells (over)expressing EAAT1 are cultured on gold-plated electrodes in a 96-well E-plate. Upon stimulation with high concentrations (10 µM – 1 mM) of substrate (i.e., L-glutamate or L-aspartate) the cells started spreading as a result of Na⁺-dependent substrate uptake *via* EAAT1 and subsequent cell swelling. The expanded electrode coverage by the cells generated an increase in impedance over time, which was expressed as Cell Index (CI) and interpreted as a readout of EAAT1 function (**Figure 7.3a**). Growth curves were recorded prior to inhibitor pretreatment and substrate stimulation and all mutants displayed similar CI traces compared to EAAT1_{WT}, which suggested that the presence of mutant EAAT1 did not substantially affect cell adhesion or proliferation during the experiments (**Supplementary Figure 7.S4**).

L-glutamate induced a concentration-dependent cellular response in EAAT1_{WT} (pEC₅₀ = 3.5 ± 0.0), which was reflected by a gradual increase of the normalized Cell Index (nCI) in the first 120 min after substrate stimulation (**Figure 7.3a–d**, **Table 7.2**). A comparable L-glutamate potency was observed for the EA6 mutant T318A (pEC₅₀ = 3.3 ± 0.0) with a slightly increased maximal response (E_{max}), whereas the L-glutamate response was completely abolished for M128R (**Figure 7.3b,d**). The allosteric site mutants V247F (pEC₅₀ = 3.8 ± 0.0) and V390M (pEC₅₀ = 3.5 ± 0.0) produced similar L-glutamate potencies compared to EAAT1_{WT}, where V247F has a 62% reduced E_{max} (**Figure 7.3b**). The potency of L-glutamate on Y127C was enhanced (pEC₅₀ = 4.1 ± 0.1), but displayed a substantial drop (94%) in E_{max} (**Figure 7.3b**). The orthosteric site mutants P392L (pEC₅₀ = 3.8 ± 0.0) and L448Q (pEC₅₀ = 3.3 ± 0.1) showed no significant change in L-glutamate potency, although the concentration-effect curve for L448Q appeared more linear and shifted rightward and did not appear to reach a maximum within the tested concentration range (**Figure 7.3c**). Both A446E and A446V produced glutamate responses with a strongly reduced E_{max}, but with significantly enhanced L-glutamate potency (pEC₅₀ = 4.4 ± 0.3 and 4.3 ± 0.2, respectively), whereas no concentration-dependent L-glutamate response was observed for R479W (**Figure 7.3c,d**).

Next, we assessed the responsiveness of the EAAT1 mutants to the endogenous substrate L-aspartate. L-aspartate induced a concentration-dependent cellular response in EAAT1_{WT} (pEC₅₀ = 3.6 ± 0.1) similar to L-glutamate (**Figure 7.3e**). The potency of L-aspartate was comparable in the EA6 mutant T318A (pEC₅₀ = 3.5 ± 0.0) with an elevated E_{max}, whereas in M128R no L-aspartate response was observed at 1 mM (**Figure 7.3e**). The response of L-aspartate in V390M (pEC₅₀ = 3.6 ± 0.0) was identical to EAAT1_{WT} (**Figure 7.3e**).

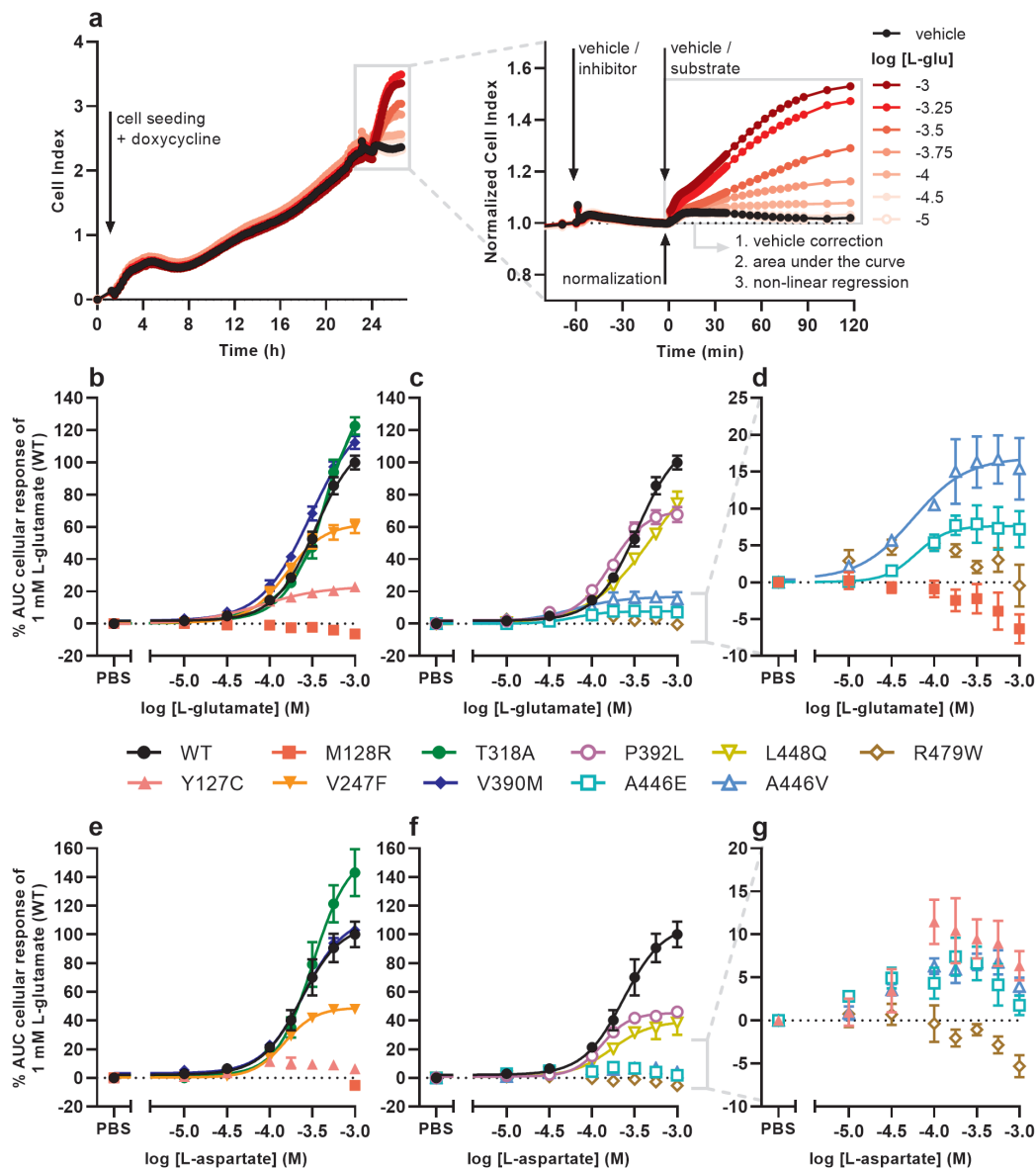


Figure 7.3 – Cellular responses of L-glutamate and L-aspartate in an impedance-based phenotypic assay on EAAT1_{WT} and mutant cells. **(a)** Illustrative graph of the assay and analysis procedure. EAAT1_{WT} cells are seeded and grown for 24 h in the presence of 1 μ g/ml doxycycline to induce EAAT1 expression. Cells are pretreated with vehicle (PBS/DMSO) or inhibitor (TFB-TBOA or UCPH-101, only in **Figure 7.4**) for 60 min and subsequently stimulated with vehicle (PBS) or substrate (L-glutamate or L-aspartate) for 120 min. The Cell Index (CI) is normalized prior to substrate stimulation and the cellular response is quantified by analyzing the net area under the curve (AUC). **(b–g)** Concentration-response curves of **(b–d)** L-glutamate and **(e–g)** L-aspartate on EAAT1_{WT} cells and **(b,e)** ataxia and allosteric site mutants and **(c,f)** orthosteric site mutants. **(d,g)** Zoom-in on mutants with low maximal cellular responses. Cellular response is expressed as the net AUC of the first 120 min after L-glutamate or L-aspartate stimulation. Graphs are normalized to the response of 1 mM L-glutamate or L-aspartate on EAAT1_{WT} cells. Data are shown as the mean \pm SEM of three to seven individual experiments each performed in duplicate.

Table 7.2 – Potencies (pEC_{50}) of L-glutamate and L-aspartate and inhibitory potencies (pIC_{50}) of TFB-TBOA and UCPH-101 on Jumpln-EAAT1_{WT} and mutant cells in an impedance-based phenotypic assay.

	L-glutamate		L-aspartate		TFB-TBOA	UCPH-101
	pEC_{50}	E_{max} (%) ^a	pEC_{50}	E_{max} (%) ^a	pIC_{50}	pIC_{50}
WT	3.5 ± 0.0	117 ± 5	3.6 ± 0.1	108 ± 9	6.7 ± 0.1	5.4 ± 0.0
Y127C	4.1 ± 0.1 ***	23 ± 3	N.D.	N.D.	6.2 ± 0.0 *	N.D.
M128R	N.D.	N.D.	N.D.	N.D.	N.D.	N.D.
V247F	3.8 ± 0.0	55 ± 9	3.8 ± 0.0	49 ± 1	5.7 ± 0.1 ****	5.3 ± 0.0
T318A	3.3 ± 0.0	156 ± 4	3.5 ± 0.0	158 ± 18	6.9 ± 0.1	5.4 ± 0.0
V390M	3.5 ± 0.0	132 ± 6	3.6 ± 0.0	112 ± 3	6.7 ± 0.0	5.4 ± 0.0
P392L	3.8 ± 0.0	71 ± 4	3.9 ± 0.0	46 ± 3	6.5 ± 0.1	N.D.
A446E	4.4 ± 0.3 ****	8 ± 2	N.D.	N.D.	7.4 ± 0.2 **	5.9 ± 0.2
A446V	4.3 ± 0.2 ****	16 ± 4	N.D.	N.D.	N.D.	N.D.
L448Q	3.3 ± 0.1	116 ± 25	3.7 ± 0.1	47 ± 13	7.9 ± 0.0 ****	5.9 ± 0.1 **
R479W	N.D.	N.D.	N.D.	N.D.	N.D.	N.D.

^a Maximal responses (E_{max}) are normalized to the cellular response of 1 mM L-glutamate or L-aspartate (100%) on Jumpln-EAAT1_{WT} cells. Data are presented as the mean ± SEM of three to seven individual experiments each performed in duplicate. Significant differences between potencies of WT and mutant cells were determined using a one-way ANOVA with Dunnett's post-hoc test. * $p < 0.05$, ** $p < 0.01$, *** $p < 0.001$, **** $p < 0.0001$, N.D. = not determined.

The mutants V247F ($pEC_{50} = 3.8 \pm 0.0$), P392L ($pEC_{50} = 3.9 \pm 0.0$) and L448Q ($pEC_{50} = 3.7 \pm 0.1$) produced similar L-aspartate potencies, but a substantially lowered E_{max} (~60%) compared to EAAT1_{WT} (Figure 7.3e,f). For Y127C, A446E and A446V a much reduced L-aspartate response was observed which dropped at high concentrations, resulting in a bell-shaped concentration-effect curve (Figure 7.3e–g). Similar to L-glutamate, no L-aspartate response was observed for R479W (Figure 7.3f,g). Collectively, these data demonstrate that the selected EAAT1 mutants impact L-glutamate and L-aspartate transport.

7.2.3 – EAAT1 mutants respond differentially to substrates in a phenotypic assay

To assess whether the selected mutants modulated the effects of the competitive (‘orthosteric’) inhibitor TFB-TBOA and the non-competitive (‘allosteric’) inhibitor UCPH-101, we pretreated the cells for 1 h with increasing concentrations of inhibitor prior to stimulation with 1 mM L-glutamate. In EAAT1_{WT}, inhibitor pretreatment itself did not result in substantial changes in the nCI (Supplementary Figure 7.S5c–f). Strikingly, the M128R pretreatment with TFB-TBOA resulted in a concentration-dependent sharp nCI increase which peaked after 10–30 min, whereas pretreatment with UCPH-101 induced a more gradual nCI increase that plateaued after 60 min (Supplementary Figure 7.S5a,b). These inhibitor responses were not observed in any of the other mutants, although V247F, A446E and A446V showed concentration-dependent decreases of the nCI upon TFB-TBOA pretreatment, which were substantially lower in magnitude compared to M128R (Supplementary Figure 7.S5d,f). This suggests that M128R displays a distinct physiological phenotype compared to EAAT1_{WT} and other mutants.

To elucidate a potential mechanism behind the M128R response to both inhibitors, we assessed whether the inhibitors displayed any interaction with each other or the substrate L-glutamate. Indeed, cells pretreated with TFB-TBOA were responsive to a subsequent stimulation with UCPH-101 and *vice versa*, indicating that the cellular responses elicited by either inhibitor are additive and are constituted by independent mechanisms (**Supplementary Figure 7.S6a,b**). Interestingly, the response caused by TFB-TBOA pretreatment was completely blocked after stimulation with 1 mM L-glutamate and a TFB-TBOA response was prevented when cells were pretreated with L-glutamate, indicating that the TFB-TBOA response is transient and originates from interactions at the substrate binding site (**Supplementary Figure 7.S6a,c**). In contrast, L-glutamate stimulation after UCPH-101 pretreatment does not reduce the nCI. The UCPH-101 response after L-glutamate pretreatment has a comparable magnitude to the UCPH-101 pretreatment on its own, suggesting that L-glutamate and UCPH-101 do not compete for the same binding site (**Supplementary Figure 7.6b,c**). In addition, the Na^+/K^+ -ATPase (NKA) inhibitor ouabain prevented any inhibitor- or substrate-induced cellular responses in M128R cells, which indicates that TFB-TBOA and UCPH-101 responses are likely dependent on ion influx (**Supplementary Figure 7.6d**).

7.2.5 – EAAT1 mutants alter TFB-TBOA and UCPH-101 inhibition

For EAAT1_{WT} and all other mutants, except M128R, we assessed the inhibitory potencies of TFB-TBOA and UCPH-101 by analyzing the response of 1 mM L-glutamate after 60 min pretreatment with increasing inhibitor concentrations. In EAAT1_{WT}, TFB-TBOA inhibited the L-glutamate response in a concentration-dependent manner ($\text{pIC}_{50} = 6.7 \pm 0.1$) (**Figure 7.4a,b, Table 7.2**). The EA6 mutant T318A ($\text{pIC}_{50} = 6.9 \pm 0.1$), allosteric site mutant V390M ($\text{pIC}_{50} = 6.7 \pm 0.0$) and orthosteric site mutant P392L ($\text{pIC}_{50} = 6.5 \pm 0.1$) did not affect the inhibitory potency of TFB-TBOA (**Figure 7.4a,b**). Both Y127C ($\text{pIC}_{50} = 6.2 \pm 0.0$) and V247F ($\text{pIC}_{50} = 5.7 \pm 0.1$) significantly decreased the potency, whereas L448Q ($\text{pIC}_{50} = 7.9 \pm 0.0$) significantly enhanced the inhibitory potency of TFB-TBOA (**Figure 7.4a,b**). Interestingly, A446E was susceptible to TFB-TBOA inhibition, showing an increased inhibitory potency ($\text{pIC}_{50} = 7.4 \pm 0.2$), whereas A446V as well as R479W did not display any sigmoidal concentration-dependent inhibition by TFB-TBOA (**Figure 7.4b,c**).

The effects of EAAT1 mutants on UCPH-101 inhibition were different from TFB-TBOA. In EAAT1_{WT}, UCPH-101 could inhibit the response of L-glutamate in a concentration-dependent manner ($\text{pIC}_{50} = 5.4 \pm 0.0$) (**Figure 7.4d,e, Table 7.2**). V247F ($\text{pIC}_{50} = 5.3 \pm 0.0$), T318A ($\text{pIC}_{50} = 5.4 \pm 0.0$) and V390M ($\text{pIC}_{50} = 5.4 \pm 0.0$) did not affect L-glutamate response inhibition by UCPH-101 (**Figure 7.4d**). In Y127C, P392L, A446V and R479W UCPH-101 was unable to inhibit the L-glutamate response at any of the tested concentrations, indicating a loss of the UCPH-101 interaction (**Figure 7.4d–f**). Similar to TFB-TBOA, both L448Q ($\text{pIC}_{50} = 5.9 \pm 0.1$) and A446E ($\text{pIC}_{50} = 5.9 \pm 0.2$) enhanced the inhibitory potency of UCPH-101, although this was not significant for A446E ($p = 0.0919$) (**Figure 7.4e,f**). Taken together, these data imply that the selected EAAT1 mutants differentially modulate both substrate and EAAT1 inhibitor interactions.

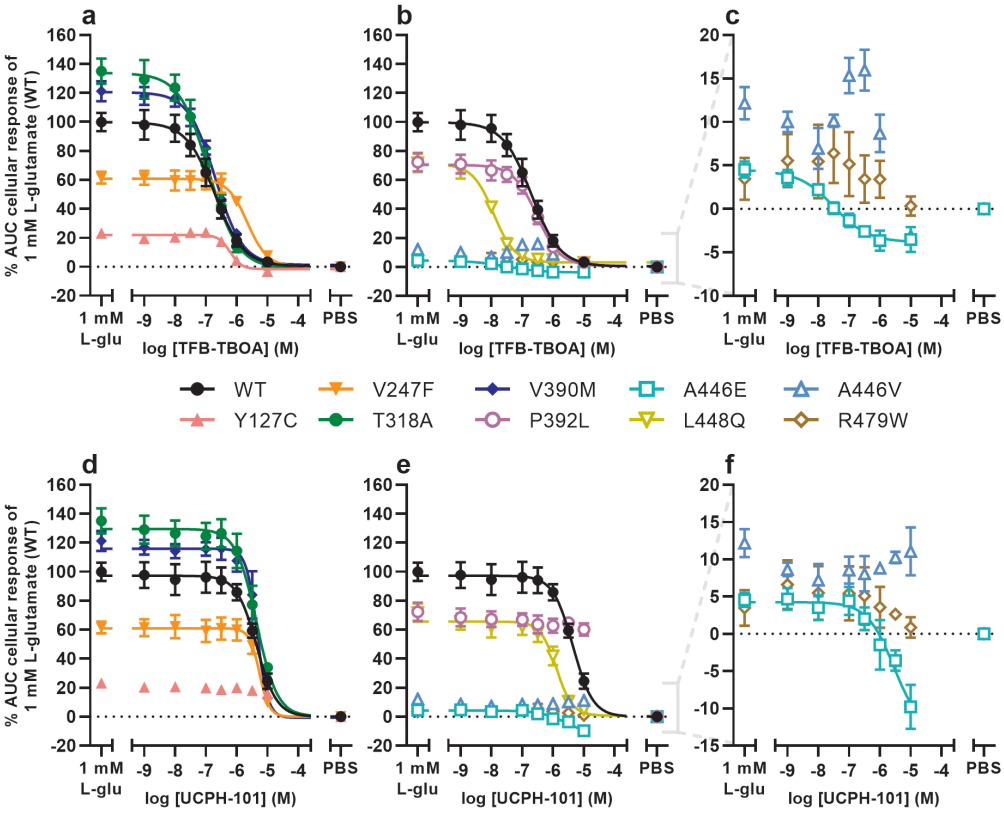


Figure 7.4 – Inhibition of L-glutamate responses by TFB-TBOA and UCPH-101 in an impedance-based phenotypic assay on EAAT1_{WT} and mutant cells. (a–f) Concentration-inhibition curves of (a–c) TFB-TBOA and (d–f) UCPH-101 on EAAT1_{WT} cells and (a,d) ataxia and allosteric site mutants, and (b,e) orthosteric site mutants. (c,f) Zoom-in on mutants with low maximal cellular responses. Cells were pretreated with TFB-TBOA, UCPH-101 or vehicle (PBS/DMSO) for 60 min and stimulated with a submaximal concentration (EC₈₀) of 1 mM L-glutamate or vehicle (PBS) for 120 min. Cellular response is expressed as the net AUC of the first 120 min after L-glutamate stimulation and graphs are normalized to the response of 1 mM L-glutamate on EAAT1_{WT} cells. Data are shown as the mean ± SEM of three individual experiments each performed in duplicate.

7.3 – Discussion

The role of glutamate and aspartate in cancer is increasingly appreciated³⁰. Indeed, the regulation of intra- and extracellular levels of these amino acids by EAATs and other transporters, in respect to the tumor microenvironment, is the subject of ongoing investigations. So far, altered function of EAAT1 as a result of single missense mutations has been linked to several extremely rare cases of episodic ataxia type 6 (EA6)¹⁶. However, there have been no reports on the contribution of genetic variants of EAATs to the development of cancer, and it remains a question to what degree loss- or gain-of-function mutations in these transporters are relevant for disease progression. In this study we identified 105 unique somatic mutations in cancer patients, none of which occurred as natural variants. Although we could not associate the genotype to disease etiology, we observed distinctive cellular responses of eight cancer-associated and two reference EA6-related EAAT1 missense mutants in a label-free phenotypic assay, which together with structural insights provides an initial understanding of altered transporter function and cell behavior.

All EAAT1 mutants were expressed at similar relative levels compared to EAAT1_{WT}, which suggests that the introduced mutations did not affect the translation of the protein (**Supplementary Figure 7.S3**). Interestingly, in previous studies several EAAT1 mutants displayed attenuated or increased glutamate uptake activity as a result of reduced (P290R, M128R^{16,31}) or enhanced (E219D, T318A^{16,17}) surface membrane density, respectively. Indeed, in our functional assay T318A showed a considerable increase in substrate E_{\max} (**Figure 7.3b,e**, **Table 7.2**), which may be attributed to an enhanced membrane insertion of EAAT1¹⁶. Most other mutants displayed a substantial decrease in substrate E_{\max} , with the maximal response being generally lower for L-aspartate than L-glutamate. To address the contribution of amino acid substitutions to their predicted effect on ligand binding affinity (**Table 7.1**) and the observed changes in substrate and/or inhibitor potency (**Figure 7.3–7.4**, **Table 7.2**), we will discuss each mutant individually.

Tyr at position 127 is located in TM3 and is conserved in all human EAATs and the archaeal Glt_{ph} (**Supplementary Figure 7.S2**), where the backbone carboxylate of Tyr is part of the third Na⁺ binding site (Na3)^{23,25,32}. Substitution of Y127 to Cys does not affect the ability of EAAT1 to translocate substrate, as we observed a concentration-dependent cellular response of L-glutamate in Y127C cells, albeit with a substantially reduced E_{\max} (**Figure 7.3b**). In addition to forming Na3, Y127 forms a hydrogen bond with the carbonitrile group of UCPH-101²². This bond likely cannot form in Y127C, which results in a loss of UCPH-101 inhibition (**Figure 7.4d**). In line with this, mutation of Y127 to Phe, Leu, Ile or Arg showed a significant drop in pIC₅₀ of UCPH-101 in a [³H]-D-aspartate uptake assay³³. The slight reduction of TFB-TBOA potency suggests that Y127C stabilizes a transporter conformation that affects the binding of the bulky inhibitor, but not the substrate.

M128 is adjacent to Y127 and is exposed to membrane lipids. The M128R mutation was found in an EA6 patient and patch clamp experiments demonstrated that M128R shows a complete loss of glutamate uptake as well as abolished anion currents that could not be explained by slightly reduced surface expression levels¹⁶. Indeed, we did not detect any

L-glutamate or L-aspartate responses in M128R (**Figure 7.3b,e**), which suggests that this mutant is likely transport incompetent. Surprisingly, we observed substantial concentration-dependent positive cellular responses when M128R cells were treated with TFB-TBOA or UCPH-101, which were not observed in EAAT1_{WT} or other mutants (**Supplementary Figure 7.S5**). A recent study demonstrated that mutation of M128 to Arg may inflict two potential disruptions to EAAT1³⁴. The positively charged Arg could flip towards the ‘inside’ of the protein and disrupt the binding of Na⁺ to Na3. Occupation of this site by Na⁺ is crucial to initiate substrate binding and translocation³⁵, which may explain the absence of glutamate transport in M128R. Secondly, the Arg in M128R could flip ‘outward’ towards the lipid bilayer. Molecular dynamics (MD) simulations revealed a local membrane deformation resulting from attraction of polar lipid head groups to the Arg, which recruited a density of water molecules halfway into the bilayer³⁴. This may provide a pathway for Na⁺ ions that enter the Na3 site to leak into the cytosol, which could result in cell volume increase and subsequent morphological changes, as we have shown in **Chapter 6**. Thus, we hypothesize that binding of TFB-TBOA or UCPH-101 to EAAT1 M128R stabilizes an Arg ‘outward’ conformation that allows uncoupled Na⁺ influx, which results in a phenotypic response in the absence of substrate (**Supplementary Figure 7.S5–7.S6**). To our knowledge, this is the first report of inhibitor-induced functional responses in glutamate transporters, which warrants further investigation and could hold promise for future therapeutic strategies.

The Val at position 247 is located in TM4c at the scaD–tranD interface, which contains mostly hydrophobic residues conferring the selectivity of UCPH-101 towards EAAT1²². Mutation to Phe did not alter L-glutamate and L-aspartate responses (**Figure 7.3**), which indicates that V247F conserves substrate translocation. Moreover, UCPH-101 inhibition was unaffected in V247F (**Figure 7.4d**) which suggests that V247 is not crucial to inhibitor binding at the allosteric site. Interestingly, the inhibitory potency of TFB-TBOA was significantly reduced in V247F (**Table 7.2**), contrary to *in silico* predictions showing a slightly enhanced TFB-TBOA binding affinity, if at all (**Table 7.1**). Increasing the bulkiness of the residue may indirectly compromise the size of the hydrophobic cavity that accommodates the trifluoromethyl moiety of TFB-TBOA. This would result in a less favorable orientation of the inhibitor and a reduced affinity for the substrate binding site.

T318A was identified in a patient with episodic ataxia, although there is no evidence that this mutation is pathogenic^{34,36}. Located in TM6 of the tranD, the Thr in EAAT1_{WT} is not involved with substrate or Na⁺ binding sites or subdomain movements. Mutation to Ala increased glutamate uptake and anion currents as a result of increased surface expression of the transporter^{16,34}. Besides an increased substrate E_{max} , we did not observe any significant changes in substrate and inhibitor potency, which suggests that T318A does not alter the function of EAAT1.

V390 is located in TM7a of tranD and is adjacent to F389 and V393, which both make hydrophobic interactions with the chromene scaffold of UCPH-101²². Substrate responses and inhibition by UCPH-101 and TFB-TBOA in V390M were nearly identical to EAAT1_{WT}, which indicates that the introduction of a Met in this position is conservative and does not alter transport function.

The Pro at position 392 is located in TM7a near V390 and is completely conserved throughout the SLC1 family and Glt_{ph}²². P392 is part of the scaD–tranD interface that lines the hydrophobic cavity of the chloride conductive pathway^{37,38}. Mutation of P392 to small hydrophobic residues (Ala, Val) resulted in slightly increased substrate affinities and anion conductances³⁹, which may be reflected by a small increase in pEC₅₀ for L-glutamate and L-aspartate in P392L (**Table 7.2**). Strikingly, while TFB-TBOA binding is unaffected, P392L causes a complete loss of UCPH-101's inhibition of the L-glutamate response (**Figure 7.4b,e**, **Table 7.2**). P392 neighbors F389 and V393, which create hydrophobic interactions with the chromene skeleton of UCPH-101²². Mutation to a slightly bulkier Leu might correct the disruption in the helical turn caused by Pro in TM7a and promote an increase in helix rigidity that displaces the location of the nonpolar residues in this region, which substantially reduces the affinity of UCPH-101 for this site.

Three mutations (A446E, A446V and L448Q) are located in HP2, which is an important structural element that regulates the access of Na⁺ and substrate to their binding sites^{20,22}. In the HP2-closed conformation, the backbone amine of A446 hydrogen bonds with the sidechain carboxylate of L-aspartate²². In our phenotypic assay both A446E and A446V displayed vastly reduced maximal substrate responses but significantly increased affinities (**Table 7.2**), which could be the result of low surface expression or a reduced turnover rate⁴⁰. Notably, mutation to Val at this position abrogates L-glutamate response inhibition, whereas a Glu substitution results in a significantly enhanced potency of TFB-TBOA (**Figure 7.4c,f**, **Table 7.2**). We hypothesize that a bulkier Val sterically clashes with the benzoxyl moiety of TFB-TBOA, which destabilizes the interaction of the inhibitor with HP2 that results in a more flexible 'open' conformation of HP2 and reduced binding affinity of the inhibitor²². Contrarily, a negatively charged Glu might engage in electrostatic interactions with the amide of the benzoylamine moiety of TFB-TBOA, which could stabilize a more favorable 'open' HP2 conformation.

The adjacent HP2 residue L448 is involved in HP2 backbone flexibility, which is essential for K⁺-dependent re-translocation of the tranD during the transport cycle⁴¹. Strikingly, the pIC₅₀ for both TFB-TBOA and UCPH-101 are markedly increased in L448Q. In a previous study, mutation of L448 to Cys reduced L-glutamate affinity and maximal transport rate, but it significantly enhanced the inhibitory potency of the competitive inhibitor DL-TBOA⁴². Similar to A446E, it is likely that the introduction of a polar residue in HP2 may stabilize an 'open' TFB-TBOA-bound conformation, but to a lesser extent a 'closed' substrate-bound conformation. Moreover, the enhanced pIC₅₀ for both UCPH-101 and TFB-TBOA may be the result of a reduced affinity of L-glutamate in the orthosteric site, which could augment the apparent inhibitory potency.

The Arg at position 479 confers substrate selectivity and is conserved among glutamate/aspartate transporters. The guanidinium group of R479 forms a hydrogen bond with the sidechain carboxylate of the substrate during translocation²². Moreover, R479 forms a salt bridge with E406 in TM7 during K⁺ re-translocation, which sterically hinders closure of HP2 and substrate binding^{23,41}. Neutralization of R479 (i.e., mutation to Ala) renders EAAT1 K⁺-independent and results in drastically reduced glutamate/aspartate affinity⁴¹,

which was also observed in Glt_{ph} upon mutation of Arg to Cys⁴³. Although R479W may still be able to form a hydrogen bond with the substrate carboxylate, the bulkiness of the indole moiety likely disrupts the electrostatic interactions in the binding site, which leads to a loss of substrate activity (**Figure 7.2b**). This was evident from the relatively high $\Delta\Delta G_{\text{bind}}$ values for R479W compared to other mutated residues (**Table 7.1**), which indicate a substantially reduced ligand binding affinity.

Taken together, we provide functional assessments of eight EAAT1 mutations that were found in cancer patients, as well as two EA6-associated mutations. We observed divergent effects of EAAT1 variants on substrate-induced cellular responses, as well as orthosteric and allosteric inhibition, in an impedance-based phenotypic assay. These results warrant follow-up experiments that investigate alterations in anion conductivity and substrate transport kinetics, which could help to explain our functional observations. Moreover, while mutations in a ligand binding site may disrupt or stabilize ligand interactions, they could potentially lead to ‘allosteric’ effects *via* disruption of conserved interaction networks⁴⁴. Although we have provided hypotheses on the effects of genetic variants based on literature and available 3D structures, we currently lack information on transporter dynamics to substantiate allosteric effects of these EAAT1 mutants. Ongoing MD simulations on substrate-, Na⁺- and inhibitor-bound EAAT1 structures may provide insight into the effects of mutated residues on subdomain dynamics. Importantly, in order to allocate these missense variants to a substantial involvement in cancer development and progression we require translational studies that link genotype to phenotype. Thus, the methods presented in this chapter may aid in the identification of pathogenic transporter variants, which may have implications for the development of selective and efficacious therapeutics.

7.4 – Materials & methods

7.4.1 – Materials

Modified Jump In T-REx HEK 293 (JumpIn) cells overexpressing human wild-type (EAAT1_{WT}) or mutant EAAT1 (see **section 7.4.6–7.4.9**) were kindly provided by the RESOLUTE consortium (Research Center for Molecular Medicine, Medical University of Vienna, Austria). L-glutamic acid monosodium salt monohydrate, L-aspartic acid monosodium salt monohydrate, doxycycline hyclate, Dulbecco’s modified Eagle’s medium (DMEM) and Dulbecco’s phosphate-buffered saline (PBS) were purchased from Sigma Aldrich (St. Louis, MO, USA). 2-amino-4-(4-methoxyphenyl)-7-(naphthalen-1-yl)-5-oxo-5,6,7,8-tetrahydro-4H-chromene-3-carbonitrile (UCPH-101) was purchased from Santa Cruz Biotechnology (Dallas, TX, USA). (2S,3S)-3-[3-[4-(trifluoromethyl)benzoylamino]benzyloxy] aspartate (TFB-TBOA) was purchased from Axon Medchem (Groningen, The Netherlands). Lipofectamine 3000, P3000 buffer, Gateway LR Clonase II enzyme mix and Proteinase K solution were purchased from ThermoFischer (Waltham, MA, USA). QuikChange II kit was purchased from Agilent Technologies (Santa Clara, CA, USA). QIAprep Spin Miniprep Kit was purchased from QIAGEN (Hilden, Germany). xCELLigence PET E-plates 96 (Agilent Technologies, Santa Clara, CA, USA) were

purchased from Bioké (Leiden, The Netherlands). All other chemicals were of analytical grade and obtained from standard commercial sources.

7.4.2 – Selection of cancer-related mutations

Cancer-related mutations were obtained from the Genomic Data Commons²⁷ version 22.0 released on January 16th 2020, as re-compiled by Bongers *et al.*⁴⁵ Somatic missense mutations were retrieved for gene SLC1A3 (EAAT1) in all cancer types. The 105 unique mutations found were mapped onto the 3D structure of EAAT1 (PDB 5LLU, 5MJU²² and 7AWM²³), with particular attention to the functional motifs and binding sites defined by Canul-Tec *et al.*^{22,23} Two sets of mutations of interest were defined by visual inspection in the proximity (i.e., 5 Å from co-crystallized ligands) of the orthosteric binding site – occupied by the substrate L-aspartate – and allosteric binding site – occupied by allosteric inhibitor UCPH-101. The “orthosteric” set of mutations included P392L, A446E, A446V, L448Q, and R479W. The “allosteric” set of mutations included Y127C, C252F, R388K, F389L, V390M, and I397V. Additionally, mutation V247F is located at the interface of the two sites and was therefore included in both sets.

As reference, we retrieved SLC1A3 (EAAT1) mutations found in natural variance in the 1000 Genomes dataset⁴⁶. This dataset was obtained from the Uniprot variance database in October 2020⁴⁷. For the purpose of comparison, we calculated the percentage of mutations in EAAT1 found in cancer patients and natural variance by dividing the number of mutations in EAAT1 by the number of patients in each dataset (10,179 and 3,202, respectively) and multiplying it by 100%.

7.4.3 – System preparation and molecular docking

The monomeric EAAT1 systems for binding affinity change predictions were prepared from chain A in PDB codes 5LLU and 5MJU²² in ICM-Pro version 3.9-2c (Molsoft LLC, San Diego)^{48,49}. The systems were prepared by optimizing the protonation states and orientation of histidine and cysteine residues, and the orientation of glutamine and asparagine residues. Moreover, the position of hydrogen atoms was sampled and optimized. Stabilizing mutations in residues selected for further analysis were reverted (i.e., C252V, T318M). We subsequently prepared L-glutamate by adding hydrogen atoms and assigning atomic charges and docked it into the orthosteric binding site of PDB 5LLU, originally occupied by L-aspartate. Upon removal of L-aspartate from the binding site, docking was performed with default settings and 10 poses stored by defining the residues surrounding L-aspartate as the binding site. We analyzed the poses in light of the experimental data available, docking scores, and interaction patterns. The pose with the highest docking score was selected for further analysis.

7.4.4 – Binding affinity change predictions

To prioritize mutations for in vitro testing, we predicted changes in EAAT1 binding affinity to endogenous substrates L-aspartate and L-glutamate, and the inhibitors TFB-TBOA (competitive) and UCPH-101 (allosteric) caused by point mutations. We performed this

analysis in ICM-Pro as follows. The difference in binding energy ($\Delta\Delta G_{\text{bind}}$ in kcal/mol) is calculated as the difference between the Gibbs binding energy (ΔG_{bind} in kcal/mol) in the mutant and the wild-type. ΔG_{bind} is calculated for fixed backbone and Monte Carlo-sampled flexible side chains in the vicinity of the mutated residue as the energy of the protein-ligand complex minus the energy of the protein and ligand separately.

For the cancer-related mutations found in the orthosteric binding site (P392L, A446E, A446V, L448Q, and R479W), we calculated $\Delta\Delta G_{\text{bind}}$ for endogenous ligands L-aspartate and L-glutamate (previously docked) in system 5LLU. Moreover, we calculated $\Delta\Delta G_{\text{bind}}$ for the competitive inhibitor TFB-TBOA in system 5MJU. For the cancer-related mutations found in the allosteric binding site (Y127C, C252F, R388K, F389L, V390M, and I397V), $\Delta\Delta G_{\text{bind}}$ was calculated for the allosteric inhibitor UCPH-101 in system 5MJU. For V247F, which is at the interface of both ligand binding sites, $\Delta\Delta G_{\text{bind}}$ was calculated for L-glutamate, L-aspartate, TFB-TBOA and UCPH-101 as described above.

7.4.5 – Structural visualization

All visualizations of EAAT1 structures were generated in PyMOL version 1.3 (Schrödinger LTD) using PDB 7AWM. Where TFB-TBOA was visualized, PDB 5MJU was superimposed on 7AWM.

7.4.6 – Mutagenesis

DNA primers for EAAT1 mutants were designed with a single or double base pair substitution for the resultant amino acid using the QuikChange Primer Design Program and synthesized by Integrated DNA Technologies (IDT, Leuven, Belgium) (Table 7.3). Site-directed mutagenesis was performed using a QuikChange II kit. In brief, per mutant 50 ng template DNA (codon-optimized ORF for EAAT1 (SLC1A3) in a pDONR221 vector (pDONR221-SLC1A3, Addgene #131889)) together with 10 μM forward and reverse primer, 1 μl dNTP mix, 2.5 μl 10x reaction buffer and 2.5 U DNA polymerase were run in a PCR thermal cycler for 22 cycles (each cycle consisted of 30 s 95°C, 1 min 55°C, 10 min 68°C). Non-mutated DNA was removed by addition of 5 U DpnI restriction enzyme for 2 h at 37°C. Mutant DNA was transformed into XL1-Blue competent cells in the presence of 50 $\mu\text{g}/\text{ml}$ kanamycin for selection. Plasmid was isolated using a QIAprep Spin Miniprep Kit verified by Sanger sequencing (Leiden Genome Technology Center, Leiden, The Netherlands).

7.4.7 – Gateway cloning

To allow stable transfection into JumpIn cells, the wild-type (WT) and mutant pDONR221-SLC1A3 plasmids were cloned into a pJTI R4 DEST CMV TO pA expression vector with a C-terminal Twin-Strep-tag and a hemagglutinin (HA)-tag using Gateway cloning. The expression vector contains a tet-operon (TO) that allows doxycycline (dox)-inducible expression of the transgene. In brief, 150 ng pDONR221-SLC1A3 plasmid and 150 ng pJTI R4 DEST CMV TO pA in TE buffer (10 mM Tris, 1 mM EDTA) were incubated with Gateway LR Clonase II enzyme mix at 25°C for 1 h. To remove endogenous nucleases,

Table 7.3 – DNA primers (forward and reverse) that were used to generate eight cancer-related and two ataxia-related EAAT1 mutants. Mutated bases are bolded.

Mutant	Forward primer (5')	Reverse primer (5')
Y127C	GAGAGCCGTGGTGTACT G TATGACCACAACCATCA	TGATGGTTGTGGTCATA C AGTACACCACGGCTCTC
M128R	TGAGAGCCGTGGTGTACTATA G ACCACAACCAT	ATGGTTGTGGT C TATAGTACACCACGGCTCTCA
V247F	AATGCCCTGGGCC TG TCTGTTCAAGCATGTGC	GCACATGCTGAACAC GAA CAGGCCCAGGGCATT
T318A	CAGCTGGCCATGTAC G CCGTGACAGTGATCG	CGATCACTGTACAGG C GTACATGGCCAGCTG
V390M	GACAAGCGGGTGACCAGATT A TGCTGCCAGTG	CACTGGCAGCA TAA ATCTGGTCACCCGCTTGTC
P392L	CAGATTGTGCTG C TAGTGGGCGCCACCA	TGGTGGCGCCCA C TAGCAGCACAATCTG
A446E	CAGGCATCCACAGG AA GGCCTGGTGACCATG	CATGGTCACCAAGGC CTT CCTGTGGGATGCCTG
A446V	GCATCCACAGG T CGGCCTGGTGAC	GTCACCAGGCC A CCTGTGGGATGC
L448Q	CACAGGCCGGCC A GGTGACCATGGT	ACCATGGTCAC T GGCCGGCCTGTG
R479W	GGTTTCGGATAGGCT G TG G ACAACCACAAACGTGCT	AGCACGTTTGTGGTT GTC A CAGCCTATCCAGAAACC

the mixture was incubated with a Proteinase K solution for 10 min at 37°C. The resulting vectors (WT or mutant pJTI-SLC1A3) were transformed into XL1-Blue competent cells in the presence of 100 µg/ml ampicillin for selection. Plasmid was isolated and sequenced as described in the previous section.

7.4.8 – Cell culture

JumpIn-EAAT1 cells were split twice per week to 10 cm dishes in culture medium (high glucose DMEM containing 10% fetal calf serum, 2 mM Glutamax, 100 IU/ml penicillin and 100 µg/ml streptomycin) at 37°C and 5% CO₂. After thawing and recovery, cells were grown for 3–5 days in culture medium with 5 µg/ml blasticidin and 2 mg/ml G418 before switching to culture medium.

7.4.9 – Generation of stably transfected WT and mutant JumpIn-EAAT1 cells

JumpIn cells were seeded at 90,000 cells/well in culture medium onto a 24-well culture plate and grown within 24 h to 60–70% confluence. Per mutant or WT, a mix of 1.8 µl P3000 buffer, 450 µg pJTI R4 Integrase plasmid and 450 µg pJTI-SLC1A3 plasmid in Opti-MEM was added to a mix of 2.1 µl Lipofectamine 3000 in Opti-MEM (90 µl total per condition) and incubated for 5 min at RT. As a control for antibiotic selection, one dish of cells was incubated with sterile water instead of pJTI-SLC1A3. Cells were transfected with 60 µl of the total mix. On the next day the transfection medium was replaced by fresh culture medium. After 24 h cells were trypsinized and seeded onto 6 cm culture dishes at 200,000 cells/well to grow for 3–4 days. When 70% confluence was reached medium was replaced with selection medium (culture medium with 1 mg/ml G418) to select for successfully transfected cells. Selection medium was refreshed every 2–3 days for 2 weeks until non-transfected cells were all dead and colonies had grown in the transfected dishes. Colonies were resuspended in selection medium and grown to confluence before cryofreezing pools of transfected cells. Prior to use in experiments, cells were cultured in regular culture medium for at least 24 h.

7.4.10 – Whole-cell HA-tag ELISA

To determine the relative amount of C-terminal HA-tagged protein expressed in doxycycline (dox)-induced JumpIn-EAAT1 WT and mutant cells, an enzyme-linked immunosorbent assay (ELISA) was performed on whole, permeabilized cells. Each condition was tested in quintuplicate per experiment. Cells were seeded in culture medium onto a 96-well culture plate coated with 0.1 mg/ml poly-D-lysine at 60,000 cells/well in the presence or absence of 1 µg/ml dox (100 µl total volume) and were grown for 22–24 h at 37°C and 5% CO₂. Cells were washed with PBS and fixed with 4% formaldehyde for 10 min, then washed with Tris-buffered saline (TBS). To allow access of the antibodies to the intracellular HA-tag, cells were incubated with permeabilization buffer (TBS + 0.5% Tween-20 (TBST), 2% bovine serum albumin (BSA) and 0.2% saponin) for 60 min at RT. After blocking and permeabilization, cells were incubated with 1:2500 rabbit anti-HA polyclonal antibody (Invitrogen, Carlsbad, CA, USA) for 60 min at RT and washed with TBST. Subsequently, cells were incubated for with 1:3000 goat anti-rabbit horse radish peroxidase (HRP)-conjugated IgG antibody (Brunschwig Chemie, Amsterdam, The Netherlands) for 30 min at RT and washed with TBS. Immunoreactivity was visualized by addition of 3,3',5,5'-tetramethylbenzidine (TMB) for 2.5 min at RT and subsequent quenching with 1 M H₃PO₄. Absorbance was measured at 450 nm using a Wallac EnVision multimode plate reader (PerkinElmer, Groningen, The Netherlands).

7.4.11 – Impedance-based phenotypic assay

To measure functional substrate responses and substrate inhibition on WT and mutant JumpIn-EAAT1 cells, we employed the label-free impedance-based phenotypic assay as described previously in **Chapter 6**. We used an xCELLigence real-time cell analyzer (RTCA) system (Agilent Technologies, Santa Clara, CA, USA) to record real-time changes in cell morphology. The assay principle is that EAAT1-mediated, Na⁺-dependent substrate influx induces cell swelling, which leads to cell spreading. This results in an increased cellular impedance over time and as such is a readout of transporter function. For the assay, JumpIn-EAAT1 cells are cultured in medium onto gold-plated electrodes of a 96-well E-plate and for each well the impedance is measured on predefined time intervals at 10 kHz. The impedance is converted to the unitless parameter Cell Index (CI), which can be plotted over time:

$$CI = \frac{(Z_i - Z_0)\Omega}{15\Omega}$$

where Z_i is the impedance at any given time point and Z_0 is the baseline impedance measured at the start of each experiment⁵⁰.

Assays were performed at 37°C and 5% CO₂ in a final volume of 100 µl/well. Baseline impedance was measured in 40 µl culture medium prior to cell seeding. Cells grown to 70–80% confluence were seeded in 50 µl at 60,000 cells/well in the presence of 1 µg/ml dox to induce EAAT1 expression and left at RT for 30 min prior to placement of the E-plate

in the RTCA recording station. After 22 h, cells were pretreated with 5 μ l vehicle (PBS/DMSO) or, in inhibitor experiments, 1 nM – 10 μ M of TFB-TBOA or UCPH-101 or 1 μ M ouabain, and impedance was recorded for 60 min. Subsequently, cells were stimulated with 5 μ l vehicle (PBS), 10 μ M – 1 mM L-glutamate (submaximal concentration [EC_{80} , 1 mM] in inhibitor experiments) or L-aspartate, 200 nM TFB-TBOA (EC_{50}) or 6.3 μ M UCPH-101 (EC_{50}), and impedance was recorded for 120 min. Each condition was tested in duplicate per experiment and levels of DMSO were kept constant at 0.1% for all assays and wells.

7.4.12 – Data analysis and statistics

7.4.12.1 – Whole-cell HA-tag ELISA

In each experiment, the mean absorbance for each condition was divided over the mean absorbance of non-induced (–dox) JumpIn-EAAT1_{WT} cells to obtain fold expression over –dox cells. To assess whether total protein expression of dox-induced (+dox) JumpIn-EAAT1 mutant cells was significantly different from +dox JumpIn-EAAT1_{WT} cells, a one-way ANOVA with Dunnett's post-hoc test was done for cells that were tested on the same ELISA plate.

7.4.12.2 – Impedance-based phenotypic assay

Data was recorded using RTCA Software v2.0 or v2.1.1 (ACEA Biosciences). Depending on the part that was used for analysis, the CI values were normalized to the time of inhibitor pretreatment or substrate stimulation yielding normalized CI (nCI) values for all subsequent data points. The nCI values were exported and analyzed in GraphPad Prism v9 (GraphPad Software, San Diego, CA, USA). Vehicle-only conditions were subtracted from all other conditions to correct for vehicle-induced, ligand-independent effects. The remaining nCI curves were quantified by analyzing the net area under the curve (AUC) of the first 120 min after substrate stimulation. The AUC values, which are expressed as the cellular response, were fitted to a sigmoidal concentration-effect curve with a variable slope to determine the potencies of the EAAT1 substrates and inhibitors. Data are shown as the mean \pm standard error of the mean (SEM) of at least three separate experiments each performed in duplicate, unless stated otherwise. Comparison of multiple mean values to a control (i.e., EAAT1_{WT}) was done using a one-way ANOVA with Dunnett's post-hoc test. Differences were considered statistically significant when p-values were below 0.05.

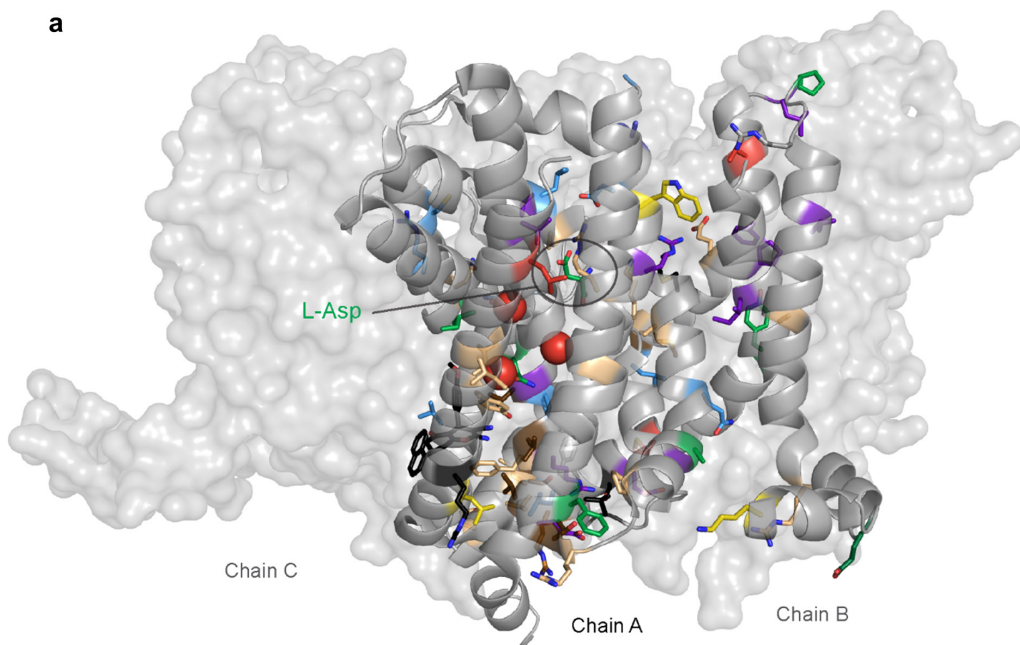
References

1. Tzingounis, A. V. & Wadiche, J. I. (2007) Glutamate transporters: confining runaway excitation by shaping synaptic transmission. *Nat. Rev. Neurosci.* **8**, 935–947.
2. Vandenberg, R. J. & Ryan, R. M. (2013) Mechanisms of glutamate transport. *Physiol. Rev.* **93**, 1621–1657.
3. Alleva, C., Machtens, J.-P., Kortzak, D., Weyand, I. & Fahlke, C. (2022) Molecular basis of coupled transport and anion conduction in excitatory amino acid transporters. *Neurochem. Res.* **47**, 9–22.
4. Peterson, A. R. & Binder, D. K. (2020) Astrocyte glutamate uptake and signaling as novel targets for antiepileptogenic therapy. *Front. Neurol.* **11**, 1006.
5. Lewerenz, J. & Maher, P. (2015) Chronic glutamate toxicity in neurodegenerative diseases—What is the evidence? *Front. Neurosci.* **9**, 1–20.
6. Yi, H., Talmon, G. & Wang, J. (2020) Glutamate in cancers: from metabolism to signaling. *J. Biomed. Res.* **34**, 260–270.
7. Freidman, N. *et al.* (2020) Amino acid transporters and exchangers from the SLC1A family: Structure, mechanism and roles in physiology and cancer. *Neurochem. Res.* **45**, 1268–1286.
8. Kortagere, S. *et al.* (2018) Identification of novel allosteric modulators of glutamate transporter EAAT2. *ACS Chem. Neurosci.* **9**, 522–534.
9. Jensen, A. A. *et al.* (2009) Discovery of the first selective inhibitor of excitatory amino acid transporter subtype 1. *J. Med. Chem.* **52**, 912–915.
10. Takano, T. *et al.* (2001) Glutamate release promotes growth of malignant gliomas. *Nat. Med.* **7**, 1010–1015.
11. Robert, S. M. & Sontheimer, H. (2014) Glutamate transporters in the biology of malignant gliomas. *Cell. Mol. Life Sci.* **71**, 1839–1854.
12. Corbetta, C. *et al.* (2019) Altered function of the glutamate–aspartate transporter GLAST, a potential therapeutic target in glioblastoma. *Int. J. Cancer* **144**, 2539–2554.
13. Garcia-Bermudez, J. *et al.* (2018) Aspartate is a limiting metabolite for cancer cell proliferation under hypoxia and in tumours. *Nat. Cell Biol.* **20**, 775–781.
14. Tajan, M. *et al.* (2018) A role for p53 in the adaptation to glutamine starvation through the expression of SLC1A3. *Cell Metab.* **28**, 721–736.
15. Bacci, M. *et al.* (2019) Reprogramming of amino acid transporters to support aspartate and glutamate dependency sustains endocrine resistance in breast cancer. *Cell Rep.* **28**, 104–118.
16. Chivukula, A. S., Suslova, M., Kortzak, D., Kovermann, P. & Fahlke, C. (2020) Functional consequences of SLC1A3 mutations associated with episodic ataxia 6. *Hum. Mutat.* **41**, 1892–1905.
17. Adamczyk, A. *et al.* (2011) Genetic and functional studies of a missense variant in a glutamate transporter, SLC1A3, in Tourette syndrome. *Psychiatr. Genet.* **21**, 90–97.
18. Kovermann, P. *et al.* (2017) Impaired K⁺ binding to glial glutamate transporter EAAT1 in migraine. *Sci. Rep.* **7**, 13913.
19. van Amen-Hellebrekers, C. J. M. *et al.* (2016) Duplications of SLC1A3: Associated with ADHD and autism. *Eur. J. Med. Genet.* **59**, 373–376.
20. Boudker, O., Ryan, R. M., Yernool, D., Shimamoto, K. & Gouaux, E. (2007) Coupling substrate and ion binding to extracellular gate of a sodium-dependent aspartate transporter. *Nature* **445**, 387–393.
21. Guskov, A., Jensen, S., Faustino, I., Marrink, S. J. & Slotboom, D. J. (2016) Coupled binding mechanism of three sodium ions and aspartate in the glutamate transporter homologue GltTk. *Nat. Commun.* **7**, 13420.
22. Canul-Tec, J. C. *et al.* (2017) Structure and allosteric inhibition of excitatory amino acid transporter 1. *Nature* **544**, 446–451.
23. Canul-Tec, J. C. *et al.* (2022) The ion-coupling mechanism of human excitatory amino acid transporters. *EMBO J.* **41**, e108341.
24. Kato, T. *et al.* (2021) Structural insights into human excitatory amino acid transporter EAAT2. *bioRxiv preprint*, 1–34.
25. Qiu, B., Matthies, D., Forte, E., Yu, Z. & Boudker, O. (2021) Cryo-EM structures of excitatory amino acid transporter 3 visualize coupled substrate, sodium, and proton binding and transport. *Sci. Adv.* **7**, eabf5814.
26. Schaller, L. & Lauschke, V. M. (2019) The genetic landscape of the human solute carrier (SLC) transporter superfamily. *Hum. Genet.* **138**, 1359–1377.
27. Jensen, M. A., Ferretti, V., Grossman, R. L. & Staudt, L. M. (2017) The NCI Genomic Data Commons as an engine for precision medicine. *Blood* **130**, 453–459.
28. Shimamoto, K. *et al.* (2004) Characterization of novel L-threo- β -Benzoyloxyaspartate derivatives, potent blockers of the glutamate transporters. *Mol. Pharmacol.* **65**, 1008–1015.
29. Cournia, Z., Allen, B. & Sherman, W. (2017) Relative binding free energy calculations in drug discovery: Recent advances and practical considerations. *J. Chem. Inf. Model.* **57**, 2911–2937.
30. Vettore, L., Westbrook, R. L. & Tennant, D. A. (2020) New aspects of amino acid metabolism in cancer. *Br. J. Cancer* **122**, 150–156.
31. Winter, N., Kovermann, P. & Fahlke, C. (2012) A point mutation associated with episodic ataxia 6 increases glutamate transporter anion currents. *Brain* **135**, 3416–3425.

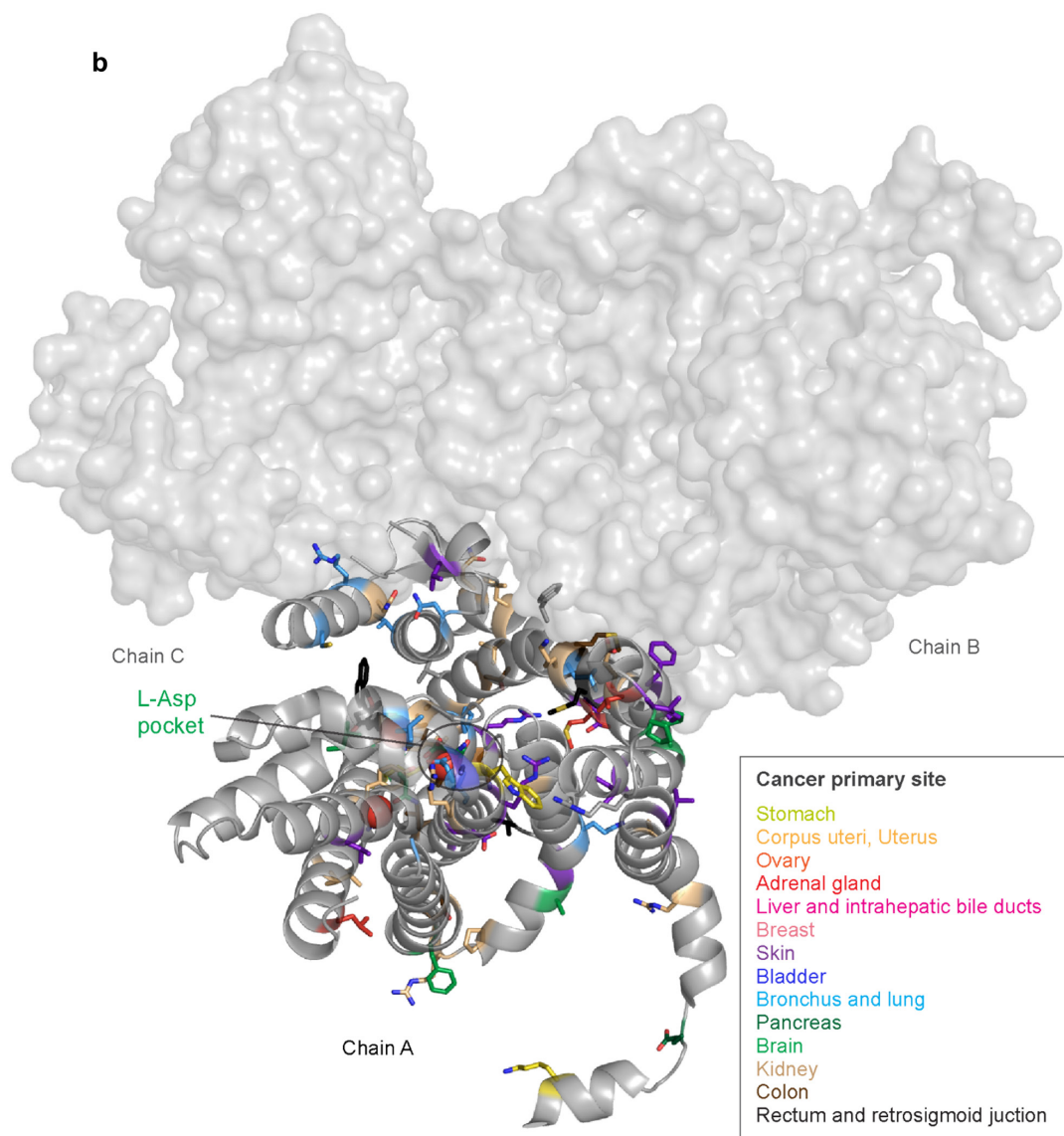
32. Alleva, C. *et al.* (2020) Na⁺-dependent gate dynamics and electrostatic attraction ensure substrate coupling in glutamate transporters. *Sci. Adv.* **6**, eaba9854.
33. Abrahamsen, B. *et al.* (2013) Allosteric modulation of an excitatory amino acid transporter: the subtype-selective inhibitor UCPH-101 exerts sustained inhibition of EAAT1 through an intramonomeric site in the trimerization domain. *J. Neurosci.* **33**, 1068–1087.
34. Wu, Q. *et al.* (2022) Ataxia-linked SLC1A3 mutations alter EAAT1 chloride channel activity and glial regulation of CNS function. *J. Clin. Invest.* **132**, e154891.
35. Bastug, T. *et al.* (2012) Position of the third Na⁺ site in the aspartate transporter GltPh and the human glutamate transporter, EAAT1. *PLoS One* **7**, e33058.
36. Choi, K.-D. *et al.* (2017) Genetic variants associated with episodic ataxia in Korea. *Sci. Rep.* **7**, 13855.
37. Seal, R. P. & Amara, S. G. (1998) A reentrant loop domain in the glutamate carrier EAAT1 participates in substrate binding and translocation. *Neuron* **21**, 1487–1498.
38. Chen, I. *et al.* (2021) Glutamate transporters have a chloride channel with two hydrophobic gates. *Nature* **591**, 327–331.
39. Cater, R. J., Vandenberg, R. J. & Ryan, R. M. (2014) The domain interface of the human glutamate transporter EAAT1 mediates chloride permeation. *Biophys. J.* **107**, 621–629.
40. Trinco, G. *et al.* (2021) Kinetic mechanism of Na⁺-coupled aspartate transport catalyzed by GltTk. *Commun. Biol.* **4**, 751.
41. Kortzak, D. *et al.* (2019) Allosteric gate modulation confers K⁺ coupling in glutamate transporters. *EMBO J.* **38**, e101468.
42. Leighton, B. H., Seal, R. P., Shimamoto, K. & Amara, S. G. (2002) A hydrophobic domain in glutamate transporters forms an extracellular helix associated with the permeation pathway for substrates. *J. Biol. Chem.* **277**, 29847–29855.
43. Scopelliti, A. J., Font, J., Vandenberg, R. J., Boudker, O. & Ryan, R. M. (2018) Structural characterisation reveals insights into substrate recognition by the glutamine transporter ASCT2/SLC1A5. *Nat. Commun.* **9**, 38.
44. Levine, M. V., Cuendet, M. A., Khelashvili, G. & Weinstein, H. (2016) Allosteric mechanisms of molecular machines at the membrane: Transport by sodium-coupled symporters. *Chem. Rev.* **116**, 6552–6587.
45. Bongers, B. J. *et al.* (2021) Pan-cancer in silico analysis of somatic mutations in G-protein coupled receptors: The effect of evolutionary conservation and natural variance. *bioRxiv preprint*, 1–41.
46. Auton, A. *et al.* (2015) A global reference for human genetic variation. *Nature* **526**, 68–74.
47. The UniProt Consortium. (2019) UniProt: a worldwide hub of protein knowledge. *Nucleic Acids Res.* **47**, D506–D515.
48. Abagyan, R., Totrov, M. & Kuznetsov, D. (1994) ICM—A new method for protein modeling and design: Applications to docking and structure prediction from the distorted native conformation. *J. Comput. Chem.* **15**, 488–506.
49. Neves, M. A. C., Totrov, M. & Abagyan, R. (2012) Docking and scoring with ICM: The benchmarking results and strategies for improvement. *J. Comput. Aided. Mol. Des.* **26**, 675–686.
50. Kho, D. *et al.* (2015) Application of xCELLigence RTCA biosensor technology for revealing the profile and window of drug responsiveness in real time. *Biosensors* **5**, 199–222.

Supplementary Information

a

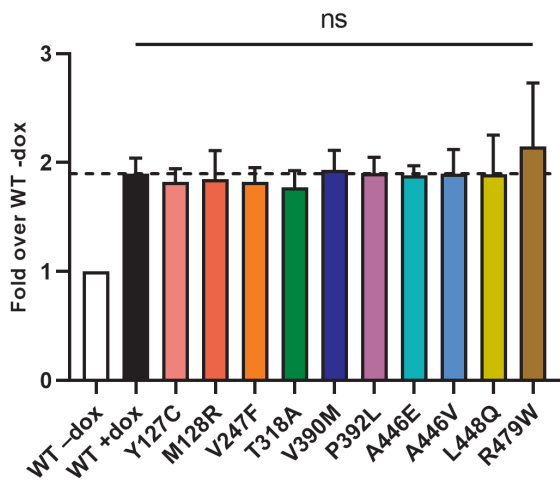


Supplementary Figure 7.S1 – Structural distribution of cancer-related mutants per cancer type. Mutations from the Genomic Data Commons mapped onto the biological assembly of EAAT1 (PDB 7AWM). Chain A is represented as a grey cartoon, while chains B and C are represented as grey surfaces. The co-crystallized substrate, L-aspartate, is represented as green sticks in chain A. The three coordinated Na⁺ ions are represented as red spheres in chain A. Residues that have been observed mutated in cancer patients are colored by cancer primary site following the colors in the key. (a) Frontal view, as aligned with cellular membrane. (b) Top view, as seen from the extracellular side.

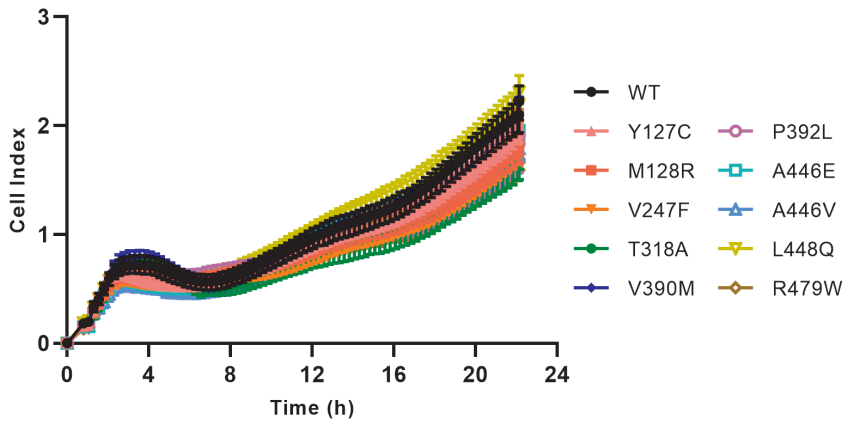


sp P43003 EAA1_HUMAN/1-542	1 - - - - - MTKSNGEPEKMGGRMERFQQGVKRTLLAKKKVQNI TKEDVKYSYLFNRNFAVLLTVAVTIVGT ILG 65
sp P43004 EAA2_HUMAN/1-574	1 MASTEGANNMPK - - - - - QVEVRMHDSHLGSEEPKRRHLGLRCDKLGKNNLLTLTVFGVILGAVCG 61
sp P43005 EAA3_HUMAN/1-524	1 - - - - - MGKPAKRGCEWKRFLKNNWVLLSTVAVVVLG I TTG 35
sp P48664 EAA4_HUMAN/1-564	1 - MSSHGNSLFLRESGQRLGRVWGLRLQESLQQRALRTRLRLQMTLLEHVLRLRRNAFILLTVSAVVIGVSLA 73
sp O00341 EAA5_HUMAN/1-560	1 - - - - - MVPHA I LARGDRVCCRRNGLL ILSVL SV I VGCLL G 34
sp Q59010 GLT_PYRHO/1-425	1 - - - - - MGLYRKYYIEPYVLQKILLGLILGAI VG 27
sp P43003 EAA1_HUMAN/1-542	66 FTLRP-YRMSYREVKYKFSFGPELLMRMLQMLVLPL I ISSLVTGMAALDSKASGKMGMRVAVVYMTTT I IAVVIG 138
sp P43004 EAA2_HUMAN/1-574	62 GLRLASPIHPDVVMI IAFPGD I LMRMLKML I LPL I ISSL I TGLSGLDAKASGR I GLTRAMVYVMTTT I IAAVLG 135
sp P43005 EAA3_HUMAN/1-524	36 VLVRHNSNLSTLEKFFAFPGEL I LMRMLKML I LPL I I SSMITGVAAALDSNVSGK I GLRAVVYVYVCTT I IAVILG 109
sp P48664 EAA4_HUMAN/1-564	74 FALRP-QQLTYRQ I KYFSFGPELLMRMLQMLVLPL I VSSSLVTGMAALDNKATGRMGMRVAVVYVCTT I IAVILG 146
sp O00341 EAA5_HUMAN/1-560	35 FFLRT-RRLSPQEI SYFOFPELLMRMLKML I LPL I VSSSLMSGLASLDAKTSRLGLVLTVAVYVLTTFMAV I VG 107
sp Q59010 GLT_PYRHO/1-425	28 L I L G H - V G Y A D A V K T Y V K P F G D L F V R L L K M L V M P I V F A S L V V G A A S I S P A R L G R V G V K I V V Y V I L T S A F A V T L G 100
sp P43003 EAA1_HUMAN/1-542	139 I I I V I I I H P G K G T K E - N M H R E G K I V R V T A A D A F L D L I R N M F P P N L V E A C F K Q F K T N Y E K R S F K V P I Q A N E T L - - 209
sp P43004 EAA2_HUMAN/1-574	136 V I L V L A I H P G N P K L K K Q L G P G K K N D E V S S L D A F L D L I R N L F P E N L V Q A C F Q Q I Q T V T K K V L V A P P P D E E A N A - - 207
sp P43005 EAA3_HUMAN/1-524	110 I V L V V S I K P G V T O K V G E I A R T G S T P E V S T V D A M L D L I R N M F P E N L V Q A C F Q Q Y K T K R E E V K P P S D - - P E M N - - 178
sp P48664 EAA4_HUMAN/1-564	147 I L M V T I I H P G K G S K E - G L H R E G R I E P T A D A F M D L I R N M F P P N L V E A C F K Q F K T Q Y S T R V R T T M V R T E N G S E 219
sp O00341 EAA5_HUMAN/1-560	108 I F M V S I I H P G S A A Q K - E T T E Q S G K P I M S A D A L L D L I R N M F P A N L V E A T F K Q Y R T K T T P V V K - S P K V A P E E A P - 178
sp Q59010 GLT_PYRHO/1-425	101 I I M A R L F N P G A G I H L A V G - - - G Q Q F Q P Q A P P L V K I L L D I V P T N P F - - - - - 143
sp P43003 EAA1_HUMAN/1-542	210 V - - - - - G A V I - N N V S E A M E T L T R - - I T E E L V P V P G S V N G V N A L G L V V F S M C F G F V I G - - - - - N 259
sp P43004 EAA2_HUMAN/1-574	208 - - - - - T S A V V S L N E T V T E V P E E - T K M V I K K G L E F K D G M N V L G L G F F I A F G I A M G - - - - - K 258
sp P43005 EAA3_HUMAN/1-524	179 - - - - - M T E - E S F T A V M T T A I S K N K T K E Y K I V G M Y S D G I N V L G L I V F C L Y F G L V I G - - - - - K 228
sp P48664 EAA4_HUMAN/1-564	220 P G A S M P P P S V E N G T S F L - E N V T R A L G T L Q E M L S F E E T V P V P G S A N G I N A L G L V V F S A F G L V I G - - - - - G 284
sp O00341 EAA5_HUMAN/1-560	179 P R R I L I Y G V Q E E N - G S H V - Q N F A L D L T P P P E - - - - V V Y K S E P T S D G M N V L G I V F F S A T G M I L G - - - - - R 238
sp Q59010 GLT_PYRHO/1-425	144 - - - - - G A - L A N G Q V L T P F F A I L G I A I T Y L M N S E N E K 175
sp P43003 EAA1_HUMAN/1-542	260 M K E Q G Q A L R E F F D S L N E A I M R L V A V I M W Y A P V G I L F L I A G K I V E M E D M G V I G G L A M Y T V T V I V G L L I H A V I V L 333
sp P43004 EAA2_HUMAN/1-574	259 M G D Q A K L M V D F F N I L N E I V M K L V I M I M W Y S P L G I A C L I C G K I I A I K D L E V V A R Q L G M Y M V T V I I G L I H G G I F L 332
sp P43005 EAA3_HUMAN/1-524	229 M G E K G Q I L V D F F N A L S D A T M K I V Q I I M C Y M P L G I L F L I A G K I I E V E D W E I F - R K L G L Y M A T V T L G L A I H S I V I L 301
sp P48664 EAA4_HUMAN/1-564	265 M K H K G R V L R D F F D S L N E A I M R L V G I I I W Y A P V G I L F L I A G K I L E M E D M A V L G G Q L G M Y T V T V I V G L F L H A G I V L 358
sp O00341 EAA5_HUMAN/1-560	239 M G D S G A P L V S F C Q C L N E S V M K I V A V A V W Y P F F G I V F L I A G K I L E M D P R A V G K K G F G Y S V T V V C G L V L H G L F I L 312
sp Q59010 GLT_PYRHO/1-425	176 V R K S A E T L D A I N G L A E A M Y K I V N G V M Q Y A P I G V F A L I A Y V M A E Q - G V K V - G E L A K V T A A V Y V G L T Q I L - - - 244
sp P43003 EAA1_HUMAN/1-542	334 P L L Y F L - - - V T R K N P W F I G G L Q A L I T A L G T S S S A T L P I T F K C L E E N N G V D K R V T R F V L P V G A T I N M D G T A L 404
sp P43004 EAA2_HUMAN/1-574	333 P L I Y F V - - - V T R K N P F S F F A G I F Q A W I T A L G T A S S A G T L P V T F R C L E E N L G I D K R V T R F V L P V G A T I N M D G T A L 403
sp P43005 EAA3_HUMAN/1-524	302 P L I Y F I - - - V V R K N P F R F A M G M A Q A L I T A L M I S S S A T L P V T F R C A E E N N Q V D K R I T R F V L P V G A T I N M D G T A L 372
sp P48664 EAA4_HUMAN/1-564	359 P L I Y F L - - - V T H R N P F F I G M L Q A L I T A M G T S S S A T L P I T F R C L E E G L G V D R R I T R F V L P V G A T I N M D G T A L 429
sp O00341 EAA5_HUMAN/1-560	313 P L L Y F F - - - I T K K N P I V F I R G I L Q A L L I A L A T S S S A T L P I T F K C L E E N N I D R R I A R F V L P V G A T I N M D G T A L 383
sp Q59010 GLT_PYRHO/1-425	245 - L V V F Y L L K I Y G I D P I S F I K K A K D A M L T A F V T R S S S G T L P V T M R V A K E - M G I S E G I Y S F T L P L G A T I N M D G T A L 316
sp P43003 EAA1_HUMAN/1-542	405 Y E A L A A I F I A Q V N N F E L N F G Q I I T I S I T A T A A S I G A A G I P Q A G L V T M V I V L T S V G L P T D D I - - - - - T L I I A V D 472
sp P43004 EAA2_HUMAN/1-574	404 Y E A V A A I F I A Q M N G V V L D G G Q I V T V S L T A L S V G A A S I P S A G L V T M L L I T A V G L P T E D I - - - - - S L L V A V D 471
sp P43005 EAA3_HUMAN/1-524	373 Y E A V A A V I F A Q L N D L D L G I Q I I T I S I T A T S A S I G A A G V P Q A G L V T M V I V L S A V G L P A E D V - - - - - T L I I A V D 440
sp P48664 EAA4_HUMAN/1-564	430 Y E A L A A I F I A Q V N N Y E L N L G Q I I T I S I T A T A A S V G A A G I P Q A G L V T M V I V L T S V G L P T D D I - - - - - T L I I A V D 497
sp O00341 EAA5_HUMAN/1-560	374 Y E A V A A I F I A Q V N N Y E L D F G Q I I T I S I T A T A A S I G A A G I P Q A G L V T M V I V L T S V G L P T D D I - - - - - T L I I A V D 497
sp Q59010 GLT_PYRHO/1-425	317 Y G V C T F F I A N A L G S H L T V G Q Q L T I V L T A V L A S I G T A G V P G A G A I M L A M V L E S V G L P L D P N V A A A Y A M I L G I D 390
sp P43003 EAA1_HUMAN/1-542	473 W F L D R L R T T T N V L G D S L G A G I V E H L S R H E L K N R D V E M G N S V I E E N E M K K P Y Q - - - - - L I A Q D N E T E - - K P I - D S - E 539
sp P43004 EAA2_HUMAN/1-574	472 W L D R M R T S V N V V G D S F G A G I V Y H L S K S E L D T I D S Q H R V H - - E D I E M T K T Q S I Y D D M K N H R E S N S N Q C V Y A A H 543
sp P43005 EAA3_HUMAN/1-524	441 W L D R F R T M V N V L G D A F G T G I V E K L S K K E L Q M D V S E V N - - - - - I V N P F A L E S T I L D N E D S D - T K K S Y N G G 507
sp P48664 EAA4_HUMAN/1-564	498 W F L D R L R T M T N V L G D S I G A A V I E H L S Q R E L E Q E A E L T - - - - - L P S L G K P Y K - - - - - S L M A Q E K G A - S R G R G G N - E 561
sp O00341 EAA5_HUMAN/1-560	452 W A L D R F R T M I N V L G D A L A A G I M A H I C R K D F A R D T G T E K L - - - - - L P C E T K P V S L Q E I V A A Q Q N G C - V K S V A E A S E 520
sp Q59010 GLT_PYRHO/1-425	391 A I L D M G R T M V N Y T G D L T G T A I V A K T E G - E L E K G V I A - - - - - 425
sp P43003 EAA1_HUMAN/1-542	540 T K M - - - - - 542
sp P43004 EAA2_HUMAN/1-574	544 S V I V D E C K V T L A - - - - - A N G K S A D C S V E E E P W K R E K 574
sp P43005 EAA3_HUMAN/1-524	508 F A V D - - - - K S D T I S F T Q T S Q F - - - - - 524
sp P48664 EAA4_HUMAN/1-564	562 S A M - - - - - 564
sp O00341 EAA5_HUMAN/1-560	521 L G P T C P H H V P V Q V E Q D E E L P A A S L N H C T I Q I S E L E T N V 560
sp Q59010 GLT_PYRHO/1-425	- - - - -

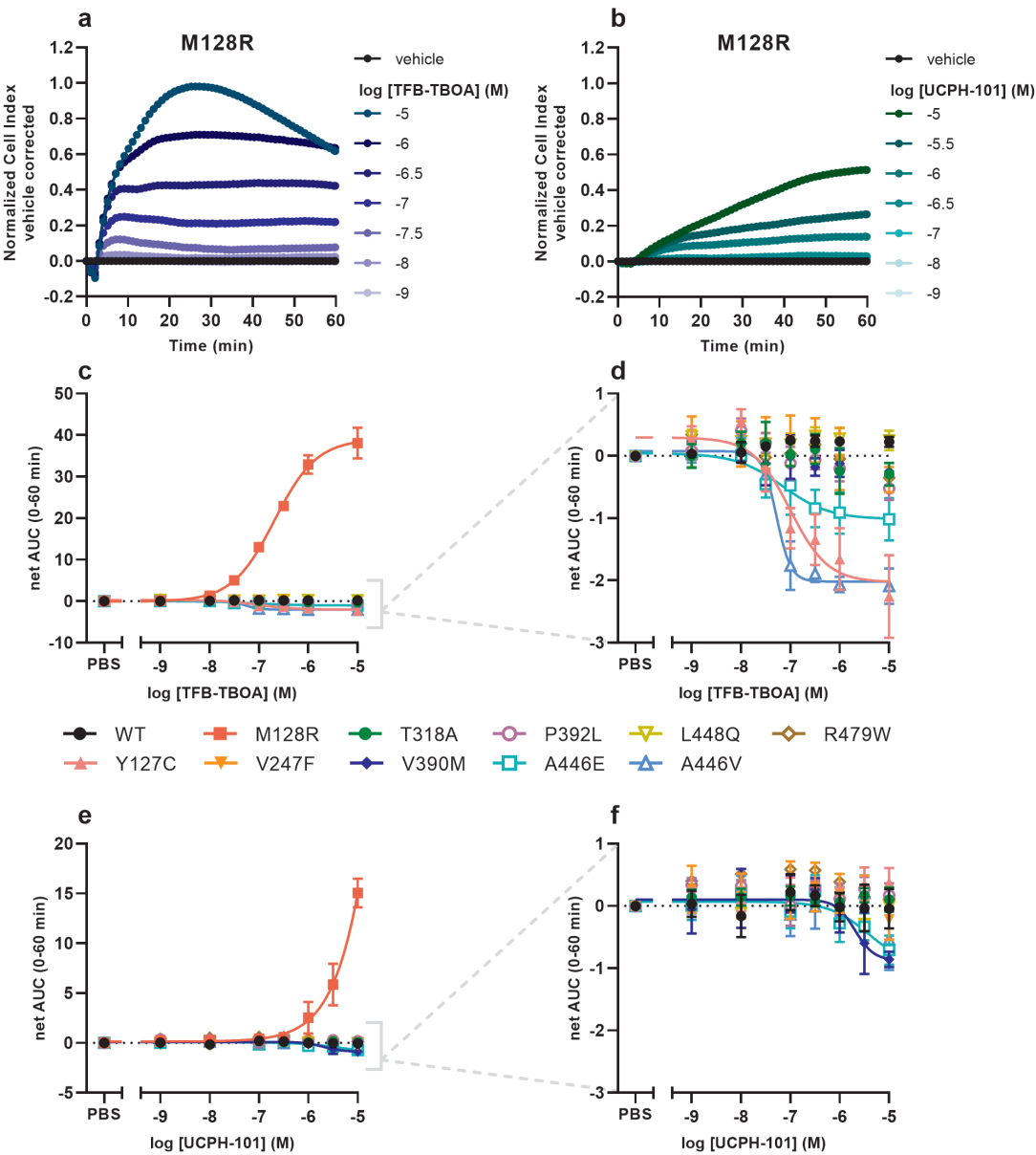
Supplementary Figure 7.S2 – Conservation of selected cancer-related mutants in EAAT family. Multiple sequence alignment of human EAATs (EAAT1–5) and *Pyrococcus horikoshii* homolog GlT_{ph} computed in Clustal-Omega. Colored, the positions of the cancer-related mutants analyzed *in vitro*: Y127C (pink), V247F (orange), V390M (dark blue), P392L (purple), A446V/E (blue), L448Q (yellow), R479W (brown). For reference, ataxia-related reference mutants are also colored: M128R (red) and T318A (green).



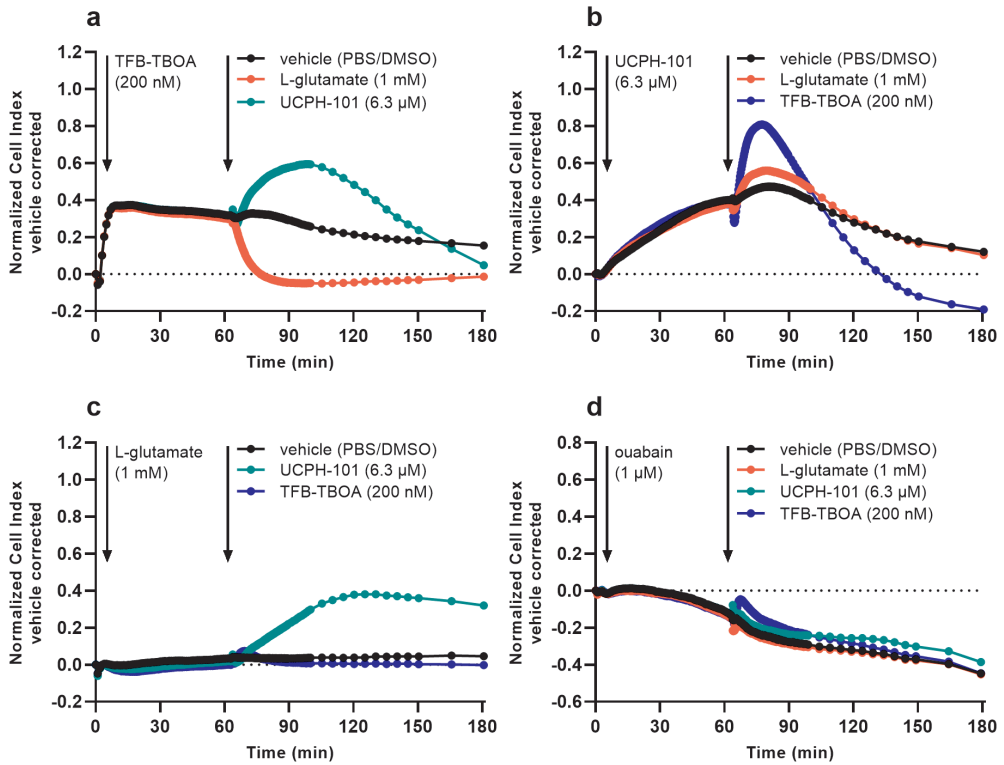
Supplementary Figure 7.S3 – Whole-cell HA-tag ELISA on EAAT1_{WT} and mutant cells. Cells were grown for 24 h in the absence (-dox, WT only) or presence (+dox, WT and mutants) of 1 µg/ml doxycycline. Presence of total HA-tagged protein (plasma membrane and cytosolic) was determined in permeabilized cells. Absorbance for each condition is expressed as fold expression over WT (-dox). Data are shown as the mean ± SEM of twelve (WT), six (M128R) or three (rest) individual experiments each performed in quintuplicate. Significant differences between EAAT1_{WT} and mutant cells were determined using one-way ANOVA with Dunnett’s post-hoc test. ns = not significant for all mutants.



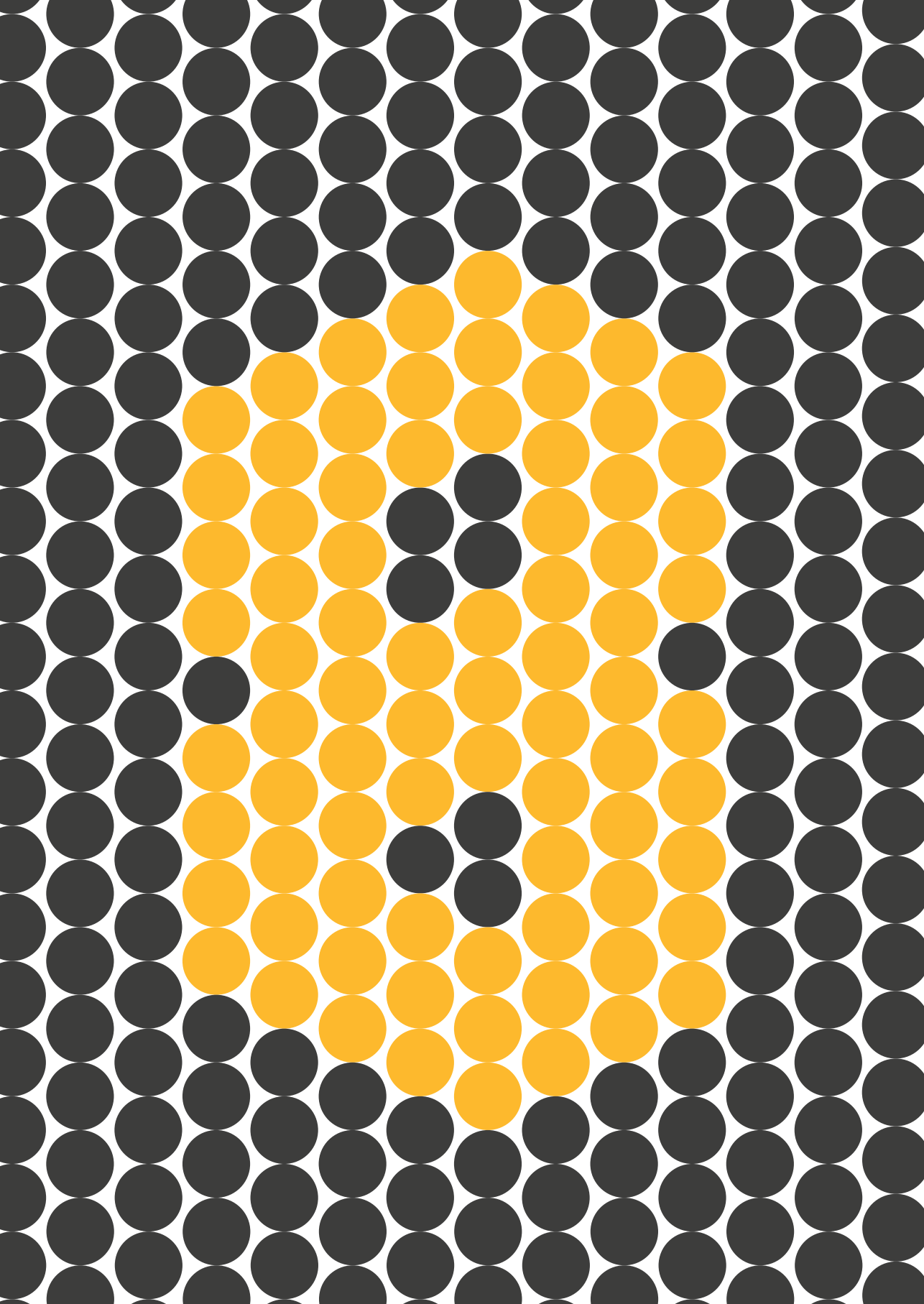
Supplementary Figure 7.S4 – Representative growth curves of EAAT1_{WT} and EAAT1 mutant cells in an impedance-based phenotypic assay. Data are shown as the mean ± SD of eight replicates from a representative experiment.



Supplementary Figure 7.S5 – Cellular responses of TFB-TBOA and UCPH-101 during pretreatment in an impedance-based phenotypic assay on EAAT_{WT} and mutant cells. **(a,b)** Vehicle-corrected normalized Cell Index traces of M128R cells pretreated with **(a)** TFB-TBOA or **(b)** UCPH-101 from a representative experiment. **(c)** Concentration-response curves of TFB-TBOA on M128R cells and **(d)** zoom-in on EAAT_{1WT} and other mutant cells. **(e)** Concentration-response curves of UCPH-101 on M128R cells and **(f)** zoom-in on EAAT_{1WT} and other mutant cells. Cellular response is expressed as the net AUC of the first 60 min after inhibitor pretreatment. Data are shown as the mean ± SEM of three individual experiments each performed in duplicate.



Supplementary Figure 7.S6 – Modulation of cellular responses by L-glutamate and inhibitors in an impedance-based phenotypic assay on M128R cells. **(a)** Pretreatment with EC_{50} (200 nM) TFB-TBOA and stimulation with vehicle, 1 mM L-glutamate or EC_{50} (6.3 μ M) UCPH-101. **(b)** Pretreatment with 6.3 μ M UCPH-101 and stimulation with vehicle, 1 mM L-glutamate or 200 nM TFB-TBOA. **(c)** Pretreatment with 1 mM L-glutamate and stimulation with vehicle, 6.3 μ M UCPH-101 or 200 nM TFB-TBOA. **(d)** Pretreatment with 1 μ M ouabain (Na^+/K^+ -ATPase inhibitor) and stimulation with vehicle, 1 mM L-glutamate, 6.3 μ M UCPH-101 or 200 nM TFB-TBOA. Data show vehicle-corrected normalized Cell Index traces of M128R cells pretreated for 60 min and subsequently stimulated for 120 min. Traces were normalized at the time point prior to pretreatment. Cells pretreated and stimulated with vehicle (PBS/DMSO) were used for vehicle-correction.



CHAPTER 8

General discussion, conclusions and future perspectives

The ubiquitous presence of solute carrier (SLC) transporters makes them indispensable in many physiological processes. When these transport proteins are dysfunctional, however, they can cause or contribute to the development of diseases. In the search towards effective therapeutics that directly or indirectly modulate the function of SLCs, it is crucial to have access to robust and reliable *in vitro* assays that can help identify substrates, inhibitors and modulators. The chapters in this thesis describe the exploration, development, validation and application of two novel types of transporter assays, which are based on the use of a label-free, impedance-based technology. The main results and conclusions of these studies will be summarized and discussed in the following sections. The findings will be put in perspective of traditional concepts and the future of label-free assays in SLC research will be speculated on. Ultimately, this thesis advocates the impedance-based label-free technology as the ‘new kid on the block’ of SLC assays and marks the advent of a novel method to investigate this protein family.

General discussion and conclusions

In order to check whether a molecule possesses any biological activity that may alleviate a patient's symptoms or prevent disease phenotypes, we need assays that mimic a biological system in which the molecule may be active. Prior to testing any molecule in live organisms – be it zebrafish or humans – we would need to know upfront whether that molecule can engage the intended target (e.g., receptor or transporter) and evokes the intended response (i.e., activation or inhibition), preferably with good pharmacokinetic properties and limited off-target toxicity. Computational models, such as the ones described in **Chapter 4**, have become increasingly powerful tools in the prediction of a molecule's activity at any biological target, which can be used to conceive previously unimagined molecular scaffolds and select candidate molecules for *in vitro* testing in an early stage of drug discovery^{1,2}. Although these computational approaches can help to cut the amount of labor-intensive wet-lab tests, the predicted molecules still need to be tested for their activity on the physical target of interest.

8.1 – The added value of cell-based label-free assays

Numerous *in vitro* model systems have been developed to test molecules and address a wide range of pharmacological research questions in various stages of the drug discovery process, being based on the use of cells (e.g., heterologous bacteria/yeast/mammalian cells, primary cells, organoids, 'organ-on-a-chip'^{3–5}) or cell-free preparations (e.g., cell extracts, membranes, purified or engineered protein^{6,7}). Where some systems allow a detailed detection and/or visualization of physiological events upon treatment, there is always a trade-off in terms of throughput (i.e., the number of molecules that can be tested within a specified time), running costs per sample, complexity of data analysis/interpretation and physiological relevance. In **Chapter 1**, the advantages and limitations of established techniques and model systems for solute carrier (SLC) transporters are summarized with regard to their trade-offs (**Table 1.1**). The main conclusion of this summary is that the current SLC assays are either label-based, low in throughput, incompatible with live cells and/or unable to perform real-time measurements. If high-throughput screening (HTS) of molecules in a closer-to-physiology setting is to the benefit of successful translational drug discovery, then there is a need for alternative assay strategies to aid in this process. Thus, cell-based label-free assays are an attractive approach to assess target pharmacology in live cells without the use of cell-intrusive and non-physiological chemical labels.

Cell-based label-free assays offer an advantage over conventional biochemical assays – in addition to offering increased physiological relevance⁸ – in that they are able to capture the sum of events that follow a perturbation of the cell (e.g., receptor activation or the uptake of cytotoxic compounds) in real-time, instead of focusing on a single pathway downstream of this perturbation (e.g., cAMP production, protein phosphorylation or apoptosis markers) at a fixed point in time^{9,10}. It is this characteristic of cell-based label-free assays that is at the basis of the assays that are described in the chapters of this thesis. The impedance-based biosensor xCELLigence has previously been used to detect changes in cells' morphology as a result of the activation of G protein-coupled receptors (GPCRs)

that are expressed on these cells^{11,12}. The intracellular signaling events that are triggered upon GPCR activation lead to ordered and dynamic rearrangement of the cytoskeleton and redistribution of proteins and organelles, which can be interpreted as the functional or phenotypic effect of receptor activation^{12,13}. For example, adenosine receptors (ARs) are activated by their endogenous ligand, adenosine, and several studies demonstrate that activation of subtypes of these receptors (A_1AR ¹⁴, $A_{2A}AR$ ¹⁵, $A_{2B}AR$ ¹⁶) by adenosine or other agonists leads to temporary contraction, spreading or shrinkage of the cells, which can be deduced from the real-time changes in electrical impedance – expressed as the Cell Index (CI) – that are recorded by the xCELLigence. Thus, the xCELLigence is able to ‘sense’ the presence of a ligand (i.e., agonist) by using cells that express a receptor that is specific to this ligand. Moreover, the sensors are highly sensitive, meaning that they can pick up signals even in conditions where the expression levels of the protein are very low (e.g., in cells with endogenous receptor expression)^{17,18} or the adhesion of the cells to the E-plate is poor¹⁹. By exploiting this sensitivity, the xCELLigence can be used to detect minute changes in agonist concentration.

8.2 – Transporters can affect the concentration of agonists at the receptor compartment

The extracellular concentration of an agonist is dictated by distinct (non-)physiological processes including enzymatic degradation or biosynthesis of the ligand²⁰, adsorption of the ligand to biological membranes or plastics (i.e., non-specific binding²¹), excretion or efflux of the ligand from cells or uptake of the ligand into cells *via* transporters²². While it is common to mitigate processes that influence the ligand concentration – e.g., by inhibition or expression of enzymes or transporters – to benefit proper assessment of receptor pharmacology, until recently there had been no reports that exploited the activation of membrane receptors to primarily investigate such processes.

Prior to the conception of the projects that are described in this thesis, it was demonstrated by colleagues that the presence of the equilibrative nucleoside transporter 1 (ENT1/SLC29A1) – a bidirectional transporter of adenosine – on an osteosarcoma cell line (U2OS) resulted in an attenuated activation of the endogenously expressed $A_{2B}AR$ by adenosine, which was measured using xCELLigence²³. This attenuation was likely the result of partial removal of the added adenosine from the extracellular compartment by ENT1. Indeed, when cells were pretreated with inhibitors of ENT1 (e.g. dipyridamole, NBTT) the apparent potency of adenosine for $A_{2B}AR$ was increased (i.e., shifted leftward) up to ten-fold, which suggested that adenosine uptake skewed the pharmacology of the endogenous agonist causing an underestimation of its potency. In this regard the cells are able to detect the reduced agonist availability at the receptor compartment, which can be interpreted as a direct causality of ENT1 function. As such, the xCELLigence is ‘sensing transport’, which offers the possibility to assess the pharmacology of molecules that modulate the transporter. For the purpose of naming simplification, we have termed the resulting method based on this concept the ‘transport activity through receptor activation’ (TRACT) assay (Chapter

3), which in this thesis refers to the xCELLigence-based assays but could more generally refer to any assay that uses receptor activation as a readout to determine transporter activity (e.g., Ca^{2+} mobilization, GTP γ S, cAMP or β -arrestin assays²⁴).

ENT1 is certainly not the only transporter that modulates agonist availability for membrane receptors (**Chapter 2**). In fact, a thorough assessment of the literature and pharmacology databases suggest that there are at least 100 unique human SLCs that are involved in the translocation of a substrate that is also a receptor agonist (**Appendix, Table A.1**). The majority of these SLCs are located at the plasma membrane, although some (mainly vesicular neurotransmitter transporters) are located at intracellular compartments. A few of these SLCs are well-known modulators of agonist levels and are common therapeutic targets – e.g., monoamine transporters (DAT, NET, SERT) decrease synaptic levels of monoamine neurotransmitters, where antidepressants primarily inhibit reuptake to enhance neurotransmitter levels, potentiate stimulatory receptor signaling and alleviate depression^{25–27}. Although these SLCs mostly operate to *reduce* extracellular agonist levels, in **Chapter 2** we advocate SLCs that have been recently demonstrated to *increase* extracellular levels of agonist *via* efflux, such as the sphingosine-1-phosphate transporter (SPNS2/SLC63A2)²⁸ and succinate efflux *via* the monocarboxylate transporter 1 (MCT1/SLC16A1)²⁹. In addition, SLCs may provide GPCRs located at intracellular membranes with their cognate ligands *via* influx, adding another layer of activation control by transporters. As is exemplified by the extensive **Table A.1**, there are many SLCs that can be ‘linked’ to a receptor *via* its substrate(s), which provides ample opportunities for label-free assay development (see **section 8.9**). Thus, we commenced by investigating which SLCs – other than ENT1 – would be suitable for functional assessment using the xCELLigence.

8.3 – Development of the TRACT assay for DAT, NET and EAAT

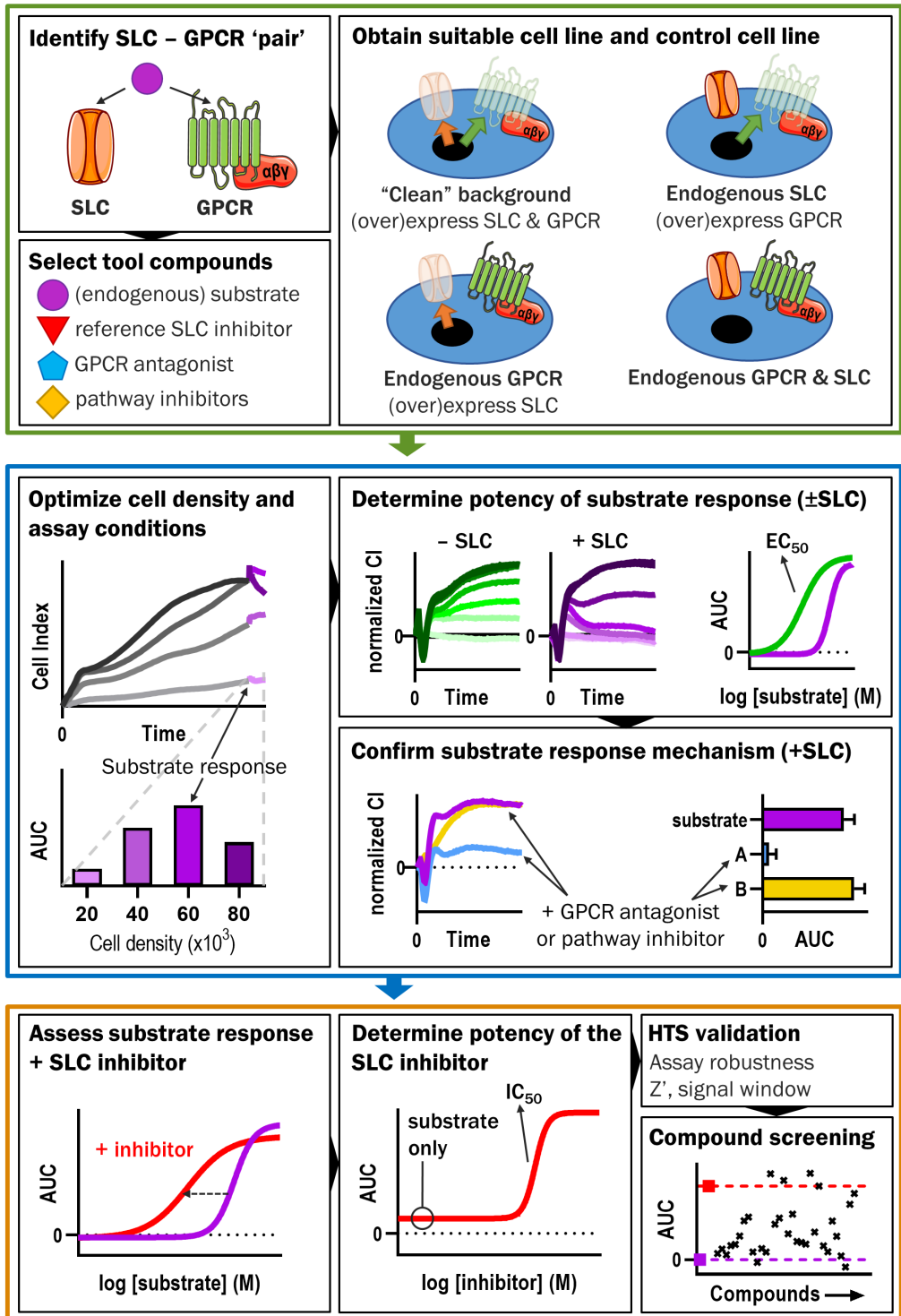
In this thesis, we focus on human SLCs that upon exogenous substrate application mediate substrate influx, i.e. remove the agonist from the receptor compartment. To start the validation of the impedance-based assay for other transporters, we initially selected SLCs that are well-studied and clinically relevant, have known substrate(s) ascribed to them and for which several validated small molecule inhibitors are available. We then identified an SLC and GPCR ‘pair’ that shared the same substrate. An important factor to consider was that the SLC and GPCR should be expressed on the same cell to facilitate sufficient removal of the substrate from the proximity of receptor compartment, similar to the study by Vlachodimou *et al.* in which cells were used with endogenous expression of both ENT1 and ARs²³. This, however, will not always be the case and in such instances where only the SLC or GPCR is expressed by the cell – or, if both are lacking – it is necessary to induce heterologous expression of the ‘missing’ protein(s) *via* transient or stable transfection of the transgene. Based on these prerequisites, three SLCs with GPCR-activating substrates were selected as ‘model’ SLCs for proof-of-concept validations of the impedance-based assay: the dopamine transporter (DAT/SLC6A2), norepinephrine transporter (NET/SLC6A2) and the excitatory amino acid transporter 1 (EAAT1/SLC1A3).

The functionality of human DAT was the first to be assessed on xCELLigence (**Chapter 3**). DAT is a well-established target of psychostimulants such as amphetamines and cocaine, as well as drugs for the treatment of depression, ADHD, narcolepsy and stimulant abuse²⁶. Thus, we selected DAT as a model SLC to validate our assay hypothesis. To this end, the human osteosarcoma U2OS cell line was selected as a model system as they are adherent – which is important for proper detection of impedance changes³⁰ – and endogenously express the dopamine receptor D1 (D₁R). Since these cells did not express DAT, we transiently transfected the U2OS cells with SLC6A3 or mock DNA prior to treatment of the cells with the endogenous substrate dopamine. As expected, the apparent potency of dopamine at D₁R was decreased in the presence of DAT and was potentiated when cells were pretreated with the DAT inhibitor GBR12909, which indicated that dopamine was efficiently removed from the extracellular compartment by DAT³¹. These findings were in line with the previously mentioned adenosine/ENT1 experiments and allowed for the determination of the inhibitory potency of GBR12909.

Although the TRACT assay principle was demonstrated in U2OS cells, the transient transfection procedure was deemed unsuitable for screening purposes and could be subject to inter-experimental variability of transporter expression levels. To attain stable transporter expression levels throughout experiments, we introduced the use of an engineered human embryonic kidney 293 (HEK293) cell line with stable site-specific integration of the transporter gene into the cell's genome, which allows for doxycycline-inducible expression of the transporter under a tetracycline repressor³². Since non-induced cells display little to no transporter expression, these cells can act as negative control to the induced, overexpressing cells. A major advantage of this so-called JumpIn system is the homogenous, consistent and high expression levels of the gene, which leads to more reproducible data across labs and experiments³³. In addition, the time required to generate JumpIn pools (~3 weeks) is considerably shorter and less error-prone than that to isolate stable monoclonal cells (~3 months), which facilitates the rapid generation of multiple JumpIn cell lines with different transporters or with genetic variants of the transporters (as is shown for EAAT1 mutants in **Chapter 7**). Thus, JumpIn cells were used for nearly all subsequent experiments and proved to be a valuable and easy-to-use tool for the set-up and validation of impedance-based transporter assays.

To demonstrate the compatibility of JumpIn cells, we used the TRACT assay in U2OS-DAT cells as a starting point for similar experiments on JumpIn cells expressing DAT (JumpIn-

→ **Figure 8.1** – Proposed workflow for TRACT assay development. **Top:** a 'toolbox' should be assembled, consisting of: an SLC–GPCR pair; substrate(s) and inhibitors; a cell line that expresses both SLC and GPCR; a control cell line that lacks the SLC. **Middle:** cell seeding density and assay conditions (e.g., buffer composition, incubation time) should be optimized to maximize the response window. This is followed by determination of the substrate potency in the presence and absence of the SLC, and a pharmacological validation of the GPCR or pathway that is involved in the substrate response. **Bottom:** the substrate response is determined in the presence of an SLC inhibitor, which provides an assay window to determine the inhibitory potency. The resulting assay should be validated to adhere to high-throughput screening (HTS) criteria, after which it can be used for compound screening.



DAT) (**Chapter 3**). Although the JumpIn cells did not express endogenous dopamine receptors, we observed dopamine induced concentration-dependent cellular responses that were attributed to the activation of alpha-2 adrenergic receptors (α_2R). Upon induction of DAT expression, the apparent potency of dopamine was significantly reduced, which was rescued by both GBR12909 and cocaine with the inhibitory potency of GBR12909 being comparable between U2OS and JumpIn cells. This indicated that receptors with differential intracellular G protein-coupling (G_{zs} for D_1R , G_{zi} for α_2R) and similar agonist potencies were both affected by the presence of an agonist uptake process.

In **Chapter 4**, we extended the TRACT assay principle to study NET, which is a drug target for depression and ADHD, and has an overlapping pharmacology with DAT²⁶. We used JumpIn cells with inducible expression of NET (JumpIn-NET), which were responsive to norepinephrine *via* activation of endogenous α_2R . Dopamine and epinephrine, which are both NET substrates, also induced α_2R -mediated cellular responses. The apparent potency of all three substrates was decreased in the presence of NET, with the shift being largest for norepinephrine (16-fold) and smallest for dopamine (3-fold). Moreover, the responses of all substrates were restored equipotently by NET inhibitor nisoxetine, where norepinephrine displayed the largest assay window (i.e., signal-to-noise ratio). The inhibitory potencies of twelve well-known NET inhibitors were in good correlation with a conventional fluorescent substrate uptake assay over a wide range of potencies, suggesting that the TRACT assay can be used to accurately characterize inhibitors. The Z' factor – which is a parameter of assay robustness and reproducibility used in HTS³⁴ – for this assay was 0.55, which is sufficient to deem the assay suitable for compound screening.

In **Chapter 6**, we attempted to set-up a TRACT assay for EAAT1, which mediates uptake of glutamate in astrocytes of the central nervous system and shows promise as a drug target for neurological disorders that involve glutamate homeostasis, such as epilepsy, ataxia and schizophrenia³⁵. As JumpIn cells do not express glutamate receptors, we performed experiments with JumpIn-EAAT1 cells transiently transfected with the metabotropic glutamate receptor 2 (mGluR₂), as we had in-house experience with mGluR₂ functional assays on xCELLigence³⁶. In non-induced cells, L-glutamate induced an mGluR₂-mediated response within 15 minutes, although the potency was substantially lower ($pEC_{50} = 4.1$) than previously reported for human mGluR₂ expressed heterologously in Chinese hamster ovary (CHO) cells on xCELLigence ($pEC_{50} = 5.3$)³⁷, which could be due to the transfection method (transient versus stable)³⁸ or cellular background (i.e., system bias)³⁹. Nevertheless, induced EAAT1 expression attenuated the L-glutamate response at mGluR₂, causing a rightward shift of the concentration-effect curve. The allosteric EAAT1 inhibitor UCPH-101 restored the apparent potency of L-glutamate on mGluR₂, but the more potent competitive inhibitor TFB-TBOA prevented all L-glutamate-induced responses. As a result, we were unable to reliably determine inhibitory potencies in the TRACT assay using this particular set-up. Interestingly, at high L-glutamate concentrations (>100 μM) a substantial mGluR₂-independent cellular response was observed that was attributed to cell swelling and spreading, providing an alternative assay window which we will discuss further in **section 8.6**.

Taken together, we demonstrated the TRACT assay principle for three human SLCs in a versatile JumpIn cell line, of which Gateway-compatible expression vectors are commercially available *via* Addgene (<http://www.addgene.org/depositor-collections/re-solute/>). In theory, any SLC–GPCR ‘pair’ that recognizes the same substrate is amenable for a TRACT assay. We have provided a visual workflow based on the assay development in **Chapter 3, 4 and 6**, which can be used as a guideline to set-up the TRACT assay for other SLCs (**Figure 8.1**). In the following section, we attempt to provide a rationale for a successful TRACT assay based on properties of the transporter and the receptor.

8.4 – A mechanistic understanding of the TRACT assay

In order to rationally approach the design of TRACT assays for new SLCs we would need to identify the key parameters that should match between the SLC and GPCR in order to ensure that the substrate uptake sufficiently affects the receptor occupancy. From a physiological perspective, it can be rationalized that saturable uptake processes are essential to remove excessive amounts of agonist from the receptor compartment to control the level of receptor activation. The initial recognition of these concepts originates from early denervation experiments in which removal of nerves from cholinergic or adrenergic tissue in humans or animals caused an increased responsiveness or sensitivity of the tissue to the corresponding neurotransmitter. In 1939, this was formulated by Walter Bradford Cannon as the ‘Law of Denervation’: “*When in a series of efferent neurons a unit is destroyed, an increased irritability to chemical agents develops in the isolated structure or structures, the effect being maximal in the part directly denervated.*”⁴⁰. This phenomenon was termed ‘supersensitivity’ and could be attained either by denervation of the tissue or pharmacological treatment with substances that enhance neurotransmitter sensitivity, such as cocaine⁴¹. In essence, the nerves were found to be responsible for the timely removal (i.e., uptake) of released neurotransmitters, which lowered the availability of the neurotransmitter to the postsynaptic tissue. It was not until the early 1960’s that researchers identified active uptake mechanisms that were saturable and adhered to Michaelis-Menten kinetics^{42–44}, suggesting the involvement of high-affinity (i.e., uptake₁, now known as neuronal NET, DAT and SERT²⁶) and low-affinity carriers (uptake₂, identified as the non-neuronal organic cation transporters [OCT1–3, SLC22A1–3]⁴⁵, and the plasma membrane monoamine transporter [PMAT, SLC29A4]⁴⁶) for the removal of released neurotransmitters.

It was soon found that uptake processes could lead to an underestimation of the true potency of an agonist and that action should be taken to prevent substantial influence of uptake on receptor activation. For example, by blocking uptake₁ cocaine sensitizes the activation of adrenergic receptors, ‘revealing’ the potency of norepinephrine^{22,47}. Likewise, the ENT1 inhibitor NBMPR (or NBTT) was used to prevent uptake of adenosine, which enhanced the potency of adenosine at AR subtypes in a cAMP assay⁴⁸. In another scenario, uptake of endogenous ligand is desired so that it does not disturb the pharmacological characterization of compounds at that ligand’s receptor. Since glutamate is present in cell culture medium and is continuously produced by cells^{36,49}, some experimental set-ups

warrant the co-expression of EAATs on mGluR-expressing cells to deplete the endogenous glutamate so it does not interfere with mGluR activation by exogenous agonists⁵⁰. These findings are at the basis of the TRACT assay principle that is described in this thesis.

If the aforementioned uptake processes are able to remove sufficient amounts of substrate from the receptor compartment, is there a general ‘rule of thumb’ that allows us to predict which SLC can be assessed *via* activation of a specific GPCR? We investigated whether an existing model could be used to explain the apparent potency shifts observed in the TRACT assays in this thesis and comparable assays from literature. In essence, the apparent potency shift of an agonist in the presence of an uptake process is the result of a discrepancy between the amount of substrate that is added to the cells and the actual substrate concentration at the receptor compartment due to the removal of the agonist. Two previously reported models describe the substrate concentration at the receptor compartment as a function of the added substrate concentration, the affinity of the substrate for the uptake process and a factor that represents the capacity or magnitude of the uptake process^{51,52}.

Before we discuss the two models, we should first describe the kinetics of a saturable uptake mechanism, of which the capacity/rate of uptake (V) is defined by the Michaelis-Menten equation:

$$V = \frac{V_{\max} \times [S]_a}{[S]_a + K_m}$$

where V_{\max} is the maximal capacity or rate of uptake at which the substrate can be transported in that system (usually in pmol/mg protein/min), K_m is the Michaelis-Menten constant, which is the concentration of substrate at which 50% of V_{\max} is achieved (sometimes referred to as substrate affinity or substrate activity), and $[S]_a$ is the substrate concentration that was added to the medium. The ratio V_{\max}/K_m is often used to express the **transport efficiency** of the system and compares the uptake of multiple substrates in the same assay system and efficiency between different transporter systems. The higher the transport efficiency, the more volume of substrate is ‘cleared’ from the medium per time unit⁴⁵.

8.4.1 – Langer & Trendelenburg model

In 1969, Langer and Trendelenburg formulated a model which states that the presence of a saturable uptake process shifts the concentration-effect curve of a transported agonist if its affinity for the uptake process is in a similar range as its potency towards the receptor⁵¹. According to this model, the substrate concentration at the receptor compartment is described, after rearrangement of the original formula, as:

$$[S]_r = \frac{[S]_a^2 + \alpha K_m [S]_a}{[S]_a + K_m}$$

where $[S]_r$ is the substrate concentration at the receptor compartment, $[S]_a$ is the added substrate concentration, K_m is the Michaelis-Menten constant and α is the maximal

hypothetical fraction of the added substrate that is present at the receptor compartment when $[S]_a \ll K_m$ (e.g., if 10% of added substrate is at the receptor compartment, then $\alpha = 0.1$) (**Figure 8.2a**). In the original article, the value of α was set at 0.1 and represented a 10-fold sensitization of the innervated tissue to norepinephrine in the presence of cocaine (i.e., uptake inhibition), although the authors stated that sensitizations up to 100-fold (i.e., $\alpha = 0.01$) were observed *in vivo*. Implicitly, α is dependent on the transport efficiency. $[S]_r$ can be introduced into the Hill equation – which describes the concentration-effect relationship of a receptor–agonist complex⁵³:

$$\text{response} = \frac{\text{Bottom} + (\text{Top} - \text{Bottom})}{1 + 10^{(\log EC_{50} - \log [S]_r)n}}$$

where **Bottom** and **Top** indicate the minimal and maximal response, respectively, **EC₅₀** is the agonist potency (i.e., substrate concentration at which 50% of the maximal response is achieved) and **n** is the Hill coefficient defining the slope of the curve. In the presence of the uptake process, Langer and Trendelenburg define three substrate concentration regions in which the agonist response at the receptor is affected (**Figure 8.2a,b**):

- in **Region I**, when $[S]_a \ll K_m$, the uptake rate is linear with the substrate concentration since the uptake rate becomes $V = (V_{\max}/K_m)[S]_a$ and $[S]_r$ is at a constant fraction of $[S]_a$ (defined by α). Here, the agonist curve shifts to the right with a magnitude dependent on α (e.g., $\alpha = 0.1$ indicates a 10-fold shift);
- in **Region II**, when $[S]_a \approx K_m$, uptake is gradually less linear and nears saturation, during which $[S]_r$ increases and gets closer to $[S]_a$. Here, two phenomena are expected to occur: 1) the rightward shift of the curves will diminish as the agonist potency (EC_{50}) increases, and 2) the slope of the curve will increase as $[S]_a$ approaches K_m ;
- in **Region III**, when $[S]_a \gg K_m$, the uptake rate equals V_{\max} and $[S]_r$ equals $[S]_a$. Here, no shift is observed as the agonist curve overlaps with the curve in the absence of uptake.

From this model, it is apparent that in Region I the agonist curve shift is dependent on the degree of transport efficiency. However, in Region II and III the transport efficiency is less important in determining $[S]_r$ and instead $[S]_r$ is driven by the K_m of the agonist. This means that even with a low value for α (i.e., a high transport efficiency) the predicted curve shifts in these regions will not increase in magnitude, despite the larger transport capacity.

To determine whether the Langer & Trendelenburg model could be used to describe the TRACT assay data in this thesis, we simulated the models using the EC_{50} and slope of the substrate response for the GPCR in the absence of uptake, the average K_m that is reported for the respective SLC in **Appendix Table A.1** (as the K_m was not determined in the current studies) and an arbitrary value for α of 0.01. The resulting simulated data points were fitted using non-linear regression with a variable slope (i.e., the Hill equation) and compared to fits that were directly derived from the substrate response curves \pm SLC of TRACT assays in the chapters of this thesis (**Figure 8.3**). In addition, we compared the

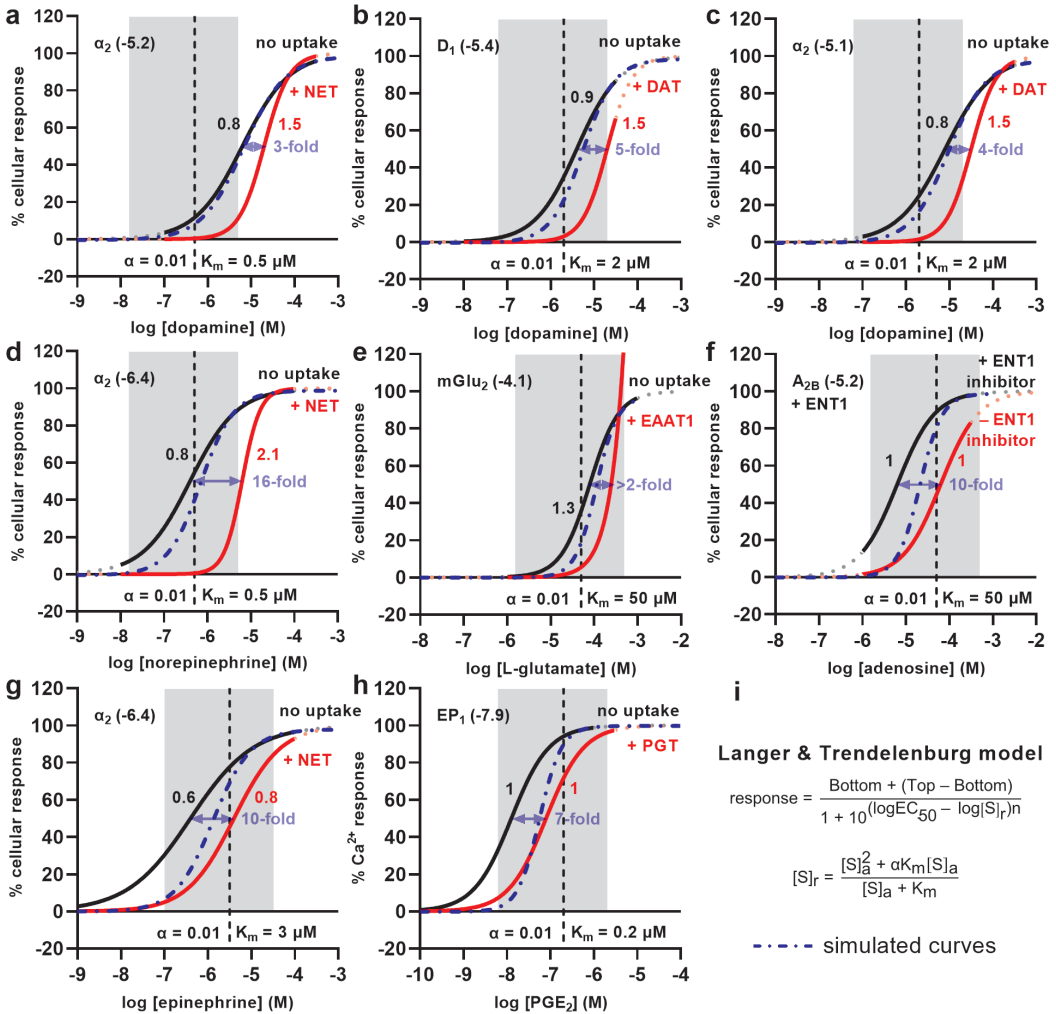


Figure 8.3 – Non-linear fits of TRACT assays reported in this thesis or in literature and simulated concentration-response curve using the Langer & Trendelenburg model. The data is presented as the relative agonist-induced response on the GPCR in the absence (black solid curve) or presence (red dashed curve) of an SLC, which were generated using EC_{50} values from the respective sources. Numbers next to the curves indicate the slope. The blue dashed curve is a simulation of the Langer & Trendelenburg model (i), using the $\log \text{EC}_{50}$ (in M, stated next to the receptor subtype) and slope in the absence of uptake (n) from the source, the average K_m reported in **Appendix Table A.1** for each substrate-SLC couple, and $\alpha = 0.01$ (signifying a 100-fold maximal curve shift; further decreasing this value did not substantially the magnitude of the curve shift). Grey area indicates Region II of uptake (check **Figure 8.2a,b**). (a) Dopamine, α_2 adrenergic receptor (α_2 , $\log \text{EC}_{50} = -5.2$), norepinephrine transporter (NET, $\log K_m = -6.3$) (**Chapter 4**). (b) Dopamine, dopamine receptor D1 (D_1 , $\log \text{EC}_{50} = -5.4$), dopamine transporter (DAT, $\log K_m = -5.7$) (**Chapter 3**). (c) Dopamine, α_2 ($\log \text{EC}_{50} = -5.1$), DAT ($\log K_m = -5.7$) (**Chapter 3**). (d) Norepinephrine, α_2 ($\log \text{EC}_{50} = -6.4$), NET ($\log K_m = -6.3$) (**Chapter 4**). (e) L-glutamate, metabotropic glutamate receptor 2 (mGluR₂, $\log \text{EC}_{50} = -4.1$), excitatory amino acid transporter 1 (EAAT1, $\log K_m = -4.3$) (**Chapter 6**). (f) Adenosine, adenosine A_{2B} receptor (A_{2B}, + 1 μM dipyrindamole (ENT1 inhibitor), $\log \text{EC}_{50} = -5.2$), equilibrative nucleoside transporter 1 (ENT1, $\log K_m = -4.3$) (Vlachodimou *et al.*)²³. (g) Epinephrine, α_2 ($\log \text{EC}_{50} = -6.4$), NET ($\log K_m = -5.5$) (**Chapter 4**). (h) PGE₂, prostaglandin receptor EP1 (EP₁, $\log \text{EC}_{50} = -7.9$), prostaglandin transporter (PGT, $\log K_m = -6.7$) (Chi *et al.*)⁵⁴. Data were simulated and visualized using GraphPad Prism v9.

model to concentration-effect curves derived from two other publications: the label-free cellular response of adenosine on U2OS cells expressing $A_{2B}AR$ and ENT1 in the presence or absence of the ENT1 inhibitor dipyridamole (**Figure 8.3f**)²³, and the Ca^{2+} response of prostaglandin PGE_2 on HEK293 cells expressing prostaglandin receptor EP_1 in the presence or absence of the prostaglandin transporter (PGT, SLCO1A2) (**Figure 8.3h**)⁵⁴.

In **Figure 8.3**, the black curve indicates the substrate-induced cellular response in the absence or inhibition of uptake, whereas the rightward-shifted red curve is the cellular response in the presence of the uptake process. In the absence of uptake, the EC_{50} value (the concentration needed for half-maximal effect) for all substrates lies within Region II or III of the uptake process, which depends on the K_m of the substrate. When imposing the simulated curves from the model (**Figure 8.3i**) into each respective graph (blue dashed curves), it is evident that the model is unable to completely describe the rightward shift of the response curve in the presence of uptake – i.e., the simulated curves do not overlap with the actual data (red curves). For example, the rightward shift of the norepinephrine response in the presence of NET is 16-fold compared to cells lacking NET, whereas the simulated curve only predicts a fraction of this shift (**Figure 8.3d**). When the EC_{50} nears Region I, as is the case with PGE_2 (**Figure 8.3h**), the simulated curve is closer to the response in the absence of uptake, although the slope of this curve is not in line with the actual data. Increasing the ‘transport efficiency’ in the model (i.e., $\alpha \rightarrow 0$) did not result in a larger rightward shift of the predicted response curve, which indicates there is a limit to this model and it does not accurately describe the observed curve shifts of the TRACT assay.

8.4.2 – Kenakin model

A second model was postulated by Kenakin in his book ‘A Pharmacology Primer’, in which he describes a saturable adsorption site that acts as a sink claiming a portion of the ligand added to the medium⁵². Foremost, this adsorption site refers to any surface in an *in vitro* experiment (e.g., the plastic of a cell culture plate) to which the ligand under investigation can bind, leading to a reduction of the free concentration and an overestimation of the true concentration (and, thus, potency) of the ligand at the receptor compartment. More generally, this model can describe any process that reduces the free ligand concentration, such as enzymatic degradation or uptake of the ligand. Thus, Kenakin defines the free ligand concentration ($[S]_r$) as the total ligand concentration ($[S]_a$) minus the ligand concentration at the adsorption site, which can be described according to the mass action equation and results in the following quadratic formula:

$$[S]_r = [S]_a - \frac{1}{2} \left([S]_a + K_m + \Omega - \sqrt{([S]_a + K_m + \Omega)^2 - 4[S]_a \Omega} \right)$$

where $[S]_r$ is the substrate concentration at the receptor compartment, $[S]_a$ is the added substrate concentration, K_m is the Michaelis-Menten constant (defined in the original model as the equilibrium dissociation constant of the ligand at the adsorption site) and Ω is the maximal capacity of the substrate removal process (defined in the original model as the maximal number of adsorption sites) (**Figure 8.2c**). It should be noted that all four

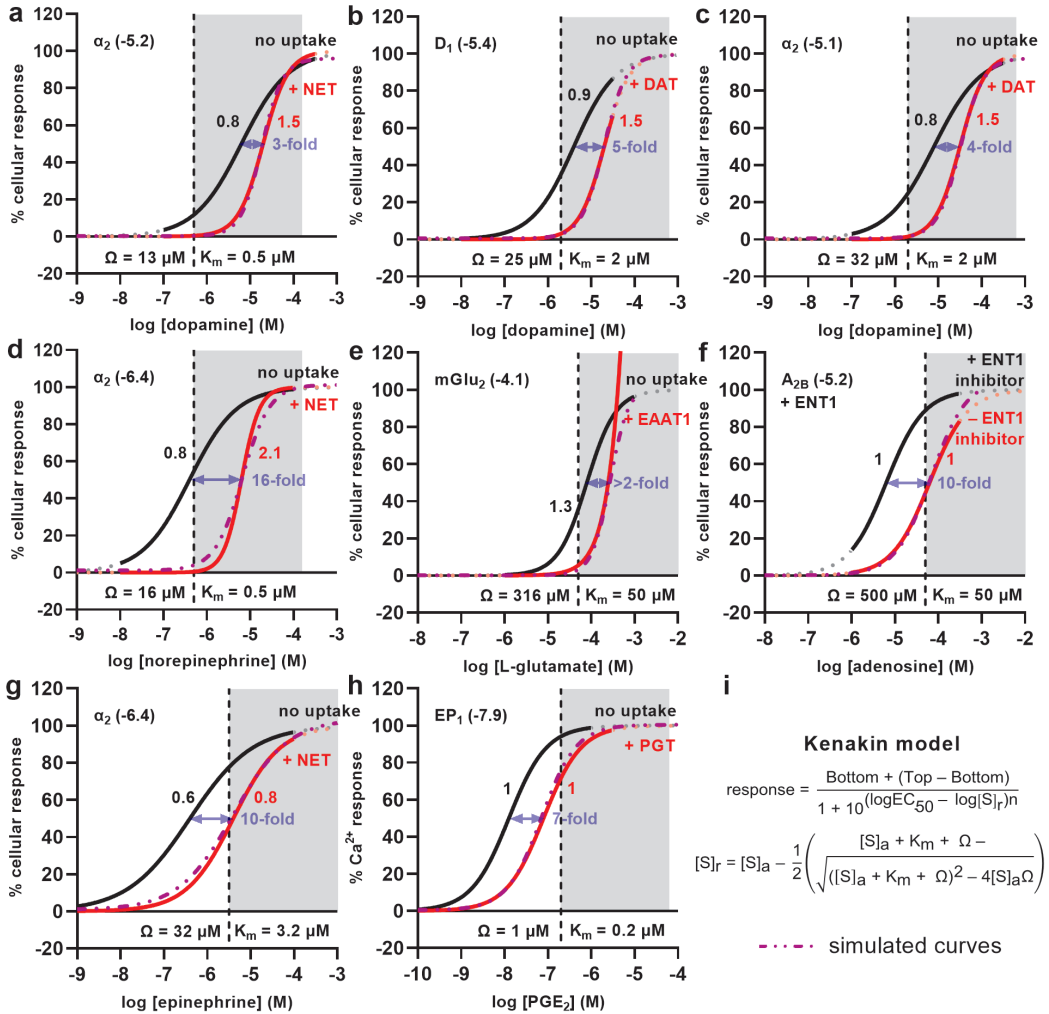


Figure 8.4 – Non-linear fits of TRACT assays in this thesis or in literature and simulated concentration-response curve using the Kenakin model. The data is presented as the relative agonist-induced response on the GPCR in the absence (black solid curve) or presence (red dashed curve) of an SLC, which were generated using EC_{50} values from the respective sources and are identical to **Figure 8.3**. Numbers next to the curves indicate the slope. The purple dashed curve is a simulation of the Kenakin model (i), using the $\log \text{EC}_{50}$ (in M, stated next to the receptor subtype) and slope in the absence of uptake (n) from the source, the average K_m reported in **Appendix Table A.1** for each substrate–SLC couple, and a manually selected value for Ω (by trial-and-error) that caused the simulation to overlap with the red curve. Grey area indicates Region B of uptake (check **Figure 8.2c,d**). (a) Dopamine, α_2 adrenergic receptor (α_2 , $\log \text{EC}_{50} = -5.2$), norepinephrine transporter (NET, $\log K_m = -6.3$), $\log \Omega = -4.9$ (**Chapter 4**). (b) Dopamine, dopamine receptor D1 (D_1 , $\log \text{EC}_{50} = -5.4$), dopamine transporter (DAT, $\log K_m = -5.7$), $\log \Omega = -4.6$ (**Chapter 3**). (c) Dopamine, α_2 ($\log \text{EC}_{50} = -5.1$), DAT ($\log K_m = -5.7$), $\log \Omega = -4.5$ (**Chapter 3**). (d) Norepinephrine, α_2 ($\log \text{EC}_{50} = -6.4$), NET ($\log K_m = -6.3$), $\log \Omega = -4.8$ (**Chapter 4**). (e) L-glutamate, metabotropic glutamate receptor 2 (mGluR_2 , $\log \text{EC}_{50} = -4.1$), excitatory amino acid transporter 1 (EAAT1, $\log K_m = -4.3$), $\log \Omega = -3.5$ (**Chapter 6**). (f) Adenosine, adenosine A_{2B} receptor (A_{2B} , $\log \text{EC}_{50} = -5.2$), equilibrative nucleoside transporter 1 (ENT1, $\log K_m = -4.3$), $\log \Omega = -3.3$ (Vlachodimos *et al.*)²³. (g) Epinephrine, α_2 ($\log \text{EC}_{50} = -6.4$), NET ($\log K_m = -5.5$), $\log \Omega = -4.5$ (**Chapter 4**). (h) PGE₂, prostaglandin receptor EP1 (EP_1 , $\log \text{EC}_{50} = -7.9$), prostaglandin transporter (PGT, $\log K_m = -6.7$), $\log \Omega = -6.0$ (Chi *et al.*)⁵⁴. Data were simulated and visualized using GraphPad Prism v9.

parameters are in the same unit of concentration (i.e., μM), indicating that Ω cannot be substituted for the maximal transport capacity (V_{max}) of the uptake process. The actual value of Ω comprises various aspects and takes into account the V_{max} , but also other factors such as the diffusion rate of the substrate into and from the receptor compartment. When $[S]_r$ is introduced into the Hill equation, similar to the Langer & Trendelenburg model, we can define two major substrate concentration regions in which the agonist response at the receptor is affected (**Figure 8.2c,d**):

- in **Region A**, when $[S]_a \leq K_m$, the uptake rate is either linear with the substrate concentration ($V = (V_{\text{max}}/K_m)[S]_a$ when $[S]_a \ll K_m$) or becomes gradually less linear as $[S]_a$ approaches K_m . In this region, $[S]_r$ is at a constant fraction of $[S]_a$ and the agonist curve shifts to the right with a magnitude dependent on the ratio between Ω and K_m ;
- in **Region B**, when $[S]_a \geq K_m$, the uptake rate gradually nears saturation, during which $[S]_r$ increases and gets closer to $[S]_a$. Here, two phenomena are expected to occur when Ω remains constant: 1) the rightward shift of the curves will diminish as the agonist potency (EC_{50}) increases, and 2) the slope of the curve will increase as $[S]_r \rightarrow [S]_a$. The end of Region A and start of Region B lie to the left when Ω decreases, and to the right when Ω increases;

In this model, the magnitude of the shift of the concentration-response curves is dependent on the transport efficiency (i.e., V_{max}/K_m) at all substrate concentrations, in contrast to the Langer & Trendelenburg model where only the curve shift in Region I was mainly governed by the transport efficiency. This means that in Region B, even when $[S]_a \gg K_m$, a curve shift and slope change may be observed when the value for Ω is sufficiently large.

The Kenakin model was used to describe the TRACT assay data in this thesis and other publications by simulation of concentration-response curves using the same EC_{50} , slope and K_m for the substrate as in **Figure 8.3**. The value for Ω was manually selected for each simulation based on the coordinates of the final curve in relation to the real data (i.e., when both curves overlap) (**Figure 8.4**). The black and red curves (i.e., substrate-induced cellular response in the absence or presence of uptake, respectively) in **Figure 8.4** are identical to **Figure 8.3**. When imposing the simulated curves from the model (**Figure 8.4i**) into each respective graph (purple dashed curves), we observe that the model is able to describe both the rightward shift as well as the change in slope of the response curve for all TRACT assays – i.e., the simulated curves overlap with the actual data (red curves). For example, the response curves for dopamine and norepinephrine on $\alpha_2\text{R}$ in the presence of NET have increased slopes, whereas the slope is not substantially increased for epinephrine (**Figure 8.4a,d,g**). According to the model, the shallow curve of epinephrine could be explained by the higher values for K_m and Ω , resulting in a parallel curve shift in Region A. Indeed, it is expected that dopamine and norepinephrine have lower K_m values than epinephrine, but the latter two substrates should have equal V_{max} values⁵⁵. Moreover, it is evident that a higher K_m value of a substrate for an SLC (e.g., L-glutamate, adenosine) requires a higher value for Ω to accompany the removal of sufficient substrate quantities in order to explain

the observed curve shifts (**Figure 8.4e,f**). It should be noted that number of variables in the Trendelenburg and Kenakin models are equal, with the only differences being the α/Ω factors and the form of the $[S]_r$ equations. Tuning the value of Ω had a profound effect on the shift and slope of the resulting simulated curve, whereas a limit was reached for these properties in the simulation with the Trendelenburg model when the value of α was further reduced. Although this may denote Ω as a ‘fudge factor’, here it illustrates that the observed curve shifts are dependent on both the substrate K_m and the V_{max} . Altogether, the Kenakin simulations illustrate that the TRACT assay should work for any SLC for which the substrate capacity, and thus the transport efficiency, is high enough in relation to the potency of that substrate on the GPCR. Since most SLCs have no reported transport efficiencies, we advise to select a GPCR for which the substrate EC_{50} is lower than $30 \times$ the substrate K_m for the SLC (see **Appendix Table A.1** for an overview of substrate affinity and potency values).

8.5 – Factors of influence in the TRACT assay

It is challenging to predict upfront whether a specific SLC–GPCR pair is amenable to assessment in the TRACT assay. Although the Kenakin model is able to describe the agonist response curve shifts that were observed in TRACT assays, there are factors and limitations to the substrate, SLC and GPCR that should be considered when selecting any SLC–GPCR pair for assessment (**Figure 8.5**).

The K_m of a substrate is a constant for a specific SLC and generally varies less across experiments, although it may be slightly higher in heterologous expression systems versus native tissue. For example, the K_m of dopamine for DAT (various species) is 0.03–0.5 μM in the brain compared to 0.1–5 μM in cells overexpressing DAT⁵⁶. In contrast, the V_{max} is considerably more prone to variation, as it is dependent on the turnover number – k_{cat} , also known as the turnover rate, which is the number of complete transport cycles a transporter makes on average per unit of time⁵⁷ – and the total number of transporters expressed on the cell ($[E_T]$), according to:

$$V_{max} = k_{cat} \times [E_T]$$

Within one cellular system, the $[E_T]$ is more or less constant for all substrates. However, the transporter density can vary greatly between endogenous cell lines and heterologous (over) expression systems, which can result in widely different V_{max} values between experiments. For example, the V_{max} of dopamine for DAT was shown to range between 0.004–1925 pmol/min/mg protein depending on the DAT species and cell line origin⁵⁶. In this thesis, K_m and V_{max} values were not determined for the respective SLC cell lines, thus no definitive conclusions can be drawn regarding the contribution of V_{max} to the value of Ω and the optimal transport efficiency. Future investigations would certainly benefit from such kinetic characterizations, which could aid in the development of better predictive models and assays. For instance, if we know which value of V_{max} corresponds to the value of Ω , we could predict the agonist curve shift of a substrate using the Kenakin model and V_{max}/K_m values that were measured in-house.

V_{\max} is influenced by both k_{cat} and $[E_T]$. The k_{cat} is specific to the substrate and defines the sum of multiple micro-rate constants that characterize a transport cycle, including substrate association to (k_{on}) and dissociation from (k_{off}) the transporter, binding of co-substrate(s), the conformational change of the transporter from an outward- to an inward-facing position, the unbinding of the (co-)substrate(s) from the transporter, and the relocation of the transporter from an inward-facing to an substrate-accessible outward-facing conformation (**Figure 8.5**)^{58,59}. Hence, the k_{cat} is influenced by factors such as the type of substrate, concentration gradients of co-substrates (e.g., ions), membrane potential, temperature, post-translational modifications to the transporter and the presence of regulatory proteins^{57,60}. The true value of k_{cat} is difficult to determine *in vitro* and is often inaccessible, although significant advancements have been made to predict micro-rate constants using systems biology simulations^{58,61,62}. In general, for ion channels – which allow free but selective diffusion of ions – the turnover number is in the range of 10^7 – 10^9 s⁻¹, whereas SLC transporters have much slower rates (10^{-1} – 10^3 s⁻¹) which often makes it difficult to detect transporter-mediated currents for large-scale electrophysiological assessments⁶¹. For example, the turnover of neurotransmitters by NET, DAT and SERT is relatively slow (0.1 – 2 s⁻¹)^{63–66}, nucleoside transport by ENT1 is 100-fold faster (200 s⁻¹)⁶⁷ and turnover of glutamate by EAATs is highly dependent on the subtype (EAAT1, 16 s⁻¹; EAAT2, 14 – 41 s⁻¹, EAAT3, 90 – 110 s⁻¹; EAAT4, <3 s⁻¹; EAAT5, <1 s⁻¹)⁶⁸. Thus, transporters with a slow k_{cat} would require a relatively higher $[E_T]$ to attain a comparable V_{\max} .

As the k_{cat} is a constant for each substrate, manipulation of the $[E_T]$ (e.g., *via* overexpression of the transporter) is experimentally the most straightforward method to change the V_{\max} and increase the specific signal-to-noise ratio of an uptake system (**Figure 8.5**). However, there is a physical limit to the amount of membrane proteins a cell can harbor at any moment, which can pose constraints on the maximal value of V_{\max} for any SLC in a specific cell type^{62,69}. For example, Belo do Nascimento *et al.* have demonstrated that the maximal uptake rate of glutamate in a HEK293 cell line with inducible expression of EAAT2 – i.e., the same JumpIn system as the cells in this thesis – does not increase linearly with increased EAAT2 expression, but rather shows saturation of the uptake capacity (V_{\max}) at higher levels of the transporter in addition to a slightly increased K_m value⁷⁰. In addition, higher transporter levels resulted in a decreased apparent potency of the EAAT2 inhibitor WAY-213,613, which was attributed to an increased number of binding sites. Similar observations were made for the serotonin (SERT, SLC6A4)⁷¹ and dopamine (DAT, SLC6A3)⁷² transporters, suggesting that alterations of ligand potency as a result of limiting transporter density might be common for most transporters. Altogether, this may indicate that not all transporters of the total transporter pool at the cell membrane are contributing to the maximal uptake activity, which could indicate a ‘transporter reserve’ analogous to the ‘receptor reserve’ concept that applies to GPCRs (**Figure 8.5**) – i.e., the occupancy of only a small fraction of the total receptors is required to produce the maximal functional response⁵². Interestingly, in the TRACT assays for DAT and NET (**Chapter 3 and 4**), as well as the phenotypic assay for EAAT1 (**Chapter 6**), we observed that inhibitory potency (IC_{50}) values of the respective SLC inhibitors were in general up to 10-fold higher compared to literature values. One cause of this may be that higher competing concentrations of

substrate were used in the TRACT assay compared to conventional assays (e.g., radioligand uptake), which could lead to increased competition with the SLC inhibitor and a rightward shift in potency. An additional explanation might be the presence of a transporter reserve in these inducible overexpression cell lines that could alter transporter kinetics and result in a slight underestimation of the true inhibitory potency. This should be considered when the TRACT assay is employed for pharmacological characterizations.

In a typical *in vitro* experiment, the volume of the extracellular compartment (i.e., the culture medium or buffer) – 100 μl in our TRACT assays – is large compared to the accessible monolayer of cells that are attached at the bottom of the microtiter plates. In the absence of a saturable uptake process, the substrate can freely diffuse to the cell membrane resulting in an equal concentration at the cell surface and in the bulk solution of the extracellular compartment. However, there is a thin unstirred water layer (μm range) coating adherent cell monolayers where free diffusion of substrate is slower than in ‘stirred’ bodies of water^{52,73,74}. In essence, this unstirred layer is directly accessible to the cell membrane and can be compared to the receptor compartment or ‘biophase’ (Figure 8.5). Especially in 96- or 384-well culture formats, this layer is larger than in perfused tissues as it is not possible to stir or constantly homogenize the extracellular medium. If there is a process that removes the substrate from this unstirred water layer, e.g., uptake *via* an SLC, then the substrate concentration in this layer depends on the uptake rate and the diffusion rate of the substrate from the bulk solution to the unstirred water layer⁷⁵. The substrate concentration in this layer will be lower than the bulk solution as long as the uptake is not saturated, even

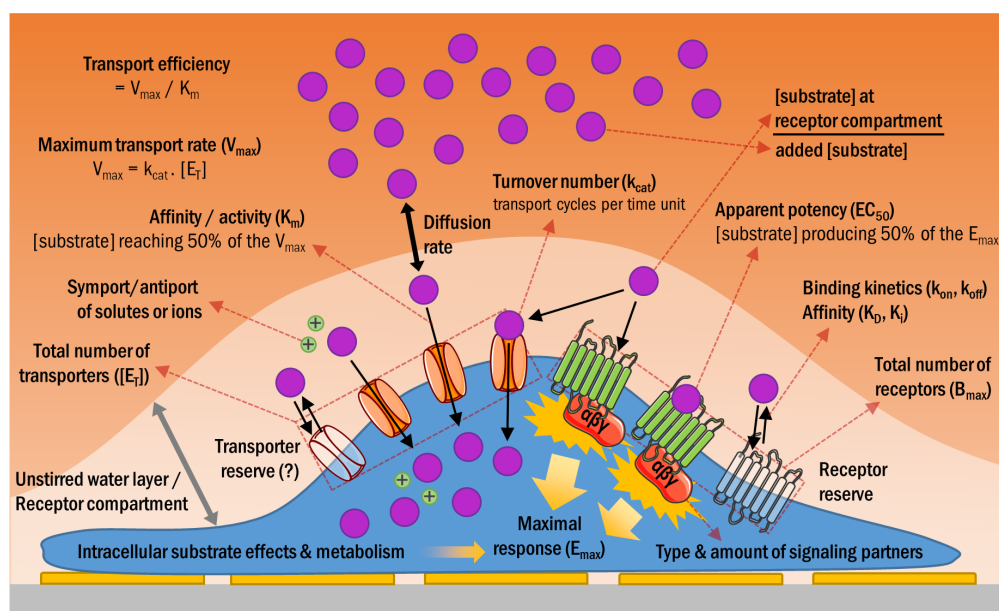


Figure 8.5 – Factors that influence the substrate-induced cellular response on cells expressing GPCRs and/or SLCs for that substrate.

in the presence of a vast excess of substrate in the bulk solution. Thus, the presence of the unstirred water layer in a microtiter format may in part explain the magnitudes of the agonist curve shifts in TRACT assays.

The readout of a TRACT assay is constituted by the activation of a GPCR by the SLC substrate, which leads to recruitment of signaling partners and subsequent changes in cell morphology that are measured as a change in impedance⁷⁶. As is evident from the Langer & Trendelenburg and Kenakin models described in the previous section, the apparent potency (EC_{50}) of the substrate on the GPCR – in relation to the K_m and capacity of the SLC – determines the extent of the response curve shift in the presence of the SLC. In general, if the SLC transport efficiency is sufficient, a higher substrate potency (i.e., lower EC_{50} value) results in a larger curve shift (**Figure 8.2b,d**). There are several factors that can influence the EC_{50} of a substrate towards a receptor (**Figure 8.5**). The total number of receptors (B_{max}) on a cell can affect the maximal response (E_{max}) and EC_{50} , as higher receptor densities increase the E_{max} and enhance the ligand potency⁵². The receptor density, just like the total number of transporters ($[E_T]$), is the most straightforward to control experimentally by using recombinant expression systems, which we used in **Chapter 6** for the transient expression of mGluR₂. It should be noted that the maximal receptor-mediated response of a substrate is limited by the availability, subtype and kinetics of intracellular signaling partners (i.e., G proteins, β -arrestins, etc.), as there is a finite number of signal amplification reactions that can occur within each cell per time unit^{13,77}. Moreover, more comprehensive GPCR concepts, such as receptor desensitization, internalization, allosteric modulation and biased agonism could all have a profound effect on the substrate EC_{50} in an impedance-based assay^{78,79}. Thus, selecting the appropriate GPCR to generate a cellular response is crucial when setting up a TRACT assay.

8.6 – GPCR-independent phenotypic SLC assays using impedance

In essence, the xCELLigence provides a phenotypic readout of a cell's function, as it is able to capture any change in cellular properties upon perturbation with a ligand; the 'phenotype' that is observed (i.e., a characteristic increase or decrease of impedance) depends on which pathway is triggered. Besides GPCR-mediated contributions to the cellular response, there may be receptor-independent mechanisms that have an effect on the magnitude of the overall response in the presence of an SLC.

In **Chapter 6 and 7**, we observed that in JumpIn cells overexpressing EAAT1 – but not mGluR₂ – the addition of glutamate or aspartate results in a strong increase of the Cell Index that peaked after two hours, which was at least six-fold greater in amplitude compared to rapid (15 min) mGluR₂-mediated responses. These responses were completely mediated by EAAT1, as both EAAT1 inhibitors UCPH-101 and TFB-TBOA inhibited the response of 1 mM glutamate/aspartate in a concentration-dependent manner. Since no GPCR was involved in this part of the response, we investigated the putative mechanism behind the EAAT1-mediated cellular response by live-cell imaging and targeted metabolomics. In actin-GFP-tagged cells, upon addition of glutamate JumpIn-EAAT1 cells started to spread on the

culture plate surface, which provides a visual explanation for the drastically increased Cell Index on xCELLigence. Glutamate uptake has previously been shown to induce cell swelling, as glutamate enters the cell with 3 Na⁺ and 1 H⁺ in exchange for 1 K⁺ which increases the cell's osmolarity causing an influx of water^{80–82}. This rapid uptake and increased cell volume may elicit intracellular Ca²⁺ elevations, ATP release and autocrine receptor activation, which results in the formation of protrusions at the cell's edges, effectively altering the cell morphology^{83,84}. The involvement of a cell swelling process in the EAAT1 cellular response was confirmed by reduced levels of intracellular taurine (i.e., an osmolyte that is released from the cell upon cell volume changes⁸⁵) and inhibition of the response by ouabain (i.e., an inhibitor of Na⁺/K⁺-ATPase, which restores the Na⁺ gradient and is crucial for glutamate uptake⁸⁶). The glutamate-induced cellular response was highly reproducible and robust, as reflected by an excellent Z' factor of 0.85, which indicates that this assay can be used to screen for EAAT1 inhibitors. Moreover, these results demonstrate that SLC function can be assessed in a phenotypic assay in the absence of a substrate-activated GPCR.

8.7 – Application of impedance-based assays in SLC drug discovery: computational methods and compound screening

The use of computational techniques based on machine learning to design, generate and predict biological activity of new molecules for drug targets has increased in recent years^{87–89}. Computer-aided drug design for SLCs has been mostly aimed at ligand-based approaches such as quantitative structure-activity relationship (QSAR) or pharmacophore modeling⁹⁰. However, as a result of the increasing number of SLC crystal structures in the last ten years, structure-based methods such as ligand docking, free energy perturbations and molecular dynamics (MD) simulations are also aiding the rational design of SLC targeting drugs⁹¹. Nevertheless, in the absence of structural information ligand-based models can be highly informative and new models are being developed to speed up the drug discovery process. For example, proteochemometric (PCM) modeling can be seen as an extension of the more conventional QSAR studies, and has been successfully used to design novel, selective compounds based on molecular descriptors that describe the similarity between ligands and the target protein^{1,92}. So far, PCM models have been used to accurately predict clinically relevant drug–transporter interactions⁹³ as well as the activity of inhibitors for organic anion transporting polypeptide 1B1 and 1B3 (OATP1B1/3, SLCO1B1/3)⁹⁴ and the sodium-glucose cotransporter 2 (SGLT2, SLC5A2)².

In **Chapter 5** we used a PCM model to perform virtual screening of a large database of synthesizable compounds (~700 million structures) to identify novel inhibitors of NET. Although several studies employed structure-based drug design – based on homology models of human SERT or *Drosophila* DAT – for the identification of prescription drugs or novel molecules that inhibit NET^{27,95}, this is the first time a large database is screened for NET using a PCM model. Using the model, which was trained on reported NET interaction data from the ChEMBL database, over 22,000 compounds were predicted to be active at NET. After similarity filtering, 32 of these compounds were synthesized and

screened at 10 μM in the TRACT assay that was described in **Chapter 4**. Interestingly, five of these compounds, which were structurally diverse, were identified as hits, with inhibitory potencies in the mid-to-low nanomolar range. The chemical space around one of these hits is currently being investigated in our lab, which might lead to the discovery of novel, potent NET inhibitors with distinct pharmacological properties. On the one hand, this study demonstrates the power of identifying new active molecular scaffolds with PCM modeling, which could become a more common approach in computer-aided drug design for SLCs. On the other hand, we demonstrate the screening potential of the TRACT assay, which shows that this assay could be used for primary and follow-up screens in SLC drug discovery programs.

8.8 – Application of impedance-based assays in SLC drug discovery: functional assessment of genetic variants

Proper functioning of SLCs is key to maintain homeostasis and warrant cell signaling. Mutations in SLC genes, causing either a loss- or gain-of-function, have been associated with faltering drug efficacy, distribution and toxicity, in addition to population-specific monogenic (inheritable) diseases^{96,97}. Genetic variability of SLCs is common in humans, as it is estimated that each individual genome contains 30 SLC variants that alter the transporter function⁹⁶. Functional characterization of SLC variants is important as it aids the association of disease phenotype with genotype, which could be the basis for the design of new therapeutic strategies. A notable example is the development and approval of sodium-glucose cotransporter 2 (SGLT2, SLC5A2) inhibitors (i.e., gliflozins) for the treatment of hyperglycemia in type 2 diabetes patients, as mutations in the SLC5A2 gene were initially associated with familial renal glucosuria⁹⁸. Other metabolic disorders, such as non-alcoholic fatty liver disease, obesity and insulin resistance are linked to polymorphisms in UCP1 (SLC25A7), NaCT (SLC13A5) and MCT11 (SLC16A11)⁹⁹. Although the clinical tyrosine kinase inhibitor linafianib has been identified as a potent UCP1 inducer – reactivating thermogenesis, for the potential treatment of obesity¹⁰⁰ –, there are no specific compounds yet that target these transporters, providing an immense opportunity for drug discovery. Over the last two decades, another major class of SLCs, the neurotransmitter transporters, has been largely associated with missense mutations that cause functional deficits and protein misfolding, which implicates transporters with various neurological diseases such as ataxia, Parkinson's disease, epilepsy and mental disorders¹⁰¹. The main hurdle towards a basic understanding of the clinical consequences of these genetic SLC variants has been the shortage of functional studies, which was mostly hampered by the lack of proper assay platforms or the absence of structural information of the protein. Thus, with the rapid increase in the number of crystal and cryo-EM structures of human SLCs^{102–104}, as well as the development of novel functional assays¹⁰⁵ – such as the ones described in this thesis – we are more than ever equipped with the right tools to characterize and mechanistically interpret SLC variants in the light of disease and drug discovery.

As another demonstration of the versatility of cell-based label-free assays, we employed the xCELLigence to investigate the functional consequences of SLC variants. We selected EAAT1 (SLC1A3) as a model transporter since we had already developed an assay for this transporter (**Chapter 6**) and disease-related mutants had been reported in literature. SLC1A3 variants have been associated with the etiology of very rare cases of episodic ataxia type 6 (EA6), which has been functionally attributed to altered chloride conductivity and/or glutamate transport¹⁰⁶. In **Chapter 7**, we identified several missense mutations of SLC1A3 in cancer patients from the Genomic Data Commons (GDC) database of the National Cancer Institute. Since 3D structures of human EAAT1 – bound to Na⁺ ions, substrates and/or inhibitors – are available^{107,108}, we rationally selected eight mutants from the GDC database based on their proximity to substrate and/or inhibitor binding sites, in addition to two EA6-related mutants (M128R, T318A) that had been reported to lose or retain glutamate transport function¹⁰⁶. Using the functional assay from **Chapter 6**, we were able to measure glutamate- and aspartate-induced cellular responses, as well as inhibitory potencies of TFB-TBOA and UCPH-101 for all mutants. Mutants showed diverse substrate responses, either a decrease in the maximal response or alteration in the substrate potency. Interestingly, while most mutants showed reduced or unaltered inhibitory potency of the EAAT1 inhibitors, two mutants (A446E, L448Q) enhanced the IC₅₀ of both TFB-TBOA and UCPH-101. Ongoing experiments using MD simulations – which have previously been used to characterize K⁺ coupling, the Cl⁻ permeation pathway and M128R mutation of EAAT1^{109–111} – could provide an additional substantiation of the *in vitro* data by investigating the conformational changes of mutant EAAT1 subdomains. These results demonstrate that xCELLigence can be used to functionally assess EAAT1 mutants, which could prove exemplary for other SLC variants that may be investigated on this platform in the future.

8.9 – Future perspectives – Label-free assays and opportunities for SLC drug discovery: where to next?

The ultimate purpose of any *in vitro* assay is to measure the activity of a molecule towards its intended target, which is exactly the rationale in early drug discovery: finding the right drug, for the right target, ideally as time- and cost-effectively as possible. The advantage of cell-based assays, as compared to purified protein or membrane fractions, is that activation or inhibition of the target of interest occurs in an environment that more closely mimics that of the cells *in vivo*⁵. The use of label-free assays, as opposed to assays based on radioactivity or fluorescence, may reduce the occurrence of artefacts and facilitates a more ‘physiologically relevant’ environment of the cell⁹. Phenotypic assays can be used as an ‘unbiased’ approach to find molecules with a desired biological effect, and by integration of phenotypic methods with target-based approaches (e.g., cells overexpressing the target of interest) the outcome can help understand complex mechanisms of action that may be more predictive of the clinical outcome of a drug treatment¹¹². Thus, with a cellular background that is appropriate for the research question or the disease under investigation, label-free phenotypic assays can inform on both the potency of a molecule and its potential adverse effects^{8,113}. This may lead to an overall better prediction of a molecule’s *in vivo* efficacy and reduce the chance

of clinical failure of drug candidates, as poor efficacy is still a major cause of failed clinical trials and drug attrition¹¹⁴. The cell-based, label-free, impedance-based phenotypic assays that are described in this thesis are an attractive alternative to traditional SLC assays (see **Table 1.1, Chapter 1**) and may be implemented in drug discovery programs in the years to come.

The use of label-free impedance-based platforms in pharmacological research and life sciences in general has increased over the last few years. Besides their common use to monitor cell proliferation and viability¹¹⁵, the applications of these technologies extend well beyond cell-based functional assays for GPCRs and SLCs. xCELLigence Cardio systems are routinely used to test the effect of compounds on cardiac contractility in (induced pluripotent stem cell-derived) cardiomyocytes, which offers fast, high-throughput screening of cardiotoxicity for drug safety assessment¹¹⁶. Moreover, real-time cell analysis is increasingly used as a platform to measure T cell-mediated killing of adherent cells¹¹⁷ and has become the most common method to evaluate cytotoxicity of chimeric antigen receptor (CAR)-T cells, a highly promising immunotherapy for solid tumors^{118,119}. In the wake of the recent COVID-19 pandemic, the xCELLigence has been used for rapid (<5 min) detection of severe acute respiratory syndrome coronavirus 2 (SARS-CoV-2) antibodies in serum samples on spike protein-coated E-plates, demonstrating the applicability of impedance measurements with cell-free approaches¹²⁰. Although the possibilities with impedance-based biosensors are broad, a potential concern is that they offer a ‘black box’ readout, which would indicate that the mechanism by which a compound elicits a cellular response is unclear judging from the impedance changes alone¹². However, just as with other functional assays a conventional solution to address this concern is to use appropriate controls, such as cell lines with and without the target of interest, the use of orthogonal assays, receptor antagonists or pathway-specific inhibitors (as shown in **Chapter 3, 4 and 6**) to deconvolute the signal and attribute parts of the response that are of interest to the research question. Thus, since impedance measurements can be used to detect a wide range of cellular behavior and are not limited to assessment of a single pathway, it is expected that versatile platforms such as xCELLigence will be implemented more often in biochemical studies.

In this thesis, we have focused on seven SLCs (DAT, NET and EAAT1/2/3/4/5) for the development of label-free impedance-based assays, of which three were assessed in a TRACT assay. However, there are many SLCs that transport a substrate that is also a GPCR ligand, which we have summarized in **Appendix Table A.1**. Besides providing an extensive overview of affinity and potency values for substrates on SLCs and GPCRs, this list may aid in the selection of SLCs for future TRACT assessment on xCELLigence; several of these – monocarboxylate transporters SMCT1/2 (SLC5A8/12), prostaglandin transporter PGT (SLCO2A1) and monoamine transporter PMAT (SLC29A4) – are subject to ongoing investigations in-house. It should be noted that the current list focuses on *human* SLCs and GPCRs, thus it does not include isoforms that are exclusively expressed in other mammals. Evidently, we did not report orphan SLCs and GPCRs (i.e., substrate is unknown). Since ~30% of SLCs and ~15% of GPCRs are considered orphan (**Chapter 2**), there may be additions to **Table A.1** in the future when these transporters and receptors are deorphanized. Even though vesicular transporters are included, we did not mention

mitochondrial transporters from the SLC25 family. Moreover, we have limited the overview to reported endogenous substrates that engage with both the SLC and GPCR, indicating that we exclude putative substrates (e.g., from large metabolic screens), substrates that *inhibit* SLCs or GPCRs, metabolic precursors of GPCR ligands (e.g., choline as a precursor of acetylcholine), non-GPCR ligands (e.g., taurine, glucose) and drugs/xenobiotics that share an SLC–GPCR pair. In line with this, we did not report substrates for other types of receptors (e.g., ligand-gated ion channels, nuclear receptors) that might result in cellular responses upon activation. Although in this thesis we emphasize TRACT assays based on modulation of GPCRs by *influx* of substrate by SLCs at the plasma membrane, there may be other possible assay set-ups to investigate SLCs with different modes of action and localizations. For example, sphingosine-1-phosphate (S1P) efflux *via* MFSD2B (SLC59A2) could be detected by applying the supernatant of the MFSD2B-expressing cells to a cell line expressing the S1P3 receptor and measuring the calcium response, as was described in a recent RESOLUTE-curated review¹⁰⁵. Such a set-up could potentially be mimicked on an xCELLigence E-plate, for example by co-culturing cells that express either the SLC or GPCR. Alternatively, vesicular loading and subsequent release of neurotransmitters (e.g., monoamines, ATP) *via* Ca^{2+} -induced exocytosis of vesicles¹²¹ may be detected in a similar manner, by using a substrate-‘producing’ cell line and a substrate-‘responsive’ cell line, although this has yet to be verified experimentally. Taken together, judging from the breadth of SLCs that are involved in the translocation of GPCR ligands, there is ample opportunity for TRACT assay development.

The advantage of impedance-based measurements is that they can capture any phenotypic event, suggesting that we can infer the effect of a substrate/compound by the presence or absence of the protein of interest rather than know upfront the mechanism *via* which a response is elicited. As we have demonstrated in **Chapter 6 and 7**, the uptake of glutamate *via* EAAT1 induces a change in cell morphology that was triggered by the large influx of Na^+ and subsequent cell swelling. While we have only observed this ‘phenotype’ so far with EAATs, there are at least 60 other SLCs that are coupled to an inward Na^+ -gradient and, thus, may result in cell swelling or changes in cell morphology upon substrate uptake (**Appendix Table A.2**). For example, Na^+ -dependent uptake of taurine, glucose and glutamine, among other amino acids, has been associated with cell swelling¹²². In addition, several of these transporters, such as NKCC1 (SLC12A2) and NHE (SLC9 family), are involved in the regulation of cell volume and may be candidates for assessment using impedance⁸⁴. One study reported a label-free assay (dynamic mass redistribution, EPIC) for the Na^+ -coupled phosphate transporter NaPi-2b (SLC34A2), where stimulation of MDCK-NaPi-2b cells with inorganic phosphate resulted in a positive DMR response¹²³. Although the authors did not provide a mechanistic explanation, we may speculate that this response was elicited by Na^+ -dependent substrate uptake and resultant cell swelling, which could make this transporter amenable for assessment on xCELLigence. It should be noted that **Table A.2** does not include those transporters that are coupled to symport or antiport of other co-substrates¹²⁴, which would expand the list substantially.

In addition to changes in cell volume, substrate uptake may disrupt intracellular processes or induce cytotoxicity. Recently, our lab demonstrated that uptake of the neurotoxin

MPP⁺ in HEK293 JumpIn cells overexpressing organic cation transporters 1–3 (OCT1–3, SLC22A1–3) induces a concentration-dependent impedance response within one hour¹²⁵. Despite the mechanism not being completely understood, we currently hypothesize that MPP⁺ disrupts the mitochondrial membrane potential, which eventually alters cell morphology. These results indicate a great unexplored potential for SLCs that could be assessed using the label-free approaches described in this thesis. Although the tables in the **Appendix** provide a guideline for the rational selection of SLCs, the best chance to determine whether xCELLigence is suitable for a specific SLC is perhaps the ‘phenotypic’ approach – add substrate to cells that express the SLC and observe changes in cellular impedance. The HEK293 JumpIn system, with inducible expression of the SLC, may be an excellent starting point to commence these efforts. To help decide whether the next SLC can be tested on xCELLigence, we have provided a illustrative decision tree (**Figure 8.6**).

Fundamental and clinical SLC research has been expanding significantly over the last decades, partly invigorated by community calls that plea for a superfamily-wide approach to deorphanize SLCs and generate reagents, structures and assays^{126–128}. The number of SLC drug targets is increasing as well, with several SLCs associated with the development and progression of cancer¹²⁹, metabolic disease⁹⁹ and neurological disorders^{130,131}. For example, the glutamate/cystine antiporter (xCT, SLC7A11) is a promising target for the treatment of various tumors as it plays a role in ferroptosis, tumor growth and chemoresistance¹³². Moreover, the amino acid transporters ASCT2 (SLC1A5) and LAT1 (SLC7A5) are associated to most hallmarks of cancer due to their involvement in energy metabolism¹³³, and the first small molecule LAT1 inhibitor JPH203 in a clinical Phase I study was well-tolerated and efficacious in patients with advanced solid tumors¹³⁴. In addition, three inhibitors of the glycine transporters (GlyT1/2, SLC6A9/5) are currently in clinical trials for the treatment of cognitive impairment associated with schizophrenia or Alzheimer’s disease¹³⁵. Drug discovery and development for these SLCs, in addition to DAT, NET and EAATs, could certainly benefit from the phenotypic impedance-based assays that have been described in this thesis. Altogether, we can conclude that up until now we have barely skimmed the surface of impedance-based assays for SLCs – the prospects for an expansion of the transporter toolbox are good and we may soon welcome this novel platform to the SLC family.

Final notes

This thesis describes the development and validation of cell-based label-free assays to assess the function of dopamine, norepinephrine and glutamate transporters. The technology that was used throughout this thesis, xCELLigence, is novel in the field of transporter research and provides an alternative approach to study SLCs. The applications of these assays range from mechanistic investigations to screening of large compound libraries, which could accelerate drug discovery efforts for SLCs. Hopefully, the data presented in this thesis will inspire SLC researchers to rethink transport assays and come up with innovative ways to study this endlessly fascinating family of membrane proteins, which, ultimately, will lead to improved therapies to the benefit of patients.

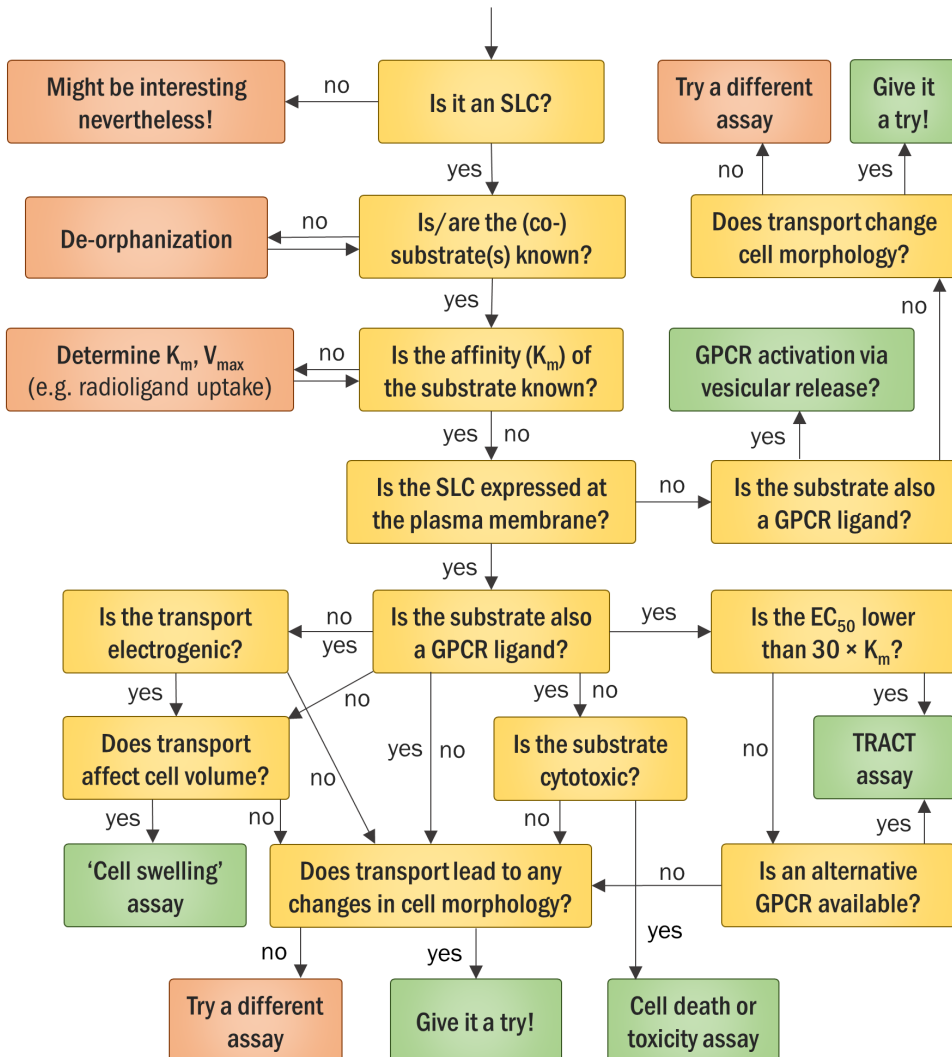


Figure 8.6 – Decision tree for impedance-based assays for SLCs. Input at the top can be any drug target. Yellow boxes indicate questions. Red boxes indicate decisions that are not related to impedance-based assays. Green boxes indicate impedance-based assays.

References

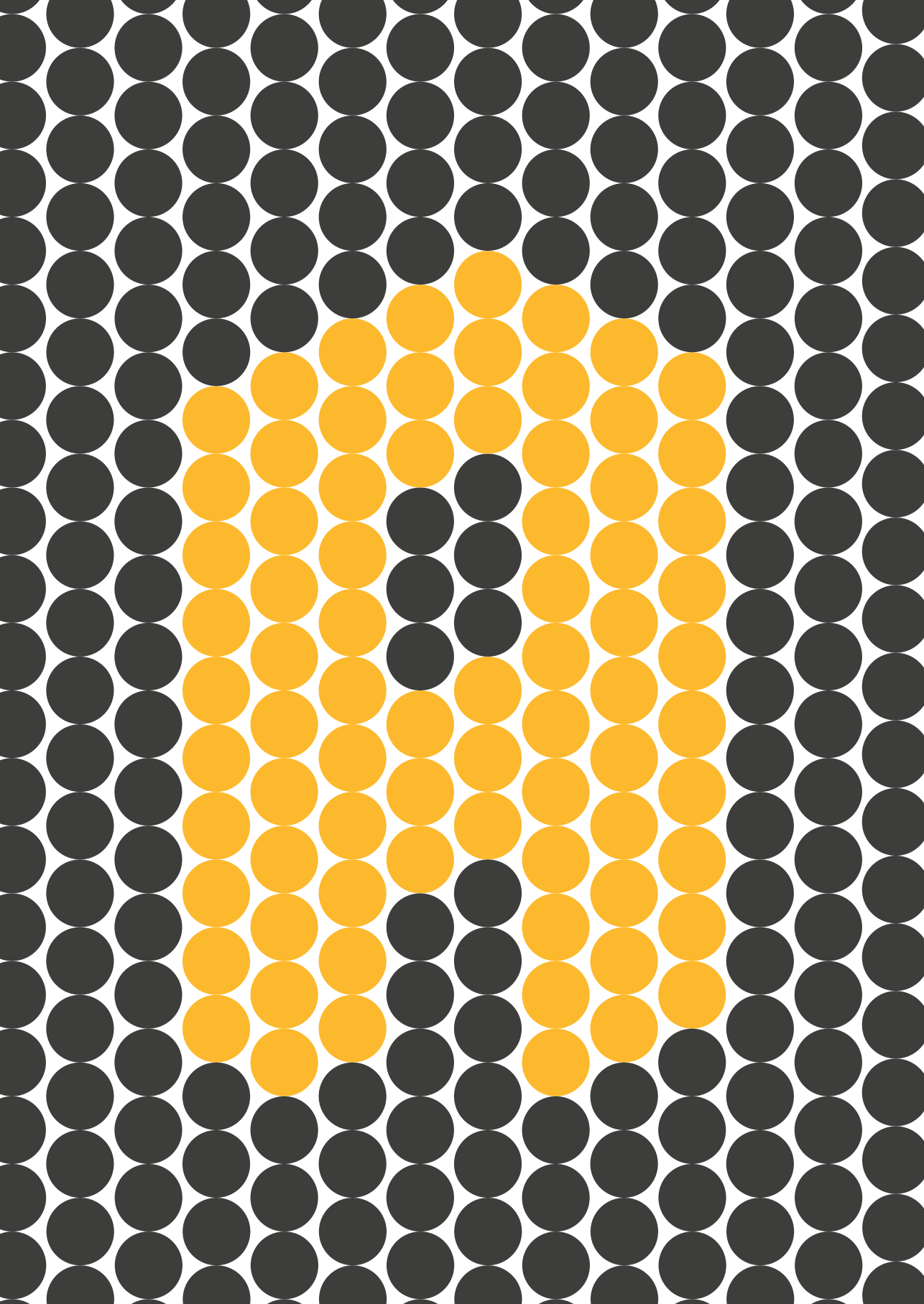
- Bongers, B. J., IJzerman, A. P. & Van Westen, G. J. P. (2019) Proteochemometrics – recent developments in bioactivity and selectivity modeling. *Drug Discov. Today Technol.* **32–33**, 89–98.
- Burggraaff, L. *et al.* (2019) Identification of novel small molecule inhibitors for solute carrier SGLT1 using proteochemometric modeling. *J. Cheminform.* **11**, 15.
- Esch, E. W., Bahinski, A. & Huh, D. (2015) Organs-on-chips at the frontiers of drug discovery. *Nat. Rev. Drug Discov.* **14**, 248–260.
- Langhans, S. A. (2018) Three-dimensional in vitro cell culture models in drug discovery and drug repositioning. *Front. Pharmacol.* **9**, 1–14.
- Michellini, E., Cevenini, L., Mezzanotte, L., Coppa, A. & Roda, A. (2010) Cell-based assays: Fuelling drug discovery. *Anal. Bioanal. Chem.* **398**, 227–238.
- Geibel, S., Flores-Herr, N., Licher, T. & Vollert, H. (2006) Establishment of cell-free electrophysiology for ion transporters: Application for pharmacological profiling. *J. Biomol. Screen.* **11**, 262–268.
- Bazzzone, A., Barthmes, M. & Fendler, K. (Academic Press, 2017). SSM-based electrophysiology for transporter research. in *Methods in Enzymology* (ed. Ziegler, C.) vol. 594 31–83.
- Hillger, J. M., Lieuw, W.-L., Heitman, L. H. & IJzerman, A. P. (2017) Label-free technology and patient cells: from early drug development to precision medicine. *Drug Discov. Today* **22**, 1808–1815.
- Lundstrom, K. (2017) Cell-impedance-based label-free technology for the identification of new drugs. *Expert Opin. Drug Discov.* **12**, 335–343.
- Fang, Y. (2011) Label-free biosensors for cell biology. *Int. J. Electrochem.* **2011**, 1–16.
- Scott, C. W. & Peters, M. F. (2010) Label-free whole-cell assays: Expanding the scope of GPCR screening. *Drug Discov. Today* **15**, 704–716.
- Doijen, J. *et al.* (2019) Advantages and shortcomings of cell-based electrical impedance measurements as a GPCR drug discovery tool. *Biosens. Bioelectron.* **137**, 33–44.
- Vázquez-Victorio, G., González-Espinosa, C., Espinosa-Riquer, Z. P. & Macías-Silva, M. (Academic Press, 2016). GPCRs and actin–cytoskeleton dynamics. in *Methods in Cell Biology* (ed. Shukla, A. K.) vol. 132 165–188.
- Jörg, M. *et al.* (2016) Novel irreversible agonists acting at the A1 adenosine receptor. *J. Med. Chem.* **59**, 11182–11194.
- Guo, D., Mulder-Krieger, T., IJzerman, A. P. & Heitman, L. H. (2012) Functional efficacy of adenosine A2A receptor agonists is positively correlated to their receptor residence time. *Br. J. Pharmacol.* **166**, 1846–1859.
- Baltos, J.-A. *et al.* (2017) Capadenoson, a clinically trialed partial adenosine A1 receptor agonist, can stimulate adenosine A2B receptor biased agonism. *Biochem. Pharmacol.* **135**, 79–89.
- Hillger, J. M. *et al.* (2016) Getting personal: Endogenous adenosine receptor signaling in lymphoblastoid cell lines. *Biochem. Pharmacol.* **115**, 114–122.
- Nederpelt, I., Vergroesen, R. D., IJzerman, A. P. & Heitman, L. H. (2016) Persistent GnRH receptor activation in pituitary α T3-1 cells analyzed with a label-free technology. *Biosens. Bioelectron.* **79**, 721–727.
- Hillger, J. M. *et al.* (2015) Whole-cell biosensor for label-free detection of GPCR-mediated drug responses in personal cell lines. *Biosens. Bioelectron.* **74**, 233–242.
- Linden, J. (1989) Adenosine deaminase for removing adenosine: how much is enough? *Trends Pharmacol. Sci.* **10**, 260–262.
- Mendel, C. M. & Mendel, D. B. (1985) ‘Non-specific’ binding. The problem, and a solution. *Biochem. J.* **228**, 269–272.
- Kenakin, T. P. (1980) Errors in the measurement of agonist potency-ratios produced by uptake processes: A general model applied to β -adrenoceptor agonists. *Br. J. Pharmacol.* **71**, 407–417.
- Vlachodimou, A., IJzerman, A. P. & Heitman, L. H. (2019) Label-free detection of transporter activity via GPCR signalling in living cells: a case for SLC29A1, the equilibrative nucleoside transporter 1. *Sci. Rep.* **9**, 13802.
- Zhang, R. & Xie, X. (2012) Tools for GPCR drug discovery. *Acta Pharmacol. Sin.* **33**, 372–384.
- Cheng, M. H. & Bahar, I. (2019) Monoamine transporters: structure, intrinsic dynamics and allosteric regulation. *Nat. Struct. Mol. Biol.* **26**, 545–556.
- Kristensen, A. S. *et al.* (2011) SLC6 neurotransmitter transporters: Structure, function, and regulation. *Pharmacol. Rev.* **63**, 585–640.
- Xue, W. *et al.* (2018) Recent advances and challenges of the drugs acting on monoamine transporters. *Curr. Med. Chem.* **25**, 1–42.
- Spiegel, S., Maczis, M. A., Maceyka, M. & Milstien, S. (2019) New insights into functions of the sphingosine-1-phosphate transporter SPNS2. *J. Lipid Res.* **60**, 484–489.
- Prag, H. A. *et al.* (2021) Mechanism of succinate efflux upon reperfusion of the ischaemic heart. *Cardiovasc. Res.* **117**, 1188–1201.

30. Lieb, S. *et al.* (2016) Label-free versus conventional cellular assays: Functional investigations on the human histamine H1 receptor. *Pharmacol. Res.* **114**, 13–26.
31. Sijben, H. J., van den Berg, J. J. E., Broekhuis, J. D., IJzerman, A. P. & Heitman, L. H. (2021) A study of the dopamine transporter using the TRACT assay, a novel in vitro tool for solute carrier drug discovery. *Sci. Rep.* **11**, 1312.
32. Yao, F. *et al.* (1998) Tetracycline repressor, tetR, rather than the tetR–mammalian cell transcription factor fusion derivatives, regulates inducible gene expression in mammalian cells. *Hum. Gene Ther.* **9**, 1939–1950.
33. Butler, R. *et al.* (2015) Use of the site-specific retargeting jump-in platform cell line to support biologic drug discovery. *J. Biomol. Screen.* **20**, 528–535.
34. Zhang, J.-H., Chung, T. D. Y. & Oldenburg, K. R. (1999) A simple statistical parameter for use in evaluation and validation of high throughput screening assays. *J. Biomol. Screen.* **4**, 67–73.
35. Todd, A. C. & Hardingham, G. E. (2020) The regulation of astrocytic glutamate transporters in health and neurodegenerative diseases. *Int. J. Mol. Sci.* **21**, 9607.
36. Doornbos, M. L. J. *et al.* (2018) Constitutive activity of the metabotropic glutamate receptor 2 explored with a whole-cell label-free biosensor. *Biochem. Pharmacol.* **152**, 201–210.
37. Doornbos, M. L. J. *et al.* (2018) Impact of allosteric modulation: Exploring the binding kinetics of glutamate and other orthosteric ligands of the metabotropic glutamate receptor 2. *Biochem. Pharmacol.* **155**, 356–365.
38. Stepanenko, A. A. & Heng, H. H. (2017) Transient and stable vector transfection: Pitfalls, off-target effects, artifacts. *Mutat. Res. Mutat. Res.* **773**, 91–103.
39. Kenakin, T. & Christopoulos, A. (2013) Signalling bias in new drug discovery: Detection, quantification and therapeutic impact. *Nat. Rev. Drug Discov.* **12**, 205–216.
40. Cannon, W. B. (1939) A law of denervation. *Am. J. Med. Sci.* **198**, 737–750.
41. Cannon, W. B. & Rosenblueth, A. (Macmillan, 1949). *The Supersensitivity of Denervated Structures*.
42. Hughes, F. B. & Brodie, B. B. (1959) The mechanism of serotonin and catecholamine uptake by platelets. *J. Pharmacol. Exp. Ther.* **127**, 96–102.
43. Iversen, L. L. (1963) The uptake of noradrenaline by the isolated perfused rat heart. *Br. J. Pharmacol. Chemother.* **21**, 523–537.
44. Iversen, L. L. (1965) The uptake of catecholamines at high perfusion concentrations in the rat isolated heart: a novel catechol amine uptake process. *Br. J. Pharmacol. Chemother.* **25**, 18–33.
45. Schömig, E., Lazar, A. & Gründemann, D. (Springer Berlin Heidelberg, 2006). Extraneuronal monoamine transporter and organic cation transporters 1 and 2: A review of transport efficiency. in *Neurotransmitter Transporters: Handbook of Experimental Pharmacology* (eds. Sitte, H. H. & Freissmuth, M.) vol. 175 151–180.
46. Engel, K., Zhou, M. & Wang, J. (2004) Identification and characterization of a novel monoamine transporter in the human brain. *J. Biol. Chem.* **279**, 50042–50049.
47. Furchgott, R. F. (Springer Berlin Heidelberg, 1972). The classification of adrenoceptors (adrenergic receptors). An evaluation from the standpoint of receptor theory. in *Catecholamines: Handbook of Experimental Pharmacology* (eds. Blaschko, H. & Muscholl, E.) vol. 33 283–335.
48. Fredholm, B. B., Irenius, E., Kull, B. & Schulte, G. (2001) Comparison of the potency of adenosine as an agonist at human adenosine receptors expressed in Chinese hamster ovary cells. *Biochem. Pharmacol.* **61**, 443–448.
49. Wahrheit, J., Nicolae, A. & Heinzel, E. (2013) Investigation of glutamine metabolism in CHO cells by dynamic metabolic flux analysis. *BMC Proc.* **7**, P44.
50. Brabet, I. *et al.* (1998) Comparative effect of l-CCG-I, DCG-IV and γ -carboxy-l-glutamate on all cloned metabotropic glutamate receptor subtypes. *Neuropharmacology* **37**, 1043–1051.
51. Langer, S. Z. & Trendelenburg, U. (1969) The effect of a saturable uptake mechanism on the slopes of dose-response curves for sympathomimetic amines and on the shifts of dose-response curves produced by a competitive antagonist. *J. Pharmacol. Exp. Ther.* **167**, 117–42.
52. Kenakin, T. P. (Elsevier, 2014). *A Pharmacology Primer: Techniques for More Effective and Strategic Drug Discovery*. Academic Press vol. 38.
53. Gesztelyi, R. *et al.* (2012) The Hill equation and the origin of quantitative pharmacology. *Arch. Hist. Exact Sci.* **66**, 427–438.
54. Chi, Y., Suadicani, S. O. & Schuster, V. L. (2014) Regulation of prostaglandin EP1 and EP4 receptor signaling by carrier-mediated ligand reuptake. *Pharmacol. Res. Perspect.* **2**, 1–11.
55. Raffel, D. M. *et al.* (2013) Radiotracers for cardiac sympathetic innervation: transport kinetics and binding affinities for the human norepinephrine transporter. *Nucl. Med. Biol.* **40**, 331–337.
56. Hovde, M. J., Larson, G. H., Vaughan, R. A. & Foster, J. D. (2019) Model systems for analysis of dopamine transporter function and regulation. *Neurochem. Int.* **123**, 13–21.
57. Stein, W. D. (Academic Press, 1986). *Transport and Diffusion Across Cell Membranes*. vol. 1.
58. Vivian, D. & Polli, J. E. (2014) Mechanistic interpretation of conventional Michaelis–Menten parameters in a transporter system. *Eur. J. Pharm. Sci.* **64**, 44–52.

59. Jardetzky, O. (1966) Simple allosteric model for membrane pumps. *Nature* **211**, 969–970.
60. Piniella, D. *et al.* (2018) Identification of novel regulatory partners of the glutamate transporter GLT-1. *Glia* **66**, 2737–2755.
61. Matsson, P. *et al.* (2015) Quantifying the impact of transporters on cellular drug permeability. *Trends Pharmacol. Sci.* **36**, 255–262.
62. Schicker, K., Farr, C. V., Boytsov, D., Freissmuth, M. & Sandtner, W. (2022) Optimizing the substrate uptake rate of solute carriers. *Front. Physiol.* **13**, 817886.
63. Paczkowski, F. A., Bönisch, H. & Bryan-Lluka, L. J. (2002) Pharmacological properties of the naturally occurring Ala457 pro variant of the human norepinephrine transporter. *Pharmacogenetics* **12**, 165–173.
64. Susic, S. & Bryan-Lluka, L. J. (2002) The role of the conserved GXXXXRXG motif in the expression and function of the human norepinephrine transporter. *Mol. Brain Res.* **108**, 40–50.
65. Gu, H., Wall, S. C. & Rudnick, G. (1994) Stable expression of biogenic amine transporters reveals differences in inhibitor sensitivity, kinetics, and ion dependence. *J. Biol. Chem.* **269**, 7124–7130.
66. Reith, M. E. A., Xu, C., Zhang, L. & Coffey, L. L. (1996) Translocation of dopamine and binding of WIN 35,428 measured under identical conditions in cells expressing the cloned human dopamine transporter. *Naunyn. Schmiedeberg. Arch. Pharmacol.* **354**, 295–304.
67. Young, J. D., Yao, S. Y. M., Baldwin, J. M., Cass, C. E. & Baldwin, S. A. (2013) The human concentrative and equilibrative nucleoside transporter families, SLC28 and SLC29. *Mol. Aspects Med.* **34**, 529–547.
68. Vandenberg, R. J. & Ryan, R. M. (2013) Mechanisms of glutamate transport. *Physiol. Rev.* **93**, 1621–1657.
69. Löwe, M., Kalacheva, M., Boersma, A. J. & Kedrov, A. (2020) The more the merrier: effects of macromolecular crowding on the structure and dynamics of biological membranes. *FEBS J.* **287**, 5039–5067.
70. Belo do Nascimento, I. *et al.* (2021) Pharmacological evidence for the concept of spare glutamate transporters. *Neurochem. Int.* **149**, 105142.
71. Scott Ramsey, I. & Defelice, L. J. (2002) Serotonin transporter function and pharmacology are sensitive to expression level. Evidence for an endogenous regulatory factor. *J. Biol. Chem.* **277**, 14475–14482.
72. Chen, N. & Reith, M. E. A. (2007) Substrates and inhibitors display different sensitivity to expression level of the dopamine transporter in heterologously expressing cells. *J. Neurochem.* **101**, 377–388.
73. Shibayama, T. *et al.* (2015) Unstirred water layers and the kinetics of organic cation transport. *Pharm. Res.* **32**, 2937–2949.
74. Korjamo, T., Heikkinen, A. T. & Mönkkönen, J. (2009) Analysis of unstirred water layer in in vitro permeability experiments. *J. Pharm. Sci.* **98**, 4469–4479.
75. Pohl, P., Saparov, S. M. & Antonenko, Y. N. (1998) The size of the unstirred layer as a function of the solute diffusion coefficient. *Biophys. J.* **75**, 1403–1409.
76. Yu, N. *et al.* (2006) Real-time monitoring of morphological changes in living cells by electronic cell sensor arrays: an approach to study G protein-coupled receptors. *Anal. Chem.* **78**, 35–43.
77. Suutari, T. *et al.* (2020) Label-free analysis with multiple parameters separates G protein-coupled receptor signaling pathways. *Anal. Chem.* **92**, 14509–14516.
78. Wootten, D., Christopoulos, A., Marti-Solano, M., Babu, M. M. & Sexton, P. M. (2018) Mechanisms of signalling and biased agonism in G protein-coupled receptors. *Nat. Rev. Mol. Cell Biol.* **19**, 638–653.
79. Christopoulos, A. & Kenakin, T. (2002) G protein-coupled receptor allosterism and complexing. *Pharmacol. Rev.* **54**, 323–374.
80. O'Connor, E. R., Kimelberg, H. K., Keese, C. R. & Giaever, I. (1993) Electrical resistance method for measuring volume changes in monolayer cultures applied to primary astrocyte cultures. *Am. J. Physiol. - Cell Physiol.* **264**, 471–478.
81. Schneider, G. H., Baethmann, A. & Kempfski, O. (1992) Mechanisms of glial swelling induced by glutamate. *Can. J. Physiol. Pharmacol.* **70**, S334–S343.
82. Koyama, Y., Sugimoto, T., Shigenaga, Y., Baba, A. & Iwata, H. (1991) A morphological study on glutamate-induced swelling of cultured astrocytes: Involvement of calcium and chloride ion mechanisms. *Neurosci. Lett.* **124**, 235–238.
83. Jakab, M. & Ritter, M. (2006) Cell volume regulatory ion transport in the regulation of cell migration. *Contrib. Nephrol.* **152**, 161–180.
84. Morishita, K., Watanabe, K. & Ichijo, H. (2019) Cell volume regulation in cancer cell migration driven by osmotic water flow. *Cancer Sci.* **110**, 2337–2347.
85. Hoffmann, E. K., Lambert, I. H. & Pedersen, S. F. (2009) Physiology of cell volume regulation in vertebrates. *Physiol. Rev.* **89**, 193–277.
86. Rose, E. M. *et al.* (2009) Glutamate transporter coupling to Na,K-ATPase. *J. Neurosci.* **29**, 8143–8155.
87. Lo, Y. C., Rensi, S. E., Torng, W. & Altman, R. B. (2018) Machine learning in chemoinformatics and drug discovery. *Drug Discov. Today* **23**, 1538–1546.

88. Paul, D. *et al.* (2021) Artificial intelligence in drug discovery and development. *Drug Discov. Today* **26**, 80–93.
89. Liu, X., Ye, K., van Vlijmen, H. W. T., IJzerman, A. P. & van Westen, G. J. P. (2019) An exploration strategy improves the diversity of de novo ligands using deep reinforcement learning: A case for the adenosine A2A receptor. *J. Cheminform.* **11**, 1–16.
90. Schlessinger, A. *et al.* (2018) Molecular modeling of drug–transporter interactions—An International Transporter Consortium perspective. *Clin. Pharmacol. Ther.* **104**, 818–835.
91. Garib Singh, R. A. & Schlessinger, A. (2019) Advances and challenges in rational drug design for SLCs. *Trends Pharmacol. Sci.* **40**, 790–800.
92. Van Westen, G. J. P., Wegner, J. K., IJzerman, A. P., Van Vlijmen, H. W. T. & Bender, A. (2011) Proteochemometric modeling as a tool to design selective compounds and for extrapolating to novel targets. *Medchemcomm* **2**, 16–30.
93. Türková, A. & Zdrážil, B. (2019) Current advances in studying clinically relevant transporters of the solute carrier (SLC) family by connecting computational modeling and data science. *Comput. Struct. Biotechnol. J.* **17**, 390–405.
94. De Bruyn, T. *et al.* (2013) Structure-based identification of OATP1B1/3 inhibitors. *Mol. Pharmacol.* **83**, 1257–1267.
95. Schlessinger, A. *et al.* (2011) Structure-based discovery of prescription drugs that interact with the norepinephrine transporter, NET. *Proc. Natl. Acad. Sci.* **108**, 15810–15815.
96. Schaller, L. & Lauschke, V. M. (2019) The genetic landscape of the human solute carrier (SLC) transporter superfamily. *Hum. Genet.* **138**, 1359–1377.
97. Lin, L., Yee, S. W., Kim, R. B. & Giacomini, K. M. (2015) SLC transporters as therapeutic targets: Emerging opportunities. *Nat. Rev. Drug Discov.* **14**, 543–560.
98. Santer, R. & Calado, J. (2010) Familial renal glucosuria and SGLT2: From a Mendelian trait to a therapeutic target. *Clin. J. Am. Soc. Nephrol.* **5**, 133–141.
99. Schumann, T. *et al.* (2020) Solute carrier transporters as potential targets for the treatment of metabolic disease. *Pharmacol. Rev.* **72**, 343–379.
100. Zhao, S. *et al.* (2019) Linifanib exerts dual anti-obesity effect by regulating adipocyte browning and formation. *Life Sci.* **222**, 117–124.
101. Bhat, S., El-Kasaby, A., Freissmuth, M. & Sucic, S. (2021) Functional and biochemical consequences of disease variants in neurotransmitter transporters: A special emphasis on folding and trafficking deficits. *Pharmacol. Ther.* **222**, 107785.
102. Bai, X. (2021) Progress in structural biology of solute carriers. *Curr. Mol. Biol. Reports* **7**, 9–19.
103. Wright, N. J. & Lee, S.-Y. (2019) Structures of human ENT1 in complex with adenosine reuptake inhibitors. *Nat. Struct. Mol. Biol.* doi:10.1038/s41594-019-0245-7.
104. Nygaard, R., Kim, J. & Mancina, F. (2020) Cryo-electron microscopy analysis of small membrane proteins. *Curr. Opin. Struct. Biol.* **64**, 26–33.
105. Dvorak, V. *et al.* (2021) An overview of cell-based assay platforms for the solute carrier family of transporters. *Front. Pharmacol.* **12**, 1–31.
106. Chivukula, A. S., Suslova, M., Kortzak, D., Kovermann, P. & Fahlke, C. (2020) Functional consequences of SLC1A3 mutations associated with episodic ataxia 6. *Hum. Mutat.* **41**, 1892–1905.
107. Canul-Tec, J. C. *et al.* (2017) Structure and allosteric inhibition of excitatory amino acid transporter 1. *Nature* **544**, 446–451.
108. Canul-Tec, J. C. *et al.* (2022) The ion-coupling mechanism of human excitatory amino acid transporters. *EMBO J.* **41**, e108341.
109. Wu, Q. *et al.* (2022) Ataxia-linked SLC1A3 mutations alter EAAT1 chloride channel activity and glial regulation of CNS function. *J. Clin. Invest.* **132**, e154891.
110. Pant, S., Wu, Q., Ryan, R. & Tajkhorshid, E. (2022) Microscopic characterization of the chloride permeation pathway in the human excitatory amino acid transporter 1 (EAAT1). *ACS Chem. Neurosci.* **13**, 776–785.
111. Kortzak, D. *et al.* (2019) Allosteric gate modulation confers K⁺ coupling in glutamate transporters. *EMBO J.* **38**, 1–17.
112. Haasen, D. *et al.* (2017) How phenotypic screening influenced drug discovery: Lessons from five years of practice. *Assay Drug Dev. Technol.* **15**, 239–246.
113. Fang, Y. (2015) Combining label-free cell phenotypic profiling with computational approaches for novel drug discovery. *Expert Opin. Drug Discov.* **10**, 331–343.
114. Shih, H. P., Zhang, X. & Aronov, A. M. (2018) Drug discovery effectiveness from the standpoint of therapeutic mechanisms and indications. *Nat. Rev. Drug Discov.* **17**, 19–33.
115. Roshan Moniri, M. *et al.* (2015) Dynamic assessment of cell viability, proliferation and migration using real time cell analyzer system (RTCA). *Cytotechnology* **67**, 379–386.
116. Scott, C. W. *et al.* (2014) An impedance-based cellular assay using human iPSC-derived cardiomyocytes to quantify modulators of cardiac contractility. *Toxicol. Sci.* **142**, 331–338.
117. Peper, J. K. *et al.* (2014) An impedance-based cytotoxicity assay for real-time and label-free assessment of T-cell-mediated killing of adherent cells. *J. Immunol. Methods* **405**, 192–198.

118. Lisby, A. N., Carlson, R. D., Baybutt, T. R., Weindorfer, M. & Snook, A. E. (Academic Press, 2022). Evaluation of CAR-T cell cytotoxicity: Real-time impedance-based analysis. in *Methods in Cell Biology* (eds. Spada, S. & Galluzzi, L.) vol. 167 81–98.
119. Cerignoli, F. *et al.* (2018) In vitro immunotherapy potency assays using real-time cell analysis. *PLoS One* **13**, e0193498.
120. Rashed, M. Z. *et al.* (2021) Rapid detection of SARS-CoV-2 antibodies using electrochemical impedance-based detector. *Biosens. Bioelectron.* **171**, 112709.
121. Pang, Z. P. & Südhof, T. C. (2010) Cell biology of Ca²⁺-triggered exocytosis. *Curr. Opin. Cell Biol.* **22**, 496–505.
122. Lang, F. *et al.* (1998) Functional significance of cell volume regulatory mechanisms. *Physiol. Rev.* **78**, 247–306.
123. Wong, S.-H., Gao, A., Ward, S., Henley, C. & Lee, P. H. (2012) Development of a label-free assay for sodium-dependent phosphate transporter NaPi-IIb. *J. Biomol. Screen.* **17**, 829–834.
124. Alexander, S. P. H. *et al.* (2021) The concise guide to pharmacology 2021/22: Transporters. *Br. J. Pharmacol.* **178**, S412–S513.
125. Mocking, T., Sijben, H., Vermeulen, Y., IJzerman, A. & Heitman, L. (2022) MPP⁺-induced changes in cellular impedance as a measure for organic cation transporter (SLC22A1-3) activity and inhibition. *Int. J. Mol. Sci.* **23**, 1203.
126. César-Razquin, A. *et al.* (2015) A call for systematic research on solute carriers. *Cell* **162**, 478–487.
127. Superti-Furga, G. *et al.* (2020) The RESOLUTE consortium: unlocking SLC transporters for drug discovery. *Nat. Rev. Drug Discov.* **19**, 429–430.
128. Hediger, M. A., Clémentçon, B., Burrier, R. E. & Bruford, E. A. (2013) The ABCs of membrane transporters in health and disease (SLC series): Introduction. *Mol. Aspects Med.* **34**, 95–107.
129. Pizzagalli, M. D., Bensimon, A. & Superti-Furga, G. (2021) A guide to plasma membrane solute carrier proteins. *FEBS J.* **288**, 2784–2835.
130. Qosa, H. *et al.* (2016) Transporters as drug targets in neurological diseases. *Clin. Pharmacol. Ther.* **100**, 441–453.
131. Aykaç, A. & Şehirli, A. Ö. (2020) The role of the SLC transporters protein in the neurodegenerative disorders. *Clin. Psychopharmacol. Neurosci.* **18**, 174–187.
132. Liu, J., Xia, X. & Huang, P. (2020) xCT: A critical molecule that links cancer metabolism to redox signaling. *Mol. Ther.* **28**, 2358–2366.
133. Lopes, C., Pereira, C. & Medeiros, R. (2021) ASCT2 and LAT1 contribution to the hallmarks of cancer: From a molecular perspective to clinical translation. *Cancers* **13**, 1–26.
134. Okano, N. *et al.* (2020) First-in-human phase I study of JPH203, an L-type amino acid transporter 1 inhibitor, in patients with advanced solid tumors. *Invest. New Drugs* **38**, 1495–1506.
135. Ackermann, T. M., Höfner, G. & Wanner, K. T. (2021) Screening for new inhibitors of glycine transporter 1 and 2 by means of MS binding assays. *ChemMedChem* **16**, 3094–3104.



APPENDIX

Table A.1–A.2

The tables in this section highlight the breadth of solute carrier (SLC) transporters that mediate the translocation of ligands/substrates that activate G protein-coupled receptors (GPCRs) (**Table A.1**) and that are co-transporters of Na⁺ (**Table A.2**).

Table A.1 – Affinity and potency values of endogenous substrates for various human solute carrier transporters and G protein-coupled receptors.

Solute carrier transporter (SLC)					Substrate		G protein-coupled receptor (GPCR)			
Gene	Protein	Affinity / activity	Comments	Mode of transport	Ref	Gene	Protein	Affinity / potency	Comments	Ref
Nucleosides & nucleotides										
SLC28A2	CNT2	6–23 μM	K _m ([³ H]ADE uptake, EP)	Influx	1	ADORA1	A ₁	100–310 nM	EC ₅₀ (cAMP assay)	2
SLC28A3	CNT3	2.2–15 μM	K _m ([³ H]ADE uptake, EP)	Influx	1	ADORA2A	A _{2A}	310–730 nM	EC ₅₀ (cAMP assay)	2
SLC29A1	ENT1	32–82 μM	K _m ([³ H]ADE uptake)	Influx / efflux	1	ADORA2B	A _{2B}	15,000 nM	EC ₅₀ (cAMP assay)	2
SLC29A2	ENT2	49–140 μM	K _m ([³ H]ADE uptake)	Influx / efflux	1	ADORA3	A ₃	290 nM	EC ₅₀ (cAMP assay)	2
SLC29A3	ENT3	1,620–1,860 μM	K _m ([³ H]ADE uptake, pH 5.5)	Influx / efflux	1					
SLC29A4	ENT4	780 μM	K _m ([³ H]ADE uptake, pH 5.5)	Influx / efflux	1					
SLC17A9	VNUT	800 μM	K _m ([³² P]ATP uptake)	Vesicular	3	P2YR1	P2Y ₁	17,700 nM	K _i ([³ H]MRS2279 binding)	4
						P2YR2	P2Y ₂	230 nM	EC ₅₀ (IP ₃ assay)	5
						P2YR11	P2Y ₁₁	38,000 nM	EC ₅₀ (IP ₃ assay, cAMP assay)	6
						P2YR12	P2Y ₁₂	690 nM	EC ₅₀ (cAMP assay)	7
						P2YR13	P2Y ₁₃	4,200 nM	EC ₅₀ (IP ₃ assay)	8
						GPR17	GPR17	37 nM	EC ₅₀ (cAMP assay)	9
SLC17A9	VNUT		Transported *	Vesicular	3	P2YR1	P2Y ₁	920 nM	K _i ([³ H]MRS2279 binding)	4
						P2YR12	P2Y ₁₂	42 nM	EC ₅₀ (cAMP assay)	7
						P2YR13	P2Y ₁₃	45–194 nM	EC ₅₀ (IP ₃ assay)	8
SLC17A9	VNUT		Transported *	Vesicular	3	P2YR4	P2Y ₄	6,600 nM	EC ₅₀ (Ca ²⁺ assay)	10
Monoamine neurotransmitters										
Acetylcholine										
SLC18A3	VACHT	970 μM	K _m ([³ H]ACH uptake)	Vesicular	11	CHRM1	M ₁	47 μM	K _i ([³ H]NMS binding)	12
SLC22A1	OCT1	117 μM	K _m (EP)	Influx / efflux	13	CHRM2	M ₂	0.3–47 μM	K _i ([³ H]NMS binding)	12,14
SLC22A2	OCT2	580 μM	IC ₅₀ ([³ H]MPP ⁺ inhibition)	Influx / efflux	13	CHRM3	M ₃	4.2–29 μM	K _i ([³ H]NMS binding)	12,14
SLC22A4	OCTN1	1,000 μM	K _m ([³ H]ACH uptake)	Influx	13	CHRM4	M ₄	5.1–32 μM	K _i ([³ H]NMS binding)	14
						CHRM5	M ₅	0.8 nM	K _i ([³ H]NMS binding)	14
SLC6A2	NET	0.1–0.7 μM	K _m ([³ H]IDA uptake)	Influx	15,17	ADRA2A	α _{2A}	2,600 nM	IC ₅₀ ([³ H]IMK912 binding)	18
SLC6A3	DAT	1.2–2.5 μM	K _m ([³ H]IDA uptake)	Influx	16,19	ADRA2C	α _{2C}	3,200 nM	IC ₅₀ ([³ H]IMK912 binding)	18
SLC18A1	VMAT1	3.8 μM	K _i ([³ H]5-HT inhibition)	Vesicular	20	DRD1	D ₁	2,340 nM	K _i ([³ H]SCH23390 binding)	21
SLC18A2	VMAT2	1.4 μM	K _i ([³ H]5-HT inhibition)	Vesicular	20	DRD2	D ₂	710 nM	K _i ([¹²⁵ I]iodosulpiride binding)	22
SLC22A1	OCT1	487 μM	IC ₅₀ ([³ H]TEA inhibition)	Influx	13	DRD3	D ₃	29 nM	K _i ([¹²⁵ I]iodosulpiride binding)	22
SLC22A2	OCT2	390–1,400 μM	K _m ([³ H]IDA uptake)	Influx	13	DRD4	D ₄	0.9–47 nM	K _i ([³ H]spiperone binding)	23,24
SLC22A3	OCT3	800–1,033 μM	K _m ([³ H]IDA uptake)	Influx	13,25	DRD5	D ₅	228 nM	K _i ([³ H]SCH23390 binding)	21
SLC29A4	PMAT	329–406 μM	K _m ([³ H]IDA uptake)	Influx	25,26	TAAR1	TA ₁	422 nM	K _i ([³ H]tyramine binding)	27
SLC6A2	NET	2.9–3.2 μM	K _m ([³ H]EPI uptake)	Influx	15,17	ADRA1A	α _{1A}	600 nM	K _i ([¹²⁵ I]HEAT binding)	28
SLC18A1	VMAT1	5.5 μM	K _i ([³ H]5-HT inhibition)	Vesicular	20	ADRA1B	α _{1B}	400 nM	K _i ([¹²⁵ I]HEAT binding)	28
SLC18A2	VMAT2	1.9 μM	K _i ([³ H]5-HT inhibition)	Vesicular	20	ADRA1D	α _{1D}	56 nM	K _i ([¹²⁵ I]HEAT binding)	28
SLC22A1	OCT1		Transported *	Influx	13	ADRA2A	α _{2A}	1,479 nM	K _i ([³ H]IMK912 binding)	29
SLC22A2	OCT2	420 μM	K _m ([³ H]EPI uptake)	Influx	13	ADRA2B	α _{2B}	6,309 nM	K _i ([³ H]IMK912 binding)	29
SLC22A3	OCT3	240–458 μM	K _m ([³ H]EPI uptake)	Influx	13,25	ADRA2C	α _{2C}	1,698 nM	K _i ([³ H]IMK912 binding)	29
SLC29A4	PMAT	951–15,323 μM	K _m ([³ H]EPI uptake)	Influx	25,26	ADRB1	β ₁	3,970 nM	K _i ([¹²⁵ I]CYP binding)	30
						ADRB2	β ₂	735 nM	K _i ([¹²⁵ I]CYP binding)	30
						ADRB3	β ₃	126,000 nM	K _i ([¹²⁵ I]CYP binding)	30
						DRD4	D ₄	14–240 nM	K _i ([³ H]spiperone binding)	24

Solute carrier transporter (SLC)				Substrate		G protein-coupled receptor (GPCR)				
Gene	Protein	Affinity / activity	Comments	Mode of transport	Ref	Gene	Protein	Affinity / potency	Comments	Ref
SLC6A2	NET	0.3–0.7 μM	K _m ([³ H]NE uptake)	Influx	15,17,31	ADRA1A	α _{1A}	990 nM	K _i ([¹²⁵ I]HEAT binding)	28
SLC6A3	DAT	20 μM	K _m ([³ H]NE uptake)	Influx	16	ADRA1B	α _{1B}	680 nM	K _i ([¹²⁵ I]HEAT binding)	28
SLC18A1	VMAT1	14 μM	K _m ([³ H]5-HT inhibition)	Vesicular	20	ADRA1D	α _{1D}	42 nM	K _i ([¹²⁵ I]HEAT binding)	28
SLC18A2	VMAT2	3.4 μM	K _m ([³ H]5-HT inhibition)	Vesicular	20	ADRA2A	α _{2A}	1,995 nM	K _i ([³ H]MK912 binding)	29
SLC22A1	OCT1		<i>Transported*</i>	Influx	13	ADRA2B	α _{2B}	2,754 nM	K _i ([³ H]MK912 binding)	29
SLC22A2	OCT2	1,500–5,450 μM	K _m ([³ H]NE uptake)	Influx	13	ADRA2C	α _{2C}	1,348 nM	K _i ([³ H]MK912 binding)	28
SLC22A3	OCT3	182–2,630 μM	K _m ([³ H]NE uptake)	Influx	13,25	ADRB1	β ₁	3,570 nM	K _i ([¹²⁵ I]CYP binding)	30
SLC29A4	PMAT	1,078–2,606 μM	K _m ([³ H]NE uptake)	Influx	25,26	ADRB2	β ₂	26,400 nM	K _i ([¹²⁵ I]CYP binding)	30
						ADRB3	β ₃	4,300 nM	K _i ([¹²⁵ I]CYP binding)	30
						DRD4	D ₄	33–1,324 nM	K _i ([³ H]spiperone binding)	24
						TAAR1	TA ₁	> 10,000 nM	K _i ([³ H]tyramine binding)	33
SLC6A4	SERT	0.5 μM	K _m ([³ H]5-HT uptake)	Influx	32	5-HT1A	5-HT _{1A}	0.2 nM	K _i ([³ H]8-OH-DPAT binding)	27
SLC18A1	VMAT1	1.3 μM	K _m ([³ H]5-HT uptake)	Vesicular	20	5-HT1B	5-HT _{1B}	4.3 nM	K _i ([³ H]5-HT binding)	34
SLC18A2	VMAT2	0.8 μM	K _m ([³ H]5-HT uptake)	Vesicular	20	5-HT1D	5-HT _{1D}	3.9 nM	K _i ([³ H]5-HT binding)	34
SLC22A1	OCT1	197 μM	K _m ([³ H]5-HT uptake)	Influx	13	5-HT1E	5-HT _{1E}	11 nM	K _i ([³ H]5-HT binding)	35
SLC22A2	OCT2	80–290 μM	K _m ([³ H]5-HT uptake)	Influx	13	5-HT1F	5-HT _{1F}	10 nM	K _i ([³ H]5-HT binding)	36
SLC22A3	OCT3	900–988 μM	K _m ([³ H]5-HT uptake)	Influx	13,25	5-HT2A	5-HT _{2A}	16 nM	K _i ([³ H]ketanserin binding)	37
SLC29A4	PMAT	114–283 μM	K _m ([³ H]5-HT uptake)	Influx	25,26	5-HT2B	5-HT _{2B}	13 nM	K _i ([³ H]mesulegine binding)	37
						5-HT2C	5-HT _{2C}	5.8 nM	K _i ([³ H]mesulegine binding)	37
						5-HT4	5-HT ₄	330–1,151 nM	K _i ([³ H]GR113808 binding)	38
						5-HT5A	5-HT _{5A}	126 nM	K _i ([³ H]5-GT binding)	39
						5-HT6	5-HT ₆	65 nM	K _i ([³ H]SD binding)	40
						5-HT7	5-HT ₇	8.1 nM	K _i ([³ H]5-HT binding)	41
						DRD1	D ₁	3,000 nM	K _i ([³ H]SCH23390 binding)	21
						DRD5	D ₅	9,690 nM	K _i ([³ H]SCH23390 binding)	21
						TAAR1	TA ₁	> 6,000 nM	K _i ([³ H]tyramine binding)	27
SLC18A1	VMAT1	4,696 μM	K _m ([³ H]5-HT inhibition)	Vesicular	20	HRH1	H ₁	1,259 nM	K _i ([³ H]neopyramine binding)	42
SLC18A2	VMAT2	143 μM	K _m ([³ H]5-HT inhibition)	Vesicular	20	HRH2	H ₂	2,000–8,100 nM	K _i ([¹²⁵ I]-APT binding)	43
SLC22A1	OCT1	3,007 μM	IC ₅₀ ([³ H]TEA inhibition)	Influx	13	HRH3	H ₃	15 nM	K _i ([³ H]methylhistamine binding)	44
SLC22A2	OCT2	940–1,300 μM	K _m ([³ H]HIS uptake)	Influx	13	HRH4	H ₄	8.1 nM	K _i ([³ H]histamine binding)	45
SLC22A3	OCT3	180–641 μM	K _m ([³ H]HIS uptake)	Influx	13,25	TAAR1	TA ₁	> 6,000 nM	K _i ([³ H]tyramine binding)	27
SLC29A4	PMAT	4,379–10,471 μM	K _m ([³ H]HIS uptake)	Influx	25,26					
SLC2A1	GLUT1		<i>Transported*</i>	Influx	46	MTNR1A	MT ₁	0.2 nM	K _i ([¹²⁵ I]iodomelatonin binding)	47
SLC15A1	PEPT1	600 μM	K _m (LC-MS/MS)	Influx / mito	48	MTNR1B	MT ₂	0.4 nM	K _i ([¹²⁵ I]iodomelatonin binding)	47
SLC15A2	PEPT2	1,000 μM	K _m (LC-MS/MS)	Influx / mito	48					
Trace amines										
SLC6A3	DAT	1.7–2.2 μM	K _m ([³ H]tyramine uptake, EP)	Influx	49	TAAR1	TA ₁	34 nM	K _i ([³ H]tyramine binding)	27
SLC6A4	SERT	53 μM	K _m ([³ H]tyramine uptake)	Influx	50					
SLC22A1	OCT1	107 μM	IC ₅₀ ([³ H]TEA inhibition)	Influx	13					
SLC22A2	OCT2		<i>Transported*</i>	Influx / efflux	51					
SLC22A3	OCT3		<i>Transported*</i>	Influx	13					
SLC29A4	PMAT	238 μM	K _m ([³ H]tyramine uptake)	Influx	26					

Solute carrier transporter (SLC)				Substrate		G protein-coupled receptor (GPCR)				
Gene	Protein	Affinity / activity	Comments	Mode of transport	Ref	Gene	Protein	Affinity / potency	Comments	Ref
Amino acids										
SLC11A1	EAAT3	62 μM	K _m (³ H)Glu uptake)	Influx	52	CASR	CaR	~1,000 μM	EC ₅₀ (allosteric modulation of Ca ²⁺)	53,54
SLC11A2	EAAT2	97 μM	K _m (³ H)Glu uptake)	Influx	52	GRM1	mGlu ₁	40–184 μM	EC ₅₀ (Ca ²⁺ , IP ₃ assay)	55,56
SLC11A3	EAAT1	48 μM	K _m (³ H)Glu uptake)	Influx	52	GRM2	mGlu ₂	1.8–26 μM	EC ₅₀ (Ca ²⁺ assay, [³⁵ S]GTPγS)	57,58
SLC11A5	ASCT2	3,900–4,800 μM	K _m (³ H)Glu uptake, ΔpH)	Influx / efflux	59	GRM3	mGlu ₃	1 μM	EC ₅₀ (Ca ²⁺ assay)	57
SLC11A6	EAAT4	2.5 μM	K _m (³ H)Glu uptake)	Influx	60	GRM4	mGlu ₄	20–38 μM	EC ₅₀ (CaMP assay)	61,62
SLC11A7	EAAT5	64 μM	EC ₅₀ (EP)	Influx	63	GRM5	mGlu ₅	2.7–4.8 μM	EC ₅₀ (Ca ²⁺ , IP ₃ assay)	64
SLC7A11	xCT	92 μM	K _m (³ H)Glu uptake)	Efflux	65	GRM6	mGlu ₆	6.7–7.6 μM	EC ₅₀ (CaMP assay, [³⁵ S]GTPγS)	58,66
SLC17A5	Sialin	~500 μM	Transported*	Vesicular	67	GRM7	mGlu ₇	56–1000 μM	EC ₅₀ (CaMP assay, [³⁵ S]GTPγS)	58,61
SLC17A6	VGLUT1	~1,000 μM	Transported*	Vesicular	68	GRM8	mGlu ₈	11 μM	EC ₅₀ (CaMP assay)	61
SLC17A7	VGLUT2	~1,000 μM	Transported*	Vesicular	68					
SLC17A8	VGLUT3	~1,000 μM	Transported*	Vesicular	68					
SLC22A7	OAT2		Transported*	Efflux	69					
SLC22A11	OAT4		Transported*	Efflux	70,71					
SLC22A13	OAT10		Transported*	Influx / efflux	72					
SLC22A13	OAT10		Transported*	Influx / efflux	71					
SLC22B1	OATP2B1		Transported*	Efflux	71					
GABA										
SLC6A1	GAT1	11–14 μM	K _m (³ H)GABA uptake, EP)	Influx	73,74	GABBR1	GABA _B	72 μM	K _d ([³ H]GCP54626 binding)	75
SLC6A6	TauT	2,400 μM	K _m (³ H)GABA uptake)	Influx	76	GABBR2	GABA _B (dimer)	0.16 μM	EC ₅₀ (Ca ²⁺ assay)	
SLC6A11	GAT3	8.1–172 μM	K _m (³ H)GABA uptake)	Influx	74,77					
SLC6A12	BGT1	18–20 μM	K _m (³ H)GABA uptake)	Influx	74,78					
SLC6A13	GAT2	8.2 μM	K _m (³ H)GABA uptake)	Influx	79					
SLC32A1	VGAT		Transported*	Vesicular	80					
SLC36A1	PAT1	3,100 μM	K _d (³ H)proline inhibition)	Influx	81					
L-DOPA										
SLC6A10	TAT1	1,212 μM	K _d ([¹⁴ C]-DOPA uptake)	Influx	82	GPR143	GPR143	9,340 nM	K _d ([³ H]-DOPA binding)	83
SLC11A4	ASCT1	68 μM	K _m (³ H)alanine uptake)	Influx / efflux	84	GPC6A	GPC6	173 μM	EC ₅₀ (Ca ²⁺ assay)	85
SLC11A5	ASCT2	29 μM	K _m (³ H)alanine uptake)	Influx / efflux	86	CASR	CaR	~1,000 μM	EC ₅₀ (allosteric modulation of Ca ²⁺)	53,54
SLC6A14	ATB ⁰⁺	99 μM	K _m / EC ₅₀ (EP)	Influx	87					
SLC6A15	B ⁺ AT2		Transported*	Influx	88					
SLC6A19	B ⁺ AT1		Transported*	Influx	89					
SLC7A8	LAT2		Transported*	Influx	90					
SLC7A9	b ⁰⁺ -AT		Transported*	Influx	91					
SLC7A10	Asc-1	9.2 μM	K _m ([¹⁴ C]-alanine uptake)	Influx / efflux	92					
SLC36A1	PAT1	6,000 μM	K _d (³ H)proline inhibition)	Influx	81					
SLC36A4	PAT4	1,480 μM	K _d (³ H)proline inhibition)	Influx	93					
SLC38A1	SNAT1		Transported*	Influx	94					
SLC38A2	SNAT2		Transported*	Influx	94					
SLC38A4	SNAT4		Transported*	Influx	94					
SLC38A5	SNAT5		Transported*	Influx	95					
SLC38A7	SNAT7		Transported*	Influx	94					

Solute carrier transporter (SLC)					Substrate	G protein-coupled receptor (GPCR)					
Gene	Protein	Affinity / activity	Comments	Mode of transport		Gene	Protein	Affinity / potency	Comments	Ref	
SLC6A14	ATB ^{0,-}	104 μM	K _m / EC ₅₀ (EP)	Influx	L-arginine	GPC6A	GPC6	44 μM	EC ₅₀ (Ca ²⁺ assay)	85	
SLC7A1	CAT-1	110–160 μM	K _m ([³ H]arginine uptake)	Influx							
SLC7A2	CAT-2	320–3,900 μM	K _m ([³ H]arginine uptake)	Influx							
SLC7A3	CAT-3	450 μM	K _m ([³ H]arginine uptake)	Influx							
SLC7A6	yLAT2	120 μM	K _m ([¹ - ¹⁴ C]arginine uptake)	Influx / efflux							
SLC7A7	yLAT1		<i>Transported*</i>	Influx / efflux							
SLC7A9	b ^{0,-} AT		<i>Transported*</i>	Influx / efflux							
SLC38A4	SNAT4		<i>Transported*</i>	Influx							
SLC38A9	SLC38A9	2,700 μM	K _m ([³ H]arginine uptake)	Lysosome							
SLC7A5	LAT1	790 μM	K _m ([¹ - ¹⁴ C]citrulline uptake)	Influx	L-citrulline	GPC6A	GPC6	287 μM	EC ₅₀ (Ca ²⁺ assay)	85	
SLC1A5	ASC2	39–1,800 μM	K _m ([³ H]citrulline uptake)	Influx / efflux		GPC6A	GPC6	590 μM	EC ₅₀ (Ca ²⁺ assay)	85	
SLC6A14	ATB ^{0,-}	633 μM	K _m / EC ₅₀ (EP)	Influx	L-glutamine	CASR	CaR	~1,000 μM	EC ₅₀ (allosteric modulation of Ca ²⁺)	53,54	
SLC6A15	B ⁰ AT2		<i>Transported*</i>	Influx							
SLC6A19	B ⁰ AT1		<i>Transported*</i>	Influx							
SLC7A5	LAT1	1,640 μM	K _m ([¹ - ¹⁴ C]glutamine uptake)	Influx / efflux							
SLC7A6	yLAT2	295 μM	K _m ([¹ - ¹⁴ C]glutamine uptake)	Influx							
SLC7A8	LAT2		<i>Transported*</i>	Influx							
SLC36A4	PA74	430 μM	K _t ([³ H]proline inhibition)	Influx							
SLC38A1	SNAT1		<i>Transported*</i>	Influx							
SLC38A2	SNAT2		<i>Transported*</i>	Influx							
SLC38A3	SNAT3	1,600 μM	K _m ([³ H]glutamine uptake)	Influx							
SLC38A5	SNAT5		<i>Transported*</i>	Influx							
SLC38A7	SNAT7		<i>Transported*</i>	Influx							
SLC38A9	SLC38A9	518 μM	K _m ([³ H]glutamine uptake)	Lysosome							
SLC6A5	GVT2	108 μM	K _m ([³ H]glycine uptake)	Influx		Glycine	GPC6A	GPC6	263 μM	EC ₅₀ (Ca ²⁺ assay)	85
SLC6A9	GVT1	70–90 μM	K _m ([³ H]glycine uptake)	Influx / efflux							
SLC6A14	ATB ^{0,-}	111 μM	K _m / EC ₅₀ (EP)	Influx							
SLC7A10	Asc-1		<i>Transported*</i>	Influx							
SLC36A1	PA71	9,900 μM	K _t ([³ H]proline inhibition)	Influx							
SLC36A2	PA72	490 μM	K _m (EP)	Influx							
SLC38A1	SNAT1		<i>Transported*</i>	Influx							
SLC38A2	SNAT2		<i>Transported*</i>	Influx							
SLC38A4	SNAT4		<i>Transported*</i>	Influx							
SLC38A5	SNAT5		<i>Transported*</i>	Influx							
SLC6A14	ATB ^{0,-}	100 μM	K _m / EC ₅₀ (EP)	Influx	L-lysine	GPC6A	GPC6	169 μM	EC ₅₀ (Ca ²⁺ assay)	85	
SLC7A1	CAT-1		<i>Transported*</i>	Influx		CASR	CaR	> 10,000 μM	EC ₅₀ (allosteric modulation of Ca ²⁺)	53,54	
SLC7A2	CAT-2		<i>Transported*</i>	Influx							
SLC7A3	CAT-3		K _m ([³ H]lysine uptake)	Influx							
SLC7A6	yLAT2	650 μM	<i>Transported*</i>	Influx / efflux							
SLC7A7	yLAT1		<i>Transported*</i>	Influx / efflux							
SLC7A9	b ^{0,-} AT		<i>Transported*</i>	Influx / efflux							
SLC38A4	SNAT4		<i>Transported*</i>	Influx							
SLC38A9	SLC38A9		<i>Transported*</i>	Influx							

Solute carrier transporter (SLC)					Substrate	G protein-coupled receptor (GPCR)				
Gene	Protein	Affinity / activity	Comments	Mode of transport		Ref	Gene	Protein	Affinity / potency	Comments
SLC6A14	ATB ^{0,-}	14 μM	K _m / EC ₅₀ (EP)	Influx	87	GPCR6A	GPCR6	854 μM	EC ₅₀ (Ca ²⁺ assay)	85
SLC6A15	B ⁰ AT2	110 μM	K _{0.5} (EP)	Influx	88					
SLC6A19	B ⁰ AT1		Transported*	Influx	89					
SLC7A5	LAT1	20 μM	K _m ([1-14C]methionine uptake)	Influx / efflux	102					
SLC7A9	b ^{0,-} AT		Transported*	Influx / efflux	93					
SLC36A4	PAT4	440 μM	K _i ([3H]proline inhibition)	Influx	93					
SLC38A1	SNAT1		Transported*	Influx	94					
SLC38A2	SNAT2		Transported*	Influx	94					
SLC38A4	SNAT4		Transported*	Influx	94					
SLC43A1	LAT3		Transported*	Influx	108					
SLC43A2	LAT4		Transported*	Influx / efflux	109					
SLC7A1	CAT-1		Transported*	Influx	107					
SLC7A2	CAT-2		Transported*	Influx	107					
SLC7A3	CAT-3		Transported*	Influx	97					
SLC6A10	TAT1	910 μM	K _m ([1-14C]ornithine uptake)	Influx	82					
SLC6A14	ATB ^{0,-}	741 μM	K _m ([1-14C]phenylalanine uptake)	Influx	87	GPCR6A	GPCR6	112 μM	EC ₅₀ (Ca ²⁺ assay)	85
SLC6A19	B ⁰ AT1	17 μM	K _m / EC ₅₀ (EP)	Influx	87					
SLC7A5	LAT1		Transported*	Influx	89					
SLC7A8	LAT2		Transported*	Influx / efflux	102					
SLC7A9	b ^{0,-} AT		Transported*	Influx	90					
SLC43A1	LAT3	6.5–1,206 μM	K _m ([1-14C]phenylalanine uptake)	Influx / efflux	91					
SLC43A2	LAT4	178–3,733 μM	K _m ([3H]phenylalanine uptake)	Influx / efflux	108					
SLC6A10	TAT1	452 μM	K _m ([3H]phenylalanine uptake)	Influx / efflux	109					
SLC6A14	ATB ^{0,-}	26 μM	K _m ([1-14C]tryptophan uptake)	Influx	82					
SLC7A5	LAT1	21 μM	K _m / EC ₅₀ (EP)	Influx	87	GPR139	GPR139	49 μM	EC ₅₀ (Ca ²⁺ assay)	110
SLC7A8	LAT2		Transported*	Influx / efflux	102	CASR	CaR	30–100 μM	EC ₅₀ (allosteric modulation of Ca ²⁺)	53,54
SLC36A4	PAT4	1.7 μM	K _i ([3H]proline inhibition)	Influx	90					
SLC1A4	ASCT1	121 μM	K _m ([3H]serine uptake)	Influx	93					
SLC1A5	ASCT2	56–6,600 μM	K _m ([3H]serine uptake)	Influx	84	GPCR6A	GPCR6	623 μM	EC ₅₀ (Ca ²⁺ assay)	85
SLC6A14	ATB ^{0,-}	43 μM	K _m / EC ₅₀ (EP)	Influx / efflux	86	CASR	CaR	~1,000 μM	EC ₅₀ (allosteric modulation of Ca ²⁺)	53,54
SLC6A15	B ⁰ AT2		Transported*	Influx	87					
SLC6A19	B ⁰ AT1		Transported*	Influx	88					
SLC7A10	Asc-1		Transported*	Influx	89					
SLC38A1	SNAT1		Transported*	Influx	92					
SLC38A2	SNAT2		Transported*	Influx	94					
SLC38A4	SNAT4		Transported*	Influx	94					
SLC38A5	SNAT5		Transported*	Influx	94					
SLC38A7	SNAT7		Transported*	Influx	95					

Solute carrier transporter (SLC)					G protein-coupled receptor (GPCR)						
Gene	Protein	Affinity / activity	Comments	Mode of transport	Ref	Substrate	Gene	Protein	Affinity / potency	Comments	Ref
Prostaglandins											
SLC02A1	PGT	83 nM	K _{1/2} ([³ H]PGE ₂ inhibition)	Influx / efflux	111	PGD ₂	PTGDR	DP ₁	1.7 nM	K ([³ H]PGD ₂ binding)	112
							PTGER1	EP ₁	5,820 nM	K ([³ H]PGE ₂ binding)	112
							PTGER2	EP ₂	2,973 nM	K ([³ H]PGE ₂ binding)	112
							PTGER3	EP ₃	421 nM	K ([³ H]PGE ₂ binding)	112
							PTGER4	EP ₄	1,483 nM	K ([³ H]PGE ₂ binding)	112
							PTGFR	FP	6.7 nM	K ([³ H]PGF _{2α} binding)	112
							TBXA2R	TP	6,602 nM	K ([³ H]SQ-29548 binding)	112
SLC02A1	PGT	82 nM	K _{1/2} ([³ H]PGE ₂ inhibition)	Influx / efflux	111	PGE ₁	PTGDR	DP ₁	53 nM	K ([³ H]PGD ₂ binding)	113
SLC03A1	OATP3A1	49 nM	K _m ([³ H]PGE ₁ uptake)	Influx / efflux	114		PTGER1	EP ₁	165 nM	K ([³ H]PGE ₂ binding)	115
							PTGER2	EP ₂	1 nM	IC ₅₀ ([³ H]PGE ₂ binding)	116
							PTGER4	EP ₄	1.5 nM	K ([³ H]PGE ₂ binding)	117
							PTGIR	IP	318 nM	K ([³ H]iloprost binding)	118
SLC02A1	PGT	100–331 nM	K _{1/2} ([³ H]PGE ₂ inhibition)	Influx / efflux	111,119	PGE ₂	PTGDR	DP ₁	307 nM	K ([³ H]PGD ₂ binding)	112
SLC03A1	OATP3A1	56 nM	K _m ([³ H]PGE ₂ uptake)	Influx / efflux	114		PTGER1	EP ₁	9.1 nM	K ([³ H]PGE ₂ binding)	112
SLC22A1	OCT1	657 nM #	K _m ([³ H]PGE ₂ uptake)	Influx	120		PTGER2	EP ₂	4.9 nM	K ([³ H]PGE ₂ binding)	112
SLC22A1	OCT2	29 nM #	K _m ([³ H]PGE ₂ uptake)	Influx	120		PTGER3	EP ₃	0.3 nM	K ([³ H]PGE ₂ binding)	112
SLC22A6	OAT1	970 nM	K _m ([³ H]PGE ₂ uptake)	Influx	120		PTGER4	EP ₄	0.8 nM	K ([³ H]PGE ₂ binding)	112
SLC22A7	OAT2	713 nM	K _m ([³ H]PGE ₂ uptake)	Influx	120		PTGFR	FP	119 nM	K ([³ H]PGF _{2α} binding)	112
SLC22A8	OAT3	345 nM	K _m ([³ H]PGE ₂ uptake)	Influx	120	TBXA2R	TP	29,000 nM	K ([³ H]SQ-29548 binding)	112	
SLC22A11	OAT4	154 nM	K _m ([³ H]PGE ₂ uptake)	Influx	120						
SLC02A1	PGT	7,202 nM	K _{1/2} ([³ H]PGE ₂ inhibition)	Influx / efflux	119	PGE ₃	PTGER1	EP ₁	110 nM	IC ₅₀ ([³ H]PGE ₂ binding)	121
							PTGER2	EP ₂	20 nM	IC ₅₀ ([³ H]PGE ₂ binding)	121
							PTGER3	EP ₃	37 nM	IC ₅₀ ([³ H]PGE ₂ binding)	121
							PTGER4	EP ₄	17 nM	IC ₅₀ ([³ H]PGE ₂ binding)	121
SLC02A1	PGT	92 nM	K _{1/2} ([³ H]PGE ₂ inhibition)	Influx / efflux	111	PGF _{2α}	PTGDR	DP ₁	861 nM	K ([³ H]PGD ₂ binding)	112
SLC16A5	MCT6	477 nM #	K _m ([³ H]PGE ₂ uptake)	Influx	122		PTGER1	EP ₁	547 nM	K ([³ H]PGE ₂ binding)	112
SLC22A1	OCT1	334 nM #	K _m ([³ H]PGE ₂ uptake)	Influx	120		PTGER2	EP ₂	964 nM	K ([³ H]PGE ₂ binding)	112
SLC22A1	OCT2	334 nM #	K _m ([³ H]PGE ₂ uptake)	Influx	120		PTGER3	EP ₃	38 nM	K ([³ H]PGE ₂ binding)	112
SLC22A6	OAT1	575 nM	K _m ([³ H]PGE ₂ uptake)	Influx	120		PTGER4	EP ₄	288 nM	K ([³ H]PGE ₂ binding)	112
SLC22A8	OAT3	1,092 nM	K _m ([³ H]PGE ₂ uptake)	Influx	120		PTGFR	FP	3.2 nM	K ([³ H]PGF _{2α} binding)	112
SLC22A11	OAT4	692 nM	K _m ([³ H]PGE ₂ uptake)	Influx	120		TBXA2R	TP	8,700 nM	K ([³ H]SQ-29548 binding)	112

Solute carrier transporter (SLC)					Substrate	G protein-coupled receptor (GPCR)					
Gene	Protein	Affinity / activity	Comments	Mode of transport		Ref	Gene	Protein	Affinity / potency	Comments	Ref
Monocarboxylates & short-chain fatty acids											
SLC5A8	SMCT1	159–252 μM	K _m (l ¹⁴ C)lactate uptake, (EP)	Influx	123	Lactate	HCAR1	HCA ₁	1,500–7,000 μM	EC ₅₀ (l ³⁵ S)GTPγS, Ca ²⁺ - assay)	124
SLC5A12	SMCT2	16,900 μM	IC ₅₀ (l ¹⁴ C)nicotinate inhibition)	Influx	126						
SLC16A1	MCT1	4,500–6,000 μM	K _m (l ¹⁴ C)lactate uptake)	Influx / efflux	126						
SLC16A3	MCT4	700–37,600 μM	K _m (pH sensor)	Influx / efflux	126						
SLC16A7	MCT2	6,500 μM	K _m (l ¹⁴ C)lactate uptake)	Influx	126						
SLC16A8	MCT3		Transported *	Influx / efflux	126						
SLC5A8	SMCT1	230 μM	K _{0.5} (EP)	Influx	127	Nicotinate	HCAR2	HCA ₂	0.1–0.25 μM	EC ₅₀ (l ³⁵ S)GTPγS)	128, 129
SLC5A12	SMCT2	3,700 μM	IC ₅₀ (l ¹⁴ C)nicotinate inhibition)	Influx	126		HCAR3	HCA ₃	~ 1,000 μM	EC ₅₀ (l ³⁵ S)GTPγS)	128, 129
SLC22A7	OAT2	17 μM	K _m (l ³ H)nicotinate uptake)	Influx	130						
SLC22A9	OAT7		Transported *	Influx / efflux	131						
SLC22A13	OAT10	22–48 μM	K _m (l ³ H)nicotinate uptake)	Influx	132						
SLC5A8	SMCT1	72 μM	K _m (EP)	Influx	123	Butyrate	FFAR3	FFA3	158 μM	EC ₅₀ (l ³⁵ S)GTPγS)	133
SLC5A12	SMCT2	2,600 μM	IC ₅₀ (l ¹⁴ C)nicotinate inhibition)	Influx	126		FFAR2	FFA2	371 μM	EC ₅₀ (l ³⁵ S)GTPγS)	133
SLC16A1	MCT1	9,000–10,000 μM	K _m (l ¹⁴ C)butyrate uptake)	Influx	126		HCAR2	HCA ₂	1,590 μM	EC ₅₀ (l ³⁵ S)GTPγS)	129
SLC22A9	OAT7	36 μM	K _m (l ¹⁴ C)butyrate uptake)	Influx / efflux	131						
SLC5A8	SMCT1	2,460 μM	K _{0.5} (EP)	Influx	134	FFAR3	FFA3	1,020 μM	EC ₅₀ (l ³⁵ S)GTPγS)	133	
						FFAR2	FFA2	431 μM	EC ₅₀ (l ³⁵ S)GTPγS)	133	
SLC5A8	SMCT1	128 μM	K _m (EP)	Influx	123	Propionate	FFAR3	FFA3	127 μM	EC ₅₀ (l ³⁵ S)GTPγS)	133
							FFAR2	FFA2	290 μM	EC ₅₀ (l ³⁵ S)GTPγS)	133
SLC5A8	SMCT1	1,442 μM	K _m (EP)	Influx	136	β-D-hydroxy-butyrate	HCAR2	HCA ₂	767 μM	EC ₅₀ (l ³⁵ S)GTPγS)	129
SLC16A1	MCT1	10,000 μM	K _m (pH sensor)	Influx	126		HCAR3	HCA ₃	> 25,000 μM	EC ₅₀ (l ³⁵ S)GTPγS)	129
SLC16A3	MCT4	130,000 μM	K _m (pH sensor)	Influx	126						
SLC16A7	MCT2		Transported *	Influx	126						

Solute carrier transporter (SLC)					G protein-coupled receptor (GPCR)							
Gene	Protein	Affinity / activity	Comments	Mode of transport	Ref	Substrate	Gene	Protein	Affinity / potency	Comments	Ref	
Other carboxylic acids & signaling lipids												
SLC13A2	NaDC1	590–800 μM	K _m ([¹⁴ C]succinate uptake)	Influx	136	Succinate	SUCNR1	SUCNR1	28–56 μM	EC ₅₀ (Ca ²⁺ assay)	137	
SLC13A3	NaDC3	2–25 μM	K _m ([³ H]succinate uptake, EP)	Influx	136							
SLC13A5	NaDC2	1,920 μM	IC ₅₀ ([¹⁴ C]citrate inhibition)	Influx	136							
SLC16A1	MCT1		Transported *	Efflux	138–140							
SLC22A6	OAT1	4,825 μM	IC ₅₀ ([³ H]PAH inhibition)	Influx	141							
SLC22A8	OAT3	55,700 μM	IC ₅₀ ([³ H]estron sulfate inhibition)	Influx	141							
SLC59A1	MFSD2A		Transported (SPNS2 complex)	Influx / efflux	142	Sphingosine-1-phosphate	S1PR1	S1P ₁	0.9–1.2 nM	EC ₅₀ ([³⁵ S]GTPγS)	143,144	
SLC59A2	MFSD2B		Transported *	Efflux	145		S1PR2	S1P ₂	2.9–8.9 nM	EC ₅₀ ([³⁵ S]GTPγS)	143,144	
SLC63A2	SPNS2		Transported *	Efflux	146		S1PR3	S1P ₃	0.2–1.1 nM	EC ₅₀ ([³⁵ S]GTPγS)	144	
							S1PR4	S1P ₄	8.6 nM	EC ₅₀ ([³⁵ S]GTPγS)	144	
							S1PR5	S1P ₅	11–44 nM	EC ₅₀ ([³⁵ S]GTPγS)	143,144	
						GPR3	GPR3	50 nM #	EC ₅₀ (Ca ²⁺ assay)	147		
						GPR6	GPR6	56 nM #	EC ₅₀ (Ca ²⁺ assay)	147		
						GPR12	GPR12	106 nM #	EC ₅₀ (Ca ²⁺ assay)	147		
						GPR63	GPR63	800 nM #	EC ₅₀ (Ca ²⁺ assay)	148		
						P2RY10	P2Y ₁₀	53 nM	EC ₅₀ (Ca ²⁺ assay)	149		
SLC10A1	NTCP	6.3 μM	K _m ([³ H]taurocholate uptake)	Influx	150	Bile acids	GPBAR1	GPBAR	0.3–7.7 μM	EC ₅₀ (cAMP assay)	151	
SLC10A2	ASBT	4.1–33 μM	K _m ([³ H]bile acid uptake)	Influx	152		S1PR2	S1P ₂		Activation *	153	
SLC22A24	SLC22A24		Transported *	Influx / efflux	154							
SLC51A/B	OSTα/β	13–1,000 μM	K _m (LC-MS/MS)	Influx / efflux	155							
SLC01A2	OATP1A2	19–60 μM	K _m ([³ H]bile acid uptake)	Influx	156							
SLC01B1	OATP1B1	0.7–47 μM	K _m (LC-MS/MS)	Influx	157							
SLC01B3	OATP1B3	0.5–42 μM	K _m (LC-MS/MS)	Influx	157							
SLC03A1	OATP3A1		Transported *	Influx / efflux	158							
SLC27A1	FA1P1		K _m ([¹⁴ C]oleic acid uptake)	Influx / efflux	159,160	(Very) long-chain fatty acids	FFAR1	FFA1	1–43 μM	EC ₅₀ (Ca ²⁺ assay)	161,162	
SLC27A2	FA1P2		Transported *	Influx / efflux	163		FFAR2	FFA4	12–63 μM	EC ₅₀ (Ca ²⁺ , DMR, β-arrestin)	164	
SLC27A4	FA1P4		Transported *	Influx / efflux	159,165							
SLC27A6	FA1P6		Transported *	Influx / efflux	159							

* no affinity or potency values reported for human orthologues, but evidence for binding or transport
disputed results

Yellow fill indicates SLC-GPCR pair that has been subject to in-house TRACT assay attempts
Blue fill indicates SLC-GPCR pair for which TRACT assays are published or reported in this thesis

Table A.2 – List of Na⁺-coupled transporters that are expressed at the plasma membrane. Transport stoichiometries were derived from the IUPHAR Guide to Pharmacology¹⁶⁶. Only transporters for which stoichiometries were described are mentioned in this table; putative and orphan transporters are not included here.

Gene	Protein	Stoichiometry
Na ⁺ -coupled transporters at the plasma membrane		
SLC1A1/2/3/6/7	EAAT3/2/1/4/5	3 Na ⁺ / 1 glu ⁻ / 1 H ⁺ in : 1 K ⁺ out (Cl ⁻ conductivity)
SLC1A4/5	ASCT1/2	1 Na ⁺ / 1 amino acid in : 1 Na ⁺ / 1 amino acid out
SLC4A4/5	NBCe1/2	1 Na ⁺ / 2–3 HCO ₃ ⁻ or 1 CO ₃ ²⁻ in/out
SLC4A7/10	NBCn1/2	1 Na ⁺ / 1 HCO ₃ ⁻ or 1 CO ₃ ²⁻ in/out
SLC4A8	NDCBE	1 Na ⁺ / 2 HCO ₃ ⁻ / 1 Cl ⁻ in/out
SLC5A1/2	SGLT1/2	1–2 Na ⁺ / 1 glucose in
SLC5A3/11	SMIT1/2	2 Na ⁺ / 1 myo-inositol in
SLC5A5	NIS	2 Na ⁺ / 1 I ⁻ in
SLC5A6	SMVT	2 Na ⁺ / 1 biotin in
SLC5A7	CHT	1 Na ⁺ / 1 choline in
SLC5A8/12	SMCT1/2	2 Na ⁺ / 1 monocarboxylate ⁻ in
SLC6A1/11/13/12	GAT1/2/3/BGT1	2–3 Na ⁺ / 1–2 Cl ⁻ / 1 GABA in
SLC6A2	NET	1 Na ⁺ / 1 Cl ⁻ / 1 NE in
SLC6A3	DAT	1–2 Na ⁺ / 1 Cl ⁻ / 1 DA in
SLC6A4	SERT	1 Na ⁺ / 1 Cl ⁻ / 1 5-HT in : 1 K ⁺ out
SLC6A5/9	GlyT1/2	2–3 Na ⁺ / 1 Cl ⁻ / 1 glycine in
SLC6A6	TauT	2 Na ⁺ / 1 Cl ⁻ / 1 taurine in
SLC6A7	PROT	2 Na ⁺ / 1 Cl ⁻ / 1 L-proline in
SLC6A8	CT1	2 Na ⁺ / 1 Cl ⁻ / 1 creatine in
SLC6A14/20	ATB ^{0,+} /SIT1	2–3 Na ⁺ / 1 Cl ⁻ / 1 amino acid in
SLC6A19/15	B ⁰ AT1/2	1 Na ⁺ / 1 amino acid in
SLC8A1	NCX1	3–4 Na ⁺ in : 1 Ca ²⁺ out (or 1 Ca ²⁺ in : 1 Na ⁺ out)
SLC9 family	NHE	1 Na ⁺ in : 1 H ⁺ out
SLC10A1/2	NTCP/ASBT	1–2 Na ⁺ / 1 bile acid in
SLC12A2/1	NKCC1/2	1 Na ⁺ / 1 K ⁺ / 2 Cl ⁻ in
SLC12A3	NCC	1 Na ⁺ / 1 Cl ⁻ in
SLC13A1/4	NaS1/2	3 Na ⁺ / SO ₄ ²⁻ in
SLC13A2	NaDC1	3 Na ⁺ / 1 dicarboxylate ²⁻ in
SLC20A1/2	Pi1T1/2	1 Na ⁺ / 1 HPO ₄ ²⁻ in
SLC23A1/2	SVCT1/2	2 Na ⁺ / 1 ascorbic acid in
SLC24A1–5	NKX1–5	4 Na ⁺ in : 1 Ca ²⁺ / 1 K ⁺ out
SLC28A1–3	CNT1–3	1 Na ⁺ / 1 nucleoside
SLC34A1/2/3	NaPi-2a/b/c	3 Na ⁺ / 1 HPO ₄ ²⁻ in
SLC38A1/2/4	SNAT1/2/4	1 Na ⁺ / 1 amino acid in
SLC38A3/5	SNAT3/5	1 Na ⁺ / 1 amino acid in : 1 H ⁺ out

Abbreviations

5-CT	5-carboxamidotryptamine	L-DOPA	L-3,4-dihydroxyphenylalanine (levodopa)
5-HT	5-hydroxytryptamine (serotonin)	LSD	lysergic acid diethylamide
5-HT _x	serotonin receptor	M _x	muscarinic acetylcholine receptor
α_x / β_x	alpha / beta adrenergic receptor	MCT	monocarboxylate transporter
A _x	adenosine receptor	mGlu _x	metabotropic glutamate receptor
ACh	acetylcholine	mito	mitochondria
ADE	adenosine	MPP+	1-methyl-4-phenylpyridinium
ADP	adenosine diphosphate	MT _x	melatonin receptor
AGT	aspartate/glutamate transporter	NaDC	Na ⁺ /dicarboxylate cotransporter
ASBT	apical Na ⁺ /bile acid transporter	NaPi-2	Na ⁺ /phosphate cotransporter
ASCT	alanine/serine/cysteine transporter	NaS	Na ⁺ /sulfate cotransporter
Asc	Asc-type amino acid transporter	N(K)CC	Na ⁺ (/K ⁺)/Cl ⁻ cotransporter
ATB ⁰⁺	B ⁰⁺ -type amino acid transporter	N(K)CX	Na ⁺ (/K ⁺)/Cl ⁻ exchanger
ATP	adenosine triphosphate	NBCe	electrogenic Na ⁺ /bicarbonate transporter
b ⁰⁺ AT	b ⁰⁺ -type amino acid transporter	NBCn	neutral Na ⁺ /bicarbonate transporter
B ⁰ AT	B ⁰ -type amino acid transporter	NDCBE	neutral Na ⁺ /bicarbonate/Cl ⁻ transporter
BGT	betaine/GABA transporter	NE	norepinephrine
cAMP	cyclic adenosine monophosphate	NET	norepinephrine transporter
CaR	calcium-sensing receptor	NHE	Na ⁺ /proton exchanger
CAT	cationic amino acid transporter	NIS	Na ⁺ /iodide cotransporter
CHT	choline transporter	NMS	N-methylscopolamine
CNT	concentrative nucleoside transporter	NTCP	Na ⁺ /bile acid cotransporter
CT1	creatine transporter 1	OAT	organic anion transporter
CYP	cyanopindolol	OATP	organic anion-transporting polypeptides
D _x	dopamine receptor	OCT	organic cation transporter
DA	dopamine	OCTN1	ergothioneine transporter
DAT	dopamine transporter	OST α/β	organic solute transporter α/β
DMR	dynamic mass redistribution	P2Y	purinergic P2Y receptor
DP ₁	prostaglandin D ₂ receptor	PAT	proton-coupled amino acid transporter
EAAT	excitatory amino acid transporter	PAH	para-aminohippurate
EC ₅₀	half maximal effective concentration	PEPT	peptide transporter
EP	electrophysiology	PGD ₂	prostaglandin D ₂
EP _x	prostaglandin E ₁₋₄ receptor	PGE _x	prostaglandin E ₁₋₃
EPI	epinephrine	PGF _{2α}	prostaglandin F _{2α}
ENT	equilibrative nucleoside transporter	PGT	prostaglandin transporter
FATP	fatty acid transport protein	PiT	Na ⁺ -dependent phosphate transporter
FFAR	free fatty acid receptor	PMAT	plasma membrane monoamine transporter
FP	prostaglandin F _{2α} receptor	PROT	proline transporter
GABA	gamma-aminobutyric acid	S1P _x	sphingosine-1-phosphate receptor
GABA _B	metabotropic GABA receptor	SERT	serotonin transporter
GAT	GABA transporter	SGLT	Na ⁺ /glucose cotransporter
Glu	glutamate	SIT	Na ⁺ /imino acid transporter
GLUT	glucose transporter	SLC	solute carrier transporter
GlyT	glycine transporter	SMCT	Na ⁺ -coupled monocarboxylate transporter
GPBAR	G protein-coupled bile acid receptor	SMIT	Na ⁺ /myo-inositol cotransporter
GPR	orphan G protein-coupled receptor	SMVT	Na ⁺ /multivitamin transporter
GPCR	G protein-coupled receptor	SNAT	Na ⁺ -coupled neutral amino acid transporter
GTP	guanosine triphosphate	SPNS	Spinster homolog/sphingolipid transporter
H _x	histamine receptor	SUCNR	succinate receptor
HCA _x	hydroxycarboxylic acid receptor	SVCT	Na ⁺ /vitamin C transporter
HIS	histamine	TA ₁	trace amine-associated receptor 1
IC ₅₀	half maximal inhibitory concentration	TAT	T-type amino acid transporter
IP	prostaglandin I ₂ receptor	TauT	taurine transporter
IP ₃	inositol triphosphate	TEA	tetraethylammonium
K _{0.5} / K _{1/2}	apparent affinity constant	TP	thromboxane receptor
K _d	dissociation constant	VACHT	vesicular acetylcholine transporter
K _i	inhibition constant	VGAT	vesicular GABA transporter
K _m	Michaelis-Menten constant	VGLUT	vesicular glutamate transporter
LAT	L-type amino acid transporter	VMAT	vesicular monoamine transporter
LC-MS	liquid chromatography-mass spectrometry	VNUT	vesicular nucleoside transporter
		y ⁺ LAT	y ⁺ L-type amino acid transporter
		xCT	cystine/glutamate transporter

References

1. Pastor-Anglada, M. & Pérez-Torras, S. (2018) Who is who in Adenosine transport. *Front. Pharmacol.* **9**, 627.
2. Yan, L., Burbiel, J. C., Maaß, A. & Müller, C. E. (2003) Adenosine receptor agonists: From basic medicinal chemistry to clinical development. *Expert Opin. Emerg. Drugs* **8**, 537–576.
3. Sawada, K. *et al.* (2008) Identification of a vesicular nucleotide transporter. *Proc. Natl. Acad. Sci. U. S. A.* **105**, 5683–5686.
4. Waldo, G. L. & Harden, T. K. (2004) Agonist binding and Gq-stimulating activities of the purified human P2Y₁ receptor. *Mol. Pharmacol.* **65**, 426–436.
5. Lazarowski, E. R., Watt, W. C., Stutts, M. J., Boucher, R. C. & Harden, T. K. (1995) Pharmacological selectivity of the cloned human P2U-purinoreceptor: potent activation by diadenosine tetraphosphate. *Br. J. Pharmacol.* **116**, 1619–1627.
6. Communi, D., Govaerts, C., Parmentier, M. & Boeynaems, J. M. (1997) Cloning of a human purinergic P2Y receptor coupled to phospholipase C and adenyl cyclase. *J. Biol. Chem.* **272**, 31969–31973.
7. Takasaki, J. *et al.* (2001) Molecular cloning of the platelet P2TAC ADP receptor: Pharmacological comparison with another ADP receptor, the P2Y₁ receptor. *Mol. Pharmacol.* **60**, 432–439.
8. Marteau, F. *et al.* (2003) Pharmacological characterization of the human P2Y₁₃ receptor. *Mol. Pharmacol.* **64**, 104–112.
9. Buccioni, M. *et al.* (2011) Innovative functional cAMP assay for studying G protein-coupled receptors: Application to the pharmacological characterization of GPR17. *Purinergic Signal.* **7**, 463–468.
10. Kennedy, C., Qi, A. D., Herold, C. L., Harden, T. K. & Nicholas, R. A. (2000) ATP, an agonist at the rat P2Y₄ receptor, is an antagonist at the human P2Y₄. *Mol. Pharmacol.* **57**, 926–931.
11. Varoqui, H. & Erickson, J. D. (1996) Active transport of acetylcholine by the human vesicular acetylcholine transporter. *J. Biol. Chem.* **271**, 27229–27232.
12. Jakubík, J., Bačáková, L., El-Fakahany, E. E. & Tuček, S. (1997) Positive cooperativity of acetylcholine and other agonists with allosteric ligands on muscarinic acetylcholine receptors. *Mol. Pharmacol.* **52**, 172–179.
13. Koepsell, H. (2020) Organic cation transporters in health and disease. *Pharmacol. Rev.* **72**, 253–319.
14. Cheng, K. *et al.* (2002) Lithocholylcholine, a bile acid/acetylcholine hybrid, is a muscarinic receptor antagonist. *J. Pharmacol. Exp. Ther.* **303**, 29–35.
15. Apparsundaram, S., Moore, K. R., Malone, M. D., Hartzell, H. C. & Blakely, R. D. (1997) Molecular cloning and characterization of an l-pinephrine transporter from sympathetic ganglia of the bullfrog, *Rana catesbeiana*. *J. Neurosci.* **17**, 2691–2702.
16. Giros, B. *et al.* (1994) Delineation of discrete domains for substrate, cocaine, and tricyclic antidepressant interactions using chimeric dopamine-norepinephrine transporters. *J. Biol. Chem.* **269**, 15985–15988.
17. Raffel, D. M. *et al.* (2013) Radiotracers for cardiac sympathetic innervation: transport kinetics and binding affinities for the human norepinephrine transporter. *Nucl. Med. Biol.* **40**, 331–337.
18. Alachkar, A., Brotchie, J. M. & Jones, O. T. (2010) Binding of dopamine and 3-methoxytyramine as l-DOPA metabolites to human α 2-adrenergic and dopaminergic receptors. *Neurosci. Res.* **67**, 245–249.
19. Giros, B. *et al.* (1992) Cloning, pharmacological characterization, and chromosome assignment of the human dopamine transporter. *Mol. Pharmacol.* **42**, 383–390.
20. Erickson, J. D., Schäfer, M. K. H., Bonner, T. I., Eiden, L. E. & Weihe, E. (1996) Distinct pharmacological properties and distribution in neurons and endocrine cells of two isoforms of the human vesicular monoamine transporter. *Proc. Natl. Acad. Sci. U. S. A.* **93**, 5166–5171.
21. Sunahara, R. K. *et al.* (1991) Cloning of the gene for a human dopamine D5 receptor with higher affinity for dopamine than D1. *Nature* **350**, 614–619.
22. Freedman, S. B. *et al.* (1994) Expression and pharmacological characterization of the human D3 dopamine receptor. *J. Pharmacol. Exp. Ther.* **268**, 417–426.
23. Van Tol, H. H. M. *et al.* (1991) Cloning of the gene for a human dopamine D4 receptor with high affinity for the antipsychotic clozapine. *Nature* **350**, 610–614.
24. Lanau, F., Zenner, M. T., Civelli, O. & Hartman, D. S. (1997) Epinephrine and norepinephrine act as potent agonists at the recombinant human dopamine D4 receptor. *J. Neurochem.* **68**, 804–812.
25. Duan, H. & Wang, J. (2010) Selective transport of monoamine neurotransmitters by human plasma membrane monoamine transporter and organic cation transporter 3. *J. Pharmacol. Exp. Ther.* **335**, 743–753.
26. Engel, K. & Wang, J. (2005) Interaction of organic cations with a newly identified plasma membrane monoamine transporter. *Mol. Pharmacol.* **68**, 1397–1407.
27. Borowsky, B. *et al.* (2001) Trace amines: Identification of a family of mammalian G protein-coupled receptors. *Proc. Natl. Acad. Sci.* **98**, 8966–8971.

28. Horie, K., Obika, K., Foglar, R. & Tsujimoto, G. (1995) Selectivity of the imidazoline α -adrenoceptor agonists (oxymetazoline and cirazoline) for human cloned α_1 -adrenoceptor subtypes. *Br. J. Pharmacol.* **116**, 1611–1618.
29. Jasper, J. R. *et al.* (1998) Ligand efficacy and potency at recombinant α_2 adrenergic receptors. *Biochem. Pharmacol.* **55**, 1035–1043.
30. Hoffmann, C., Leitz, M. R., Oberdorf-Maass, S., Lohse, M. J. & Klotz, K.-N. (2004) Comparative pharmacology of human β -adrenergic receptor subtypes - characterization of stably transfected receptors in CHO cells. *Naunyn. Schmiedeberg's. Arch. Pharmacol.* **369**, 151–159.
31. Pacholczyk, T., Blakely, R. D. & Amara, S. G. (1991) Expression cloning of a cocaine- and antidepressant-sensitive human noradrenaline transporter. *Nature* **350**, 350–354.
32. Ramamoorthy, S. *et al.* (1993) Antidepressant- and cocaine-sensitive human serotonin transporter: molecular cloning, expression, and chromosomal localization. *Proc. Natl. Acad. Sci.* **90**, 2542–2546.
33. Kalipatnapu, S., Pucadyil, T. J., Harikumar, K. G. & Chattopadhyay, A. (2004) Ligand binding characteristics of the human serotonin 1A receptor heterologously expressed in CHO cells. *Biosci. Rep.* **24**, 101–115.
34. Weinshank, R. L., Zgombick, J. M., Macchi, M. J., Branchek, T. A. & Hartig, P. R. (1992) Human serotonin 1D receptor is encoded by a subfamily of two distinct genes: 5-HT(1D α) and 5-HT(1D β). *Proc. Natl. Acad. Sci. U. S. A.* **89**, 3630–3634.
35. McAllister, G. *et al.* (1992) Molecular cloning of a serotonin receptor from human brain (5HT1E): A fifth 5HT1-like subtype. *Proc. Natl. Acad. Sci. U. S. A.* **89**, 5517–5521.
36. Adham, N. *et al.* (1993) Cloning of another human serotonin receptor (5-HT(1F)): A fifth 5-HT1 receptor subtype coupled to the inhibition of adenylate cyclase. *Proc. Natl. Acad. Sci. U. S. A.* **90**, 408–412.
37. Knight, A. R. *et al.* (2004) Pharmacological characterisation of the agonist radioligand binding site of 5-HT2A, 5-HT2B and 5-HT2C receptors. *Naunyn. Schmiedeberg's. Arch. Pharmacol.* **370**, 114–123.
38. Blondel, O., Gastineau, M., Dahmoune, Y., Langlois, M. & Fischmeister, R. (1998) Cloning, expression, and pharmacology of four human 5-hydroxytryptamine₄ receptor isoforms produced by alternative splicing in the carboxyl terminus. *J. Neurochem.* **70**, 2252–2261.
39. Rees, S. *et al.* (1994) Cloning and characterisation of the human 5-HT5A serotonin receptor. *FEBS Lett.* **355**, 242–246.
40. Kohen, R. *et al.* (1996) Cloning, characterization, and chromosomal localization of a human 5-HT₆ serotonin receptor. *J. Neurochem.* **66**, 47–56.
41. Bard, J. A. *et al.* (1993) Cloning of a novel human serotonin receptor (5-HT₇) positively linked to adenylate cyclase. *J. Biol. Chem.* **268**, 23422–23426.
42. Moguilevsky, N. *et al.* (1994) Stable expression of human H1-histamine-receptor cDNA in Chinese hamster ovary cells: Pharmacological characterisation of the protein, tissue distribution of messenger RNA and chromosomal localisation of the gene. *Eur. J. Biochem.* **224**, 489–496.
43. Tahara, A. *et al.* (1998) Pharmacological characterization of the human vasopressin receptor subtypes stably expressed in Chinese hamster ovary cells. *Br. J. Pharmacol.* **125**, 1463–1470.
44. Lovenberg, T. W., Pyati, J., Chang, H., Wilson, S. J. & Erlander, M. G. (2000) Cloning of rat histamine H3 receptor reveals distinct species pharmacological profiles. *J. Pharmacol. Exp. Ther.* **293**, 771–778.
45. Liu, C. *et al.* (2001) Cloning and pharmacological characterization of a fourth histamine receptor (H4) expressed in bone marrow. *Mol. Pharmacol.* **59**, 420–426.
46. Hevia, D. *et al.* (2015) Melatonin uptake through glucose transporters: A new target for melatonin inhibition of cancer. *J. Pineal Res.* **58**, 234–250.
47. Audinot, V. *et al.* (2003) New selective ligands of human cloned melatonin MT1 and MT2 receptors. *Naunyn. Schmiedeberg's. Arch. Pharmacol.* **367**, 553–561.
48. Huo, X. *et al.* (2017) Human transporters, PEPT1/2, facilitate melatonin transportation into mitochondria of cancer cells: An implication of the therapeutic potential. *J. Pineal Res.* **62**, 1–18.
49. Sitte, H. H. *et al.* (1998) Carrier-mediated release, transport rates, and charge transfer induced by amphetamine, tyramine, and dopamine in mammalian cells transfected with the human dopamine transporter. *J. Neurochem.* **71**, 1289–1297.
50. Hilber, B. *et al.* (2005) Serotonin-transporter mediated efflux: A pharmacological analysis of amphetamines and non-amphetamines. *Neuropharmacology* **49**, 811–819.
51. Sarkar, S. & Berry, M. D. (2020) Involvement of organic cation transporter 2 and a Na⁺-dependent active transporter in p-tyramine transport across Caco-2 intestinal cells. *Life Sci.* **253**, 117696.
52. Arriza, J. *et al.* (1994) Functional comparisons of three glutamate transporter subtypes cloned from human motor cortex. *J. Neurosci.* **14**, 5559–5569.
53. Conigrave, A. D., Quinn, S. J. & Brown, E. M. (2000) L-Amino acid sensing by the extracellular Ca²⁺-sensing receptor. *Proc. Natl. Acad. Sci.* **97**, 4814–4819.
54. Liu, H. *et al.* (2020) Illuminating the allosteric modulation of the calcium-sensing receptor. *Proc. Natl. Acad. Sci. U. S. A.* **117**, 21711–21722.

55. Desai, M. A., Burnett, J. P., Mayne, N. G. & Schoepp, D. D. (1995) Cloning and expression of a human metabotropic glutamate receptor 1 α : Enhanced coupling on co-transfection with a glutamate transporter. *Mol. Pharmacol.* **48**, 648–657.
56. Lin, F. F. *et al.* (1997) Cloning and stable expression of the mGluR1b subtype of human metabotropic receptors and pharmacological comparison with the mGluR5a subtype. *Neuropharmacology* **36**, 917–931.
57. Monn, J. A. *et al.* (2015) Synthesis and pharmacological characterization of C4-(thiotriazolyl)-substituted-2-aminobicyclo[3.1.0]hexane-2,6-dicarboxylates. Identification of (1R,2S,4R,5R,6R)-2-amino-4-(1H-1,2,4-triazol-3-ylsulfanyl)bicyclo[3.1.0]hexane-2,6-dicarboxylic acid (LY2812). *J. Med. Chem.* **58**, 7526–7548.
58. Filosa, R. *et al.* (2006) Synthesis and biological evaluation of (2S)- and (2R)-2-(3'-phosphonobicyclo[1.1.1]pentyl)glycines as novel group III selective metabotropic glutamate receptor ligands. *Bioorganic Med. Chem.* **14**, 3811–3817.
59. Scalise, M. *et al.* (2020) The human SLC1A5 neutral amino acid transporter catalyzes a pH-dependent glutamate/glutamine antiport, as well. *Front. Cell Dev. Biol.* **8**, 1–16.
60. Fairman, W. A., Vandenberg, R. J., Arriza, J. L., Kavanaugh, M. P. & Amara, S. G. (1995) An excitatory amino-acid transporter with properties of a ligand-gated chloride channel. *Nature* **375**, 599–603.
61. Wu, S. *et al.* (1998) Group III human metabotropic glutamate receptors 4, 7 and 8: Molecular cloning, functional expression, and comparison of pharmacological properties in RGT cells. *Mol. Brain Res.* **53**, 88–97.
62. Flor, P. J. *et al.* (1995) Molecular cloning, functional expression and pharmacological characterization of the human metabotropic glutamate receptor type 4. *Neuropharmacology* **34**, 149–155.
63. Arriza, J. L., Eliasof, S., Kavanaugh, M. P. & Amara, S. G. (1997) Excitatory amino acid transporter 5, a retinal glutamate transporter coupled to a chloride conductance. *Proc. Natl. Acad. Sci.* **94**, 4155–4160.
64. Daggett, L. P. *et al.* (1995) Molecular and functional characterization of recombinant human metabotropic glutamate receptor subtype 5. *Neuropharmacology* **34**, 871–886.
65. Bassi, M. T. *et al.* (2001) Identification and characterisation of human xCT that co-expresses, with 4F2 heavy chain, the amino acid transport activity system xc-. *Pflugers Arch. Eur. J. Physiol.* **442**, 286–296.
66. Laurie, D. J., Schoeffer, P., Wiederhold, K. H. & Sommer, B. (1997) Cloning, distribution and functional expression of the human mGlu6 metabotropic glutamate receptor. *Neuropharmacology* **36**, 145–152.
67. Miyaji, T., Omote, H. & Moriyama, Y. (2011) Functional characterization of vesicular excitatory amino acid transport by human sialin. *J. Neurochem.* **119**, 1–5.
68. Shigeri, Y., Seal, R. P. & Shimamoto, K. (2004) Molecular pharmacology of glutamate transporters, EAATs and VGLUTs. *Brain Res. Rev.* **45**, 250–265.
69. Fork, C. *et al.* (2011) OAT2 catalyses efflux of glutamate and uptake of orotic acid. *Biochem. J.* **436**, 305–312.
70. Skwara, P., Schömig, E. & Gründemann, D. (2017) A novel mode of operation of SLC22A11: Membrane insertion of estrone sulfate versus translocation of uric acid and glutamate. *Biochem. Pharmacol.* **128**, 74–82.
71. Lofthouse, E. M. *et al.* (2015) Glutamate cycling may drive organic anion transport on the basal membrane of human placental syncytiotrophoblast. *J. Physiol.* **593**, 4549–4559.
72. Schulz, C. *et al.* (2014) SLC22A13 catalyses unidirectional efflux of aspartate and glutamate at the basolateral membrane of type A intercalated cells in the renal collecting duct. *Biochem. J.* **457**, 243–251.
73. Loo, D. D. F., Eskandari, S., Boorer, K. J., Sarkar, H. K. & Wright, E. M. (2000) Role of Cl⁻ in electrogenic Na⁺-coupled cotransporters GAT1 and SGLT1. *J. Biol. Chem.* **275**, 37414–37422.
74. Kvist, T., Christiansen, B., Jensen, A. & Bräuner-Osborne, H. (2009) The four human γ -aminobutyric acid (GABA) transporters: pharmacological characterization and validation of a highly efficient screening assay. *Comb. Chem. High Throughput Screen.* **12**, 241–249.
75. Wood, M. D. *et al.* (2000) The human GABAB1b and GABAB2 heterodimeric recombinant receptor shows low sensitivity to phaclofen and saclofen. *Br. J. Pharmacol.* **131**, 1050–1054.
76. Richter, M., Moroniak, S. J. & Michel, H. (2019) Identification of competitive inhibitors of the human taurine transporter TauT in a human kidney cell line. *Pharmacol. Reports* **71**, 121–129.
77. Damgaard, M. *et al.* (2015) Identification of the first highly subtype-selective inhibitor of human GABA transporter GAT3. *ACS Chem. Neurosci.* **6**, 1591–1599.
78. Rasola, A., Galletta, L. J. V., Barone, V., Romeo, G. & Bagnasco, S. (1995) Molecular cloning and functional characterization of a GABA/betaine transporter from human kidney. *FEBS Lett.* **373**, 229–233.
79. Christiansen, B., Meinild, A. K., Jensen, A. A. & Bräuner-Osborne, H. (2007) Cloning and characterization of a functional human γ -aminobutyric acid (GABA) transporter, human GAT-2. *J. Biol. Chem.* **282**, 19331–19341.

80. Gasnier, B. (2004) The SLC32 transporter, a key protein for the synaptic release of inhibitory amino acids. *Pflügers Arch. Eur. J. Physiol.* **447**, 756–759.
81. Larsen, M., Larsen, B. B., Frølund, B. & Nielsen, C. U. (2008) Transport of amino acids and GABA analogues via the human proton-coupled amino acid transporter, hPAT1: Characterization of conditions for affinity and transport experiments in Caco-2 cells. *Eur. J. Pharm. Sci.* **35**, 86–95.
82. Kim, D. K. *et al.* (2002) The human T-type amino acid transporter-1: Characterization, gene organization, and chromosomal location. *Genomics* **79**, 95–103.
83. Lopez, V. M., Decatur, C. L., Stamer, W. D., Lynch, R. M. & McKay, B. S. (2008) L-DOPA is an endogenous ligand for OA1. *PLoS Biol.* **6**, e236.
84. Damseh, N. *et al.* (2015) Mutations in SLC1A4, encoding the brain serine transporter, are associated with developmental delay, microcephaly and hypomyelination. *J. Med. Genet.* **52**, 541–547.
85. Wellendorph, P. *et al.* (2005) Deorphanization of GPRC6A: A promiscuous L- α -amino acid receptor with preference for basic amino acids. *Mol. Pharmacol.* **67**, 589–597.
86. Scalise, M. *et al.* (2014) Transport mechanism and regulatory properties of the human amino acid transporter ASCT2 (SLC1A5). *Amino Acids* **46**, 2463–2475.
87. Sloan, J. L. & Mager, S. (1999) Cloning and functional expression of a human Na⁺ and Cl⁻-dependent neutral and cationic amino acid transporter B0+. *J. Biol. Chem.* **274**, 23740–23745.
88. Takanaga, H., Mackenzie, B., Peng, J. Bin & Hediger, M. A. (2005) Characterization of a branched-chain amino-acid transporter SBAT1 (SLC6A15) that is expressed in human brain. *Biochem. Biophys. Res. Commun.* **337**, 892–900.
89. Kleta, R. *et al.* (2004) Mutations in SLC6A19, encoding B0AT1, cause Hartnup disorder. *Nat. Genet.* **36**, 999–1002.
90. Rossier, G. *et al.* (1999) LAT2, a new basolateral 4F2hc/CD98-associated amino acid transporter of kidney and intestine. *J. Biol. Chem.* **274**, 34948–34954.
91. Yan, R. *et al.* (2020) Cryo-EM structure of the human heteromeric amino acid transporter b0,+AT-rBAT. *Sci. Adv.* **6**, 1–11.
92. Nakauchi, J. *et al.* (2000) Cloning and characterization of a human brain Na⁺-independent transporter for small neutral amino acids that transports D-serine with high affinity. *Neurosci. Lett.* **287**, 231–235.
93. Pillai, S. M. & Meredith, D. (2011) SLC36A4 (hPAT4) is a high affinity amino acid transporter when expressed in *Xenopus laevis* oocytes. *J. Biol. Chem.* **286**, 2455–2460.
94. Bröer, S. (2014) The SLC38 family of sodium-amino acid co-transporters. *Pflügers Arch. Eur. J. Physiol.* **466**, 155–172.
95. Ramachandran, S. *et al.* (2021) Expression and function of SLC38A5, an amino acid-coupled Na⁺/H⁺ exchanger, in triple-negative breast cancer and its relevance to macropinocytosis. *Biochem. J.* **478**, 3957–3976.
96. Closs, E. I., Gräf, P., Habermeier, A., Cunningham, J. M. & Förstermann, U. (1997) Human cationic amino acid transporters hCAT-1, hCAT-2A, and hCAT-2B: Three related carriers with distinct transport properties. *Biochemistry* **36**, 6462–6468.
97. Vékony, N., Wolf, S., Boissel, J. P., Gnauert, K. & Closs, E. I. (2001) Human cationic amino acid transporter hCAT-3 is preferentially expressed in peripheral tissues. *Biochemistry* **40**, 12387–12394.
98. Bröer, A., Wagner, C. A., Lang, F. & Bröer, S. (2000) The heterodimeric amino acid transporter 4F2hc/y+LAT2 mediates arginine efflux in exchange with glutamine. *Biochem. J.* **349**, 787–795.
99. Torrents, D. *et al.* (1998) Identification and characterization of a membrane protein (y+L amino acid transporter-1) that associates with 4F2hc to encode the amino acid transport activity y+L. A candidate gene for lysinuric protein intolerance. *J. Biol. Chem.* **273**, 32437–32445.
100. Scalise, M. *et al.* (2019) Insights into the transport side of the human SLC38A9 transporter. *Biochim. Biophys. Acta - Biomembr.* **1861**, 1558–1567.
101. Werner, A. *et al.* (2017) Reconstitution of T cell proliferation under arginine limitation: Activated human T cells take up citrulline via L-Type amino acid transporter 1 and use it to regenerate arginine after induction of argininosuccinate synthase expression. *Front. Immunol.* **8**.
102. Yanagida, O. *et al.* (2001) Human L-type amino acid transporter 1 (LAT1): characterization of function and expression in tumor cell lines. *Biochim. Biophys. Acta - Biomembr.* **1514**, 291–302.
103. Fei, Y. J. *et al.* (2000) Primary structure genomic organization, and functional and electrogenic characteristics of human system N 1, a Na⁺- and H⁺-coupled glutamine transporter. *J. Biol. Chem.* **275**, 23707–23717.
104. Morrow, J. A. *et al.* (1998) Molecular cloning and functional expression of the human glycine transporter GlyT2 and chromosomal localisation of the gene in the human genome. *FEBS Lett.* **439**, 334–340.
105. Kim, K. M. *et al.* (1994) Cloning of the human glycine transporter type 1: Molecular and pharmacological characterization of novel isoform variants and chromosomal localization of the gene in the human and mouse genomes. *Mol. Pharmacol.* **45**, 608–617.

106. Bröer, S. *et al.* (2008) Iminoglycinuria and hyperglycinuria are discrete human phenotypes resulting from complex mutations in proline and glycine transporters. *J. Clin. Invest.* **118**, 3881–3892.
107. Devés, R. & Boyd, C. A. R. (1998) Transporters for cationic amino acids in animal cells: Discovery, structure, and function. *Physiol. Rev.* **78**, 487–545.
108. Babu, E. *et al.* (2003) Identification of a novel system L amino acid transporter structurally distinct from heterodimeric amino acid transporters. *J. Biol. Chem.* **278**, 43838–43845.
109. Boday, S. *et al.* (2005) Identification of LAT4, a novel amino acid transporter with system L activity. *J. Biol. Chem.* **280**, 12002–12011.
110. Liu, C. *et al.* (2015) GPR139, an orphan receptor highly enriched in the habenula and septum, is activated by the essential amino acids L-tryptophan and L-phenylalanine. *Mol. Pharmacol.* **88**, 911–925.
111. Lu, R., Kanai, N., Bao, Y. & Schuster, V. L. (1996) Cloning, in vitro expression, and tissue distribution of a human prostaglandin transporter cDNA (hPGT). *J. Clin. Invest.* **98**, 1142–1149.
112. Abramovitz, M. *et al.* (2000) The utilization of recombinant prostanoid receptors to determine the affinities and selectivities of prostaglandins and related analogs. *Biochim. Biophys. Acta - Mol. Cell Biol. Lipids* **1483**, 285–293.
113. Wright, D. H., Metters, K. M., Abramovitz, M. & Ford-Hutchinson, A. W. (1998) Characterization of the recombinant human prostanoid DP receptor and identification of L-644,698, a novel selective DP agonist. *Br. J. Pharmacol.* **123**, 1317–1324.
114. Adachi, H. *et al.* (2003) Molecular characterization of human and rat organic anion transporter OATP-D. *Am. J. Physiol. - Ren. Physiol.* **285**, 1188–1197.
115. Sharif, N. A. & Davis, T. L. (2002) Cloned human EP1 prostanoid receptor pharmacology characterized using radioligand binding techniques. *J. Pharm. Pharmacol.* **54**, 539–547.
116. Bastien, L., Sawyer, N., Grygorczyk, R., Metters, K. M. & Adam, M. (1994) Cloning, functional expression, and characterization of the human prostaglandin E2 receptor EP2 subtype. *J. Biol. Chem.* **269**, 11873–11877.
117. Davis, T. L. & Sharif, N. A. (2000) Pharmacological characterization of [3H]-prostaglandin E2 binding to the cloned human EP4 prostanoid receptor. *Br. J. Pharmacol.* **130**, 1919–1926.
118. Stitham, J. *et al.* (2007) New insights into human prostacyclin receptor structure and function through natural and synthetic mutations of transmembrane charged residues. *Br. J. Pharmacol.* **152**, 513–522.
119. Gose, T. *et al.* (2016) Prostaglandin transporter (OATP2A1/SLCO2A1) contributes to local disposition of eicosapentaenoic acid-derived PGE3. *Prostaglandins Other Lipid Mediat.* **122**, 10–17.
120. Kimura, H. *et al.* (2002) Human organic anion transporters and human organic cation transporters mediate renal transport of prostaglandins. *J. Pharmacol. Exp. Ther.* **301**, 293–298.
121. Wada, M. *et al.* (2007) Enzymes and receptors of prostaglandin pathways with arachidonic acid-derived versus eicosapentaenoic acid-derived substrates and products. *J. Biol. Chem.* **282**, 22254–22266.
122. Murakami, Y. *et al.* (2005) Functional characterization of human monocarboxylate transporter 6 (SLC16A5). *Drug Metab. Dispos.* **33**, 1845–1851.
123. Coady, M. J. *et al.* (2004) The human tumour suppressor gene SLC5A8 expresses a Na⁺ + -monocarboxylate cotransporter. *J. Physiol.* **557**, 719–731.
124. Ahmed, K. *et al.* (2010) An autocrine lactate loop mediates insulin-dependent inhibition of lipolysis through GPR81. *Cell Metab.* **11**, 311–319.
125. Gopal, E. *et al.* (2007) Cloning and functional characterization of human SMCT2 (SLC5A12) and expression pattern of the transporter in kidney. *Biochim. Biophys. Acta - Biomembr.* **1768**, 2690–2697.
126. Bosshart, P. D., Charles, R., Garib Singh, R. A., Schlessinger, A. & Fotiadis, D. (2021) SLC16 family: From atomic structure to human disease. *Trends Biochem. Sci.* **46**, 28–40.
127. Gopal, E. *et al.* (2007) Transport of nicotinate and structurally related compounds by human SMCT1 (SLC5A8) and its relevance to drug transport in the mammalian intestinal tract. *Pharm. Res.* **24**, 575–584.
128. Wise, A. *et al.* (2003) Molecular identification of high and low affinity receptors for nicotinic acid. *J. Biol. Chem.* **278**, 9869–9874.
129. Taggart, A. K. P. *et al.* (2005) (D)- β -hydroxybutyrate inhibits adipocyte lipolysis via the nicotinic acid receptor PUMA-G. *J. Biol. Chem.* **280**, 26649–26652.
130. Mathialagan, S. *et al.* (2020) Nicotinic acid transport into human liver involves organic anion transporter 2 (SLC22A7). *Biochem. Pharmacol.* **2**, 113829.
131. Ho, J. S. *et al.* (2007) Novel liver-specific organic anion transporter OAT17 that operates the exchange of sulfate conjugates for short chain fatty acid butyrate. *Hepatology* **45**, 1046–1055.
132. Bahn, A. *et al.* (2008) Identification of a new urate and high affinity nicotinate transporter, hOAT10 (SLC22A13). *J. Biol. Chem.* **283**, 16332–16341.

133. Brown, A. J. *et al.* (2003) The orphan G protein-coupled receptors GPR41 and GPR43 are activated by propionate and other short chain carboxylic acids. *J. Biol. Chem.* **278**, 11312–11319.
134. Miyauchi, S., Gopal, E., Fei, Y. J. & Ganapathy, V. (2004) Functional identification of SLC5A8, a tumor suppressor down-regulated in colon cancer, as a Na⁺-coupled transporter for short-chain fatty acids. *J. Biol. Chem.* **279**, 13293–13296.
135. Martin, P. M. *et al.* (2006) Identity of SMCT1 (SLC5A8) as a neuron-specific Na⁺-coupled transporter for active uptake of L-lactate and ketone bodies in the brain. *J. Neurochem.* **98**, 279–288.
136. Pajor, A. M. (2014) Sodium-coupled dicarboxylate and citrate transporters from the SLC13 family. *Pflügers Arch. - Eur. J. Physiol.* **466**, 119–130.
137. He, W. *et al.* (2004) Citric acid cycle intermediates as ligands for orphan G-protein-coupled receptors. *Nature* **429**, 188–193.
138. Prag, H. A. *et al.* (2021) Mechanism of succinate efflux upon reperfusion of the ischaemic heart. *Cardiovasc. Res.* **117**, 1188–1201.
139. Reddy, A. *et al.* (2020) pH-gated succinate secretion regulates muscle remodeling in response to exercise. *Cell* **183**, 62–75.
140. Bisbach, C. M., Hass, D. T., Thomas, E. D., Cherry, T. J. & Hurley, J. B. (2022) Monocarboxylate transporter 1 (MCT1) mediates succinate export in the retina. *Investig. Ophthalmology Vis. Sci.* **63**, 1.
141. Kaufhold, M. *et al.* (2011) Differential interaction of dicarboxylates with human sodium-dicarboxylate cotransporter 3 and organic anion transporters 1 and 3. *Am. J. Physiol. - Ren. Physiol.* **301**, 1026–1034.
142. Wang, Z. *et al.* (2020) Mfsd2a and Spns2 are essential for sphingosine-1-phosphate transport in the formation and maintenance of the blood-brain barrier. *Sci. Adv.* **6**, eaay8627.
143. Im, D. S., Clemens, J., Macdonald, T. L. & Lynch, K. R. (2001) Characterization of the human and mouse sphingosine 1-phosphate receptor, SIP5 (Edg-8): Structure–activity relationship of sphingosine 1-phosphate receptors. *Biochemistry* **40**, 14053–14060.
144. Pan, S. *et al.* (2006) A monoselective sphingosine-1-phosphate receptor-1 agonist prevents allograft rejection in a stringent rat heart transplantation model. *Chem. Biol.* **13**, 1227–1234.
145. Vu, T. M. *et al.* (2017) Mfsd2b is essential for the sphingosine-1-phosphate export in erythrocytes and platelets. *Nature* **550**, 524–528.
146. Hisano, Y., Kobayashi, N., Kawahara, A., Yamaguchi, A. & Nishi, T. (2011) The sphingosine 1-phosphate transporter, SPNS2, functions as a transporter of the phosphorylated form of the immunomodulating agent FTY720. *J. Biol. Chem.* **286**, 1758–1766.
147. Uhlenbrock, K., Gassenhuber, H. & Kostenis, E. (2002) Sphingosine 1-phosphate is a ligand of the human gpr3, gpr6 and gpr12 family of constitutively active G protein-coupled receptors. *Cell. Signal.* **14**, 941–953.
148. Niedernberg, A., Tunaru, S., Blaukat, A., Ardati, A. & Kostenis, E. (2003) Sphingosine 1-phosphate and dioleoylphosphatidic acid are low affinity agonists for the orphan receptor GPR63. *Cell. Signal.* **15**, 435–446.
149. Murakami, M., Shiraishi, A., Tabata, K. & Fujita, N. (2008) Identification of the orphan GPCR, P2Y10 receptor as the sphingosine-1-phosphate and lysophosphatidic acid receptor. *Biochem. Biophys. Res. Commun.* **371**, 707–712.
150. Hagenbuch, B. & Meier, P. J. (1994) Molecular cloning, chromosomal localization, and functional characterization of a human liver Na⁺/bile acid cotransporter. *J. Clin. Invest.* **93**, 1326–1331.
151. Kawamata, Y. *et al.* (2003) A G protein-coupled receptor responsive to bile acids. *J. Biol. Chem.* **278**, 9435–9440.
152. Craddock, A. L. *et al.* (1998) Expression and transport properties of the human ileal and renal sodium-dependent bile acid transporter. *Am. J. Physiol. - Gastrointest. Liver Physiol.* **274**, 157–169.
153. Liu, R. *et al.* (2015) Taurocholate induces cyclooxygenase-2 expression via the sphingosine 1-phosphate receptor 2 in a human cholangiocarcinoma cell line. *J. Biol. Chem.* **290**, 30988–31002.
154. Yee, S. W. *et al.* (2019) Unraveling the functional role of the orphan solute carrier, SLC22A24 in the transport of steroid conjugates through metabolomic and genome-wide association studies. *PLOS Genet.* **15**, e1008208.
155. Suga, T., Yamaguchi, H., Ogura, J. & Mano, N. (2019) Characterization of conjugated and unconjugated bile acid transport via human organic solute transporter α/β . *Biochim. Biophys. Acta - Biomembr.* **1861**, 1023–1029.
156. Kullak-Ublick, G. A. *et al.* (1995) Molecular and functional characterization of an organic anion transporting polypeptide cloned from human liver. *Gastroenterology* **109**, 1274–1282.
157. Suga, T. *et al.* (2017) Preference of conjugated bile acids over unconjugated bile acids as substrates for OATP1B1 and OATP1B3. *PLoS One* **12**, e0169719.
158. Pan, Q. *et al.* (2018) Solute carrier organic anion transporter family member 3A1 is a bile acid efflux transporter in cholestasis. *Gastroenterology* **155**, 1578–1592.
159. Gimeno, R. E. *et al.* (2003) Characterization of a heart-specific fatty acid transport protein. *J. Biol. Chem.* **278**, 16039–16044.
160. Schaffer, J. E. & Lodish, H. F. (1994) Expression cloning and characterization of a novel adipocyte long chain fatty acid transport protein. *Cell* **79**, 427–436.

161. Itoh, Y. *et al.* (2003) Free fatty acids regulate insulin secretion from pancreatic β cells through GPR40. *Nature* **422**, 173–176.
162. Briscoe, C. P. *et al.* (2003) The orphan G protein-coupled receptor GPR40 is activated by medium and long chain fatty acids. *J. Biol. Chem.* **278**, 11303–11311.
163. Falcon, A. *et al.* (2010) FATP2 is a hepatic fatty acid transporter and peroxisomal very long-chain acyl-CoA synthetase. *Am. J. Physiol. - Endocrinol. Metab.* **299**, 384–393.
164. Watson, S. J., Brown, A. J. H. & Holliday, N. D. (2012) Differential signaling by splice variants of the human free fatty acid receptor GPR120. *Mol. Pharmacol.* **81**, 631–642.
165. Stahl, A. *et al.* (1999) Identification of the major intestinal fatty acid transport protein. *Mol. Cell* **4**, 299–308.
166. Alexander, S. P. H. *et al.* (2021) The concise guide to pharmacology 2021/22: Transporters. *Br. J. Pharmacol.* **178**, S412–S513.

SUMMARY

Transport proteins are present in virtually all biological membranes of living organisms. These so-called ‘transporters’ are required for a cell to take up nutrients and excrete waste, which serves the purpose of ensuring that cell’s growth and survival as well as facilitate its communication with neighboring cells. The largest class of transporters is the superfamily of solute carriers (SLCs), which in humans comprises over 450 members divided into 66 subfamilies, each with their own substrate specificity and transport mechanism. Due to their critical role in the proper functioning of cells, it may not be surprising that SLCs play a role in the development and progression of diseases. So far, SLCs have been the target of frequently prescribed drugs, such as neurotransmitter transporters (targets of antidepressants) and $\text{Na}^+/\text{K}^+/\text{Cl}^-$ -transporters (targets of loop diuretics). However, the majority of SLCs are poorly studied despite their tremendous potential as drug targets. Thus, there is a need for the development of new methods that can be used to study the function of SLCs as well as identify modulators (e.g., inhibitors). The advantages and limitations of current in vitro methods to study SLCs are summarized in Chapter 1. Moreover, the concept of cell-based label-free assays is introduced as an innovative approach to assess transport function in a setting that is closer to a cell’s physiological environment. Throughout the five experimental chapters of this thesis, the impedance-based technology xCELLigence is used as a core platform for the development and application of novel functional assays for three types of SLC: dopamine (DAT), norepinephrine (NET) and glutamate (EAAT) transporters.

In humans, activation of G protein-coupled receptors (GPCRs) on the cell surface and other cellular membranes leads to cellular responses that control a wide variety of physiological processes. Some of the endogenous ligands that activate these GPCRs – such as neurotransmitters or signaling lipids – are transported from the extracellular space into the cell by SLCs. This regulation is necessary to prevent excessive GPCR activation, which is at the basis of drugs that inhibit such SLCs (i.e., antidepressants) and increase extracellular amounts of the endogenous ligands. Although several of these SLC–GPCR ‘pairs’ have been identified over the past century, there have been recent insights into novel regulatory mechanisms of SLCs that modulate the activation of GPCRs. Chapter 2 describes SLCs that mediate the efflux of ligands, as well as SLCs that grant ligand access to intracellular receptors. Identification of such mechanisms could help to understand disease etiology and target selection for drug discovery.

In Chapter 3, the development of the ‘transport activity through receptor activation’ (TRACT) assay is reported for the human dopamine transporter (DAT, SLC6A3), which is a drug target for treatment of depression and substance abuse disorders. Dopamine, which is the substrate of DAT, is an endogenous agonist for dopamine receptors and adrenergic receptors. Activation of these receptors on live cells leads to changes in cell morphology, which can be measured in real-time as a change in electrical impedance using the label-

free technology xCELLigence. In two human cell lines with heterologous DAT expression, dopamine-induced activation of the dopamine D1 receptor (D1R) or the alpha-2 adrenergic receptor (α 2R) was attenuated as a portion of the extracellular dopamine was taken up into the cell via DAT. Pharmacological inhibition or the absence of DAT restored the apparent potency of dopamine on D1R and α 2R. This provided an assay window to measure the inhibitory potency of GBR12909 and cocaine, which are well-known DAT inhibitors. This chapter demonstrates a novel application of a cell-based label-free biosensor, which may be used to identify new DAT inhibitors.

In Chapter 4, the concept of the TRACT assay is extended to the human norepinephrine transporter (NET, SLC6A2), which is an established drug target for a range of psychiatric disorders. Here, NET was overexpressed in an inducible human embryonic kidney 293 (HEK293)-JumpIn cell line, which endogenously expresses the α 2R. Three endogenous NET substrates – norepinephrine, dopamine and epinephrine – activated α 2R, resulting in a concentration-dependent cellular response. This response was attenuated in the presence of NET for all three substrates and could be rescued by the NET inhibitor nisoxetine. Using norepinephrine as a substrate, the inhibitory potencies of several reported NET inhibitors were determined in the TRACT assay, showing a good correlation with a conventional fluorescent substrate uptake assay. Moreover, the assay was validated in a manual high-throughput screening (HTS) set-up, which suggests that the TRACT assay can be used in the future for screening of NET inhibitors.

The TRACT assay that was developed in Chapter 4 was applied in Chapter 5 to screen a set of compounds that were predicted to be NET inhibitors using a computational modeling pipeline. Similarity networks were used to make a selection of the SLC bioactivity data from the ChEMBL database, which was then used to train a proteochemometric (PCM) model. After further optimization, this model was applied to screen the Enamine REAL database that contains over 600 million make-on-demand molecules. From this screen, the molecules with the highest predicted affinity of 46 chemically diverse clusters were identified, of which 32 molecules were purchased for in vitro testing. Using the TRACT assay, five compounds were found to have submicromolar potencies towards NET. This chapter demonstrates that the TRACT assay could be successfully used to identify and characterize unknown NET inhibitors.

Chapter 6 describes the development of an impedance-based phenotypic assay for the Na⁺-dependent excitatory amino acid transporters (EAATs, SLC1 family), which mediate the uptake of glutamate and aspartate in the central nervous system and peripheral tissues. Initial attempts were made to set up a TRACT assay for EAAT1, by using HEK293-JumpIn cells with inducible overexpression of EAAT1 and transient expression of the metabotropic glutamate receptor 2 (mGluR-2). The presence of EAAT1 attenuated the glutamate-induced mGluR2 response, although this response was inconsistently restored by two EAAT1 inhibitors. Interestingly, a receptor-independent glutamate response was observed in cells lacking mGluR2, which could be inhibited by EAAT1 inhibitors UCPH-101 and TFB-TBOA in a concentration-dependent manner. Live-cell imaging revealed that the cells started spreading upon treatment with glutamate, which concurs with the observed increase

in impedance. This response was observed with both L- and D-isomers of glutamate and aspartate, suggesting that it is substrate-independent. Moreover, the response was prevented in the presence of the Na^+/K^+ -ATPase inhibitor ouabain, which indicates that it is ion-dependent. Targeted metabolomics showed a decrease of intracellular taurine levels upon glutamate or aspartate treatment of the cells, which indicates an effect on cell volume. Taken together, these data suggest that substrate uptake via EAAT1 induces cell swelling, which triggers changes in cell morphology that are detected in the impedance-based assay. This distinct ‘phenotype’ was also observed in a breast cancer cell line with endogenous EAAT1 expression, as well as HEK293-JumpIn cells overexpressing EAAT2 or EAAT3, suggesting that the mechanism is shared between cell types and SLCs. Validation of this assay in a manual HTS set-up confirmed that this phenotypic approach may be used for EAAT drug discovery and holds promise for the study of other transport proteins that modulate cell shape.

In Chapter 7, the phenotypic assay from Chapter 6 was applied to assess the function of disease-associated variants of EAAT1. Using *in silico* methods, several EAAT1 missense mutations were identified in cancer patients listed in the Genomic Data Commons dataset. Eight of these mutations were selected for *in vitro* testing based on their close proximity to the substrate and inhibitor binding sites. Moreover, two mutations found in patients with episodic ataxia type 6 (EA6) were included for testing. Substrate responses (glutamate and aspartate) and inhibitory potency of orthosteric (TFB-TBOA) and allosteric (UCPH-101) inhibitors were differentially affected by the tested mutants, suggesting either a gain- or loss-of-function. Interestingly, one of the EA6 mutants – M128R – was found to be ‘activated’ upon treatment with TFB-TBOA and UCPH-101, which was not observed for wild-type EAAT1 or other mutants. These data demonstrate the ability of the impedance-based phenotypic assay to detect altered functionality in transporter variants, which could substantiate mechanistic studies and aid drug discovery efforts.

Chapter 8 provides a general discussion on the various assays that have been presented throughout this thesis. Moreover, a mechanistic substantiation is provided for the TRACT assay, using two models previously described in literature. The main conclusions are presented and the future of cell-based label-free assays in SLC drug discovery is speculated on. Of note, the Appendix provides two insightful tables that summarize SLC–GPCR pairs that share the same substrate, as well as SLCs that are Na^+ -dependent. Thus, Chapter 8 and the Appendix provide a starting point for the selection of the next SLC that can be assessed using impedance-based assays. Taken together, the findings in this thesis have unveiled cell-based label-free assays as a novel addition to the SLC toolbox, which may prove to be useful in upcoming drug discovery campaigns.

NEDERLANDSE SAMENVATTING

Transporteiwitten zijn aanwezig in vrijwel alle biologische membranen van de cellen van levende organismen. Deze zogenaamde ‘transporters’ zijn benodigd voor een cel om nutriënten op te nemen en afval uit te scheiden, om er voor te zorgen dat de cel kan groeien, overleven en communiceren met naburige cellen. De grootste klasse van transporters is de superfamilie van de solute carriers (SLCs, lett. ‘vervoerders van opgeloste stoffen’). De mens bevat genen voor meer dan 450 SLCs die verdeeld kunnen worden in 66 subfamilies, elk met zijn eigen specifieke substraten en transportmechanisme. Dankzij de cruciale rol die SLCs spelen in het goed functioneren van cellen, is het niet verrassend dat SLCs ook betrokken zijn bij vele ziekten. Tot dusver zijn enkele SLCs het aangrijpingspunt van vaak voorgeschreven geneesmiddelen, zoals neurotransmittertransporters (antidepressiva) en natrium-kalium-chloridetransporters (lisdiuretica). De overgrote meerderheid van SLCs is echter nog nauwelijks bestudeerd, ondanks hun enorme potentie als aangrijpingspunt voor geneesmiddelen. Mede hierdoor is er vraag naar de ontwikkeling van nieuwe methoden die gebruikt kunnen worden om de functie van SLCs te bestuderen en modulatoren (bijv. remmers) te identificeren. De voordelen en beperkingen van de huidige in vitro methoden (‘petrischaal’-experimenten) om SLCs te bestuderen, worden in Hoofdstuk 1 samengevat. Bovendien wordt het concept van op cellen gebaseerde labelvrije methoden geïntroduceerd als een innovatieve aanpak om transportfunctionaliteit te bestuderen in een omgeving die dichter dan gebruikelijk in de buurt komt van het fysiologische milieu van een cel. In de vijf experimentele hoofdstukken van dit proefschrift wordt de op impedantie gebaseerde technologie xCELLigence gebruikt als dé methode voor het ontwikkelen en toepassen van nieuwe functionele methoden voor drie soorten SLCs: de dopamine- (DAT), noradrenaline- (NET) en glutamaattransporters (EAAT).

In de mens leidt de activatie van G-eiwitgekoppelde receptoren (GPCRs) op het celmembraan tot cellulaire responsen die een breed scala aan fysiologische processen beïnvloeden. Enkele lichaamseigen liganden die deze GPCRs activeren, zoals neurotransmitters of signaallipiden, worden door SLCs vanuit de extracellulaire ruimte de cel in getransporteerd. Deze vorm van regulatie is nodig om excessieve activatie van GPCRs te voorkomen. Daarnaast ligt dit principe aan de basis van geneesmiddelen die zulke SLCs remmen (bijv. antidepressiva), waardoor de extracellulaire hoeveelheid van de lichaamseigen liganden wordt verhoogd. Alhoewel er in de afgelopen eeuw enkele van deze SLC–GPCR ‘paren’ werden geïdentificeerd, zijn er recentelijk nieuwe inzichten ontstaan over regulerende mechanismen waarmee transporters receptoractivatie kunnen moduleren. Hoofdstuk 2 beschrijft SLCs die de uitstroom van liganden faciliteren, evenals SLCs die liganden toegang verlenen tot intracellulaire receptoren. Het identificeren van zulke mechanismen kan bijdragen aan het begrijpen van ziekteoorzaken en het selecteren van aangrijpingspunten voor geneesmiddelontwikkeling.

Hoofdstuk 3 beschrijft de ontwikkeling van de ‘transportactiviteit via receptor activatie’ (TRACT) methode voor de humane dopaminetransporter (DAT, SLC6A3), die een aangrijpingspunt is voor de behandeling van depressie en middelenmisbruik. Het belangrijkste substraat van DAT, dopamine, is een lichaamseigen agonist (activator) van dopamine- en adrenerge receptoren. Activatie van deze receptoren op levende cellen leidt tot veranderingen in de celmorfologie, hetgeen in ‘real-time’ gemeten kan worden als een verandering in elektrische impedantie met de labelvrije technologie xCELLigence. In twee humane cellijnen met heterologe expressie van DAT werd activatie van de dopaminereceptor D1 (D1R) of de alfa-2 adrenerge receptor (α 2R) door dopamine verzwakt, omdat een deel van de extracellulaire dopamine door DAT in de cel werd opgenomen. Farmacologische blokkade of de afwezigheid van DAT resulteerde in het herstel van deze receptoractivatie. Hierdoor ontstond een farmacologisch raamwerk (d.w.z. het verschil tussen de maximale en minimale respons) dat het mogelijk maakte om de werkingssterkte (potentie) te bepalen van twee goed bestudeerde DAT-remmers: GBR12909 en cocaïne. Dit hoofdstuk toont een nieuwe toepassing van een celgebaseerde labelvrije biosensor, die gebruikt kan worden om nieuwe DAT-remmers te vinden.

In Hoofdstuk 4 wordt het concept van de TRACT methode uitgebreid naar de humane noradrenalinetransporter (NET, SLC6A2), die een bekend aangrijpingspunt is voor geneesmiddelen ter behandeling van een reeks psychiatrische aandoeningen. In onze studie werd NET tot overexpressie gebracht in een induceerbare humane embryonale nier 293 (HEK293)-JumpIn cellijn, die tevens endogeen α 2R tot expressie brengt. Drie lichaamseigen substraten van NET – noradrenaline, dopamine en adrenaline – konden α 2R activeren, wat leidde tot een concentratieafhankelijke cellulaire respons. Deze respons werd voor alle drie de substraten verzwakt in aanwezigheid van NET en kon worden hersteld door de NET-remmer nisoxetine. Met behulp van noradrenaline als substraat zijn de werkingssterktes van verschillende gerapporteerde NET-remmers bepaald met de TRACT methode, welke goed overeenkwamen met de werkingssterktes die bepaald waren met een conventionele opnamemethode van een fluorescent substraat. Bovendien werd de methode gevalideerd in een handmatige ‘high-throughput screening’ (HTS)-opstelling, hetgeen suggereert dat de TRACT methode gebruikt kan worden voor het screenen van hele bibliotheken van NET-remmers.

In Hoofdstuk 5 werd de TRACT methode van Hoofdstuk 4 toegepast voor het screenen van een reeks moleculen waarvan met behulp van een in silico (computergestuurde) modelleringspijplijn werd voorspeld dat ze NET-remmers zouden zijn. Gelijkwaardigheidsnetwerken (similarity networks) werden gebruikt om een selectie te maken van de bioactiviteitsgegevens van SLCs uit de ChEMBL-database, die vervolgens werden gebruikt om een proteochemometrisch (PCM) model te trainen. Na verdere optimalisatie werd dit model toegepast om de Enamine REAL-database, die meer dan 600 miljoen ‘make-on-demand’ moleculen bevat, te screenen. Uit elk van de resulterende 46 chemisch diverse clusters werden de moleculen met de hoogste voorspelde affiniteitswaarden geselecteerd, waarvan uiteindelijk 32 moleculen werden gekocht voor in vitro experimenten. Met behulp van de TRACT methode bleken vijf moleculen een submicromolaire werkingssterkte te hebben op NET. Dit hoofdstuk laat zien dat de TRACT methode met succes kan worden

gebruikt om onbekende NET-remmers te identificeren en karakteriseren.

Hoofdstuk 6 beschrijft de ontwikkeling van een op impedantie gebaseerde fenotypische methode voor de natrium-afhankelijke exciterende aminozuurtransporters (EAATs, SLC1 familie), die betrokken zijn bij de opname van glutamaat en aspartaat in het centrale zenuwstelsel en perifere weefsels. Initieel werd gepoogd een TRACT methode op te zetten voor EAAT1 door gebruik te maken van HEK293-JumpIn cellen met induceerbare expressie van EAAT1 en tijdelijke expressie van de metabotrope glutamaatreceptor 2 (mGluR2). De aanwezigheid van EAAT1 zorgde voor een verzwakking van de door glutamaat geïnduceerde mGluR2-respons. Deze respons kon echter niet consistent worden hersteld door twee EAAT1-remmers. Interessant was dat er een receptoronafhankelijke glutamaatrespons werd waargenomen in cellen zonder mGluR2, welke concentratieafhankelijk kon worden geblokkeerd door EAAT1-remmers UCPH-101 en TFB-TBOA. Met behulp van microscopie op de levende cellen kon worden vastgesteld dat de cellen zich verspreidden na behandeling met glutamaat, wat overeenkwam met de verhoogde impedantierepons. De respons werd waargenomen met zowel L- als D-isomeren van glutamaat en aspartaat, hetgeen suggereert dat de respons substraatonafhankelijk is. Bovendien werd de respons voorkomen in aanwezigheid van de natrium-kaliumpomppremmer ouabaine, wat aangeeft dat de respons ion-afhankelijk is. Gerichte metabolomics experimenten toonden een afname aan van intracellulaire taurinespiegels na behandeling van de cellen met glutamaat of aspartaat, wat duidt op een effect op het celvolume. Samengevat suggereren deze data dat substraatopname via EAAT1 celzwellen induceert, wat veranderingen in celmorphologie veroorzaakt die worden gedetecteerd met de impedantiemethode. Dit duidelijke ‘fenotype’ werd ook waargenomen in een borstkankercellijn met endogene EAAT1-expressie, evenals in HEK293-JumpIn cellen met overexpressie van EAAT2 of EAAT3, wat suggereert dat het mechanisme wordt gedeeld tussen celtypen en SLCs. Validatie van deze methode in een handmatige HTS-opstelling bevestigt dat deze fenotypische aanpak kan worden gebruikt voor EAAT1 geneesmiddelontdekking. Daarnaast is de methode veelbelovend voor het bestuderen van andere transporteiwitten die de celvorm beïnvloeden.

In Hoofdstuk 7 werd de fenotypische methode uit Hoofdstuk 6 toegepast om de functie van ziekte-geassocieerde genetische varianten van EAAT1 te bepalen. Met behulp van in silico methoden werden verschillende EAAT1 missense-mutaties geïdentificeerd bij kankerpatiënten die vermeld staan in de Genomic Data Commons-dataset. Acht van deze mutaties werden geselecteerd voor in vitro experimenten op basis van hun nabijheid tot de bindingsplaatsen van het substraat en de EAAT1-remmers. Daarnaast werden tijdens de experimenten twee mutaties meegenomen die gevonden zijn bij patiënten met episodische ataxie type 6 (EA6). Substraatresponsen (glutamaat en aspartaat) en de werkingssterkte van orthostere (d.w.z. dezelfde bindingsplek als het lichaamseigen substraat) en allosterie (d.w.z. andere bindingsplek dan het lichaamseigen substraat) EAAT1-remmers werden verschillend beïnvloed door de geteste mutanten, wat duidt op een toename of verlies van functie. Interessant genoeg bleek een van de EA6-mutanten – M128R – ‘geactiveerd’ te worden na behandeling met TFB-TBOA en UCPH-101, wat niet werd waargenomen in wild-type EAAT1 of andere mutanten. Deze data laten zien dat de op impedantie gebaseerde fenotypische methode het mogelijk maakt om veranderde functionaliteit

van transportervarianten te detecteren. De methode zou gebruikt kunnen worden om mechanistische studies te onderbouwen en geneesmiddelontdekking te ondersteunen.

Tot slot verschaft Hoofdstuk 8 een algemene discussie over de verschillende methoden die in dit proefschrift zijn gepresenteerd. Bovendien wordt er een mechanistische onderbouwing gepresenteerd voor de TRACT methode, met behulp van twee eerder in de literatuur beschreven modellen. De belangrijkste conclusies worden gepresenteerd en er wordt gespeculeerd over de toekomst van celgebaseerde labelvrije testen tijdens het ontwikkelen van geneesmiddelen voor SLCs. Noemenswaardig is de Appendix, die twee inzichtelijke tabellen bevat: een samenvatting van SLC–GPCR paren die hetzelfde substraat delen en een overzicht van SLCs die natrium-afhankelijk zijn. Op deze manier bieden Hoofdstuk 8 en de Appendix een startpunt voor het selecteren van de volgende SLC die kan worden bestudeerd met behulp van impedantie. Alles bij elkaar dragen de bevindingen in dit proefschrift celgebaseerde labelvrije methoden aan als een nieuwe toevoeging aan de SLC-gereedschapskist, waarmee hopelijk een nuttige bijdrage wordt geleverd aan het geneesmiddelontwikkelingstraject.

LIST OF PUBLICATIONS

Part of this thesis

Gorostiola Gonzalez, M.[†], **Sijben, H.J.**[†], Dall'Acqua, L., Liu, R., IJzerman, A.P., van Westen, G.J.P., Heitman, L.H. (2022) Molecular insights into disease-associated glutamate transporter variants using *in silico* and *in vitro* approaches. (manuscript in preparation)

Bongers, B.J.[†], **Sijben, H.J.**[†], Hartog, P.B.R., IJzerman, A.P., Heitman, L.H., van Westen, G.J.P. (2022). Proteochemometric modelling identifies novel norepinephrine transporter inhibitors. *Journal of Chemical Information and Modelling* (manuscript submitted)

Sijben, H.J., Dall'Acqua, L., Liu, R., Jarret, A., Christodoulaki, E., Onstein, S., Wolf, G., Verburgt, S.J., Le Dévédec, S.E., Wiedmer, T., Superti-Furga, G., IJzerman, A.P., Heitman, L.H. (2022). Impedance-based phenotypic readout of transport function: a case for glutamate transporters. *Frontiers in Pharmacology*, **13**, 872335

Sijben, H.J., Superti-Furga, G., IJzerman, A.P., Heitman, L.H. (2022). Targeting solute carriers to modulate receptor–ligand interactions. *Trends in Pharmacological Sciences*, **43**(5), 358–361

Sijben, H.J., van Oostveen, W.M., Hartog, P.B.R., Stucchi, L., Rossignoli, A., Maresca, G., Scarabottolo, L., IJzerman, A.P., Heitman, L.H. (2021). Label-free high-throughput screening assay for the identification of norepinephrine transporter (NET/SLC6A2) inhibitors. *Scientific Reports*, **11**, 12290

Sijben, H.J., van den Berg, J.J.E., Broekhuis, J.D., IJzerman, A.P., Heitman, L.H. (2021). A study of the dopamine transporter using the TRACT assay, a novel *in vitro* tool for solute carrier drug discovery. *Scientific Reports*, **11**, 1312.

[†] These authors have contributed equally

Other publications

Mocking, T.A.M., **Sijben, H.J.**, Vermeulen, Y.W., IJzerman, A.P., Heitman, L.H. (2022). MPP⁺-induced changes in cellular impedance as a measure for organic cation transporter (SLC22A1-3) activity and inhibition. *International Journal of Molecular Sciences*, **23**(3), 1203

Dvorak, V., Wiedmer, T., Ingles-Prieto, A., Altermatt, P., Batoulis, H., Bärenz, F., Bender, E., Digles, D., Dürrenberger, F., Heitman, L.H., IJzerman, A.P., Kell, D.B., Kicking, S., Körzö, D., Leippe, P., Licher, T., Manolova, V., Rizzetto, R., Sassone, F., Scarabottolo, L., Schlessinger, A., Schneider, V., **Sijben, H.J.**, Steck, A., Sundström, H., Tremolada, S., Wilhelm, M., Wright Muelas, M., Zindel, D., Stepan, C.M., Superti-Furga, G. (2021) An overview of cell-based assay platforms for the solute carriers family of transporters. *Frontiers in Pharmacology*, **12**, 722889

Superti-Furga, G., Lackner, D., Wiedmer, T., Ingles-Prieto, A., Barbosa, B., Girardi, E., Goldmann, U., Gürtl, B., Klavins, K., Klimek, C., Lindinger, S., Liñeiro-Retes, E., Müller, A.C., Onstein, S., Redinger, G., Reil, D., Sedlyarov, V., Wolf, G., Crawford, M., Everley, R., Hepworth, D., Liu, S., Noell, S., Piotrowski, M., Stanton, R., Zhang, H., Corallino, S., Faedo, A., Insidioso, M., Maresca, G., Redaelli, L., Sassone, F., Scarabottolo, L., Stucchi, M., Tarroni, P., Tremolada, S., Batoulis, H., Becker, A., Bender, E., Chang, Y., Ehrmann, A., Müller-Fahrnow, A., Pütter, V., Zinder, D., Hamilton, B., Lenter, M., Santacruz, D., Viollet, C., Whitehurst, C., Johnsson, K., Leippe, P., Baumgarten, B., Chang, L., Ibig, Y., Pfeifer, M., Reinhardt, J., Schönbett, J., Selzer, P., Seuwen, K., Bettembourg, C., Biton, B., Czech, J., de Foucauld, H., Didier, M., Licher, T., Mikol, V., Pommereau, A., Puech, F., Yaligara, V., Edwards, A., Bongers, B.J., Heitman, L.H., IJzerman, A.P., **Sijben, H.J.**, van Westen, G.J.P., Grixti, J., Kell, D.B., Mughal, F., Swainston, N., Wright-Muelas, M., Bohstedt, T., Burgess-Brown, N., Carpenter, L., Dürr, K., Hansen, J., Scacioc, A., Banci, G., Colas, C., Digles, D., Ecker, G., Füzi, B., Gamsjäger, V., Grandits, M., Martini, R., Troger, F., Altermatt, P., Doucerain, C., Dürrenberger, F., Manolova, V., Steck, A., Sundström, H., Wilhelm, M., Steppan, C. M. (2020). The RESOLUTE consortium: unlocking SLC transporters for drug discovery. *Nature Reviews Drug Discovery*, **19**(7), 429–430.

Martella, A., **Sijben, H.**, Rufer, A.C., Grether, U., Fingerle, J., Ullmer, C., Hartung, T., IJzerman, A.P., van der Stelt, M., Heitman, L.H. (2017). A novel selective inverse agonist of the CB2 receptor as a radiolabeled tool compound for kinetic binding studies. *Molecular Pharmacology*, **92**(4), 389–400.

Poster and oral communications

- | | |
|-----------|--|
| 3-5-2018 | LACDR Spring Symposium (<i>poster</i>) |
| 16-2-2019 | LACDR Spring Symposium (<i>poster</i>) |
| 5-8-2019 | BioParadigms BioMedical Transporters Conference 2019
(Lucerne, Switzerland) (<i>poster</i>) |
| 23-9-2019 | FIGON Dutch Medicines Days (<i>poster</i>)
Awarded with the Poster Competition Prize |
| 2-7-2020 | LACDR Spring Symposium (<i>poster</i>) |
| 31-5-2021 | LACDR Spring Symposium (<i>oral</i>) |
| 27-9-2021 | FIGON Dutch Medicines Days (<i>poster</i>) |
| 7-10-2021 | 6th RESOLUTE Consortium Meeting (Basel, Switzerland) (<i>oral</i>) |
| 14-4-2022 | LACDR Spring Symposium (<i>poster</i>)
Awarded with the Poster Competition Prize |

CURRICULUM VITAE

Huub Sijben was born in Woerden, The Netherlands, on August 8th 1993. He graduated from pre-university education at the Katholieke Scholengemeenschap Etten-Leur in 2011. That same year, he started the Bachelor's program Bio-Pharmaceutical Sciences at Leiden University. In his second year, he became a board member of the study association L.P.S.V. „Aesculapius” for one year, for which he organized a study trip to Vienna and Budapest amongst other activities. At the end of his Bachelor's program, Huub performed an internship at the division of Medicinal Chemistry of the Leiden Academic Centre for Drug Research (LACDR) under the supervision of dr. Maarten Doornbos and prof. dr. Laura Heitman. This project focused on the effect of ions on activation of the human metabotropic glutamate receptor 2 (mGluR2).

In September 2015, Huub started the Master's program Bio-Pharmaceutical Sciences at Leiden University with an emphasis on molecular pharmacology. He performed a nine-month internship at the division of Drug Discovery and Safety (formerly Medicinal Chemistry) of the LACDR under the supervision of dr. Andrea Martella and prof. dr. Laura Heitman. This project was in collaboration with Hoffmann-La Roche and focused on the characterization of a novel radiolabeled inverse agonist for the human cannabinoid receptor 2, which resulted in a co-authorship on a publication in *Molecular Pharmacology*. After finishing this project, Huub wrote a literature review on the use of nanoparticles in allergy vaccines under the supervision of dr. Romain Lebox. For his second research project, he performed a six-month internship at the biopharmaceutical company Heptares (currently Sosei Heptares) in Welwyn Garden City, United Kingdom, under the supervision of dr. Elena Segala. This project was in collaboration with prof. dr. Ad IJzerman from the division of Drug Discovery and Safety of the LACDR and focused on the ligand binding mechanisms of partial and inverse agonists of the adenosine A2A receptor using X-ray crystallography. Huub successfully obtained his Master's degree with a cum laude distinction in 2017.

After his studies, Huub coordinated a second-year Bachelor's practical course on Cellular Biochemistry at Leiden University. He then pursued his interest in molecular pharmacology and started as a PhD candidate at the division of Drug Discovery and Safety of the LACDR in 2018 under the supervision of prof. dr. Laura Heitman and prof. dr. Ad IJzerman. The project was part of the European

RESOLUTE consortium, which is funded by the Innovative Medicines Initiative (IMI), European Union and major pharmaceutical companies (EFPIA). The topic of his research was the development of cell-based label-free assays for solute carrier transporters, with the aim to use such assays in drug discovery. During his PhD, Huub frequently joined consortium meetings and work package videoconferences, where he presented his work via oral and poster presentations. Moreover, he presented posters at national and international conferences, being awarded with a poster prize at the FIGON Dutch Medicines Days 2019 in Leiden. Huub initiated several collaborations with RESOLUTE partners that resulted in two joint publications, both of which are included in this thesis.

Huub continued his career as a Research Scientist at Artica Therapeutics, taking on new challenges in drug discovery and development.

ACKNOWLEDGEMENTS

Prior to the start of my PhD trajectory, I looked up to the immense and daring task of compiling and writing this thesis. While four years may seem a long time at first, the pace at which time flies by during this academic journey can only be comprehended by living the experience firsthand. This might seem frightening if you are in the understanding that you are at it on your own. Although I am indeed the single person whose name is on the title page of this book, luckily I have never been alone during this four year adventure (which half of the time coincided with the COVID-19 pandemic). In fact, I have had the pleasure to work with the most experienced, fun, social and helpful people I could have ever wished for. I have reserved this section to express my gratitude towards those who have significantly contributed to the scientific content, substantially increased my motivation and considerably decreased my worries.

First and foremost, I owe my PhD position at the DDS division as well as most of my knowledge on the topics of this thesis to my promotors Ad IJzerman and Laura Heitman. It is under their supervision that I gained the confidence and perseverance to set up several interesting projects and bring them to completion. Their approach to conduct research by creating a socially open and kind environment has been a source of inspiration – one that certainly keeps me motivated for the years to come.

Moreover, I am indebted to the partners of the RESOLUTE consortium, which has been an integral part of my PhD. Without the many (virtual) work package meetings and near endless supply of cell lines and reagents my projects would not have advanced at the rate that they have. Thanks to Giulio, Daniel, Alvaro, Tabea and all the others for keeping the SLC spirit afloat, even over great distances and during lockdowns. Also, a big thanks to the CeMM and Axxam teams, which have greatly contributed to several chapters of this thesis.

Although an interesting topic is important to keep a PhD going, having a nice work environment is even more essential to get things done. Therefore, I want to thank all of my colleagues who I have had the pleasure to work with over the past years. Special thanks to Anna – who taught me how to study transporters using xCELLigence – Cas, Chenlin, Jara, Jeremy, Henk, Lisa, Maarten, Natalia, Rongfang, Tamara, Xue, Xuesong and Yao for being an amazing Bio Group.

Thanks to Lia, the best secretary ever! Thanks to Brandon, Marina and Gerard, who have contributed their computational genius to this thesis. And of course thanks to everybody else for the fun times!

Most of the data in this thesis have been generated by highly motivated students, without whom I would still be doing experiments in the lab. Thanks to Jeremy, Julie, Wieke, Peter, Laura and all other internship students for sitting through our meetings and data sessions, and for all of your enthusiasm and endurance in the lab.

Lots of thanks and respect to my friends and family who took the time to listen to my complaints, ideas, poster presentations and proud moments.

Lastly and most importantly, I could not have done any of this without the love and unconditional support of Fleur. You got me through low points, helped me put things into perspective, kept me motivated and celebrated all victories over the past years.

